University of California
Santa Barbara

An Apparatus for Dynamical Quantum Emulation Using Ultracold Lithium

A dissertation submitted in partial satisfaction
of the requirements for the degree

Doctor of Philosophy
in
Physics

by

Zachary A. Geiger

Committee in charge:

Professor David M. Weld, Chair
Professor Matthew P.A. Fisher
Professor Andrew Jayich

January 2018

The Dissertation of Zachary A. Geiger is approved.

Professor Matthew P.A. Fisher

Professor Andrew Jayich

Professor David M. Weld, Committee Chair

December 2017

An Apparatus for Dynamical Quantum Emulation Using Ultracold Lithium

by

Zachary A. Geiger

On Wednesdays, we wear pink.

Karen Smith, *Mean Girls* (2004)

Acknowledgements

I'd first like to thank my friends and family who have supported me for these past 6 (ish) years. Grad school is a marathon–not a sprint–and it takes a healthy amount of support to pull through the tough times. And for that support, I am forever grateful.

I came to UCSB in September of 2011. David (Weld) was a new faculty member at the time and was looking for new students. When I joined his group the lab was a box of computer parts and a temporary lab bay. I joined for the promise of being able to do *all the things*, and I certainly got what I wanted. From days spent drilling holes in concrete or covered in machine grease, to pondering the finer points of strongly driven quantum systems, graduate school has taught me more than I could have imagined at the outset. I'm grateful to have had David's guidance and mentorship.

Special thanks to Ruwan, Shankari, Kurt, and Kevin. You all made the many hours we spent together enjoyable and instructive. Thanks to my two postdocs, Slava and Toshi: You both showed me that life goes on after getting a PhD. Thanks to partner in machine crime, Kevin, for keeping me on the right side of sanity. Particular thanks to Kurt for his data analysis and theoretical understanding.

To the army of undergrads (in no particular order) Eric, Jacob, Eli, Ian, Andrew, Max, Shura, Ted, Alan, Krutik, Morgan, Ian, Yi, Shuo, James (Hannibal), Erica, Anne, Delia, Vincent, Robert: Mentoring you all has taught me a lot!

Also thanks to: the Sherwin Group for hours of lunchtime entertainment; UCSB Staff: Mike, Jennifer, Dave, Jeff, Guy, Lynne, Dan, Daniel. I'd also like to thank Jean Carlson, Joan-Emma Shea, and Karina Roitman for introducing me to Physics Circus and letting me help inspire the next generation of young physicists-to be.

To present (Peter, Misha, and Quinn) and future Welders: these machines build us as much as we build them. **Use them well**.

Curriculum Vitæ
Zachary A. Geiger

Education

2017	Ph.D. in Physics (Expected), University of California, Santa Barbara.
2014	M.A. in Physics, University of California, Santa Barbara.
2011	B.S. in Physics, *Cum Laude*, University of California, San Diego.
2011	B.A. in Mathematics - Applied Science, *Cum Laude*, University of California, San Diego.

Publications

- Rajagopal, S. V., Fujiwara, K. M., Senaratne, R., Singh, K., **Geiger, Z. A.**, & Weld, D. M. (2017). Quantum Emulation of Extreme Non-Equilibrium Phenomena with Trapped Atoms. Annalen Der Physik, 529(8), 1700008.
- Senaratne, R., Rajagopal, S. V., **Geiger, Z. A.**, Fujiwara, K. M., Lebedev, V., & Weld, D. M. (2015). Effusive atomic oven nozzle design using an aligned microcapillary array. Review of Scientific Instruments, 86(2), 23105.
- Senaratne, R., Rajagopal, S. V., Shimasaki, T., Dotti, P., Fujiwara, K., Singh, K. **Geiger, Z. A.**, & Weld, D. M. (2017). Cold-Atom Quantum Simulation of Ultrafast Dynamics, *in submission*.

Abstract

An Apparatus for Dynamical Quantum Emulation Using Ultracold Lithium

by

Zachary A. Geiger

Quantum emulation of extreme non-equilibrium phenomena is a natural application of the precision and control of ultracold atomic physics experiments. In particular, "Floquet engineering" with an explicitly time-dependent Hamiltonian enables the creation of states of matter that can only exist in the presence of strong driving. In this work, we create and study such tunable strongly driven quantum systems. We use quantum degenerate lithium as a platform because of its light mass, fast tunneling rates, and broadly tunable Feshbach resonance, which allow the study of a wide variety of systems: noninteracting Bosons, strongly interacting many body systems, and bright solitons, to name a few. We describe the experimental setup used to create a ^{7}Li Bose-Einstein condensate as an archetypal quantum platform, and then discuss three key results: the first direct measurement of position-space Bloch oscillations in a cold atom system, the creation of a massive relativistic harmonic oscillator, and finally the demonstration of a new method for controlled long-range quantum coherent transport enabled by Floquet band engineering.

Contents

Introduction

This work consists of five chapters. Chapters 1-4 can be considered a technical handbook for readers interested in understand the workings of the apparatus at levels both conceptual (chapters 1 and 2) and practical (chapters 3 and 4). Chapter 5 contains our work on quantum emulation of dynamical systems.

- **Chapter 1**: A very brief description of some of the more salient theoretical concepts required to understand the atomic physics discussed in this thesis.
- **Chapter 2**: A detailed description of all of the cooling steps we use to make a ^{7}Li Bose-Einstein Condensate (BEC). It is focused on concepts, and relevant experimental parameters.
- **Chapter 3**: A machine-specific guide to the laser systems (separated into subsystems based on functional purpose) used to cool and control atoms. Also included are lattice and scattering length calibration.
- **Chapter 4**: A guide to the mechanical and electrical design, construction, and commissioning of the Lithium apparatus. Included are details on achieving UHV (baking), electromagnet construction, magnetic field calibration, and the surrounding support systems for the experiment (water cooling and computer control).
- **Chapter 5**: A report of some of our experimental results regarding the observation

Acronym	**Meaning**
AMO	Atomic, Molecular, and Optical
AOM	Acousto-Optic Modulator
BEC	Bose Einstein Condensate
BO	Bloch Oscillation
CF	Conflat Flange
CMOT	Compressed MOT
CW	Continuous Wave
D1	$2\ ^2S_{1/2} \rightarrow 2\ ^2P_{1/2}$ transition
D2	$2\ ^2S_{1/2} \rightarrow 2\ ^2P_{3/2}$ transition
DP	Double Pass
EOM	Electro-Optical Modulator
E_R	Recoil Energy
FB	Feshbach
GM	Gray Molasses
HF	High Field
HO	Harmonic Oscillator
IMC	Image Cycler (beam)
IMR	Image Repumper (beam)
MOT	Magneto Optical Trap
MOTc	MOT Cycler (beam)
MOTr	MOT Repumper (beam)
MT	Magnetic Trap
OD	Optical Density
ODT	Optical Dipole Trap
PCO	Imaging Camera
PSD	Phase Space Density
RF	Radio Frequency
RHO	Relativistic Harmonic Oscillator
SHO	Simple Harmonic Oscillator
TA	Tapered Amplifier
TC(1,2)	Transverse Cooling(1,2)
UHV	Ultra High Vacuum
VSCPT	Velocity-Selective Coherent Population Trapping
XODT	Crossed Optical Dipole Trap
ZS	Zeeman Slower

Table 0.1: Useful acronyms

Chapter 1

Just Enough Atomic Physics to Dance with the Red Devil

This introductory chapter is intended to give the reader just enough of an understanding of atomic physics to make sense of the work that follows. It will not form a complete basis for understanding the true richness of the field. For much more thorough discussions of the fundamentals of AMO physics, please see the works of:

- Foot, *Atomic Physics*[1], a good intro to the field, also covers basics of laser cooling and spectroscopy.
- Cohen-Tannoudji and Guery-Odelin, *Advances in atomic physics: an overview*[2], for a discussion of more advanced techniques.
- Friedrich, *Theoretical Atomic Physics*[3], especially useful for understanding selection rules, and internal states.
- Pethick and Smith, *Bose-Einstein Condensation in Dilute Gases*[4], excellent understanding of cooling techniques and the fundamentals of BEC.

- Ketterle, Durfee, and Stamper-Kurn, *Making, probling, and understanding Bose-Einstein condensates*[5], practically everything you wanted to know about BECs and more.

1.1 Level Structure and Russell-Saunders Notation

It is useful to think about the internal states of the atom in terms of the electron's state and allowed transitions thereof. The main handles we have to control atoms in the laboratory are transitions that change the valence electron's state (most commonly electric dipole transition at optical frequencies, and magnetic dipole transitions in the microwave/radiofrequency (RF) regime). Russell-Saunders notation, or term-symbol notation, is a useful shorthand for writing the internal states of the electron assuming the spin-orbit (LS) coupling is small, making L (the orbital angular momentum) and S (the electron spin) good quantum numbers. Another (high magnetic field) limit is the JJ coupling, where M_I and M_J (the projection of the nuclear spin and electron spin onto an external magnetic field) are considered separately (the Paschen-Back regime). Put simply, the notation reads:

$$N\ ^{2S+1}L_J, \tag{1.1}$$

where N is the principal quantum number (usually omitted in this work), S is the spin quantum number, L is the orbital angular momentum quantum number, and J is the total angular momentum quantum number ($J = L + S$). This term typically refers to the valence electron in the case of alkali atoms (like ^{7}Li). For instance, the ground state of ^{7}Li is the $2^2S_{1/2}$ state, where $N = 2$ (the two inner electrons forming a closed shell for $N = 1$, while the valence electron occupies the $N = 2$ orbital), $S = 1/2$ (the electron is

spin up or spin down), $L = 0$ (indicated with by S in the usual spectroscopic notation [where S= 0, P=1, D= 2, F= 3, etc.]), and $J = L + S = 0 + 1/2 = 1/2$ (indicating that only the electron spin affects the total angular momentum, since the orbital is spherically symmetric).

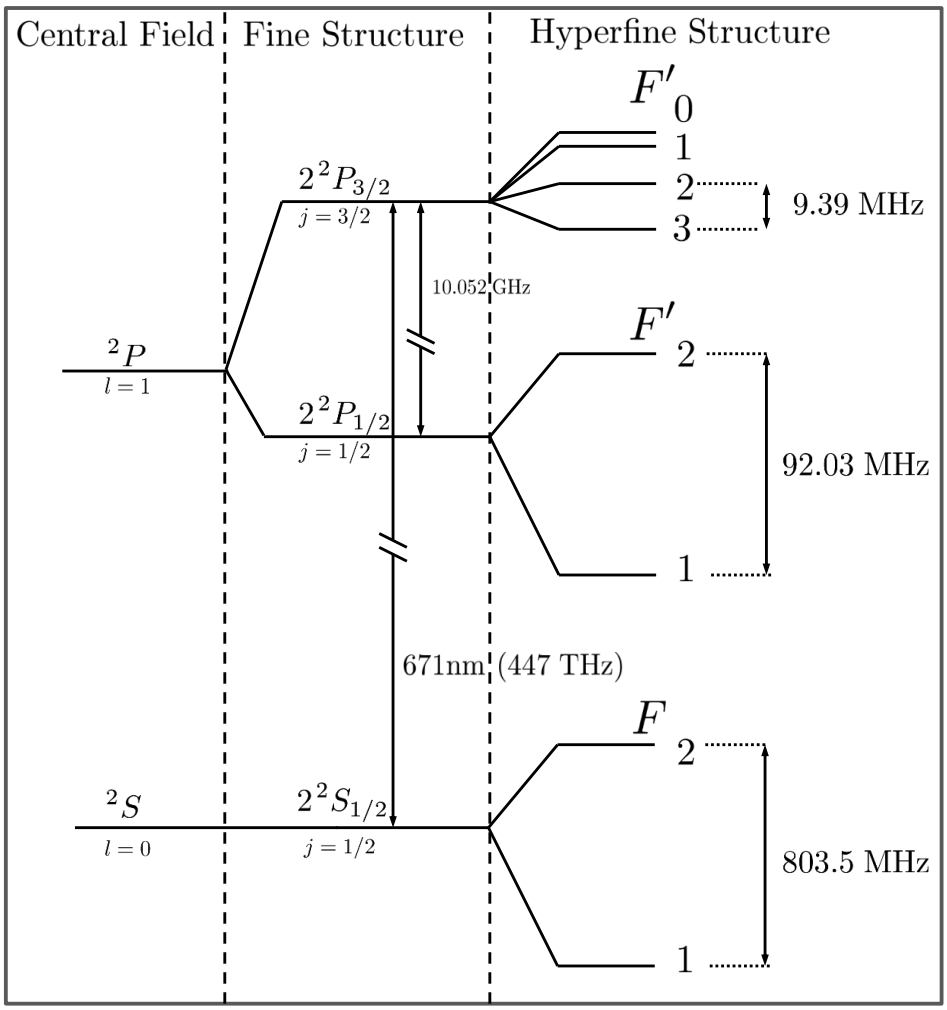

Figure 1.1: Central Field, Fine Structure and Hyperfine Structure splitting of Energy Levels in ^{7}Li, with some relevant energy scales shown[6]. Figure not to scale.

The $S \to P$ transition is known as the central field splitting, but does not take into account the electron spin (only its principal quantum number N). In lithium the central field splitting is around 671 nm (447 THz).

The fine structure splitting takes the spin-orbit coupling into account. The first transitions in ^{7}Li involve a change in the orbital of the electron from the spherically symmetric s-orbital to the double-lobe p-orbital ($L = 1$), which gives the electron a non-zero orbital angular momentum. Further, the electron spin can either be aligned with the orbital angular momentum, or anti-aligned, giving the fine structure splitting between the $2^2P_{3/2}$ ($J = L + S = 1 + 1/2 = 3/2$) and $2^2P_{1/2}$ ($J = L - S = 1 - 1/2 = 1/2$) states (the D2 and D1 lines, respectively).

Finally, the hyperfine structure splitting takes into account the interaction between the electron and the atom's nuclear spin. ^{7}Li's nucleus is a composite of three protons and four neutrons, and has a nuclear spin, I, of 3/2. The hyperfine splitting results from the energy difference depending on the alignment of these two spins. This is summarized with the quantum number $F = I + J$. For the ground state ($2^2S_{1/2}$) and first excited state ($2^2P_{1/2}$), F can be 2 ($3/2 + 1/2$) or 1 ($3/2 - 1/2$). For the second excited state ($2^2P_{3/2}$), F can take any integer value between 3 ($3/2 + 3/2$) and 0 ($3/2 - 3/2$). As a shorthand, an atom in the $F = 2$, m_F=2 ground state can be written as (2,2) or more formally as $|2, 2\rangle$. These numbers allow us to easily discuss and describe the cooling process.

In summary, Russell-Saunders notation is a shorthand for labeling the relevant internal states of the atom and provides a useful language for discussing allowed transitions.

1.2 Optical Transitions

Atom-photon interactions allow us to control the internal and external degrees of freedom of our systems primarily via laser cooling and optical pumping. We primarily discuss the internal states of the atoms in terms of the quantum numbers F and m_F (the projection of F onto an external magnetic field).

The most relevant states/optical transitions are the ground state $F = 2$ to excited state (usually indicated by $'$) $F' = 3$ transition (the so-called "cycling" transition), and $F = 1$ to $F' = 2$ (the "repumping" transition). The two ground states ($F = 1$ and $F = 2$) are split by 803.5 MHz. The cycling transition is normally one that drives the atom in a closed transition, that is, the spontaneous decay from the excited state should ideally be only to the original ground state. This means that a single laser frequency (and polarization) is capable of driving a large number of transitions without causing the atom to decay into an optically inaccessible state. In atoms that have a well-resolved upper hyperfine mainifold (e.g. in Rubidium, where the splitting is tens of MHz [7]) this cycling transition is "closed," that is, the probability of decay into the other ground state is small. Lithium's "cycling" transition is unresolved as a consequence of the $F' = 3$ and $F' = 2$ upper hyperfine states being separated by ≈ 9 MHz, which is comparable to the linewidth of the transition (Γ=5.9 MHz). Due to this small splitting, and the experimental reality of imperfect polarization of laser beams in the lab, there is a reasonably high probability (about one in five) that an atom excited with $F = 2 \rightarrow F' = 3$ light will instead end up in $F' = 2$, and then decay into the $F = 1$ ground state, rendering the atom optically dark to the "cycling" light, thus necessitating the use of a second resonant beam (the repumper) to address these atoms.

Despite being well resolved, the upper hyperfine states found in the $2^2P_{1/2}$ manifold (the D1 transition) does not have a "stretched" state that allows a σ_+ transition to occur, and so optical pumping on the D1 line is as poor if not worse than for $2^2P_{3/2}$ (D2).

1.3 Zeeman Shift

An applied magnetic field can change the energy of an atomic transition provided the states couple to the magnetic field (i.e. have $m_F \neq 0$). To first order, the D1 and D2

transitions have a Zeeman shifts of ≈ 1.4 MHz/G. The change in energy from an applied field $\vec{B}$ of a state with quantum number m_F is[1]:

$$\Delta E = g_F m_F \mu_b B \tag{1.2}$$

The sign of this energy shift depends on the atom's Lande g-factor g_F. We use the Zeeman shift to change the energy of electric dipole transitions to compensate for the Doppler shift in the Zeeman slower. Additionally, the Zeeman shift gives rise to the ability to trap atoms in a magnetic field gradient (the magnetic trap and magneto-optical trap, or MOT), provided the atoms have energy that increases with increasing field strength ("low field seeking"). Specifically for the $2S_{1/2}$ states: $F = 2 : g_F = 1/2, F = 1 : g_F = -1/2$, so $|F, m_F\rangle = |1, -1\rangle, |2, 1\rangle,$ and $|2, 2\rangle$ are all magnetically trappable, while $|1, 1\rangle, |2, -1\rangle$, and $|2, -2\rangle$ are "high field seeking" and are anti-trapped. States $|1, 0\rangle,$ and $|2, 0\rangle$ experience no first order Zeeman shift and are almost unperturbed by magnetic fields.

For higher applied fields $\vec{B}$, F and m_F are no longer good quantum numbers and we must switch to the JJ coupling scheme, where the spin of the nucleus and the spin of the electron are treated separately. For a more complete treatment of the Zeeman shifts in this regime, see Fig. 3.12.

1.4 Feshbach Resonances

One important tool we use in the experiment is the ability to change the s-wave scattering length by means of a Feshbach resonance[8][9]. If we consider the scattering process in terms of the interatomic potential (see Fig. 1.2 for illustration), then we can conceive of the resonance as an interaction between a scattering state in one potential

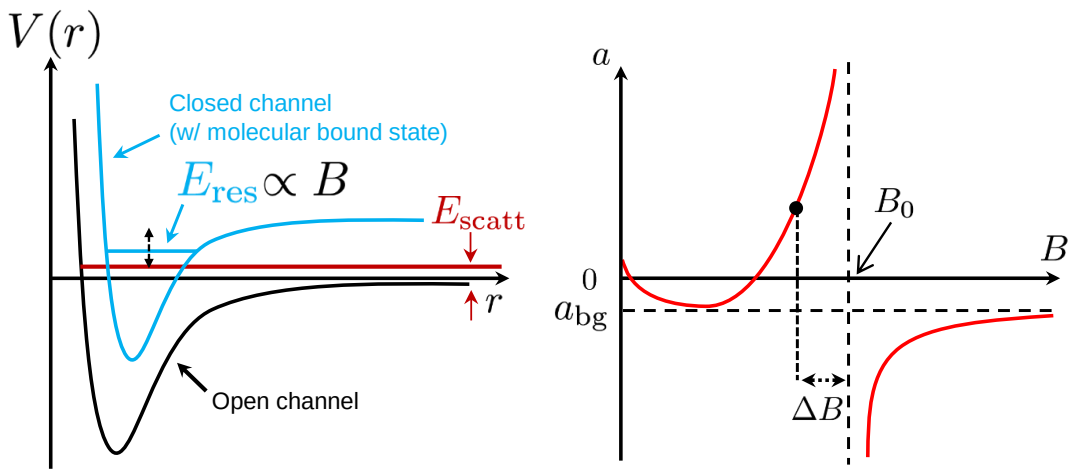

Figure 1.2: Schematic of a Feshbach resonance. Left: simplified potential with molecular bound state energy E_{res}, which shifts with applied magnetic field B. When $E_{\text{res}} = E_{\text{scatt}}$ the scattering length a diverges. Right: cartoon of scattering length a as a function of the magnetic field B.

(the open channel) and a bound state in another potential (the closed channel). The relative energy of the closed channel changes in response to an applied magnetic field $\vec{B}$. When the energy of the bound state equals the scattering energy ($E_{\text{res}} = E_{\text{scatt}}$) the scattering length a diverges. The two atoms cannot actually form a molecule while conserving both energy and momentum, so no molecule forms in this two body scattering process. The exact functional form of the scattering length a as a function of applied field $\vec{B}$ is difficult to calculate, but an approximation to the scattering length near the resonance takes the functional form[10]:

$$a(B) = a_{\text{bg}}\left(1 - \frac{\Delta}{B - B_0}\right), \tag{1.3}$$

where for ^{7}Li $a_{\text{bg}} = -24.5$, $\Delta = 192.3$, $B_0 = 736.8$. $a > 0$ a_0 means that the atoms have repulsive interactions when they scatter, while $a < 0$ a_0 indicates the atoms will attract

$\boldsymbol{B}$ (G)	$\boldsymbol{a}$ (a_0)
0	7.7
$\approx$ 162	0
$\approx$ 375	-4.5
543.6	0
720	294
736.8	$\pm\infty$

Table 1.1: s-wave scattering lengths for collisions between $|1,1\rangle$ atoms for selected values of the applied magnetic field (the "Feshbach" field). The slope of the scattering length around $B = 543.6$ G is roughly 0.07 a_0/G. Numbers from [10] and [11].

each another ("clump up"). This approximation is accurate near the resonance ($\pm$100 G), but is not as good of an estimate of the scattering length near $a = 0\ a_0$ (the zero crossing) around 543.6 G. According to coupled channel calculations[11] the slope of the scattering length is estimated to be half as much as the number predicted by Eqn. 1.3 (see Table 1.1). Tuning the scattering length not only allows for the creation of large Bose Einstein condensates, but also enables the study of a wide variety of systems: from non-interacting bosons ($a = 0\ a_0$), to strongly attractively interacting clouds ($a \to \infty$), and it even allows for the formation of solitons ($a < 0\ a_0$). This broad Feshbach resonance allows for a powerful experimental tool: the precise, easily to implement, control over ^{7}Li's scattering length.

1.5 Bose-Einstein Condensation

Lithium's $|2,2\rangle$ state has a negative scattering length at $\vec{B} = 0$, which limited early attempts to create BECs using ^{7}Li[12][13]. The Feshbach resonance for the $|1,1\rangle$ state allows a to be tuned to a region where Bose Einstein condensation is possible (a few hundred a_0)[14]. To understand the basics of Bose Einstein condensation, we'll first start with non-interacting Bosons. Bose Einstein condensation can roughly be understood in terms of particle-wave duality; this treatment largely follows [15]. We can use the thermal

de Broglie wavelength (λ_{dB}) to get a useful approximation for the wavelength of a matter wave. Bose Einstein condensation occurs when $\lambda_{\mathrm{dB}} \approx$ the spacing between atoms. The thermal de Broglie wavelength of a particle can be calculated as

$$\lambda_{\mathrm{dB}} = \frac{\hbar}{\sqrt{2\pi m k_{\mathrm{B}} T}}, \tag{1.4}$$

where the wavefunction overlap between particles determines by the phase-space density (PSD for short) D:

$$D = n\lambda_{\mathrm{dB}}^3. \tag{1.5}$$

The phase space density gives a useful shorthand for not only how dense a cloud is, but how cold it is. To achieve a BEC, the cloud must have not only sufficient density, but also low enough temperature such that the particles wavefunctions overlap. A hot, dense cloud can still have a low PSD, for instance.

The formation of a BEC can be derived from purely statistical arguments. An ideal gas of bosons (in 3D) will obey the Bose distribution for identical particles with energy ϵ_ν (Eqn. 1.6). The modification from the plain Maxwell-Boltzmann statistics comes from the fact that two Bosons are quantum mechanically indistinguishable from one another (Fermions obey a similar distribution, except with a +1 in the denominator instead of the -1 for Bosons, or +0 for classical particles). The number of particles N_ν in state ν in a system with chemical potential μ and temperature T is:

$$N_\nu = \frac{1}{e^{(\epsilon_\nu - \mu)/k_{\mathrm{B}}T} - 1}, \tag{1.6}$$

where we can calculate the total number of particles in the system by summing over all energies ν such that $N = \sum_\nu N_\nu$, under assumption that the chemical potential (μ) is less than the ground state energy (ϵ_0) (which is physically motivated by arguing that

states must have occupation number ≥ 0).

The total number of particles can be split into the sum of the ground state fraction (N_0) and thermal component (N_{th}), calculated by summing over all energies $\nu > 0$:

$$N = N_0 + N_{\text{th}} = N_0 + \sum_{\nu=1}^{\infty} \frac{1}{e^{(\epsilon_\nu - \mu)/k_{\text{B}}T} - 1}, \tag{1.7}$$

where for a fixed temperature T, N_{th} reaches a maximum when $\mu = \epsilon_0$, meaning the thermal component is

$$N_{\text{th,max}} = \sum_{\nu=1}^{\infty} \frac{1}{e^{(\epsilon_\nu - \epsilon_0)/k_{\text{B}}T} - 1}, \tag{1.8}$$

which means that as $T \to 0$, the thermal fraction decreases to the point where $N_{\text{th}} < N$, the total number of particles in the system. As the temperature decreases, n_0 the fraction of atoms occupying the ground state can be calculated as the ratio of condensed atoms to the total number:

$$n_0 = \frac{N_0}{N} = 1 - \left(\frac{T}{T_c}\right)^{3/2}, \tag{1.9}$$

where the critical temperature where $N_{\text{th,max}}$ reaches N, and BEC formation begins is

$$T_c = \frac{\hbar\bar{\omega}}{k_{\text{B}}} \left(\frac{N}{\zeta(3)}\right)^{1/3} \approx 4.5 \frac{\bar{\omega}/2\pi}{100 \text{ Hz}} N^{1/3} \text{ nK}, \tag{1.10}$$

where $\bar{\omega} = (\omega_x \omega_y \omega_z)^{1/3}$ is the geometric average of the trap frequencies and $\zeta(3)$ is the Riemann zeta function ($\zeta(3) \approx 1.2$). This means that the number of particles in the ground state N_0 must approach N as $T \to 0$, causing formation of a pure Bose-Einstein Condensate (BEC) of N particles with ground state energy ϵ_0 (at $T = 0$). For example, in a system of $5{\times}10^5$ ^{7}Li atoms in a crossed optical dipole trap with $\omega_x = \omega_y = 1/2\ \omega_z$, $T_c \approx 750$ nK.

1.6 Interacting Bose Gas

The above treatment considered only non-interacting Bosons. In reality, atomic systems will interact with some finite energy. We can treat the BEC as a macroscopic particle with a single wavefunction Ψ, and use the Gross-Pitaevskii equation[16] to describe the time evolution of this wavefunction using the time dependent Schrödinger equation with external potential $V(\mathbf{r})$ and mean-field interaction strength g:

$$i\hbar\frac{\partial\Psi(\mathbf{r},t)}{\partial t} = \left(-\frac{\hbar^2}{2m}\nabla^2 + V(\mathbf{r}) + g|\Psi(\mathbf{r},t)|^2\right)\Psi(\mathbf{r},t), \tag{1.11}$$

to model the dynamics of the Bose gas. Particularly useful is the notion that $|\Psi(\mathbf{r},t)|^2 = N/V$, which can be used to calculate the energy scales of the mean-field particle interaction $g|\Psi^2|$ for comparison to other times scales in the problem (for instance, the tunneling rate J in the Bose-Hubbard model).

Further, approximating the BEC as a gas of noninteracting Bosons can lead to some problems. Namely, approximating the size of the cloud as the ground state harmonic oscillator wavefunction (a_{HO}) leads to a prediction of a much smaller spatial extent than is actually observed. For a crossed optical dipole trap with transverse frequencies ω_x, ω_y of 1 kHz (and $\omega_z = 2$ kHz):

$$\bar{\omega} = (\omega_x\omega_y\omega_z)^{1/3} \tag{1.12}$$

$$a_{\mathrm{HO}} = (\hbar/m\bar{\omega})^{1/2} = 2.7\ \mu\mathrm{m} \tag{1.13}$$

Our observed cloud sizes are about 15 times bigger than this estimate (see Fig. 2.20a). The Thomas-Fermi radius gives an estimate which includes the repulsive interaction

(scattering) between neighboring atoms, expressed as a modification to a_{HO}[17]:

$$R_{\mathrm{TF}} = a_{\mathrm{HO}} \left(\frac{N_{\mathrm{atoms}} \cdot a}{a_{\mathrm{HO}}} \right)^{1/5}. \tag{1.14}$$

For our system, $a = 294\ a_0$, and $N_{\mathrm{atoms}} \approx 3 \times 10^5$ give $R_{\mathrm{TF}} = 20\ \mu$m (corresponding to a 4σ diameter of 80 μm, much closer to the observed cloud size). As an aside, R_{TF} only approaches a_{HO} when $a < 0.01\ a_0$.

Chapter 2

The Road to BEC

A "castle" of cooling techniques are required to cool lithium to quantum degeneracy. Here is a summary of our process to make a Bose Einstein condensate (BEC) and the approximate temperatures, atom numbers and densities (PSD) achieved:

Stage	**Temperature**	**Atom Number**	**PSD**
Oven	720 K (1290 m/s)	1.2×10^{12}/s	N/A
Zeeman Slower	1 K (50 m/s)	3×10^{8}/s	N/A
MOT	1 mK	5×10^{9}	10^{-7}
CMOT	0.5 mk	5×10^{9}	10^{-7}
GM	100 μK	3×10^{9}	10^{-5}
RF Evap	10 μK	80×10^{6}	10^{-2}
ODT	4 μK	20×10^{6}	10^{-1}
BEC	100 nK	1×10^{5}	10

Table 2.1: List of cooling stages, approximate temperatures (velocities where appropriate), atom numbers (flux where appropriate), and approximate PSD.

These cooling techniques can roughly be divided into two categories: optical cooling and evaporative cooling. The magneto optical trap (MOT) and compressed magneto optical trap (CMOT) are forms of Doppler (optical) cooling, while gray molasses (GM) is a form of sub-Doppler (optical cooling). MOTs can cool below the Doppler limit, but lithium's unresolved excited states limit the temperature to around 1 mK. All of optical

cooling techniques are fundamentally limited by the momentum carried by a single photon (known as the recoil limit, discussed below). To cool beyond this limit and make a BEC, we employ evaporative cooling: first in a magnetic trap with radiofrequency evaporation (RF evap), and then later in an optical dipole trap (ODT) with optical evaporation. The final result of these cooling stages is a BEC at a temperature a few billionths of a degree above absolute zero.

2.1 Doppler Cooling (Optical Molasses)

Doppler cooling exploits the fact that electronic dipole transitions are relatively narrow (roughly speaking, only photons within the linewidth Γ of the transition excite the atom), and that photons carry momentum $p = \hbar k$ and can remove energy from an atom or gas of atoms. An ideal optical transition for cooling would be between "stretched" states, or a transition from a ground state $|F, m_F\rangle$ to an excited $|F', m_{F+1}\rangle$ state that could only spontaneously decay back to the original state due to selection rules. Laser light with specific energy and polarization would therefore allow the atom to undergo an unlimited number of optical transitions without fear of the atom being pumped into any other ground state. In principle addressing such a transition with a red-detuned photon would continuously remove energy from the atom until it reached the recoil limit. For this reason we refer to this transition as the "cooling" or "cycling" transition. In reality, transitions tend to be much more narrow (on the order of MHz) than the splitting between ground states (hundreds of MHz), and imperfect optical pumping means that atoms do not always return to their initial state, making them optically inaccessible to the applied laser light (a "dark" state).

Lithium is an atom with poor optical pumping. Specifically, it lacks a well resolved upper hyperfine manifold. The $F' = 2$ and $F' = 3$ manifolds of the $^2P_{3/2}$ excited state are

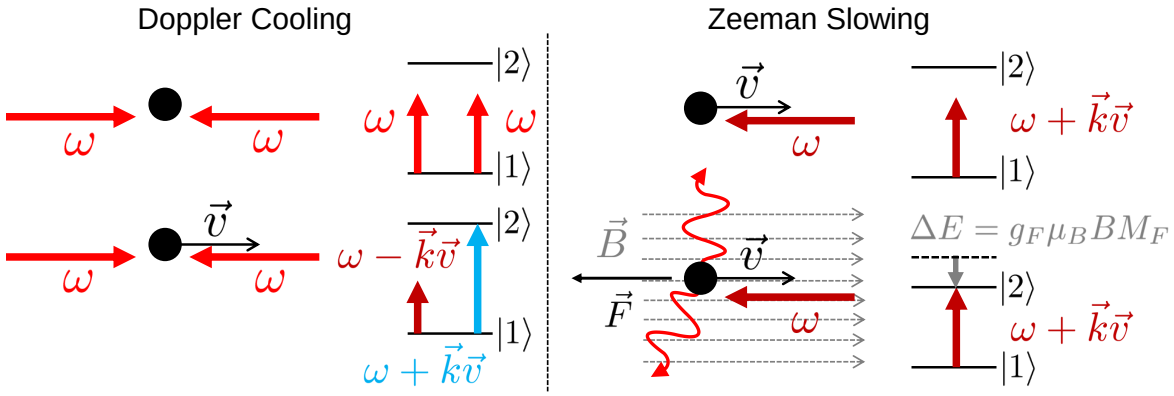

Figure 2.1: Left: illustration of Doppler cooling. In the atom's frame of reference, the Doppler shift alters the apparent frequency of counter propagating photons, making the transition resonant (farther off-resonant) with the $|1\rangle \rightarrow |2\rangle$ transition when the atom is moving toward (away from) a laser beam with frequency ω. Right: illustration of Zeeman slowing. An applied magnetic field changes the energy of the $|1\rangle \rightarrow |2\rangle$ transition (Zeeman shift), counteracting the effect of the Doppler shift.

close enough in energy that "cycling" light can excite an atom not only into $F' = 3$, but also $F' = 2$, after which it can decay into the lower energy $F = 1$ ground state (see Fig 1.1). Practically speaking, this means that during Doppler cooling atoms will leave the $F = 2$ ground state and end up in the $F = 1$ ground state where they are optically dark to the cycling light. We therefore must apply an additional color of light, with an added 813.5 MHz of energy (the splitting between $F = 1$ and $F = 2$ ground states, plus 10 MHz to address the upper hyperfine splitting between $F' = 2$ and $F' = 3$) to "repump" atoms out of the $F = 1$ manifold and allow them to be cooled by the "cycler" light again. For lithium, the branching ratio between these two states is approximately 5:1[3], meaning the required intensity of this repump light is 10-20% of the cycling light.

See Figure 2.1 for schematic of Doppler cooling. The basic principle is as follows: A red-detuned photon (less energy than the transition) will not be absorbed by an atom unless the atom is traveling towards the photon. The blueshift caused by this motion brings the photon into resonance with the atomic transition, causing the atom to absorb

the photon lose momentum. A blue-detuned photon (more energy than the transition) will conversely only be absorbed if the atom is traveling away from the photon and has a sufficient redshift (and cause the atom to gain momentum). The net effect of applying red-detuned light to atoms is that the atoms will absorb photons and slow down if they are traveling the direction of the applied light: this creates a *frictional* force proportional to their velocity v. A single red-detuned beam of light can be used to slow a beam of atoms (as in the case of the Zeeman slower), while multiple beams of red-detuned light can be used to create optical molasses (in two or three dimensions), or in the presence of a magnetic field *gradient*, give rise to an additional *spatially dependent* force, creating a magneto-optical trap (MOT) (see section 2.3 for a detailed description).

In our experiment we employ multiple stages of optical molasses to cool the transverse directions of motion in the atomic beam. Although referred to as transverse cooling (TC), the two stages of transverse cooling (TC1 and TC2) are in fact two stages of 2D optical molasses. The first stage corrects the initial angular deviation of the atoms coming out of the oven and nozzle. We find that due to slight misalignment of the two halves of the machine, TC1 improves the MOT loading rate most when the 2.5 mW of optical power cools the upward motion of the atomic beam (the vertical degree of freedom); although this improvement is marginal at best, perhaps 5-10%. The second stage of transverse cooling keeps the atomic beam from spreading after the Zeeman slower. The slower only cools along the direction of the atom's motion (from the oven to the main chamber) and causes heating in the transverse directions as the atoms undergo spontaneous emission. TC2 keeps the atoms from spreading apart due to this extra heating, giving them time to enter the trapping region of the MOT. In order to save optical power, we retro-reflect the light from TC2, recycling the 4.5 mW of combined cycler-repump power. TC2 improves our MOT load rate by approximately a factor of two.

Doppler cooling is ultimately limited by the linewidth Γ of the optical transition used

to cool the atoms (see [1] pages 185-190). The atoms will undergo a random walk in velocity space and ultimately cool to a temperature of:

$$k_{\mathrm{B}}T_{\mathrm{Doppler}} = \frac{\hbar\Gamma}{2} \tag{2.1}$$

Sub-Doppler cooling techniques (polarization gradient, or "Sisyphus", cooling, and gray molasses among them) exist which can cool below this temperature. Ultimately however, cooling with resonant laser light is limited by the energy associated with a single photon's momentum. The so-called recoil limit can be calculated using the atom's mass m and the wavenumber of the light k:

$$k_{\mathrm{B}}T_{\mathrm{recoil}} = \frac{\hbar^2 k^2}{2m} \tag{2.2}$$

For lithium, the linewidth of the D1 and D2 transitions are both 5.9 MHz[18] which gives a corresponding Doppler temperature of $T_{\mathrm{Doppler}} = 140\ \mu$K (recall factor 2π in Γ when calculating) and a recoil temperature of $T_{\mathrm{recoil}} = 6\ \mu$K [1], both well above the temperatures required for Bose-Einstein condensation. There exist additional optical cooling techniques for cooling below both T_{Doppler} and T_{recoil}, namely velocity selective coherent population trapping and sup-recoil/polarization gradient or "Sisyphus" cooling, and those will be discussed in section 2.5.

2.2 Zeeman Slower

We generate a beam of atoms by creating a hot gas in the oven (with temperatures around 450°C) and passing it through a nozzle directed toward the main chamber. As atoms exit the oven they travel toward the main chamber at rates of over 1000 m/s. The

[1] Foot calculates $T_{\mathrm{recoil}} = 3\ \mu$K using $\frac{1}{2}k_{\mathrm{B}}T_{\mathrm{recoil}}$, while others, including this work, use $k_{\mathrm{B}}T_{\mathrm{recoil}}$

MOT has a limited capture velocity of approximately 50 m/s, due to the finite number of photons that an atom can scatter before it leaves the trapping region generated by the laser light. This limitation necessitates a pre-cooling of the atomic beam as it comes out of the oven. We cool atoms by shooting a beam of counter-propagating resonant light towards them, causing stimulated emission and momentum transfer from the photons, slowing the atoms (see Fig. 2.1 for illustration). As they slow down, the Doppler shift causes the apparent color of the light decrease, which changes the resonant condition of the transition over the scale of a GHz (recall the linewidth of lithium's main transition is 5.9 MHz). The Zeeman slower is a tapered solenoid that compensates this Doppler shift with an applied Zeeman shift ($\Delta E_{\text{Zeeman}} = g_F m_F \mu_b B = 1.4$ MHz/G for the D2 transition). We use a spin-flip Zeeman slower designed to capture a velocity class of atoms at (and below) 1000 m/s and deliver them at an exit velocity of 50 m/s. A spin-flip slower (as opposed to a decreasing field slower) allows the slower light to be far-detuned from the zero-field D2 transition, allowing the light to pass through the MOT without perturbing it.

To get estimate the number of atoms delivered in this way, we integrate the Maxwell-Boltzmann speed distribution (Eqn. 2.4), sometimes referred to as the 1D Maxwell-Boltzmann distribution, which indicates that a peak capture velocity of 1000 m/s will capture 72% of the atoms in the beam. This is only a 10% reduction compared to using the peak velocity of 1290 m/s, but corresponds to a 194 G lower peak field (an 18% reduction). Note that integrating the Maxell-Boltzmann distribution alone (Eqn. 2.3) would indicate a capture fraction of only 24%.

$$\mathrm{P_{MB}} = 4\pi v^2 \sqrt{\left(\frac{m}{2\pi k_{\mathrm{B}} T}\right)^3} \exp\left(-\frac{m v^2}{2 k_{\mathrm{B}} T}\right) \tag{2.3}$$

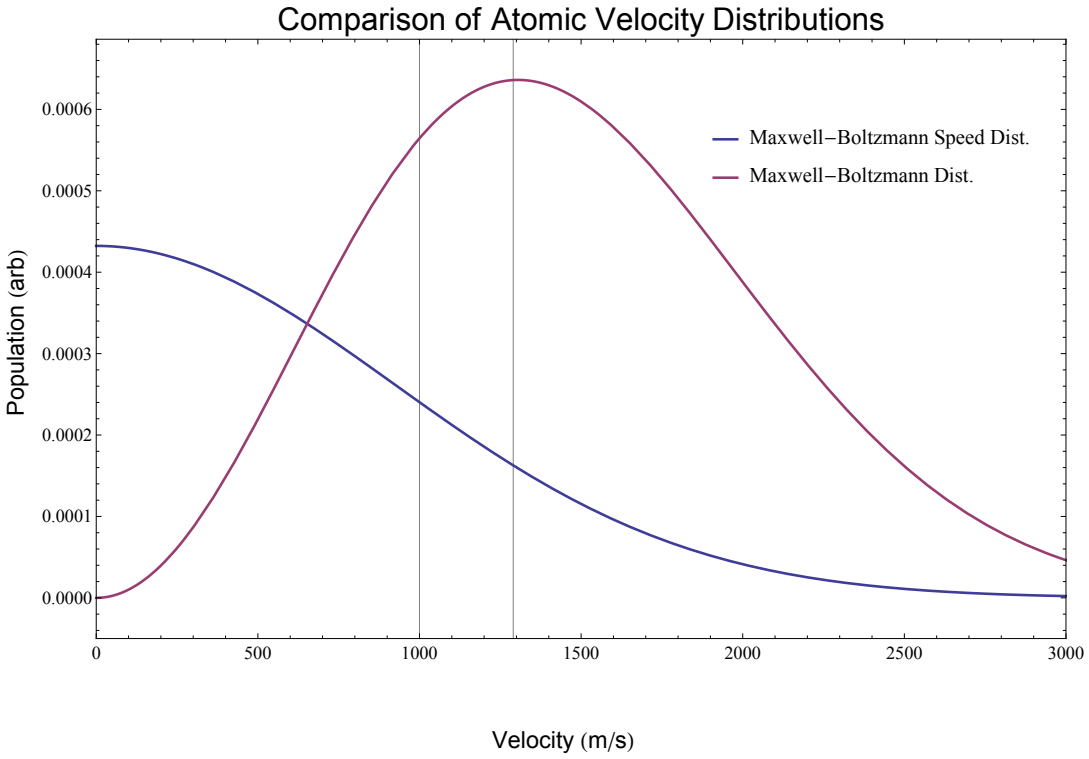

Figure 2.2: Comparison of the thermal distribution of ^{7}Li atoms at 450°C for a gas (Maxwell-Boltzmann, Egn. 2.3) versus a collimated beam (Maxwell-Boltzmann speed distribution, Eqn. 2.4). Vertical lines indicate capture velocity of 1000 m/s and the most probable velocity ($\approx$ 1290 m/s).

$$\mathrm{P_{MB1D}} = \sqrt{\frac{m}{2\pi k_\mathrm{B} T}} \exp\left(-\frac{mv^2}{2k_\mathrm{B}T}\right) \tag{2.4}$$

The slowing light is focused roughly on the nozzle (approximately two meters from where it enters the vacuum chamber), which places the most intense part of the beam on the atoms when they are the fastest. An injection-locked slave laser delivers 60 mW of light through a home-built resonant Electro-Optical Modulator (EOM), which generates 30% sidebands at $\pm$813.5 MHz (the frequency of the hyperfine splitting of the two ground states in lithium, plus the additional energy shift of the excited state) for optical repumping. We only make use of one of the sidebands, the other one is sufficiently

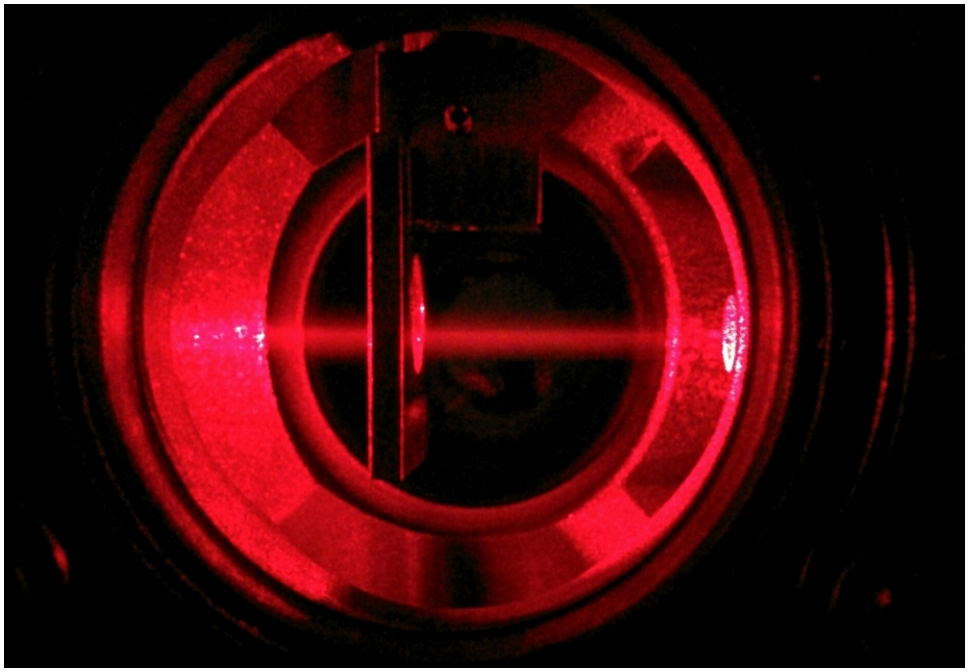

Figure 2.3: Atomic beam fluorescence as atoms leave the oven. Zeeman slower light focused on the nozzle (hidden on the left side of the image) causes atoms to fluoresce as they travel towards the main chamber. The cold plate is pictured in the center, while the first differential pumping tube can be seen just on the right side of the image. Chapter:4 contains details about the physical components pictured here.)

far detuned to not affect the atoms. Ultimately, our experiment operates with 45 mW of light in the slower (about 27 mW "cycling" and 8 mW "repumping" light)

See section 4.3.7 for a discussion of the physical construction of the slower. The chapter on optical systems contains details about the slower's beam path.

2.3 Magneto-Optical Trap (MOT)

The magneto-optical trap (MOT) is in some sense the first step in creating a BEC; it is the first stage when atoms are truly trapped in the machine. The slowed atomic beam that is delivered from the Zeeman slower enters the main chamber where a weak quadrupolar magnetic field (∇B = 20 G/cm) and 6 beams of light intersect. The laser beams are detuned from resonance by -2.5 Γ (red-detuned). As atoms travel away from

the field zero, the Zeeman shift brings the transition into resonance and causes the atoms to experience a force which pushes them back towards the center of the trap.

Maxwell's equations specify that $\nabla \cdot B = 0$, meaning that for a pair of Helmholtz coils, the magnetic field gradient is twice as strong in the z direction as it is in the x or y directions. This means that the magnetic field gradient (and hence the trapping force) along z is twice as strong as in x or y. Following the treatment in [1], the trapping force of the MOT can be expressed:

$$F_{\mathrm{MOT}} = F^{\sigma^+}_{\mathrm{scatt}}(\omega - kv - (\omega_0 + \beta z)) - F^{\sigma^-}_{\mathrm{scatt}}(\omega - kv - (\omega_0 + \beta z)) \tag{2.5}$$

$$\simeq -2\frac{\partial F}{\partial \omega} kv + 2\frac{\partial F}{\partial \omega_0}\beta z \tag{2.6}$$

$$= -\alpha v - \frac{\alpha}{k}\beta z \tag{2.7}$$

where $\beta \cdot z = (g\mu_B/\hbar)\nabla B_z z$ is the position-dependent force derived from the differential Zeeman shift between the ground and excited states along z ($g = 1.4$ MHz/G for ^{7}Li) and α is the frictional (optical molasses) force:

$$\alpha = 2k\frac{\partial F}{\partial \omega} = 4\hbar k^2 \frac{I}{I_{\mathrm{sat}}} \frac{-2\delta/\Gamma}{[1 + (2\delta/\Gamma)^2]^2}. \tag{2.8}$$

Helpful quantities used to estimate the MOT's performance are the maximum force (F_{max}) and capture velocity (v_{catpure}) possible for a beam with red detuning Γ: $F_{\mathrm{max}} = \hbar k\Gamma/2$; $v_{\mathrm{capture}} \simeq \pm\Gamma/k$. Often it is experimentally useful to further red-detune the MOT beams to increase the size of the MOT (which allows for increased atom number).

2.3.1 Initial MOT

We first attempted to use a retro-reflected configuration for our MOT beams, which in theory would have allowed for twice the optical power in each beam. The main limitation

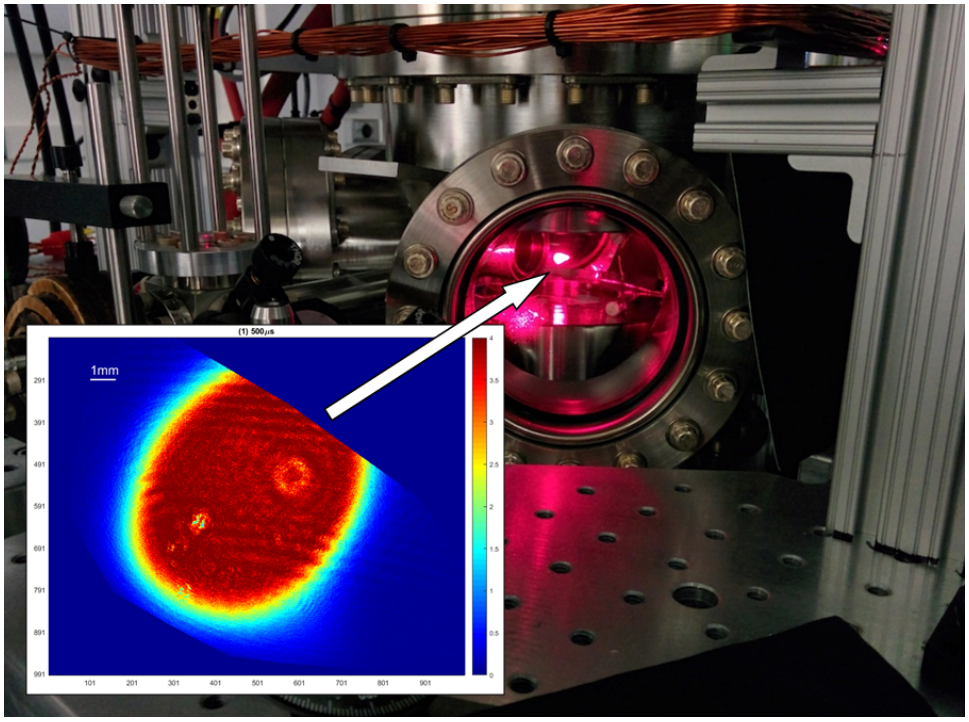

Figure 2.4: Picture of the MOT. The glowing red ball inside the vacuum chamber is approximately 5×10^9 lithium atoms fluorescing due to resonant light used to create the trap. Inset: absorption image of $\approx 3\times10^9$ atoms in the MOT; the image is partially occluded by the chamber, which blocks a portion of the imaging light.

with this scheme is that the MOT becomes optically dense as it loads, which causes the inner region of the MOT beam to lose substantial power. This results in very weak trapping when the beams are retro-reflected, leading to poor confinement of the atoms and ultimately a small MOT-number. We eventually switched to using a 2:6 fiber splitter (custom from OZ Optics), which allows us to directly couple the cycler and repumper light into the same beam path on the machine table.

Our general procedure for obtaining a first MOT is outlined below:

- Ensure the atomic beam is delivering atoms into main chamber. Aligning the machine axis to the slower laser is usually sufficient. Use fluorescence of atoms in the atomic beam (see Fig. 2.3) to ensure atoms are being cooled (it is difficult to see fluorescence in the main chamber due to the increased size of the atomic beam).

- Fix the polarization of each of the MOT beams to the correct handedness (our MOT uses σ^+ for the horizontal beams and σ^- for the vertical beams. For reference, our system's layout is identical to [1] Fig. 9.9(b)).

- Using the geometry of the main chamber (ie. the position of the beams on the viewports), align the beams roughly onto the center of the trapping region where the MOT will form. Large MOT beams make this alignment less sensitive.

- Ensure each pair of beams are co-linear with their partner (ie. the up-going beam is overlapped onto the down-going beam), and that their divergence is roughly equal.

- Power balance each pair of beams. An iris of fixed size and a power meter allow easy measurement of approximate size/power/focusing of each beam pre- and post-chamber.

- Modulate the current in the MOT magnets around the design current/gradient slowly (approximately 1 Hz). Look for fluorescence to happen in the shape of a spherical shell near the center of the chamber. Use motion of the fluorescence as a sensitive indicator of the MOT beams' alignment. Move the beams in pairs until the fluorescence is maximized and shell appears spherical.

- Once the shell is only increasing/decreasing in size and not moving macroscopically, stop modulating the current and a small MOT should form.

- Using a camera to observe the size and shape of the MOT. Small adjustments to each beam's divergence will alter the MOT's shape and position. It is critical to load the MOT at the center of the magnetic field gradient to prevent heating in the magnetic trap later.

- Use a photodiode to observe the MOT fluorescence. A square wave on/off modulation on the repumping light is a good way of looking at the loading rate of the atoms in the MOT. Use this signal to tweak the MOT load rate by adjusting the beams' alignment and focusing/divergence. Optimize the current in the Zeeman slower sections (from closest to the main chamber → oven).

2.3.2 Current MOT

Our MOT numbers were limited by the geometry of the chamber. The side re-entrant window forced the angle of the 4 horizontal MOT beams to be approximately 63° instead of an orthogonal 90°, thereby reducing our lateral confinement. We remedied this problem by adding two additional 2:2 fiber splitters (Thorlabs TW630R5A2) on the two most powerful arms of the already existing 2:6 fiber splitter we were using to make our MOT. This gave us four 'strong' beams (used for the vertical and helper beams) and four 'weak' beams (used for the remaining horizontal beams). The horizontal "MOT helper" beams (E→W and W→E) enable us to increase our MOT numbers in excess of 5×10^9. Additionally, we had to employ Thorlabs filter flippers (MFF101) to allow us to use the size re-entrant axis for lattices.

Each MOT beam is approximately 1" in diameter, but they have slightly different focal conditions as constrained by the CMOT dymanics (see section below).

The MOT consists of approximately 80 mW of cycling power and 20 mW of repump power detuned at -2.5Γ from resonance. This creates a trapping volume on the scale of 1 cm with a capture velocity near 50 m/s.

Beam	Power (mW)
NW→SE	9.0
SE→NW	7.5
NE→SW	8.0
SW→NE	9.0
E→W	22.0
W→E	11
Top→Bottom	18.5
Bottom→Top	23.0

Table 2.2: Summary of MOT beams and powers. Cardinal directions indicate the direction of propagation through the main chamber (see Figure 2.5). Repump/Cycler ratio ≈ 20%. Total optical power ≈ 110 mW. We reference the power in the SW→NE beam as an indicator of overall MOT power and fiber coupling efficiency. Beam power levels fluctuate from day-to-day on the scale of a few tenths of mW.

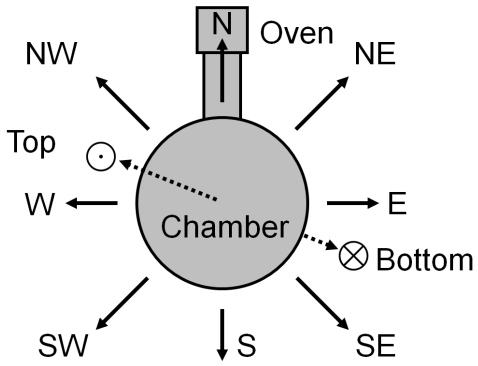

Figure 2.5: Schematic layout of machine indicating cardinal directions relative to the oven. See corresponding table of powers (Table 2.2).

2.4 Compressed MOT (CMOT)

In the second stage of cooling we increase the field gradient from 20 G/cm to 100 G/cm during the last 28 ms of the MOT stage (while a shutter turns off the Zeeman slower light). We then bring the cycling laser closer to resonance (decreasing the detuning from -4.5Γ to -2Γ in 1 ms, optical power decreases by a factor of 2 to ≈ 5 mW), which causes the density of the atomic cloud to increase roughly by a factor of 2. The repumper is kept at a fixed frequency, but decreased in intensity by a factor of 4 (nearly turning it off). This does a few things: the increased field gradient squeezes the atoms together,

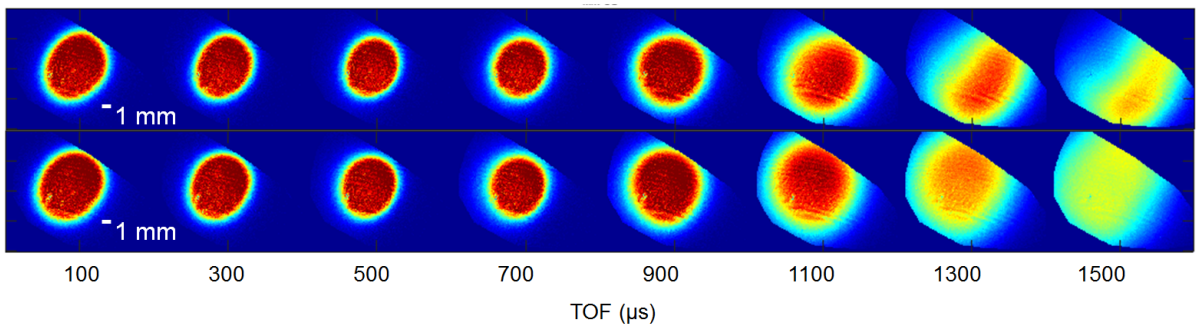

Figure 2.6: *In situ* images of the CMOT showing unbalanced (top) vs balanced (bottom) intensity in the CMOT beams. Only the focal degree of freedom has been adjusted between the two, but the atoms are no longer pushed to the right when the beams are well balanced. The temperature of the atoms pictured is ≈ 0.5 mK.

but causes heating. The cycler moving closer to resonance kicks the outer shell of atoms towards the center, while decreasing the intensity of the repumper effectively makes the center of the cloud optically dark. The atoms effectively absorb a few photons and are driven towards the center of the MOT before entering the dark ground state. The new effect of these operations squeezes the five billion atoms into a smaller region of space, where they can be further cooled using gray molasses. We avoid using these parameters to load the MOT because the capture velocity and trap volume are too small to load a large MOT. Using the MOT $\rightarrow$ CMOT technique does not change the PSD, but creates a cloud with a smaller spatial extent, which is ideal for increasing the PSD in the next step: gray molasses.

We found it necessary to use the cloud's motion while it is being compressed to adjust the divergence of each MOT beam. If the beams are not properly power balanced, macroscopic motion of the cloud results (and usually leads to poor compression as the atoms escape in the direction of the relatively weaker beam, see for instance Fig. 2.6). It is important to do this both in the horizontal and vertical directions.

See the section on optical systems (specifically, see Figure 3.1) for details on how we generate light for the MOT and CMOT stages.

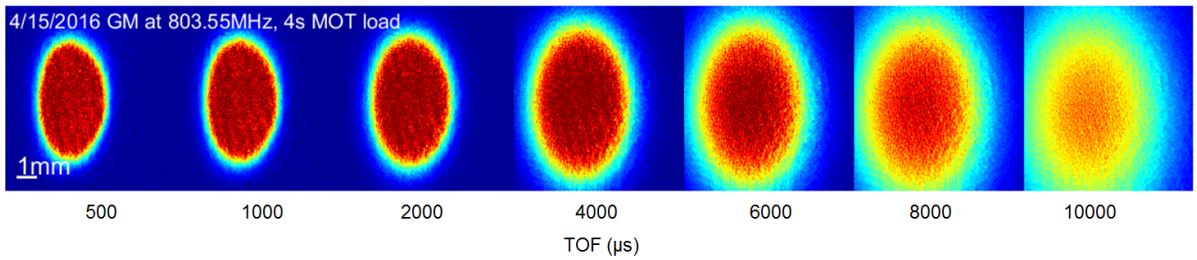

Figure 2.7: Time of flight measurement of atomic cloud after gray molasses cooling (pictured from the side) with the two-photon detuning $\delta = +4.5\Gamma$ and single photon detuning $\Delta + \epsilon$, where $\Delta = 803.55$ MHz and $\epsilon = 0$. $T_{\mathrm{RMS}} = 61$ μK. Note the increased time scale vs. the previous stage (CMOT), which indicates a much slower rate of expansion of the atomic cloud.

2.5 Gray Molasses (GM)

Gray molasses, also known as D1 cooling (or GM for short), was first implemented in a lithium experiment in 2013 [19], followed shortly by [20]. Prior to this, the small hyperfine splitting of lithium's excited states were believed to prevent this technique from working (due to poor optical pumping). Previous experiments indicated that GM was possible for Sodium ([21][22]).

Gray molasses is a two-photon, sub-Doppler cooling technique. Use of the D1 transition in lithium allows addressing of specific excited states (not possible on the D2 line) to create a Λ-type Raman transition. Virtual occupation of the excited state transfers the atoms into a superposition of an optically coupled "bright" state and a non-coupled "dark" state. The evolution between these two states is dependent on the atom's velocity, forming a kind of velocity selective coherent population trapping (VSCPT) where atoms either enter a velocity class near zero (in this case, 60 μK), or have enough velocity to continue to undergo transitions.

Following the treatment in [23] (section 2.4 "Subrecoil Cooling"). The atom-laser

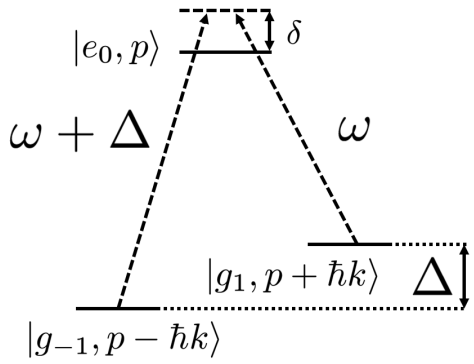

Figure 2.8: Schematic for two photon (Λ-type) Raman-transition between two ground states (separated by energy Δ) via virtually occupied excited state e_0. Photons ω and $\omega + \Delta$ are detuned from the excited state e_0 by energy δ.

interaction H_{AL} in the plane wave basis in a Λ scheme takes the form:

$$H_{\mathrm{AL}} = \frac{\hbar\Omega}{2\sqrt{2}} \left(|e_0\rangle\langle g_1| e^{-ikz} - |e_0\rangle\langle g_{-1}| e^{ikz} \right) e^{-i\omega t} + \mathrm{H.c.} \tag{2.9}$$

Using the translation operator,

$$e^{\pm ikz} = \int dp |p\rangle\langle p \mp \hbar k|, \tag{2.10}$$

we can rewrite the excited state in the dressed atom picture, as a superposition of the two ground states and their associated photon momenta as

$$H_{AL}|e_0, p\rangle = \frac{\hbar\Omega}{2\sqrt{2}} \left(|g_1, p + \hbar k\rangle - |g_{-1}, p - \hbar k\rangle \right) e^{-i\omega t}, \tag{2.11}$$

where we can now write the three states (coupling (c), non-coupling (nc), and excited

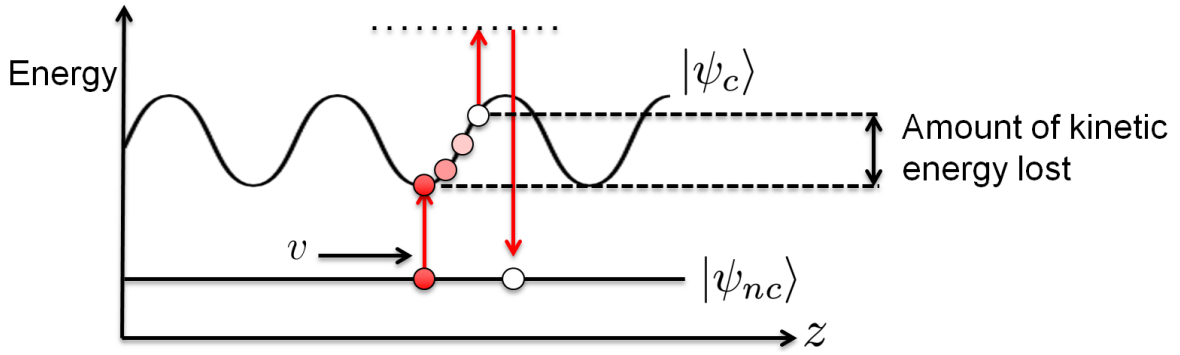

Figure 2.9: Illustration of Gray Molasses cooling. Two-photon process drives transition between "bright" ($|\psi_c\rangle$) and "dark" ($|\psi_{nc}\rangle$) states. Motional coupling (see Eqn 2.14) preferentially cools hot atoms.

(e)) of the system as a superposition of the original states

$$\begin{aligned} |\psi_c(p)\rangle &= \frac{1}{\sqrt{2}}\left(|g_1, p+\hbar k\rangle - |g_{-1}, p-\hbar k\rangle\right) \\ |\psi_{nc}(p)\rangle &= \frac{1}{\sqrt{2}}\left(|g_1, p+\hbar k\rangle + |g_{-1}, p-\hbar k\rangle\right) \\ |\psi_e(p)\rangle &= |e_0, p\rangle \end{aligned} \tag{2.12}$$

where the interaction between these composite states with the light field is

$$\begin{aligned} H_{AL}|\psi_c(p)\rangle &= \frac{\hbar\Omega}{2}e^{-i\omega t}|\psi_e(p)\rangle \\ H_{AL}|\psi_e(p)\rangle &= \frac{\hbar\Omega}{2}e^{i\omega t}|\psi_c(p)\rangle \\ H_{AL}|\psi_n c(p)\rangle &= 0 \end{aligned} \tag{2.13}$$

Importantly, the "bright" (coupling) and "dark" (non-coupling) states have different polarization-dependent energy shifts, which means the transition between bright and dark states is not only velocity selective, but behaves much in the same way as polarization gradient (Sisyphus) cooling (see Fig. 2.9 for illustration). Namely, the bright state has non-zero energy at periodically spaced points in the electromagnetic field, while the dark

state remains unperturbed. A transition from the bright state to the dark state extracts a small amount of energy from the atom, causing cooling to occur. This process would only happen once if the dark state never became optically addressable, but the coupling and non-coupling states are not eigenstates of the momentum operator. This means that for finite values of the atom's momentum, the dark state will evolve into the bright state on time scales associated with the atom's momentum:

$$\langle \psi_c(p)|\frac{\mathbf{p}^2}{2M}|\psi_{nc}(p)\rangle = \frac{\hbar k p}{M} \tag{2.14}$$

this effect is twofold: (1) the rate of escape from "dark" (non-coupling) state is proportional to p, so colder atoms accumulate in the dark state as a function of time and (2) this "motional coupling" allows the cooling process to occur many times for hot atoms, causing them to lose energy and cool.

We use the resonant condition where the single-photon (relative) detuning Δ between the two colors of light satisfies the condition $\Delta_{1\to 2} = \Delta_{2\to 3}$. The two-photon detuning (common) detuning from the upper hyperfine state ($F' = 2$) is approximately 4.5Γ. Practically speaking, we generate the D1/gray molasses light using a slave laser and a tapered amplifier to generate around 100 mW of light just for this step (after an 80 MHz switching AOM and 803.5 MHz EOM to apply a 1-2% sideband). A separate beam path into the chamber allows us to control the size of the beam independently from the MOT beams (please see the chapter on optical systems for more details). We align the horizontal and vertical beams (each between 45 and 50 mW optical power, approximately 1/2" beam diameter) onto a MOT at high field gradient ($\approx$ 60 G/cm) to move the atoms to their position after the CMOT step but before GM. After the CMOT stage, the GM light is immediately applied to the atoms which cools them to 60 μK in 1 ms. We initially thought that GM required no external magnetic fields and had time to allow the

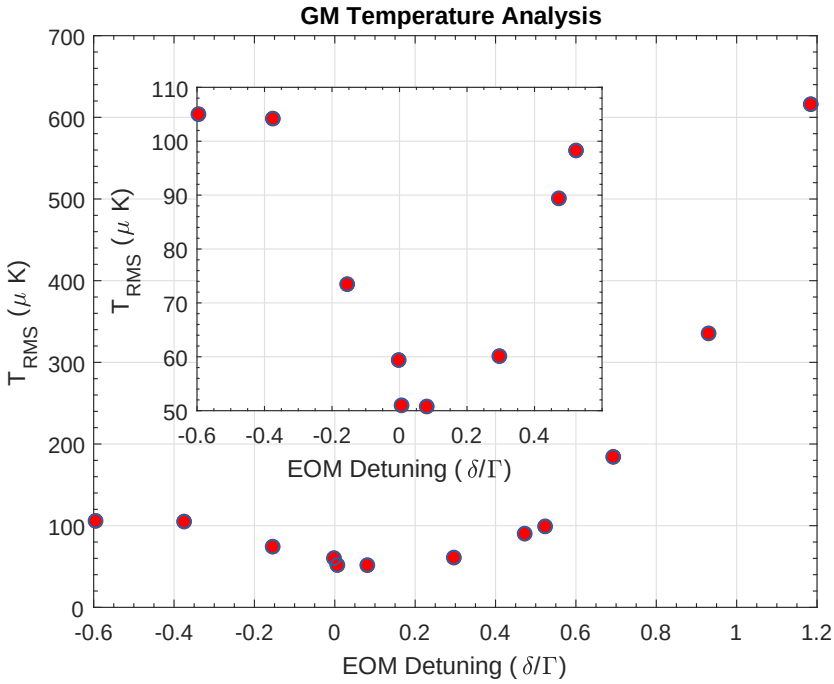

Figure 2.10: Temperatures after gray molasses as a function for EOM detuning (single-photon detuning). The lowest final temperature ($\approx$ 50 μK) is obtained at the Raman condition (Δ = 803.5 MHz). Results are consistent with those observed in [19].

magnetic fields to settle to near zero, but found that cloud PSD in the magnetic trap was unchanged by the addition of this wait time. It's likely the case that the added expansion of the cloud during this waiting time counteracted the benefits of GM.

2.6 Radio Frequency (RF) Evaporation

Optical cooling for lithium using 671 nm light is practically limited to around 60 μK (it is possible to achieve colder temperatures using the $2S - 3P$ transition at 323 nm, but working at UV wavelengths requires special experimental consideration[24]). Cooling beyond this limit requires the use of evaporative cooling, which is only limited by the atom number. We perform forced evaporation in an optically plugged quadrupolar

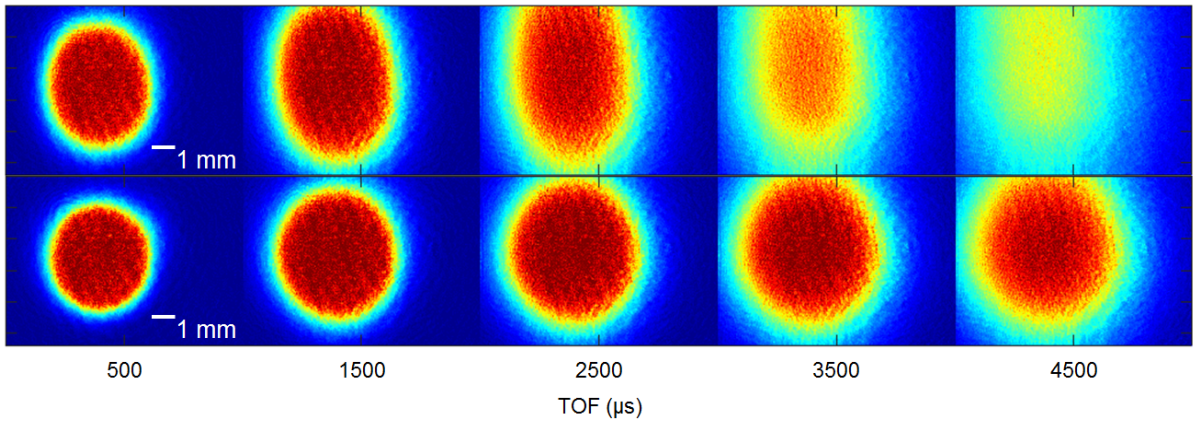

Figure 2.11: TOF images from the XZ-axis (side imaging) after D1 Pumping showing breakdown of optical pumping. Top: pumping at the two-photon resonant condition causes heating as the atoms absorb excess photons from the applied laser. Bottom: away from the two-photon condition atoms absorb only enough photons to pump across the ground state manifold until they are optically dark to the applied light. MT capture efficiency exceeds 90% for the properly pumped atoms.

magnetic trap. Thermalization rates and final achievable temperatures depend strongly on precise control of the internal states of the atoms.

2.6.1 Magnetic Trapping and Spin Polarization (D1 Pumping)

An applied magnetic field gradient can confine atoms (with non-zero m_F) due to the Zeeman shift. Three of the eight ground states in ^{7}Li are magnetically trappable: $|F = 2, m_F = 2\rangle$, $|F = 2, m_F = 1\rangle$, and $|F = 1, m_F = -1\rangle$. These states have a positive Zeeman shift and require additional energy to escape an increasing magnetic field as the atoms move away from the zero field crossing at the center of the trap. This forms a magnetic trap (MT). The others spin species are either untrapped ($m_F = 0$), or anti-trapped, i.e. they gain energy as they move away from the trap center and are expelled from the trap. Further, thermalization is only possible with inter-atomic collisions, which in general are spin changing collisions in the gas of atoms unless the gas is spin-polarized. Spin changing collisions will distribute atoms into all of the Zeeman sublevels and drastically

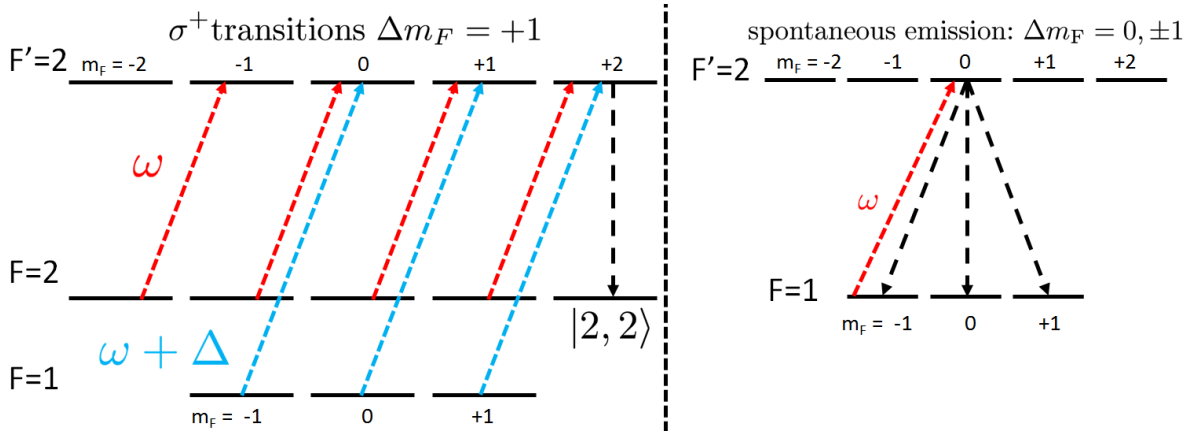

Figure 2.12: Schematic of D1 optical pumping (spin polarization). σ^+ light resonant with both ground states pumps atoms across the hyperfine manifold until they spontaneously emit a photon and enter the $|2,2\rangle$ dark state. Conservation of angular momentum requires atoms that absorb a σ^+ photon increase their m_F quantum number by $+1$. Atoms can spontaneously emit a photon with $\Delta m_F = 0, \pm 1$, but the applied σ^+ light drives net population transfer to higher m_F states. Here $\Delta = 803.5$ MHz, the ground state hyperfine splitting at zero field. Changing Δ results in two-photon (angular momentum conserving) transitions and is not ideal for optical pumping (see Figure 2.12).

reduce the efficiency of evaporation.

To spin-polarize the gas, we use resonant σ^+ polarized D1 light resonant with the $F = 2 \rightarrow F' = 2$ transition and a weak vertical bias field (to create a quantization axis). Since there is no $|F' = 2, m_F = 3\rangle$ state in the $^2P_{1/2}$ excited state manifold, once atoms are in the $|F = 2, m_F = 2\rangle$ state they become optically dark to the applied light. We generate this light from the gray molasses slave/TA by selecting the 0^{th} order light from the GM AOM and sending it through another AOM which has a 95 MHz detuning. This brings the light into resonance with the D1 transition (see B.2). We increase the amplitude of the repumping sideband generated by the 803.5 MHz GM EOM to have equal power in the "cycling" and "repump" transitions. Specifically, we want to avoid two-photon transitions when both photons have the same polarization, because such a stimulated process conserves angular momentum, and therefore cannot pump atoms into a different ground state. Initially we attempted to pump the atoms using the D2 transition, but

found this was largely not possible with the unresolved excited state hyperfine structure in ^{7}Li.

Empirical optimization for atom number and density in the magnetic trap gave us an ideal pumping time of 450 μs for a 70 mW beam. The overall detuning/time is set by the requirement that the atoms not expand too much before they are captured in the magnetic trap. Residual $|2,1\rangle$ atoms will scatter and cause heating and loss in the atomic cloud, but these effects are negligible and the atoms escape during the initial stages of evaporation before the atoms are cooled significantly.

In order to catch the atoms after they are optically pumped, we need to apply a magnetic field gradient as fast as possible (diabatic loading, recommended by [25]). Allowing the cloud to expand causes heating once the trap is turned on, but slowly ramping the magnets (adiabatic loading) loses density and results in a lower PSD than diabatic loading. To this end, we built a high voltage capacitor bank, connected to our inner MOT coils, to turn on our magnetic field to 80 G/cm in 100 μs. The outer coils are turned on (induction limited to a few hundred μs) and then both electromagnets are ramped to their combined peak gradient value of 420 G/cm in a few hundred ms, at which point we begin the process of radiofrequency (RF) evaporation. See Section 4.3.5 for more details on the construction and characterization of the high voltage power supply system.

2.6.2 RF Evaporation

Radio frequency (RF) evaporation essentially relies on selectively forcing the hottest atoms to escape from the magnetic trap, analogous to evaporation and cooling of coffee in a cup. The hottest atoms escape from the trap, while the remaining atoms rethermalize to a lower temperature. The ejected atoms carry away a large fraction of the cloud's temperature (cooling the cloud from 300 μK to 10 μK). Essentially there is no lower limit

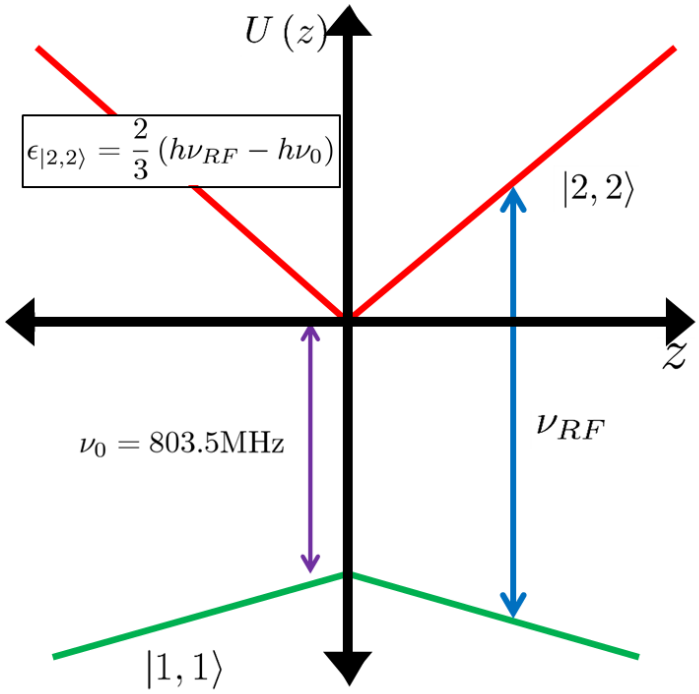

Figure 2.13: Schematic of RF evaporation. High energy (hot) atoms make large excursions from the center of the trap ($|z| > 0$) where they experience large Zeeman shifts (≈ 300 MHz). Radiation with frequency v_{RF} drives the $|2,2\rangle \rightarrow |1,1\rangle$ transition for atoms with sufficiently high energy. v_{RF} is decreased over time, further ejecting atoms until only a small fraction of very cold atoms remain.

to the temperatures achievable by evaporation, but it is an incredibly lossy process (our typical ramps lose >90% of the atoms in the trap). The rate of the evaporation is set by the thermalization rate of the atomic cloud; it is important to optimize the evaporation parameters (RF sweep, magnetic gradient relaxation) to achieve low temperatures via runaway evaporation and avoid simply dropping atoms from the trap. If properly optimized, RF evaporation increases the phase space density of the cloud increases by three orders of magnitude (from 10^{-5} during GM to 10^{-2} after RF evaporation). The question remains: how to selectively force the hottest atoms to escape?

The answer lies in the simple fact that the hottest atoms have the highest energy and will explore the edges of the magnetic trap before turning around (thereby experiencing

larger Zeeman shifts compared to the colder atoms). Blue-detuned RF radiation drives a transition between the $|2,2\rangle$ (low-field seeking, $\Delta E \propto |B|$) and $|1,1\rangle$ (high-field seeking, $\Delta E \propto -|B|$) states, which have a zero field splitting of 803.5 MHz. With a wavelength of around 37 cm, the radiation uniformly addresses the atoms. Initially, the atoms are trapped in a field gradient of 420 G/cm. With a spatial extent of around 1 cm, the atoms in the magnetic trap at the edge will experience a large Zeeman shift ($\approx$ 300 MHz) compared to those near the center of the trap.

We apply radiation at 927 MHz while compressing the atoms to remove the hottest ones that have excessively large energy. Over the course of 4 s, we sweep the frequency of the RF from 885 MHz down to 805.3 MHz (just above resonance), while simultaneously relaxing the magnetic field gradient from 420 G/cm to 42 G/cm. This cools the atoms from around 300 μK down to 10 μK. RF evaporation was optimized empirically in four separate sections, which roughly produced a linear ramp.

Stage	**Duration (s)**	**RF Frequency (MHz)**	**∇B (G/cm)**
A	0.05	927	422
B	0.75	885→857	422
C	0.75	857→829	422
D	2.5	829→805.3	422→42

Table 2.3: Optimized radio frequency evaporation stages with names, durations, frequency ranges, and applied field gradients.

Our machine uses a quadrupolar magnetic field gradient to form the magnetic trap. This gives rise to an issue: due to the laws of electrodynamics, there must exist a field minimum at the center of the trap. Near the center of the trap, the Larmor frequency of the atoms approaches the rate of change in the magnetic field's direction. This means that atoms can undergo spontaneous spin flips as the quantization axis changes rapidly in the vicinity of the field zero. These Majorana spin-flips cause an anti-evaporation process, whereby the coldest, densest atoms are ejected from the trap. Our measurements indicate

Shim	Current (mA)	B field (G)
Transverse	270	0.16
Vertical	430	0.34
Slower	90	0.06

Table 2.4: List of the currents required to cancel the earth's magnetic field to ± 10 mG.

that the heating rate is as high as 25 μK/s at the max gradient (420 G/cm), and decreases to roughly 2.5 μK/s at 40 G/cm. Some experiments (see [5] for a good summary) use more complicated magnetic trap geometries, most commonly the Ioffe-Pritchard type trap. However these traps require significant effort to design and engineer compared to a quadrupolar trap. Additionally, the potential they create is often elongated along one direction, which practically limits the maximum achievable density.

To eliminate this trap hole, we use a high power, blue-detuned laser beam (Sprout-G, 532 nm, 10 W) to push the atoms away from the center of the magnetic trap. See 3.2.1 for details of the system. In order to work properly, the plug beam must be focused sufficiently to produce an anti-trap on the temperature scale of 10 μK. This can be achieved by focusing 10 W beam to a $1/e^2$ diameter of around 60 μm. The beam must overlap with the region of "death" around the field zero, most importantly when the magnetic trap is weak and the atoms are the coldest and densest. DC fields will cause the magnetic field zero (and hence the atoms) to move, and so must be compensated with shim coils. The primary field to compensate is the Earth's magnetic field, but stray fields in lab must also be counteracted. To give a rough idea of the scales involved, see Table 2.4. The quadrature sum of the shim coils generates a field of 0.38 G, which roughly matches the Earth's average magnetic field of $\approx$ 0.5 G. See Fig. 2.14 for an example of a well shimmed magnetic trap. The cloud center moves less than 2 pixels (5 μm) over a range of field gradients spanning 42-380 G/cm. Section 4.3.6 contains a discussion of the design and construction of the shim coils.

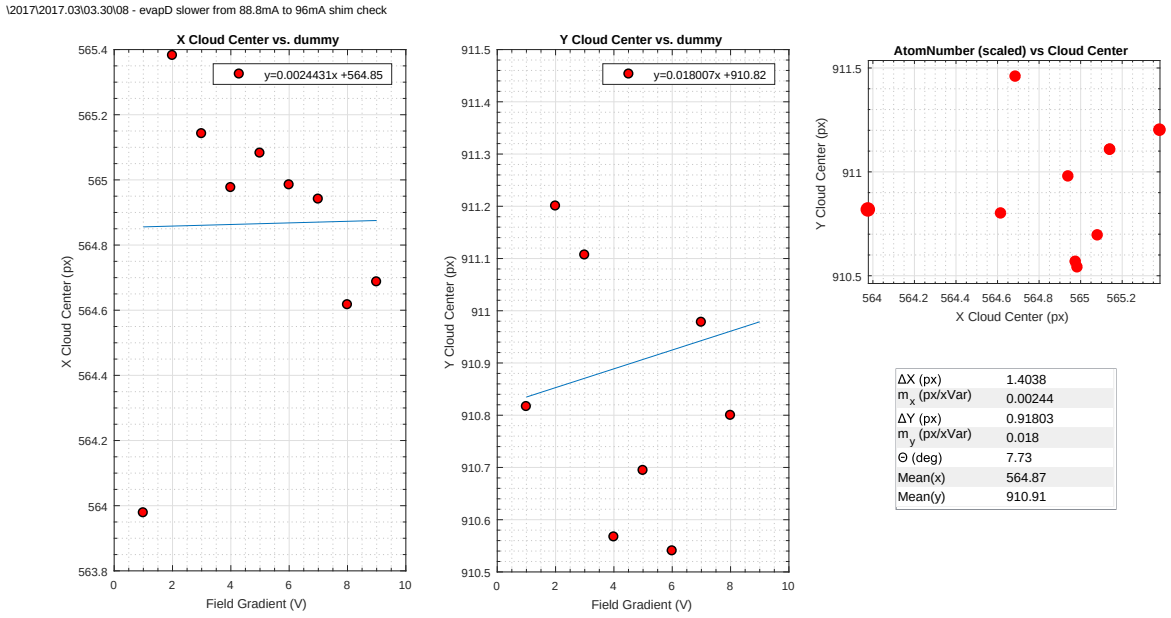

Figure 2.14: Shimming (canceling) Earth's magnetic field. Left and middle figures: Cloud center position in the X and Y (N→S and E→W) directions plotted as a function of the magnetic trap's gradient (∇B_z: 1-10 V = 42-422 G/cm). Top right shows cloud size plotted in X-Y space. Cloud center motion is less than 1.5 pixels $\approx$ 4 μm over this range of gradients, indicating the cloud will not move macroscopically during evaporation.

2.7 Optical Evaporation

Lithium presents a particularly unique challenge for evaporative cooling. Unlike Rubidium, which can undergo Bose condensation in a magnetic trap[26], lithium's $|2,2\rangle$ state used for RF evaporation has a negative scattering length (attractive interactions) at zero temperature and applied field (^{7}Li $|2,2\rangle$ a = -27.7 a_0, no Feshbach resonance; ^{7}Li $|1,1\rangle$ a = 7.7 a_0 Feshbach resonance at 735 G[6]). This means that any condensate that forms as the atoms cool is unstable to collapse due to three-body collisions. This fact was a major limitation in early lithium experiments, until [14] figured out that the $|1,1\rangle$ state had a favorable scattering length due to the presence of a Feshbach resonance. This requirement necessitates the presence of a DC magnetic field to control the scattering

length of the atoms, and obviates the use of a quadrupolar magnetic trap for BEC formation, plug beam or no. The general procedure is as follows, starting from a cold gas in the magnetic quadrupole trap:

- First load the atoms into the crossed optical dipole trap.
- Transfer the atoms from the $|2,2\rangle$ state into the $|1,1\rangle$ state.
- Apply a DC bias field to control the scattering length via the Feshbach resonance.
- Reduce the optical power in the crossed ODT (XODT) to cause evaporation and BEC formation.

2.7.1 Optical Dipole Traps

After RF evaporation, we load the atoms into a crossed optical dipole trap (XODT), which uses an optical potential to confine the atoms and allows the simultaneous application of a DC magnetic field to control the scattering length using the $|1,1\rangle$ state's broad Feshbach resonance at 736 G. We focus two 8 W 1064 nm laser beams near the center of the magnetic trap.

Assuming the beam is Gaussian (a reasonable approximation for light coming out of a fiber), we can model its spatial extent if we know f, the focal length of the objective lens, and d, the input beam diameter. The beam *waist* ω_0 (where it reaches 1/e of its original value, also known as the beam *radius*) is[27]:

$$w_0 = \frac{1}{2}\left(\frac{4\lambda}{\pi}\right)\left(\frac{f}{d}\right), \tag{2.15}$$

while the distance along the direction of propagation where the beam reaches $1/\sqrt{2}$ of its

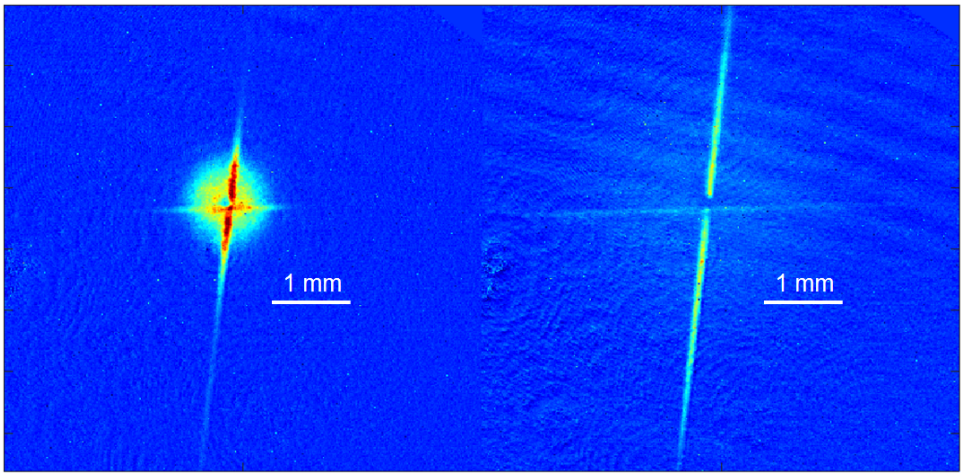

Figure 2.15: TOF images showing the intersection of the ODT beams and the plug beam. Left: 500 μs TOF. Right: 5000 μs TOF. Intersection of the ODT and Plug beams prevents the formation of a single crossed optical dipole trap.

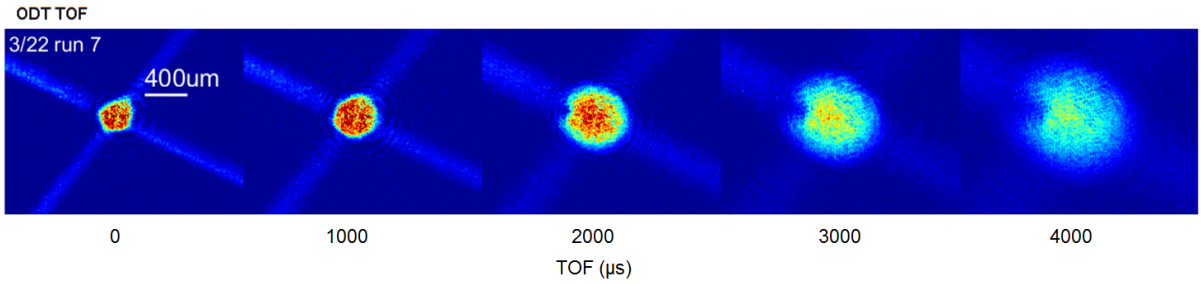

Figure 2.16: TOF images showing a 20×10^9 atoms at a temperature of around 4 μK. After sufficiently long time of flight, the atoms interact with the remnant plug beam (located to the left of the ODT).

peak intensity (known as the Rayleigh range) is:

$$z_R = \frac{\pi {\omega_0}^2}{\lambda}. \tag{2.16}$$

These can be used to calculate the functional form of the trap in cylindrical coordinates

(r and z):

$$\delta = 2\pi c \left(\frac{1}{671 \text{ nm}} - \frac{1}{1064 \text{ nm}} \right) \tag{2.17}$$

$$U_{\text{ODT}} = \frac{\hbar}{8} \frac{(2\pi\Gamma)^2}{\delta} \frac{I}{I_{\text{sat}}} \tag{2.18}$$

$$U(r,z) = -\frac{U_{\text{ODT}}}{(z/z_R)^2 + 1} \exp\left(-\frac{2(r/w_0)^2}{(z/z_R)^2 + 1} \right) \tag{2.19}$$

Where $\text{I}_{\text{sat}} = 2.54$ mW/cm^2 is the saturation intensity and Γ the linewidth (5.9 MHz) of the D2 transition in ^{7}Li, and δ is the relative detuning of the trapping light from the D2 transition. Further, we can calculate the rate of spontaneous scattering (a heating process) of lattice photons in the usual way (from [1]):

$$R_{\text{scatt}} = \frac{\Gamma}{2} \frac{\Omega^2/2}{\delta^2 + \Omega^2/2 + \Gamma^2/4} \tag{2.20}$$

$$F_{\text{scatt}} = \hbar k \frac{\Gamma}{2} \frac{I/I_{\text{sat}}}{1 + I/I_{\text{sat}} + 4\delta^2/\Gamma^2} \tag{2.21}$$

$$\frac{I}{I_{\text{sat}}} = \frac{2\Omega^2}{\Gamma^2} \tag{2.22}$$

For a 10 W 1064 nm beam with a 28 μm beam waist, $U_{\text{ODT}} = 400\mu$K, while $R_{\text{scatt}} = 7.5$ mHz. This means on average an atom will only scatter a lattice photon once every 133 s.

One consideration for transferring between traps is mode-matching. The volume of the XODT is considerably smaller than that of the MT. This gives a set of constraints on the optical dipole trap beams, namely that they be powerful enough to create a trap deep enough to load the atoms (tightly focused), but large enough to capture sufficient atom number from the magnetic trap. The use of a 50 W 1064 nm fiber laser system (see section 2.7.1) allows us to create multiple 8 W beams. Our initial traps were too tightly focused (≈ 75 μm beam waist), and only captured around $4{\times}10^6$ atoms. We now use beams of

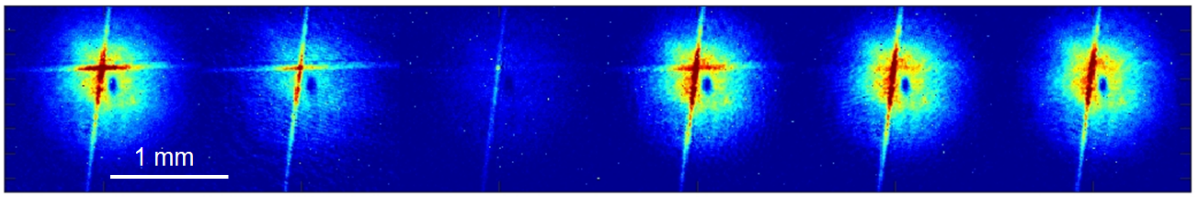

Figure 2.17: Vertical scan (into the page) of the second (horizontal) ODT beam. When the two ODT beams overlap, the atoms are tightly confined in the region of maximum intensity (the XODT) formed by the combined optical potential. Also visible is the plug beam pushing atoms from the center of the trap.

around 180 μm in size to capture 1.6-2$\times 10^7$ atoms from the evaporated cloud after RF evap (only 20% efficient). Curiously, the MT at the end of evaporation does not appear to be an entirely thermal cloud. TOF measurements of the MT's temperature indicate that we end our evaporation around 8 μK (and 8×10^7 atoms), but similar measurements indicate that the atoms in the XODT are at a lower temperature of 4 μK, indicating that the central region of the cloud holds the coldest atoms.

Alignment of the first ODT beam is relatively insensitive. It is sufficient to place the ODT beam just off the center of the cloud (looking from above) and image it from the side to set the vertical position. In our system, the plug beam will stop the ODT from loading properly (it will cut the ODT in half, or cause an accumulation of atoms not at the center of the optical potential, see figure 2.15). We move the ODT to just outside this region. The second ODT beam is aligned in a similar way, except its vertical alignment is more sensitive: it needs to overlap with both the MT and the existing ODT beam. We employ a Newport Picomotor kinematic mirror mount (Model 8821-L) to enable a fine scan of the beam's position (as in Fig. 2.17). As a subtle point: if the second ODT beam is slightly above or slightly below the first, the apparent atom number in the XODT is higher than if they are truly overlapped. This is because the two traps capture a large number of atoms from the MT, but fail to form a good trap themselves. In practice, we scan the vertical position of the second ODT beam until it is in the center of this

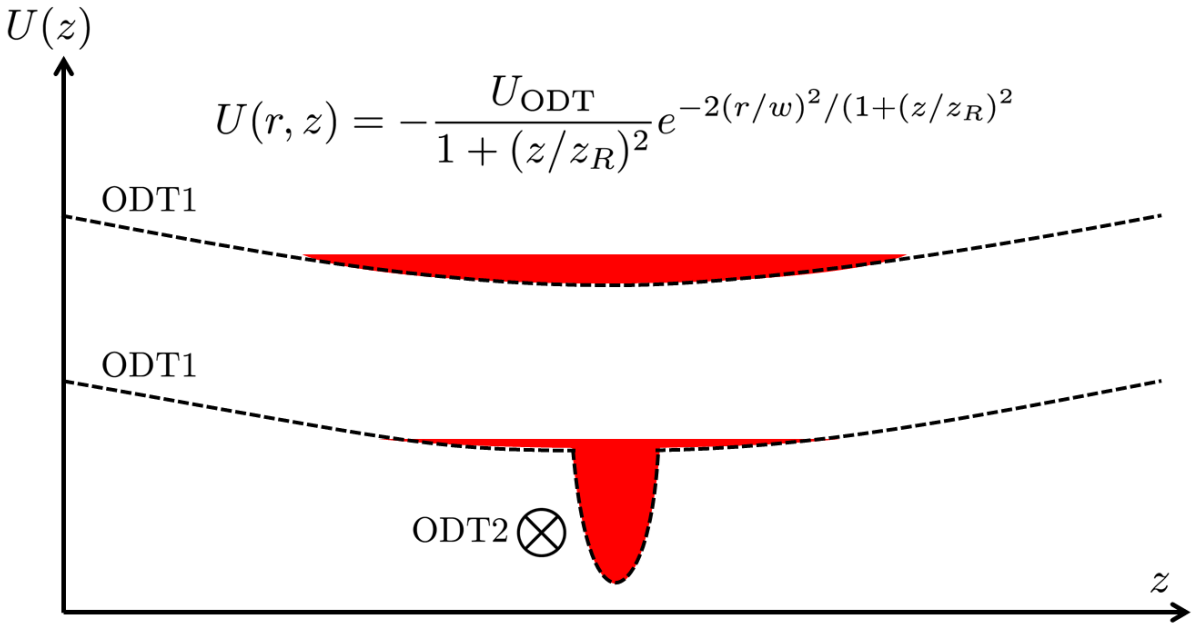

Figure 2.18: Schematic of optical dipole trap loading (top) and crossed optical dipole trap loading (bottom). Two intersecting far-red-detuned beams intersect in the center of the trap to create an optical potential tens of μK deep. z_R is the Rayleigh range and w is the beam waist. See equation2.17 for details.

double-maxima, forming a trap depth profile as illustrated in Fig. 2.18.

2.7.2 State Transfer and Feshbach Field Application

In order to access the Feshbach resonance, we must transfer the atoms from the $|2,2\rangle$ ground state into $|1,1\rangle$. Happily, this is the very transition that we were already using to perform RF evaporation, and we just need to be precise about the frequencies involved. It is possible to use two different techniques to perform this transfer, a short pulse that is resonant with the transition, or a slower sweep that goes from just above the transition (in energy) to just below it. The latter is a process known as Rapid Adiabatic Passage and is more robust if time is not a strong constraint (a pulse requires a precise RF source, precise pulse length and timing, and is susceptible to local magnetic field inhomogeneities). We apply a weak magnetic bias field to lift the hyperfine state degeneracy. The RF sweep we

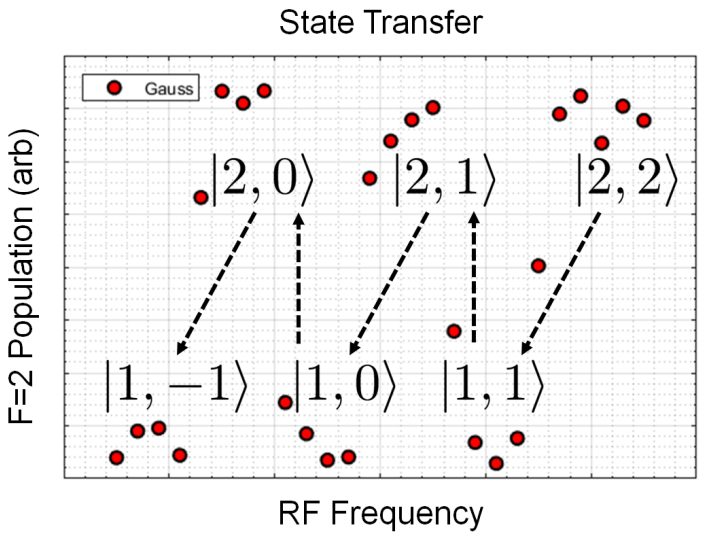

Figure 2.19: Population of $F = 2$ manifold atoms (imaging without repump light) as a function of final RF frequency. As the sweep decreases in frequency, atoms populate sequentially decreasing m_F levels (separated by $\approx$ 500 kHz) in each F manifold, allowing precise control over the desired ground state. 65 ms total sweep duration.

use lasts 65 ms and spans 809.56 MHz to 807.45 MHz, which pumps 98% of the atoms from $|2,2\rangle$ into the $|1,1\rangle$ state. We can image the atoms with a repumper and without a repumper to distinguish the relative populations (Fig. 2.19).

We also use this time to operate the relays and switch the MOT magnets from their gradient (anti-Helmholtz) configuration to their DC (Helmholtz) configuration, in anticipation of applying the Feshbach field.

Initially, we only used the innermost set of coils for applying the Feshbach (FB) field, as we only had one set of relays. We discovered that doing so led to mechanical instability as a result of uneven heating between the inner and outer coils. The main problem was that the coils were shifting ever so slightly and moving the MT field zero, which is equivalent to a misaligning the plug beam. Recall that motion on the scale of 5-10 μm (of an object with a 6" outer diameter suspended on threaded rods) is sufficient to prevent effective RF evaporation. After building a second set of relays, we were able to use both sets of coils to share the thermal load, and reduce the required current from

approximately 300 A in one coil to 120 A in both coils (which reduces the heat generated by roughly one third).

Currently, the presence of a strong magnetic field gradient required re-configuring the electromagnets further. They now run approximately the same, 400 A, current but the evenness of the heating seems to be the primary issue when it comes to thrmo-mechanical stability. See the section on MOT coils (4.3.1) for details about the current configuration. With the addition of an extra set of shim coils, we are able to hold the atoms in a nearly magnetic field gradient-free environment for experiments.

2.7.3 Optical Evaporation and Condensate Formation

The final stage of cooling is optical evaporation. To facilitate thermalization, we tune the scattering length to around 294 a_0, where the atoms will thermalize on short enough time scales to allow optical evaporation to proceed in an exponential manner, while maintaining trap lifetimes of many seconds. The mechanism is much the same to the RF evaporation described above, where the hottest atoms are encouraged to leave the trap, leaving the remaining population to thermalize to a lower temperature. The mechanism of selecting the hottest atoms is an even simpler one, however: the hottest atoms have the largest velocity and so explore the regions where the optical trapping potential is the weakest. By simply reducing the power in the optical potential (using an AOM to adjust the power), the hottest atoms escape. We use a closed-loop PID feedback system to keep the ODT powers at the desired level very precisely. The ramp parameters (functional form, final depth optical potential, and the speed) are all determined experimentally. Our final ODT ramp parameters are an exponential ramp ($\propto e^{-t/\tau}$) from 8 W to 2 W in 4.5 s with a time constant $\tau = 2.25$ s.

Once the cloud reaches a critical PSD ($\zeta(3/2) = 2.6$), macroscopic numbers of atoms

Condition	$a_{\mathbf{scatt}}$ (a_0)	XODT Lifetime (s)	BEC Lifetime (ms)
No state transfer, 0 G	7.7	1.5	NM
740 G	-1146	NM	< 1 (est)
732 G	957	3	10
722 G	294	10	100
543.6 G	0	NM	> 500

Table 2.5: Table of measured lifetimes of atoms in the XODT and the BEC at different scattering lengths. NM means quantity was not measured. Strongly attractive (repulsive) interactions below (above) the Feshbach resonance at 737 G enable the creation of a Unitary Bose (Tonks-Girardeau) gas under the right conditions (not realized in this work).

begin to enter the ground state of the trap. As the optical potential is lowered further and the cloud continues to cool, increasing numbers of atoms enter ground state until the condensed fraction roughly approaches $T/T_c = 1$. Recall $T_c \approx 4.5\,\bar{\omega}N^{1/3}/(2\pi\cdot 100\text{ Hz})$ nK estimates $T_c = 700$ nK (for 1 kHz transverse trap frequencies and 5×10^5 atoms, $\lambda_{dB} \approx 1\ \mu$m). Further evaporation creates a nearly pure condensate with 2×10^5 atoms at a temperature around 20 nK. The limitation of how far one can evaporate is set by atom number and the ability of the optical potential to confine the atoms against gravity. Eventually the ODTs are insufficient to hold the atoms and they are lost from the trap.

A note on metastability. A BEC is in fact a metastable state, as lithium atoms *much* prefer the solid phase at these temperatures. Two-body collisions (s-wave scattering events) occur frequently but cannot create a bound state while conserving both energy and momentum, which prevents molecule (and hence solid) formation. At the densities achieved in a BEC ($10^{13}/\text{cm}^3$), three-body losses are the primary loss mechanism, and easily dominate background gas collision rates at UHV pressures. However, these loss rates scale with the scattering length a_{scatt}, resulting in typical lifetimes of the BEC that are much longer than the relevant experimental time scales (typically hundreds of ms), especially at $a_{\text{scatt}} \approx 0$. In principle, the lifetime of the atoms in the condensate are then only limited by background gas collisions and technical sources of heating (mostly

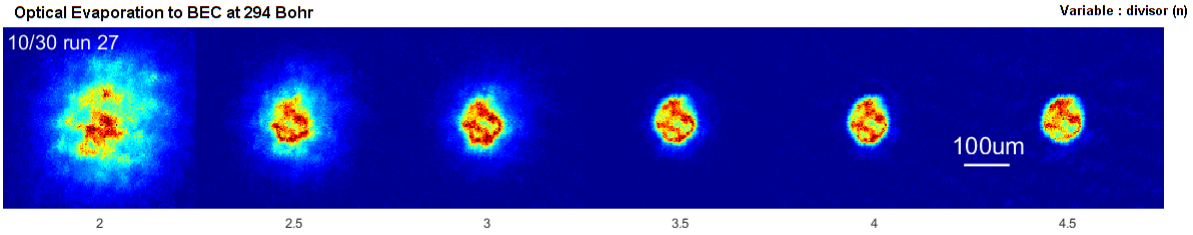

(a) Optical evaporation at $a_{\text{scatt}} = 294$ Bohr, $\approx 4 \times 10^5$ atoms pictured here.

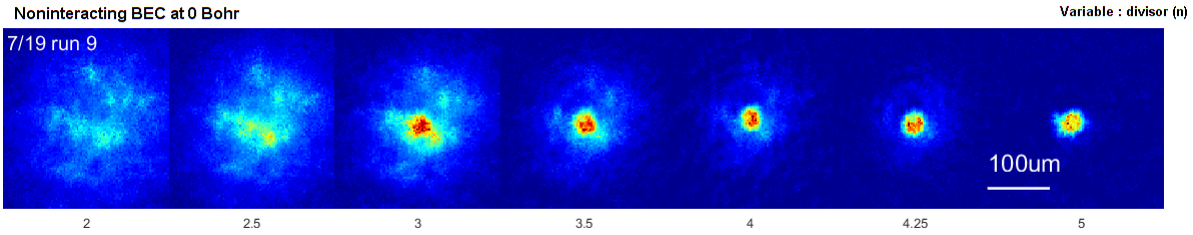

(b) Optical evaporation at $a_{\text{scatt}} = 294\ a_0$ and then ramp to $a_{\text{scatt}} = 0\ a_0$ (non-interacting)

Figure 2.20: Condensate formation as a function of decreasing optical dipole trap power (expressed as the original power/n, where n is some divisor). (a) optical evaporation to BEC at 294 Bohr, then 3 ms free expansion to resolve the condensate fraction and thermal fraction. (b) same evaporation as (a) followed by a Feshbach field ramp from 720 G to 543 G. The cloud size decreases dramatically when the atoms no longer scatter off one another. Note the nearly 100% condensate fraction for low values of the final trap depth.

pointing noise from the ODTs). See Table 2.5 for lifetimes at various scattering lengths.

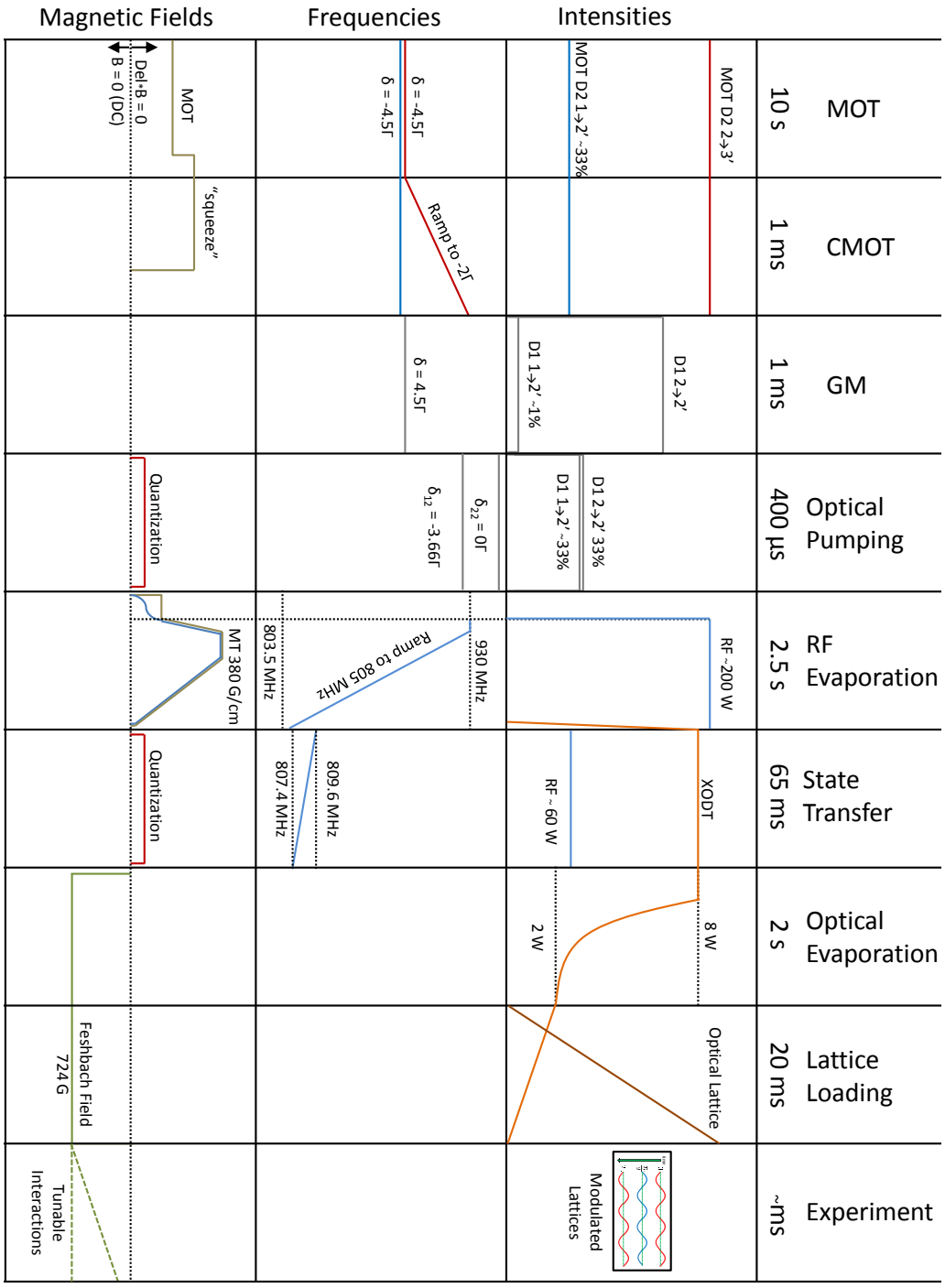

Figure 2.21: Summary of cooling sequence to generate a BEC.

Chapter 3

Optical Systems

Precise control over the internal and external degrees of freedom of an atom requires light of specific frequency (wavelength), power, and polarization. Generally the light required for an AMO experiment comes in two types: resonant or near-resonant (detunings on the order of tens of MHz), and far off-resonant (detunings typically of hundreds of nm or more). Resonant light addresses atomic dipole transitions, while off-resonant light exerts forces via the AC Stark effect. This chapter will detail the optical components that generate all of the light used in the experiment.

3.1 Resonant Light

Our resonant optical system consists of one master laser, three tapered amplifiers, two slave diodes, one spectroscopy cell, three electro-optical modulators, and approximately twenty acousto-optical modulators. See appendix B for a layout of the laser table as of August 8th, 2016 when we first attained a BEC. Similarly, appendix B also contains a summary of the different wavelengths we generate (and the relevant AOM RF frequencies) from a photon-energy perspective (instead of the usual atom level picture).

3.1.1 Master Laser

The master laser is the heart of any atomic physics experiment. We use a Toptica TA-Pro laser as our main source. It consists of an external cavity diode laser (ECDL) and a tapered amplifier (TA), also known as a master oscillator power amplifier (MOPA) system. We use an AR coated 671-nm laser diode (LD-0670-35-AR-2) in a DL-Pro module to control the frequency of the laser light very precisely (see section 3.1.3 for a discussion of laser locking). The output of the diode is used to seed a 300 mW tapered amplifier, which retains the spectral purity of the master diode. The output of the master laser is divided using polarization optics (typically Thorlabs PBS-101 beamsplitter cubes) and frequency shifted with acousto-optic modulators. Although the TA-Pro and BoosTA modules we purchased from Toptica were rated for 500 mW each, they failed to perform to their rated specification after a few months of operation. Eventually we gave up on trying to optimize both devices and proceeded with the assumption that they were instead 300 mW devices. We verified the linewidth of the master laser by performing a self-heterodyne measurement using a 6 km optical fiber; the measured linewidth of the master laser was 500 kHz, sufficiently narrow to address the $\Gamma = 5.9$ MHz D1 and D2 transitions in ^{7}Li.

3.1.2 MOT and Transverse Cooling

As described in chapter 2, there are two main transitions needed to address ^{7}Li atoms: cycling ($F = 2$, "MOTc") and repumping ($F = 1$, "MOTr"). We lock the master laser to the crossover transition (see section 3.1.3), and then use two double pass (DP) AOMs to span the ≈ 800 MHz frequency difference between the two ground states. Each arm is essentially then sent directly into a tapered amplifier to boost the required power to acceptable levels. Small amounts of light are chipped off from the MOT arms to form

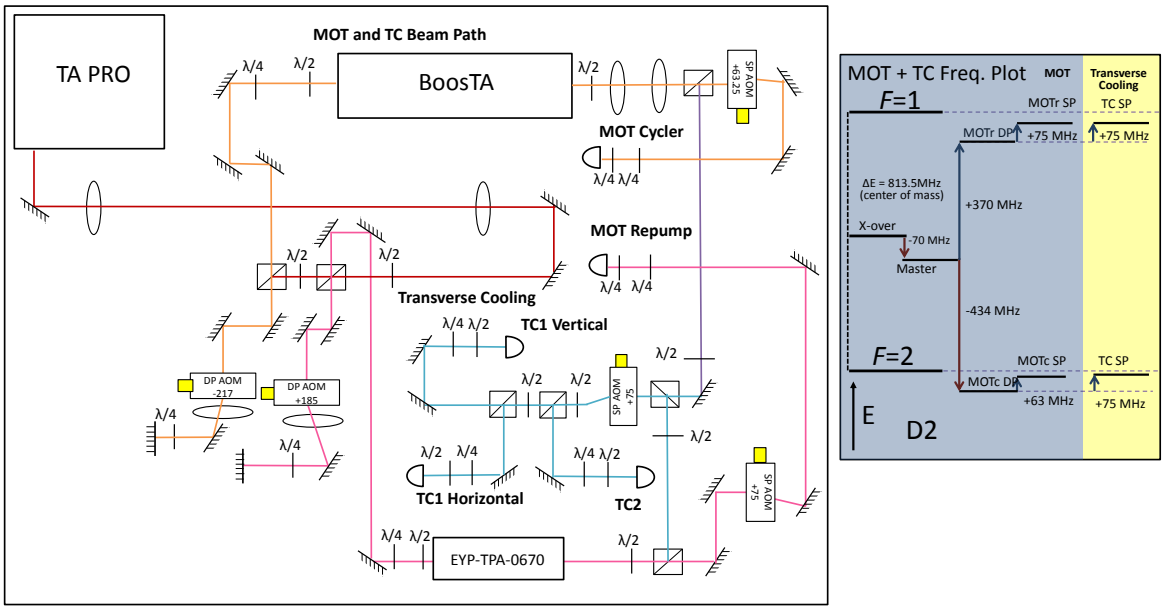

Figure 3.1: Layout and Frequency diagram of the MOT and transverse cooling system. Lenses on the DP AOMs form cat's-eye beam paths[28], allowing for a broader range of frequency tunability. Numbers on top of AOMs indicate their frequency shift in MHz.

the transverse cooling (TC) beams, but only 15 mW are used in this way. The majority of the 300 mW each TA outputs is directed to the 2:6 fiber splitter that forms the MOT.

Approximately 100 mW of light is not sent to either MOTc or MOTr AOM and goes on to form the spectroscopy and slave laser seed beams (for both the Zeeman slower and gray molasses injection lock systems).

3.1.3 Spectroscopy

In order to control the master laser's frequency to the degree required for experiments (MHz level precision on a 450 THz absolute frequency, $\approx$ 10 ppb), we must lock its frequency to an atomic transition. We do so using saturated-absorption spectroscopy (see [1] section 8.3 for a detailed treatment). In this technique, we apply two laser beams

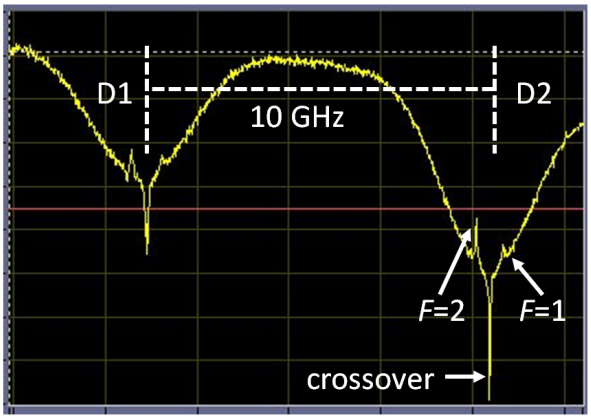

Figure 3.2: Example scan of the master laser across the D1 and D2 transitions showing the hyperfine sublevels. The master laser is locked to the crossover resonance between the $F = 1$ and $F = 2$ ground states.

to a thermal cloud of atoms held in the spectroscopy cell. The high power pump beam and the low power probe beam are spatially overlapped on the atoms while the transmission of the probe beam is monitored by a photodiode. We use a -70 MHz double pass AOM to apply a 260 kHz modulation to create a lock in signal to feed to the DigiLock lock-in (on the master laser's control box). It is possible to apply the lock-in modulation to the master laser's diode directly, but this adds noise at the modulation frequency everywhere on the laser's output and is not desirable (hence the need to use an external AOM). Importantly, this adds a -70 MHz offset to our lock point (the halfway point between the probe and -140 MHz pump beams), as shown in Fig. 3.1.

Figure 3.2 illustrates what lithium's saturated absorption signal looks like. The feature on the left is the D1 line (which is overlapped with the ^{6}Li D2 transition), while the feature on the right is the D2 transition. We lock our laser to the ^{7}Li D2 transition's crossover resonance. Without a pump beam, only the Doppler broadened absorption profiles are resolved.

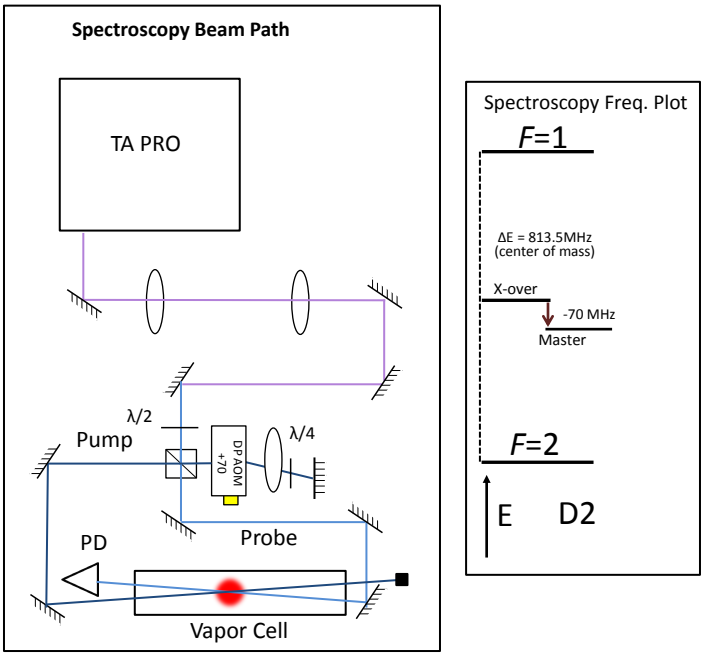

Figure 3.3: Schematic of spectroscopy optical system and frequency.

3.1.4 Tapered Amplifiers

The majority of our optical power is generated using tapered amplifier chips. These are semiconductor gain media that are physically wider on one end than the other. By injecting a small amount of light into the narrow end of the TA, one can increase the optical power by a factor of about ten (30 mW to 300 mW). We developed a design for a monolithic-type mount that would be passively stable. We've since built over six tapered amplifiers with the design. The lithium TA chips we use (Eagleyard Model EYP-TPA-0670-00500-2003-CMT02-0000) are rated for 500 mW, but we derate their performance to 300 mW.

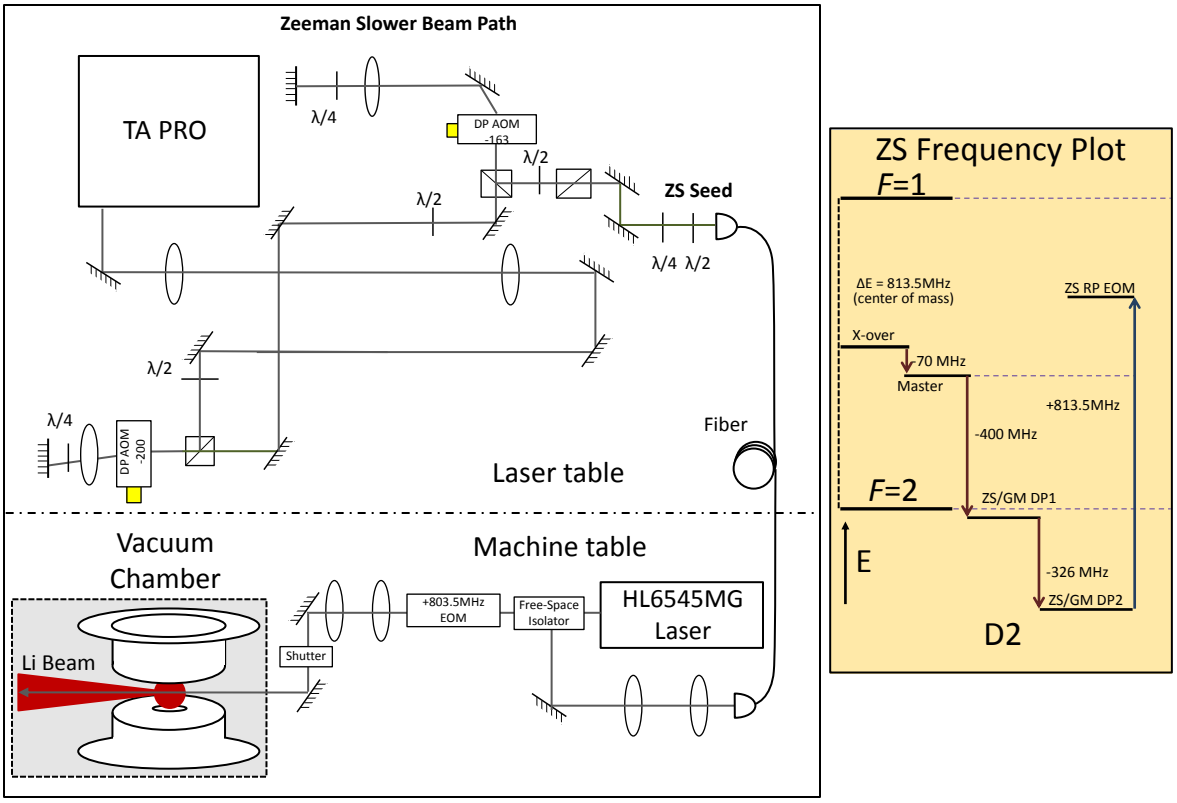

Figure 3.4: Schematic of Zeeman slower (ZS) slave layout and corresponding frequency.

3.1.5 Slave Lasers

Slave lasers are a tool that can turn a few hundred μW of light into tens or even hundreds of mW, and also can serve as a frequency selector (provided the cavity quality factor Q is high enough). We currently use two slave lasers in our setup, one for generating light for the Zeeman slower, and one for generating gray molasses light.

The basic principle of operation for a slave laser is simple. Tune a single mode laser diode's output with temperature and current until its natural wavelength is near the desired wavelength (in our case, 670.9 nm). Then take a small amount ($\approx$ 200 μW) of the light from the master laser and inject it into the slave laser diode's front facet. If the wavelength of the slave diode's output is close to the wavelength of the injected light, the slave diode will serve as an electrically-pumped gain medium that undergoes stimulated

Component	Part Number
Diode	HL6535MG
Diode Holder	Arroyo 224
Controller	Arroyo ComboSource 6305
Isolator	IO-5-670-HP

Table 3.1: Summary of the components used in our two slave laser systems.

emission at the master laser's wavelength. In this way, we can amplify 200 μW to 120 mW (a factor of 600 increase).

Each slave laser consists of a diode mounted in an Arroyo Instruments 224 TEC TO-Can mount controlled by a Arroyo Instruments ComboSource 6305 driver. This combination allows for easy tuning of the current and wavelength, and provides a stable platform for a variety of diodes. The slave diode we use (HL6535MG, center wavelength 660 nm, rated for 120 mW) natively lases a full 10 nm below our desired wavelength, but provides a high power output (at low cost). To compensate for this, we pull the diode with temperature to about 70°C (diode dependent) before injecting it.

Frequency selection is an added bonus of using a slave laser instead of a tapered amplifier. In order to generate light for gray molasses (see 3.1.6) we injection lock our slave laser to a sideband generated by a 9.2 GHz EOM. By tuning the current of the slave diode we can choose whether the slave laser is injected by the -1, 0, or +1 order of the EOM, despite all components existing in the same beam. In essence, we use the slave laser as a highly nonlinear filter for the desired frequency component. For the GM slave diode, it is possible to lock to each order independently; each one is separated by approximately 2-3 mA in diode current.

3.1.6 Gray Molasses

The optical system for gray molasses consists of a 9.2 GHz EOM, a slave laser for frequency selection and power generation, a tapered amplifier on the machine table for

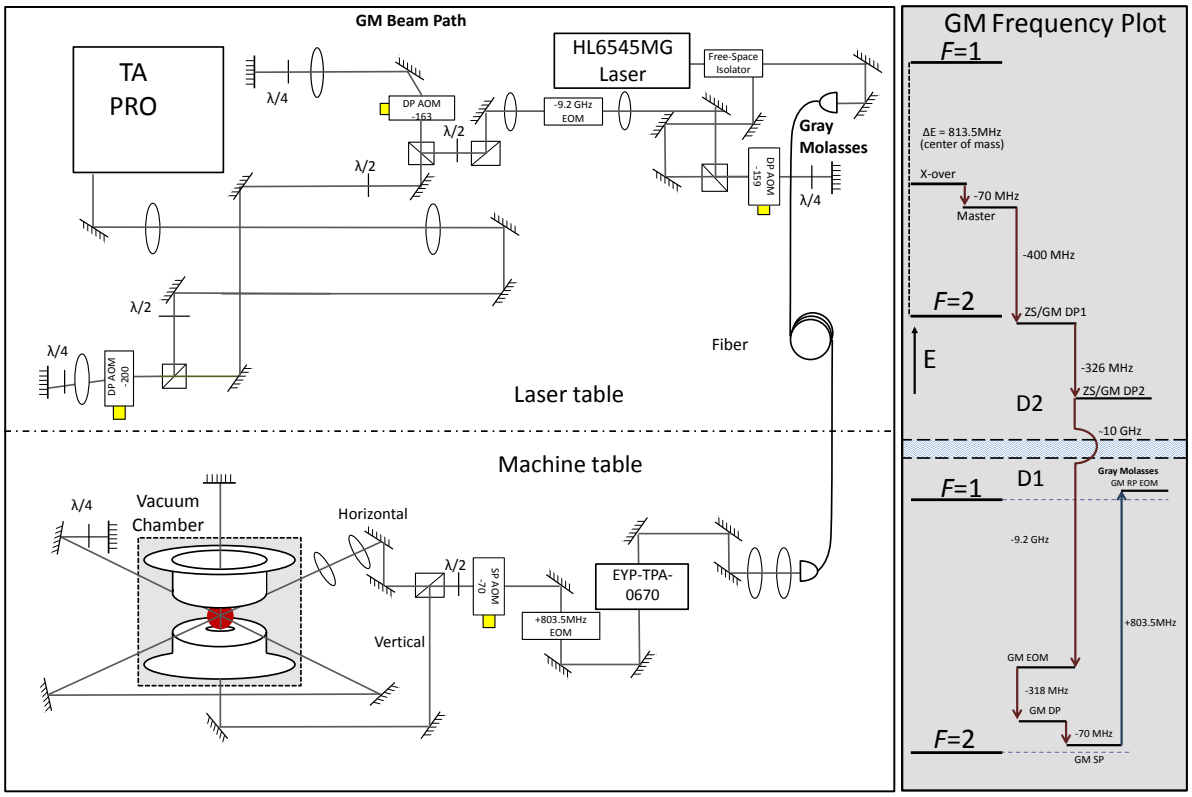

Figure 3.5: Schematic of the Gray Molasses optical system and corresponding frequency.

power, and finally another EOM to apply a sideband at 803.5 MHz to create the weak sideband required for the two-photon cooling (ignoring switching AOMs). To maximize the amount of optical power applied to the atomic cloud, we split the beam into a vertical axis and a horizontal axis. The vertical axis is retro-reflected and the horizontal axis is not only retro-reflected, but is arranged in a bow-tie configuration to completely recycle the horizontal path's power. We initially thought that the polarization of the beams would be crucial, but discovered that we did not require further polarization optics after splitting the beams to ensure we could reach the desired temperatures. The power of the beam is summarized in Table 3.2 to give a sense of the stages required to generate the light.

Stage	Power
Seed	200 μW
Slave	100 mW
TA Seed	40 mW
TA Output	300 mW
803.5 MHz EOM	100 mW
80 MHz AOM	80 mW

Table 3.2: Table of powers at various points along the GM beam path.

3.1.7 D1 Pumping

After the atoms are cooled during gray molasses, they must be spin polarized in order to effectively load the magnetic trap. The light for spin polarizing ("D1 pumping") is generated from the 0^{th} order of the gray molasses AOM. The light instead passes through a separate single pass AOM to bring it onto resonance with the D1 $F = 2 \rightarrow F' = 2$ transition. We increase the amplitude of the RF applied to the GM EOM to generate 50% sidebands (opposed to the 1% sidebands used in GM) and change the frequency to 825 MHz (experimentally optimized) to detune away from the two photon (Raman) resonance. It is not possible to spin polarize a gas of atoms with a two photon process, since the stimulated process does not change the entropy of the system.

3.1.8 Imaging

We use a standard absorption imaging technique to take pictures of our atomic clouds (as opposed to more complicated methods [13],[29]). We apply a short pulse of resonant light (approx 5-15 μs in duration) to the atoms. Regions of higher atomic density absorb more of the probe beam and cast a shadow onto the camera's sensor (we refer to this as the Probe with Atoms image, or PWA). This also heats the atoms and causes them to escape from any applied trap. We then wait a short period of time, and apply the same light to the camera for the same amount of time (Probe without Atoms, or PWOA). We

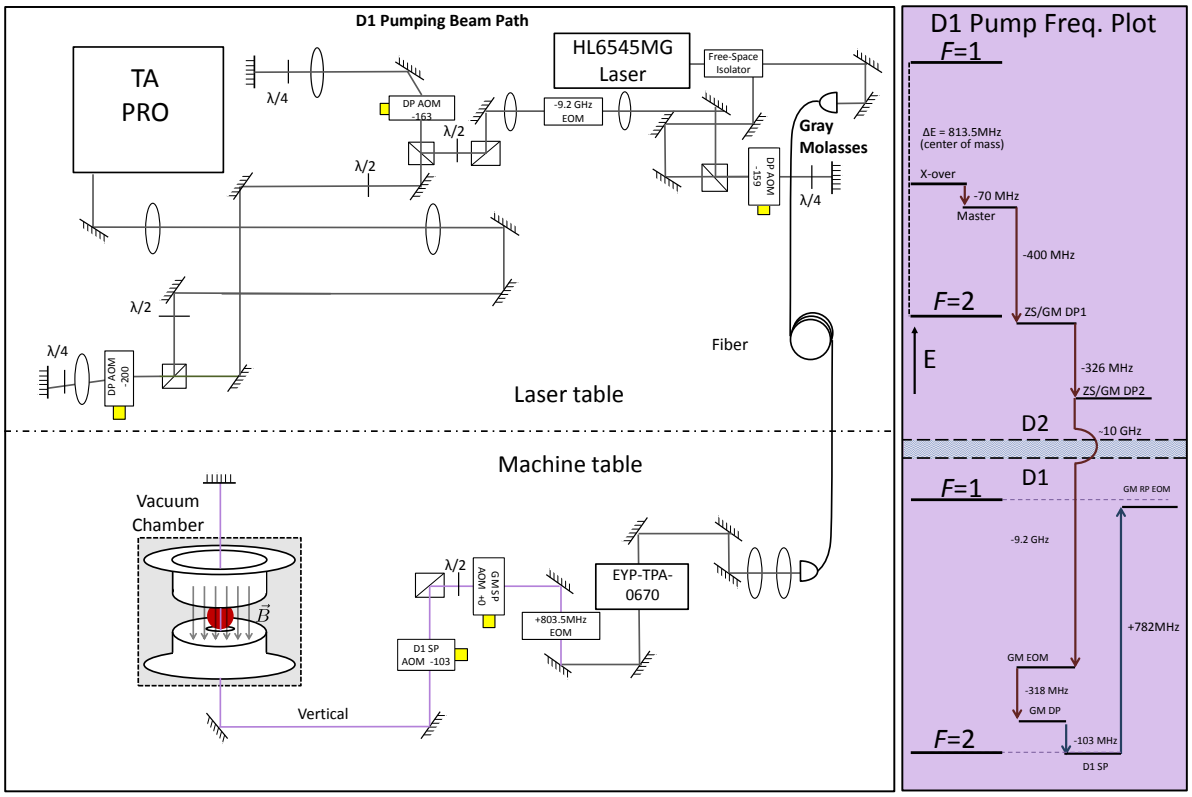

Figure 3.6: Schematic of the D1 Pumping optical system and corresponding frequency.

then take a third image without light to enable us to measure and subtract dark counts from our camera (i.e. background light in the system, or "Dark" image). We use the Optical Density (OD) as a measure of the amount of light the atoms absorb, which gives us an indication of how many atoms are in a given pixel-volume on the sensor. We can calculate the OD of a given pixel as the ratio of the number of counts in that pixel:

$$\mathrm{OD} = \ln\left(\frac{\text{PWA - Dark}}{\text{PWOA - Dark}}\right) \tag{3.1}$$

The measurable OD is limited by the bit depth of the pixels (the dynamic range) and the noise of the system. We use a PCO.edge 5.5 sCMOS camera as our main imaging camera (6.5 μm $\times$ 6.5 μm pixel size, 16 bit depth, approximate quantum efficiency (QE) of 50% at 671 nm). For beam alignment and side imaging, we use Basler aCA1920-25um CMOS

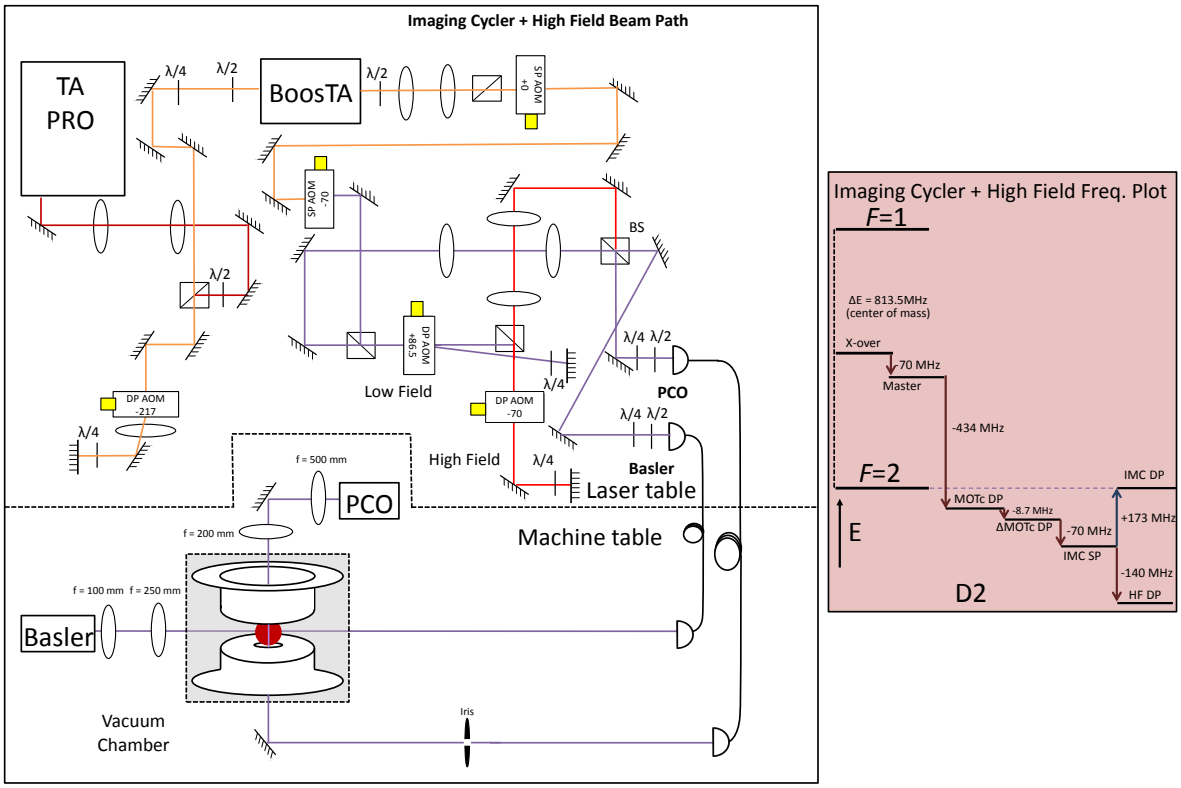

Figure 3.7: Schematic and frequency chart for low and high field imaging light. A beam splitter (BS) couples light into both the vertical and horizontal imaging axes simultaneously, allowing for easy switching between the two. When the IMC DP AOM (+ order) is off, the light passes to a separate DP AOM (− order), shifting the imaging light to be resonant with the high field transition.

cameras (2.2 μm × 2.2 μm pixel size, 12 bit depth, 56% QE (typical)). Importantly, knowledge of the magnification of the imaging system and the pixel size of the camera allows calculation of the physical size of the atomic cloud. For instance in Fig. 3.7, the Basler has a magnification factor of 100/250 (0.4) and a pixel size of 2.2 μm/pixel, meaning one pixel on the sensor corresponds to 5.5 μm of real space. Most frequently, we use the PCO camera with a magnification of 500/200 = 2.5 (200 mm objective lens, 500 mm refocusing lens), meaning each pixel corresponds to 6.6 μm/2.5 = 2.6 μm distance on the atoms. Practically speaking, the resolution of our imaging system is limited by the amount of light we can extract from the vacuum chamber (by the wavelength of light,

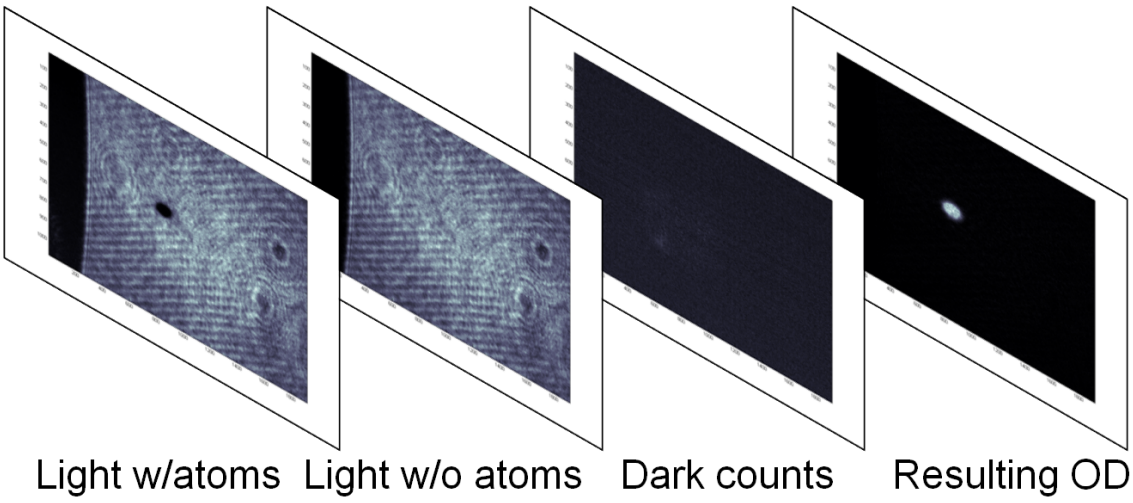

Figure 3.8: Example image stack used to calculate optical density from standard absorption technique. Left→right: PWA, PWOA, Dark, resulting OD.

and the available solid angle, or Numerical Aperture (NA)). For a 1" lens with $f = 200$ mm focal distance, we could at best hope for diffraction-limited spot size d (the Abbe diffraction limit) of:

$$\lambda = 671 \text{ nm}, \tag{3.2}$$

$$\text{NA} = 2.54 \text{ cm}/(2 \times 200 \text{ mm}), \tag{3.3}$$

$$d = \frac{\lambda}{2\text{NA}} = 5.27 \ \mu\text{m}. \tag{3.4}$$

The detuning of the light is crucially important for imaging atoms. Near resonant, but not on resonant light will experience a density-dependent phase shift as it passes through the atomic cloud. When dealing with optically dense clouds, this causes the probe beam to focus in regions around the atomic cloud, appearing as negative ODs in the composite images. When calculating the detuning of our imaging beams, we initially took the ground state splitting of lithium to be $\Delta = 803.5$ MHz but eventually discovered

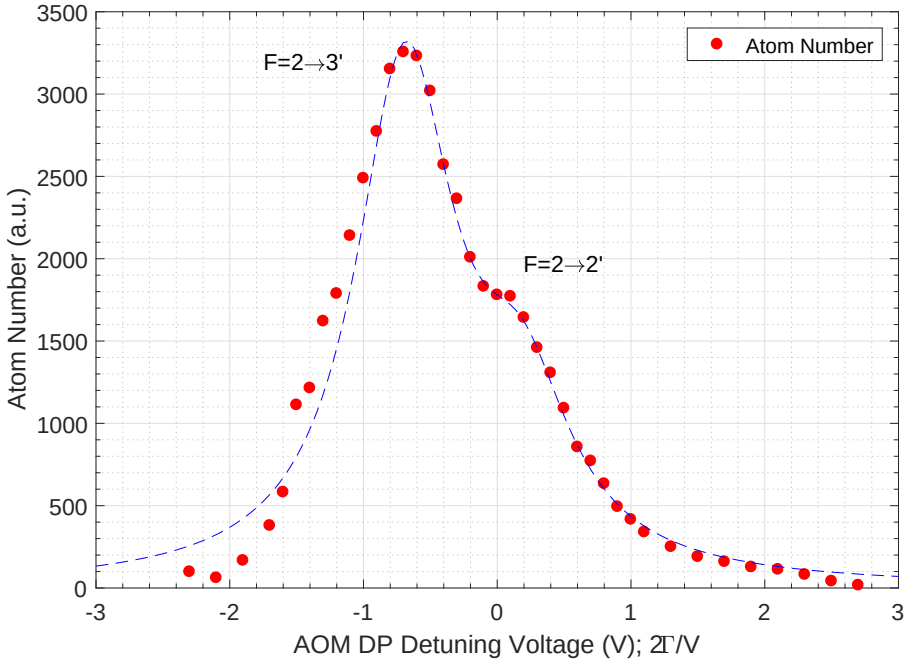

Figure 3.9: Unresolved upper hyperfine transition in Lithium. Red circles indicate measured atom number in the magnetic trap as a function of changing imaging detuning. Dashed line represents fit to double Lorentzian with a 10.44 MHz energy offset.

that due to the unresolved upper hyperfine splitting of the $^2P_{3/2}$ states that the more correct number to use is actually the "center of mass" splitting $\Delta_{\mathrm{COM}} = 815.3$ MHz, which takes into account the 10 MHz difference between $F' = 2$ and $F' = 3$ (see Fig. 3.9). By scanning the detuning of our imaging beam we can address the much stronger $F = 2 \rightarrow F' = 3$ transition.

By taking the imaging light (IMC) off of the MOT cycler's beam path (the light is normally diverted by an AOM into the 2:6 MOT fiber splitter), we can have nearly unlimited light for imaging (recall imaging works best in the regime where $I < I_{\mathrm{sat}}$). Further, the additional power from the BoosTA ($\approx$ 300 mW) allows us to split the imaging path into two parts. We use a beam splitter to couple the vertical imaging fiber simultaneously with the horizontal imaging fiber. This allows us to seamlessly switch

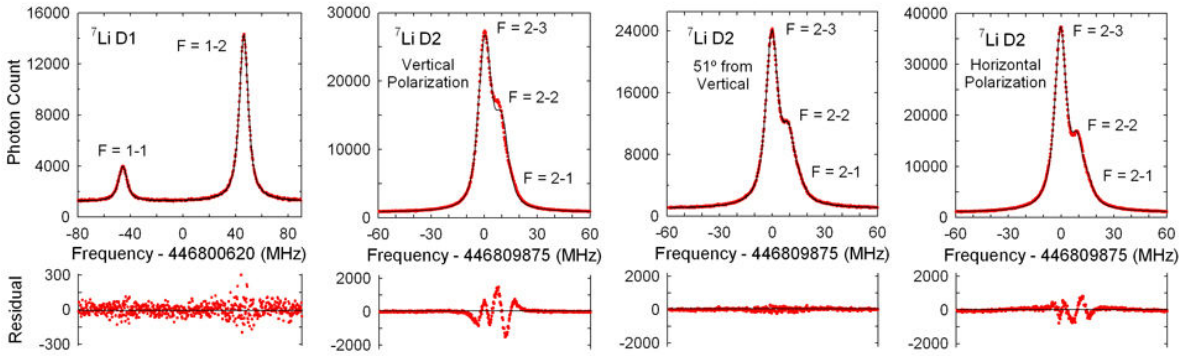

Figure 3.10: Unresolved upper hyperfine transition in lithium from NIST[18]. Compare the 3rd figure here to Figure 3.9 above.

Image Axis Name	Camera	Pixel Size (μm)	Magnification
Main	PCO.edge 5.5	6.5 x 6.5	2.5
ODT1	Basler acA1920-25um	2.2 x 2.2	0.4
ODT2	Basler acA1920-25um	2.2 x 2.2	0.8
Plug	Basler acA1920-25um	2.2 x 2.2	2
Kapitza Lattice	Basler acA1920-25um	2.2 x 2.2	2.5

Table 3.3: Summary of the imaging systems used in our experiment. The majority of images are taken with the PCO sCMOS camera. Basler cameras are mainly used for beam alignment.

between looking at the atoms from the top and from the side[1]. Additionally, we only ever image the atoms either at low field or at high field, which means it is possible to further recycle the MOT light to create light that is appropriate for imaging at high magnetic fields ($\approx$ 700 G, see section 3.1.9).

As a further complication, the unresolved upper hyperfine state of ^{7}Li means that imaging at low field requires a repumper (IMR), otherwise the atoms would only absorb a few photons before becoming optically dark to the cycling/imaging transition. In other words, each atom would only absorb a few photons before the entire cloud became optically transparent, resulting in a weak absorption signal. As with nearly every other

[1]It is possible to image from the top and side *simultaneously*, however the apparent atom number is decreased due to optical pumping effects.

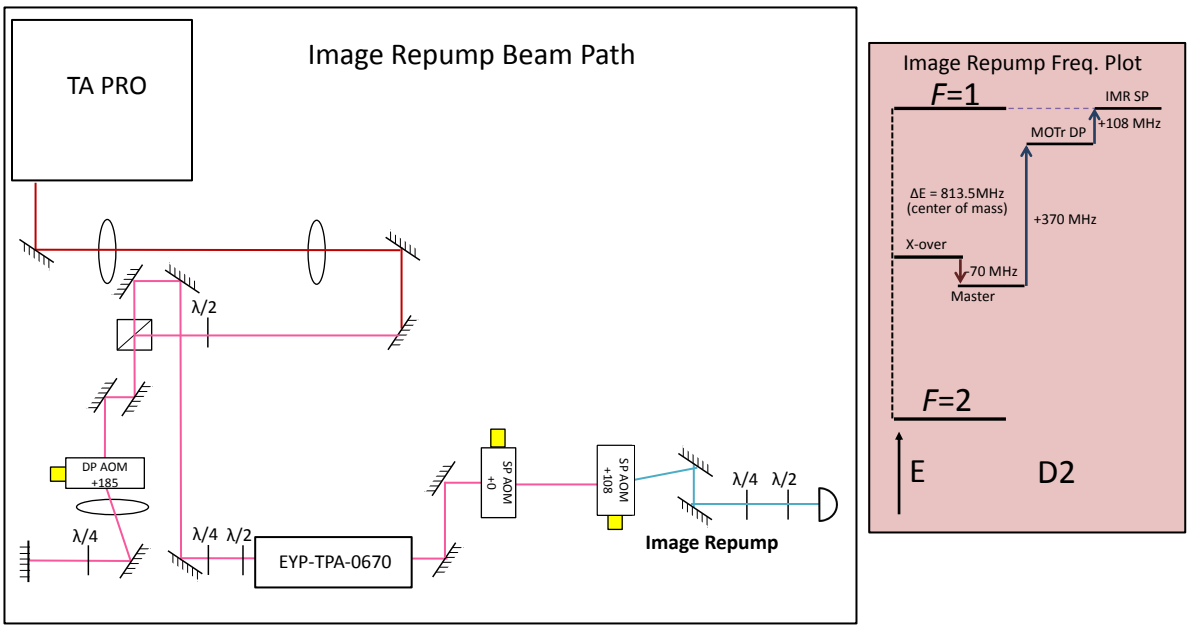

Figure 3.11: Schematic and frequency chart for low field repumping light.

optical transition we address, the imaging repumper ensures that the atoms can undergo many transitions before this becomes a problem. We play the same trick with the IMR light as we do IMC: use the 0^{th} order from the AOM that normally diverts the light into the fiber splitter for the MOT to send more than 100 mW to the imaging beam path (see Fig. 3.11).

3.1.9 High Field (HF) Imaging

Lithium's tunable interactions are an immensely powerful experimental tool. Tuning the scattering length allows studies of non-interacting Bosons ($a_{\text{scatt}} = 0$), strongly interacting Bose gases, nearly infinitely strongly interacting systems ($a_{\text{scatt}} \to \pm\infty$), and solitons ($a_{\text{scatt}} < 0$). All of these scattering lengths are accessible over a range of fields from ≈ 500 G $\to 740$ G. Tuning the scattering length over this range comes at a price: the

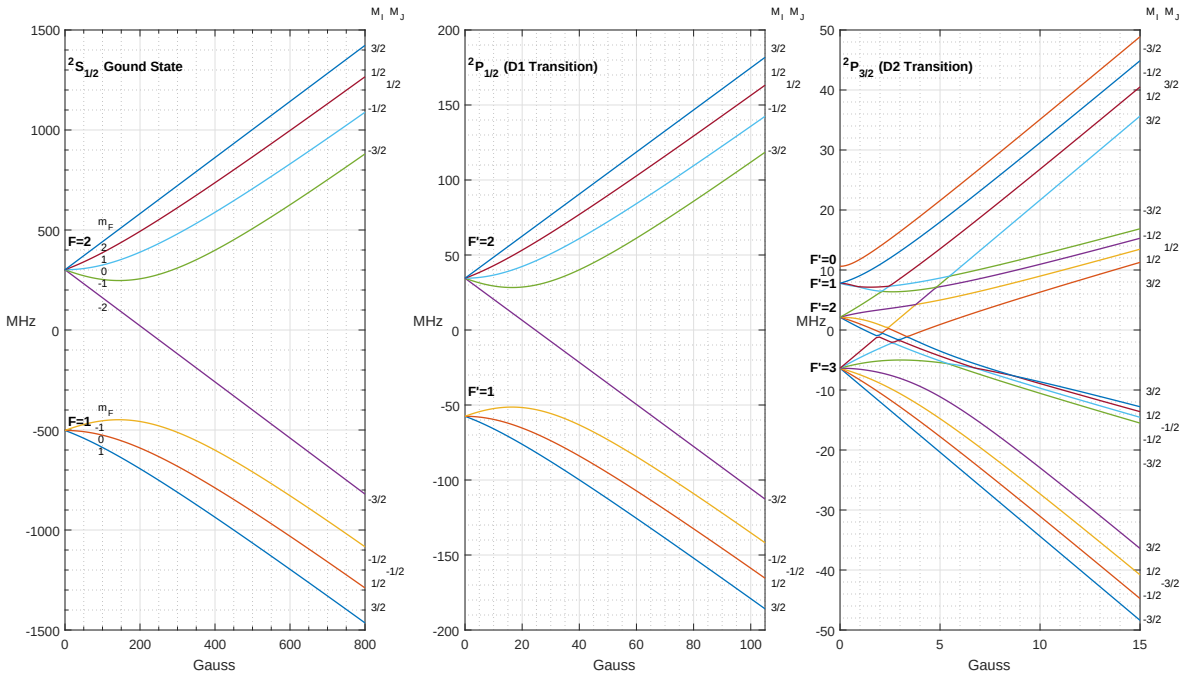

Figure 3.12: Zeeman shifts for all F, m_F sublevels. As the applied field increases, F and m_F are no longer good quantum numbers, but M_I and M_J are (the Paschen-Back regime). Energies are computed relative to the fine structure energy splitting. Note inverted structure of D2 excited state ($F' = 3$ is the lowest energy). HF imaging light addresses the $|M_I, M_J\rangle : |3/2, -1/2\rangle \rightarrow |3/2, -3/2\rangle$ transition (equivalent to the zero-field D2 transition: $|F, m_F\rangle : |1, 1\rangle \rightarrow |3', 3\rangle$).

frequency of light required to image the atoms at different applied magnetic fields can vary by as much as a GHz. We leverage the fact that the $|M_I, M_J\rangle : |3/2, -1/2\rangle \rightarrow |3/2, -3/2\rangle$ transition has energy (at 720 G applied field) close to that of the cycling transition ($F = 2 \rightarrow F' = 3$) at zero-field to generate high field imaging light with the addition of only a single AOM. The idea is illustrated in Fig. 3.7: at zero-field a double pass AOM (specifically the IMC DP + AOM) brings the light into resonance with the zero-field transition. To achieve high-field (720 G) imaging, we take the 0^{th} order off of the IMC DP AOM and direct it to a double pass (HF DP -) AOM. The high field transitions are sufficiently split to avoid lithium's unresolved upper hyperfine manifold, meaning no re-pumping light is required to image the atoms at the high field/zero interaction condition

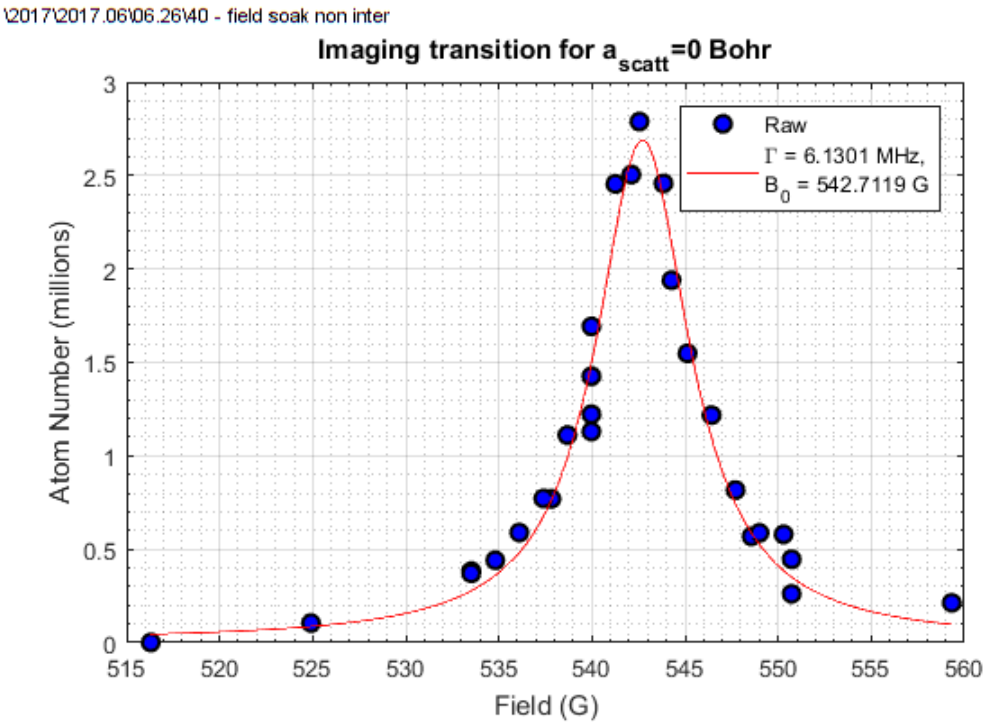

Figure 3.13: Atom number vs. Feshbach field near the zero-field crossing (543.6 G). Data fit to Lorentzian to extract the transition's linewidth Γ, in good agreement with the accepted value of 5.9 MHz.

(500-720 G). To generate light at the zero-crossing ($a_{\text{scatt}} = 0\ a_0$, 543.6 G), we take the single pass off the IMC DP AOM (which is normally double-passed to generate D2 light, not shown in Fig. 3.7). Our system is laid out in a similar manner to [30].

Transition	**ΔE from D2 transition**	**Field (G)**	**AOM**
D2 (Zero Field)	0 MHz	0	+173 MHz (IMC DP)
High Field	-313 MHz	720	-140 MHz (HF DP)
Zero Crossing	-86.5 MHz	543.6	+86.5 MHz (IMC SP)

Table 3.4: Summary of imaging transitions. High Field and Zero Crossing both address the $|M_I, M_J\rangle : |3/2, -1/2\rangle \rightarrow |3/2, -3/2\rangle$ transition.

Further, we can adjust the frequency of all of the imaging light ±30 MHz using the MOT cycler double pass AOM (before the BoosTA). The ability to scan over this range gives us precise control over the energy of the imaging light. This allows us to measure the linewidth of a given transition by fixing the frequency of the light and scanning the

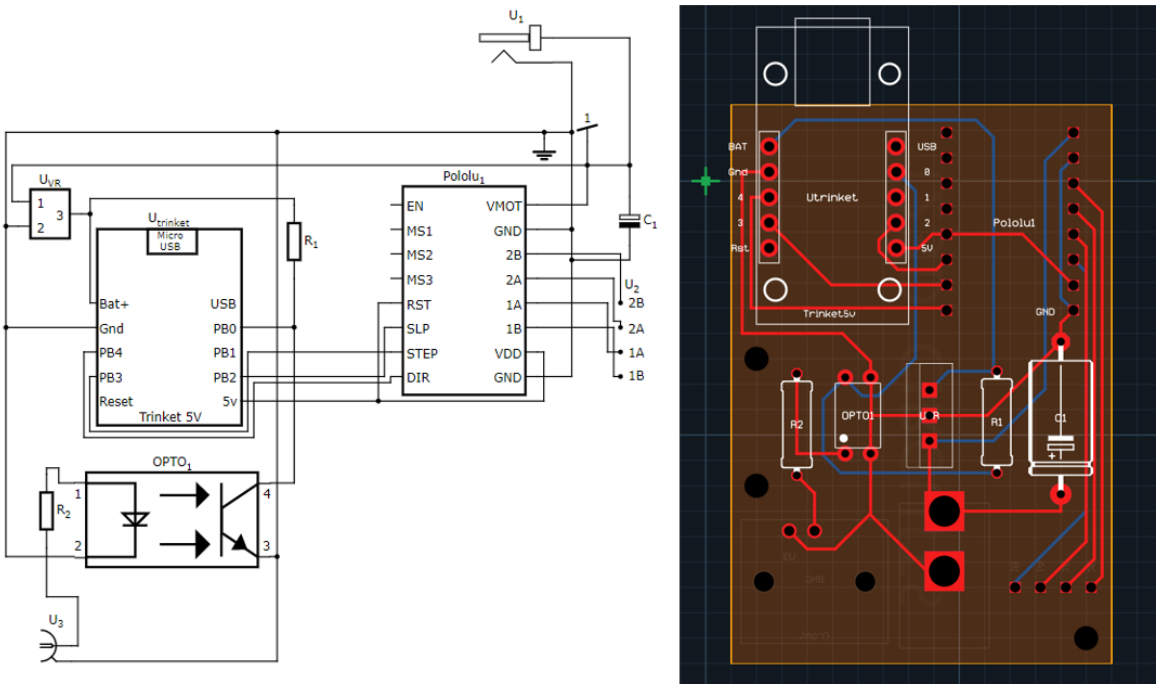

Figure 3.14: Circuit layout and PCB for shutters.

applied field (see Fig. 3.13 for an example of scanning the field near the zero scattering length crossing). Conversely, we can use the fixed energy of a transition to calibrate the magnetic field applied to the atoms to within a few G.

3.1.10 Optical Shutters

An AOM alone is insufficient to completely switch a laser beam on/off. Their single-pass extinction ratio is typically only around 30 dB (limited by the RF driver that powers the AOM), which means that they can couple a surprising number of photons into an optical fiber, even when "off." These stray photons can limit BEC lifetime and wreak havoc with the production of cold clouds. Most notably, the imaging system is particularly sensitive to stray light entering through optical fibers. Optical density is logarithmically sensitive to the number of absorbed photons, so carefully controlling and being able to completely turn off light coupled into optical fibers is of utmost importance.

ID	QTY	Component
Utrinket	1	Adafruit Trinket 5 V
UVR	1	LM7805 Voltage Regulator (5 V)
R1, R2	2	1 kΩ Resistor
OPTO1	1	PC817 Optocoupler
C1	1	1 μF Capacitor
U3	1	Right Angle BNC Connector
U1	1	DC Barrel Jack 2.0 mm
Pololu1	1	A4988 Stepper Motor Driver
U2	1	Screw Terminal 4 Holes

Table 3.5: Table of electrical components used in the optical shutter.

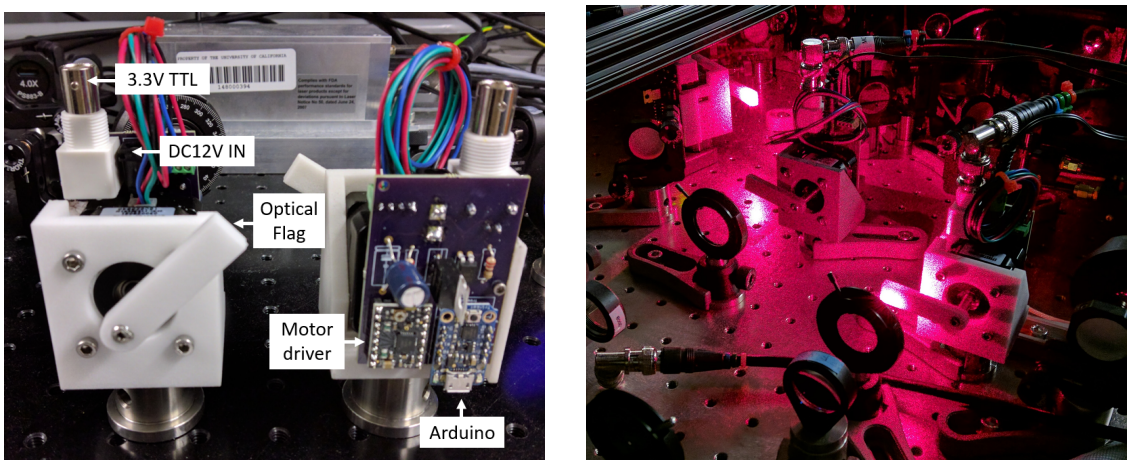

(a) Prior to installation showing relevant features and inputs.

(b) Three shutters blocking ≈ 100 mW laser beams.

Figure 3.15: Stepper motor based optical shutters.

To this end, we designed optical shutters to physically block the laser beam. Our first two optical shutters designs were based off of a modified hard drive, with a circuit actuating the read head of the drive to block the laser light. A single Arduino controlled ten shutters, which led to a large uncertainty in the delay between the trigger and when the shutter actually began to actuate. Further, the design coupled electrical noise into the machine, which required painstaking electrical isolation for each shutter.

At the suggestion of Julio Barreiro (professor at UCSD), we switched to a design based on a stepper motor and an A4988 stepper motor driver. To remove timing uncertainty

and the difficulties associated with making sufficiently fast pulse trains in Cicero[31] (see 4.5 for details on the computer control system named Cicero), we elected to design a circuit that incorporated an ATtiny85 (an Arduino based controller). Instead of a central Arduino that controls multiple shutters, each shutter has a dedicated unit that handles triggering and pulse train generation. The Arduino operates at a relatively fast 16 MHz clock rate, which allows a much shorter uncertainty in the timing of the trigger and the actuation of the optical flag on the shutter. An optocoupler further separates the inductive noise of the motor from Cicero, while the 3D printed mount (made of Nylon) electrically isolates the shutter from the optical table.

These shutters exhibit a characteristic rise/fall time of $<$100 μs. A $\approx$ 2 ms delay between the trigger and the actuation of the shutter (the motor driver requires 1 ms to activate its charge pump), is easily pre-triggered in Cicero. The uncertainty in this delay time is less than 100 μs, which allows us to switch beams rapidly and with sufficient confidence to use them (instead of AOMs) for switching on time scales longer than a few ms (e.g. turning off the Zeeman slower laser beam). We use AOMs for switching on time scales of a few μs.

3.2 Off-Resonant Light

The off-resonant laser system is divided into two main parts: 532 nm (repulsive, for plugging the magnetic trap) and 1064 nm (attractive, for creating optical dipole traps and lattices). The hundreds of nm detunings used to manipulate atoms in this way requires multiple Watts of CW optical power. As a consequence, these two high power laser systems reside on the machine table itself, which allows for free-space coupling of laser light into the main chamber (and hence the atoms).

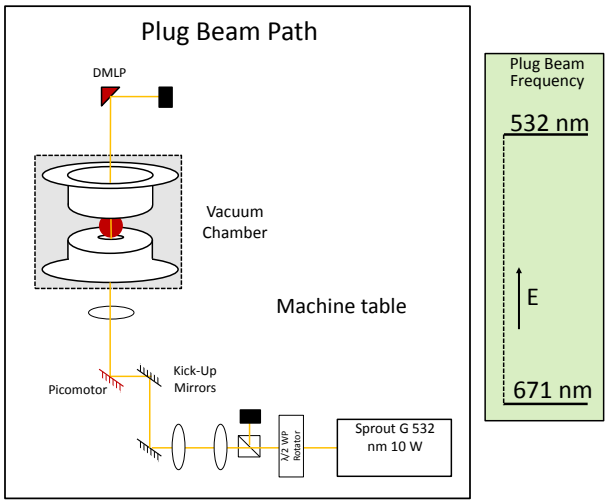

Figure 3.16: Schematic of the plug beam optical system and corresponding frequency

3.2.1 532nm (Mag Trap Plug)

We use a Lighthouse Photonics Sprout-G 10 W laser to plug the magnetic field zero in our quadrupolar magnetic trap. The beam is focused to a spot size of 15 μm $1/e^2$ radius. We use a telescope to make the beam approximately 1" in diameter before the lens that focuses it into the chamber (an $f = 300$ mm, ND:YAG, V-coated for 532 nm). Initially we tried to use an AOM for fast switching of the plug beam, but this compromised the mode. We use a Pacific Laser Equipment waveplate rotator (part number: RSC-103E) to control the power in the beam and turn it from 10 W to 300 mW in around 200 ms. A beam shutter blocks the rest of the light from entering the chamber after evaporation has completed.

We made an imaging system to align the beam onto the atoms using a dichroic mirror to protect the imaging camera. We later discovered that once the beam intersected the evaporated cloud, we could use the depleted region of atoms as a marker for the beam's position (see the hole in the evaporated cloud induced by the plug beam in Fig. 2.16).

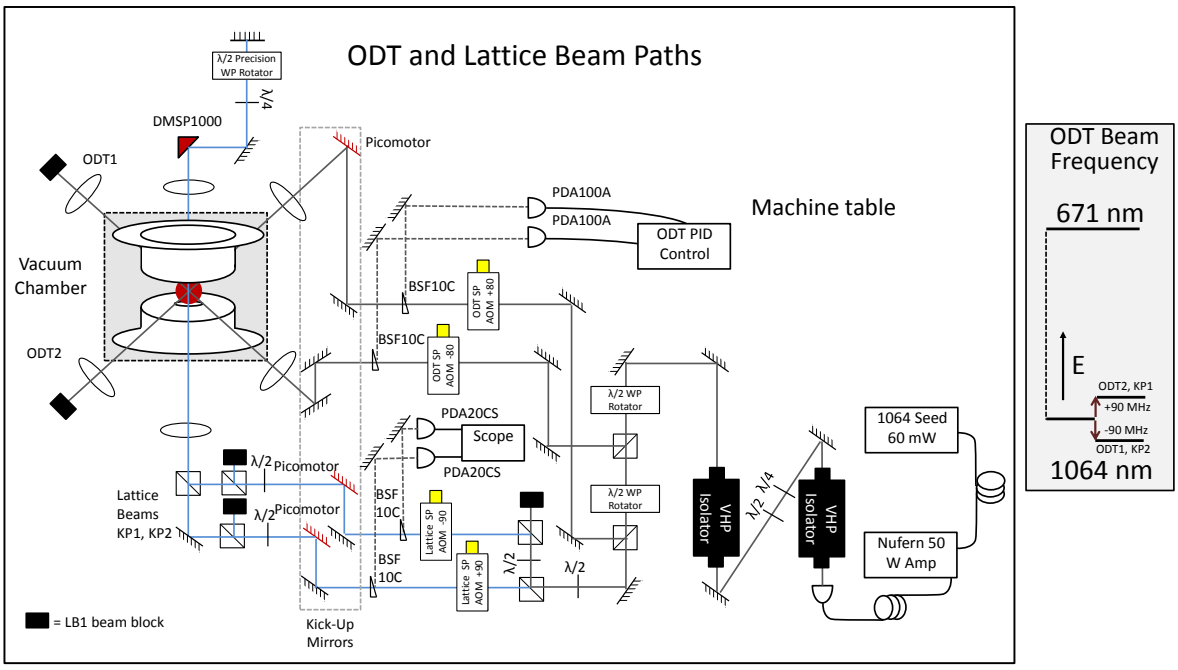

Figure 3.17: Schematic of the ODT and lattice beams' optical system and corresponding frequency.

3.2.2 1064 nm (ODT and Lattices)

We use a Nufern 50 W fiber amplifier (NUA-1064-PD-0050-D0) and an Orbits Lightwave 60 mW 1064 nm seed laser (Ethernal Slow Light Laser System SYS-50000A10645T) to provide laser light for our far-off-resonant traps (FORTs) and optical lattices. Two Thorlabs IO-5-1064-VHP free space isolators provide in excess of 60 dB isolation for the fiber laser system.

A series of half wave plates and polarizing beamsplitter cubes direct the laser power into two 80 MHz AOMs (IntraAction ATM-802DA6). Care must be taken to use different diffraction orders (e.g. +80 MHz and -80 MHz) for the two ODT beams to keep the two beams from creating an interference pattern on the atoms. The 2 mm beams are focused onto the atoms with $f = 200$ mm lenses mounted on Newport 9066 precision stages. This creates ODTs with a measured $1/e^2$ diameter of approximately 200 μm.

We use Newport 8821 Picomotor piezo actuated mirror mounts to finely control the position of the second ODT in order to create a deep crossed optical dipole trap (XODT). We can load 2×10^7 atoms into our XODT from the RF evaporated cloud.

Home built PID controllers allow us to control the optical power in the beams to perform forced evaporation using an analog input from Cicero (0-10 V). The beams are picked off and monitored using Thorlabs BSF-10C beam samplers and PDA100A photodiodes with appropriate neutral density (ND) filters.

We use the same kind of waveplate rotators (see Sec. 3.2.1) to redirect optical power from the ODTs into the lattice beams over the course of optical evaporation (4.5 s).

To measure the power in the lattice beams we use two fast InGaAs photodiodes (Thorlabs PDA20CS). Special care must be taken when monitoring 1064 nm beams at high frequencies. The InGaAs photodiodes are necessary because 1064 nm photron energy is close to the bandgap of the Si used in Thorlabs' PDA100A photodiodes (1.1 eV = 1.13 μm). The skin depth of the silicon diverges as it approaches the bandgap (which fails to cause carrier excitation in the active region of the sensor). This in turn causes a characteristic double-decay (with carrier diffusion causing a slow voltage-response) when using Si photodiodes at bandwidths above $\approx$ 10 kHz.

3.3 Optical Lattices

The majority of our experiments rely on BECs loaded into optical lattices. The optical lattice is the experimental test bed we use to build Hamiltonians to study. As such, it is important to understand the practical considerations of aligning optical lattices to atoms.

Step zero is making a BEC and aligning the lattice beams to its position. The BEC's position is determined by the position of the optical dipole traps, so aligning everything

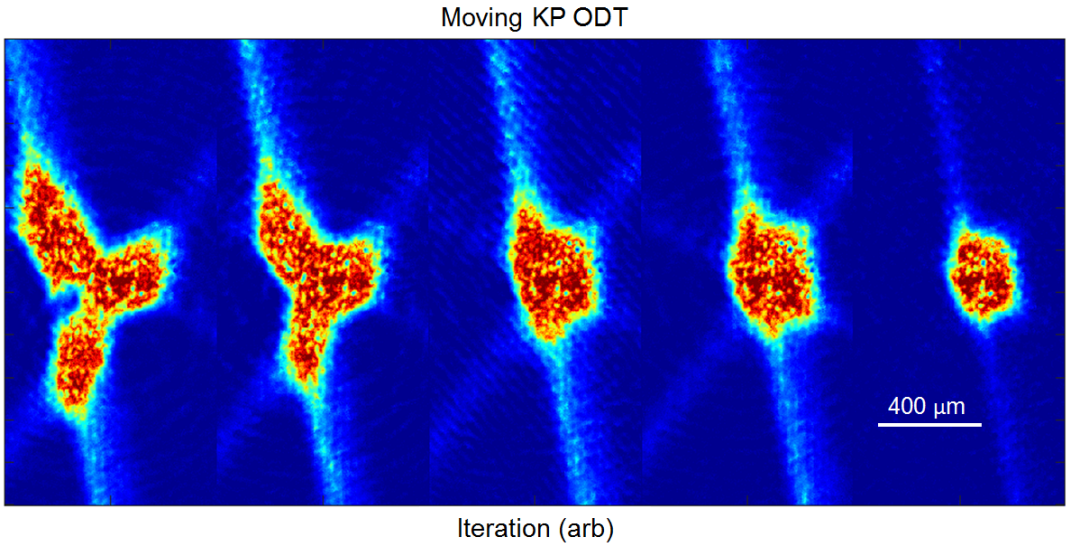

Figure 3.18: Horizontal alignment of the lattice beam onto the XODT. Left panel clearly shows interaction between the 3 ODT beams and the blue-detuned plug beam. As the lattice beam moves toward the center of the ODT, the atoms are more well confined and make smaller excursions from the center of the cloud, indicating a deeper total optical potential (i.e. good alignment).

is a matter of overlapping three beams. On the length scales of a BEC, the optical lattice is roughly a tube ($\approx$ 3 mm $\times$ 200 μm), which means that the alignment of the initial dipole trap (before retroreflection) is a two dimensional problem. It is usually sufficient to observe the BEC along the desired lattice direction, and then overlap the focused spot of the lattice onto the camera at the same position as the BEC. Properly focusing and imaging a lattice beam is difficult, and one must take special care to ensure that the lattice beam is going through the center of each focusing optic (the lens that focuses the lattice into the chamber, the lens that recollimates the beam, and the lens that images the beam onto the camera).

We struggled for many months with abnormally low lattice depths (typically a factor of two less than the theoretically predicted number) until we used the BEC's motion to focus the lattice beams. We had observed similar misfocusing of 1064 nm beams with the ODT beams in the past resulting from chromatic aberration between the 671 nm light

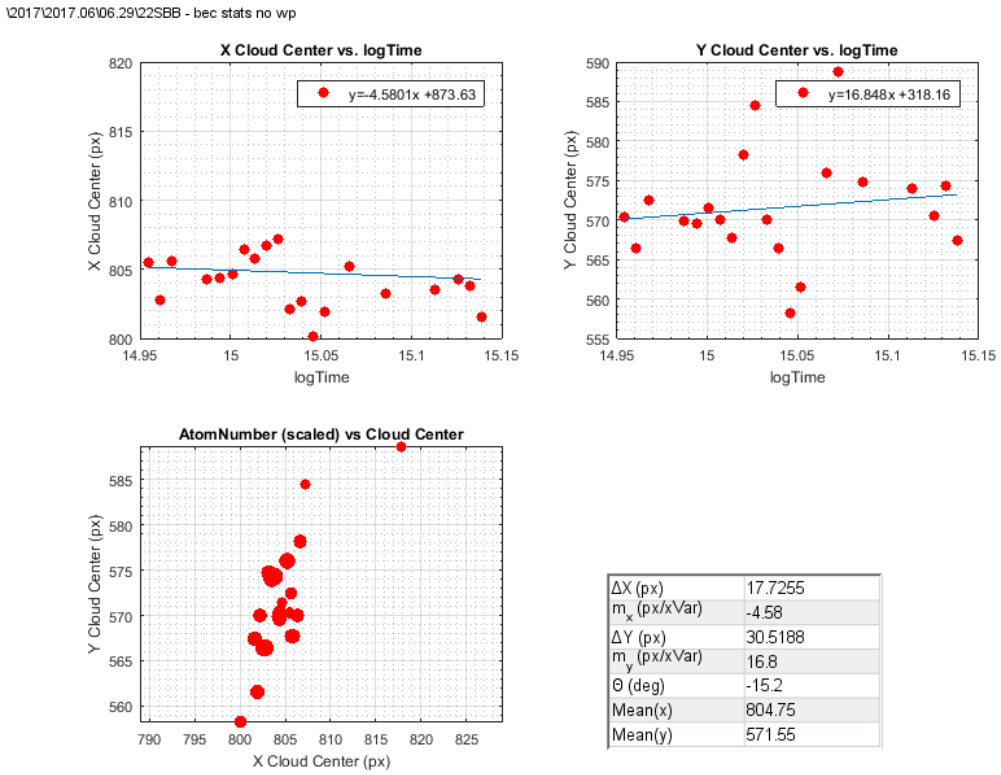

Figure 3.19: Measurement of the BEC's average position from the side using the Basler ACE camera. Atom number fluctuations and vibrations cause uncertainty in the measured position.

used to image the BEC and the 1064 nm light that makes up the lattice (on the order of a few mm). The ultimate metric for determining the focus of a beam is to use the atoms. We create a BEC at a high-field (around 720 Gauss), and then ramp the field quickly to zero Gauss, where ^{7}Li has a small, positive scattering length ($a = 7.7\ a_0$). Doing so removes the presence of any magnetic field curvature generated by the Feshbach magnets, which in our experiment gives rise to oscillations on the scale of around 13 Hz (which is greater than the trap frequency associated with the axial trap frequency of the optical trap, around 3 Hz). Ramping to zero field quickly is important because the scattering length becomes negative below about 540 Gauss, which can lead to the formation of solitons. Once the magnetic fields have turned off (in $\approx 100\ \mu$s), we turn off the optical

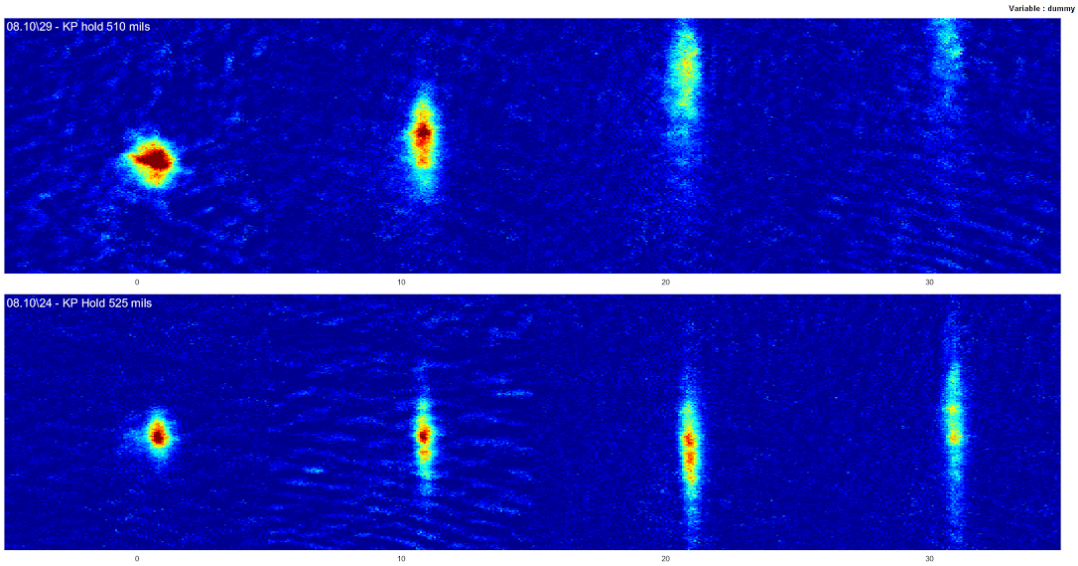

Figure 3.20: Focusing the lattice beam. Movement of BEC at $B = 0$ G in lattice ODT (for short times). Upward motion indicates the beam is not focused at the atoms. Bottom: with the objective lens moved back 15 mils ($\approx 400\mu$m), the atoms are pulled down, indicating the focus has moved through the location of the BEC.

dipole traps and allow the atoms to undergo simple harmonic motion in the lattice beam's ODT (i.e. without retro-reflection). If the beam is focused not on the position of the atoms, they will oscillate in the direction of increasing optical intensity. Adjusting the position of the focusing objective lens will correct for this misalignment.

Lattice depth is usually reported in units of the recoil energy $E_R = \hbar^2 k^2/2m \approx 25$ kHz. This gives a rough estimate of how much energy it takes to excite an atom out of the lattice, and allows easy comparison between experiments that use different atomic species.

3.3.1 Kapitza-Dirac Diffraction

To measure our lattice depths, we use a technique called Kapitza-Dirac diffraction[32]. What is particularly enjoyable is the reversal of roles from what one typically observes in physics labs: in AOMs for instance, a light wave is made to diffract off of a standing wave

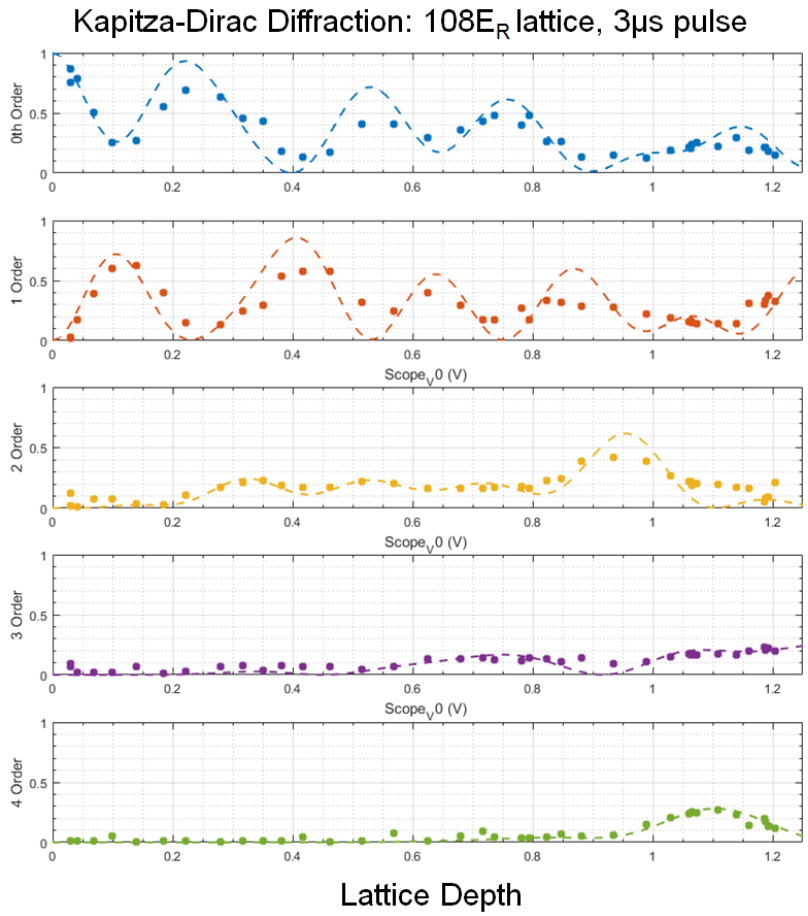

Figure 3.21: Kapitza Dirac diffraction. Each plot represents the population in a given diffracted order (±4 presented here), ovarlaid is the theoretical prediction (dashed) for a lattice of depth specified (108 E_R).

of phonons, or in the double-slit experiment where light generates an interference pattern after interacting with matter; whereas in Kapitza-Dirac diffraction, a coherent *matter-wave* (the BEC) diffracts off a standing wave of light (the lattice). Fundamentally the calibration is performed by varying the depth of the applied optical lattice and observing the population of the diffracted orders. The Hamiltonian governing atoms in an optical

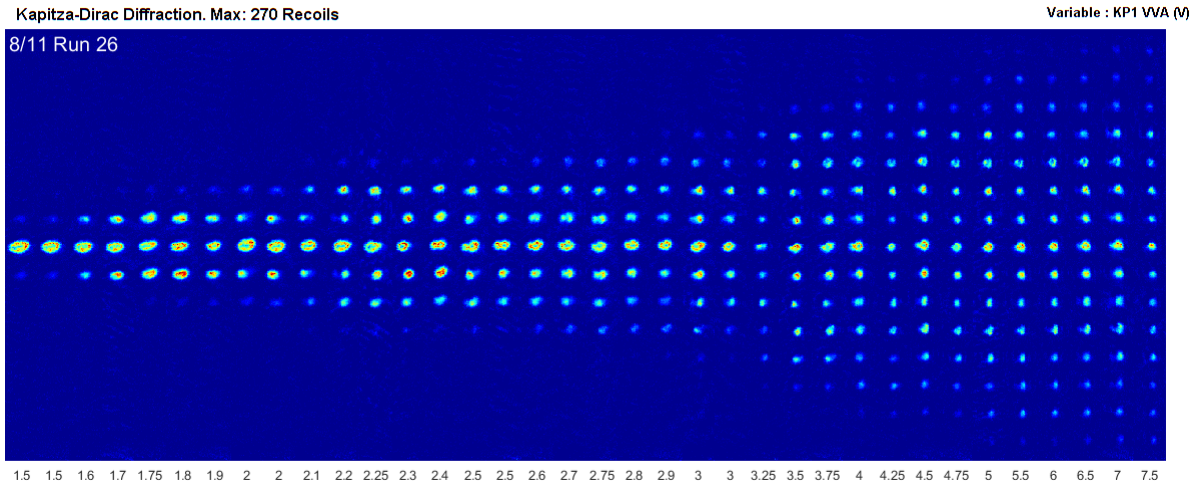

Figure 3.22: Increasing number of diffracted orders as a function of lattice depth. 270 E_R lattice applied for 3 μs followed by 1250 μs of free expansion.

lattice can be expressed:

$$\hat{\mathbf{H}} = -\frac{\hbar^2}{2m}\partial_x^2 + V_0 \cos^2(kx) \tag{3.5}$$

$$= -\frac{\hbar^2}{2m}\partial_x^2 + \frac{V_0}{2}(1 + \cos(2kx)) \tag{3.6}$$

In the limit that the atoms have negligible kinetic energy and undergo a stimulated emission process (giving them $\pm 2n\hbar k$ momentum, where k is the wavenumber of the lattice photons, and $n \in \mathbb{Z}$), we can expand the wavefunction in the planewave basis:

$$\psi(x,t) = \sum_{n=-\infty}^{\infty} c_n(t) e^{i2nkx} \tag{3.7}$$

$$c_n(t=0) = \delta_{n0} \tag{3.8}$$

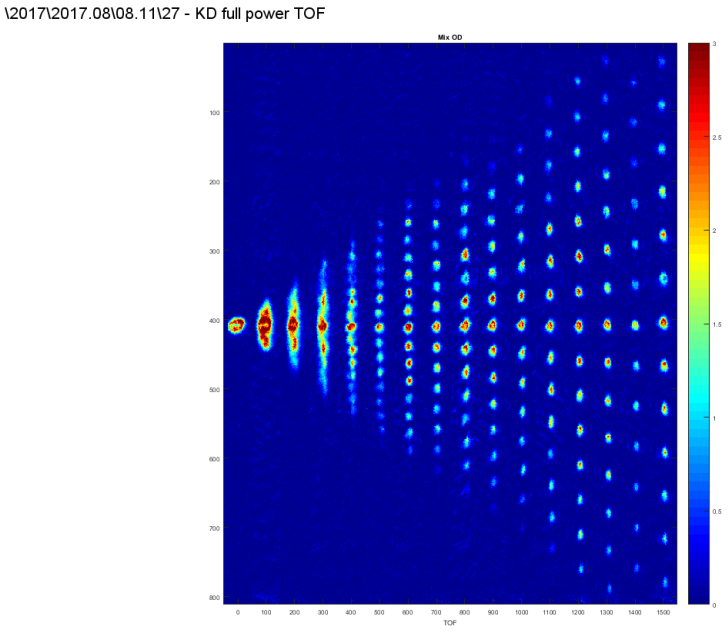

Figure 3.23: Diffraction of a BEC (matter wave) off of a standing wave of light.

With the relevant operators:

$$\partial_x^2 |n\rangle = -4n^2k^2|n\rangle \tag{3.9}$$

$$\cos^2(kx)|n\rangle = \frac{1}{2}|n\rangle + \frac{1}{4}|n+1\rangle + \frac{1}{4}|n-1\rangle \tag{3.10}$$

The TDSE for the coefficients of the plane wave basis is then given by:

$$i\hbar\dot{c_n} = 4E_R n^2 + V_0\frac{(c_{n+1} + 2c_n + c_{n-1})}{4} \tag{3.11}$$

In the uniform lattice regime (where the transverse extent of the lattice beam and cloud are ignored), solutions to the above differential equation take the form of a Bessel functions (in the Raman-Nath regime, again see [32]). With lattice inhomogeneity, the different transverse parts of the cloud experience different lattice depths, and so the overall distribution is washed out. This can be compensated experimentally by making the

transverse extent of the lattice beams larger, at the cost of optical power and total lattice depth. Our proposed experiments require deep optical lattices, so this was not a trade-off we could make.

Lithium presents a technical challenge for deep lattice experiments, as its light mass reduces the effective optical trapping power of a lattice beam. In other words, the lighter the atom, the more optical power required to trap the atoms against their thermal motion. Further, Kapitza-Dirac diffraction is also challenging because the ideal Raman-Nath pulse duration is only a few hundred ns. The benefit of using lithium is that its light mass pushes the time scales of any experiment up by about a factor of ten from those performed with heavier elements such as rubidium or strontium.

3.3.2 Amplitude Modulation Spectroscopy

It is also possible to calibrate lattice depth using a method called amplitude modulation spectroscopy. This is especially useful in the shallow lattice regime, where Kapitza-Dirac diffraction is poor. The band structure of the optical lattice means that there exist transitions between low energy band and higher bands, separated by energies on the scale of hundreds of kHz. Only even parity transitions are allowed (e.g. $1\rightarrow3$, $1\rightarrow5$, etc.) due to the drive preserving the symmetry of the wavefucntion. First the atoms are adiabatically loaded into the ground state of the lattice. Then, a small modulation (typically 10-20%) of the lattice depth is applied for a short amount of time (0.5 ms), and the resulting cloud is band-mapped (see Fig. 5.7 for schematic) to resolve the excited band population.

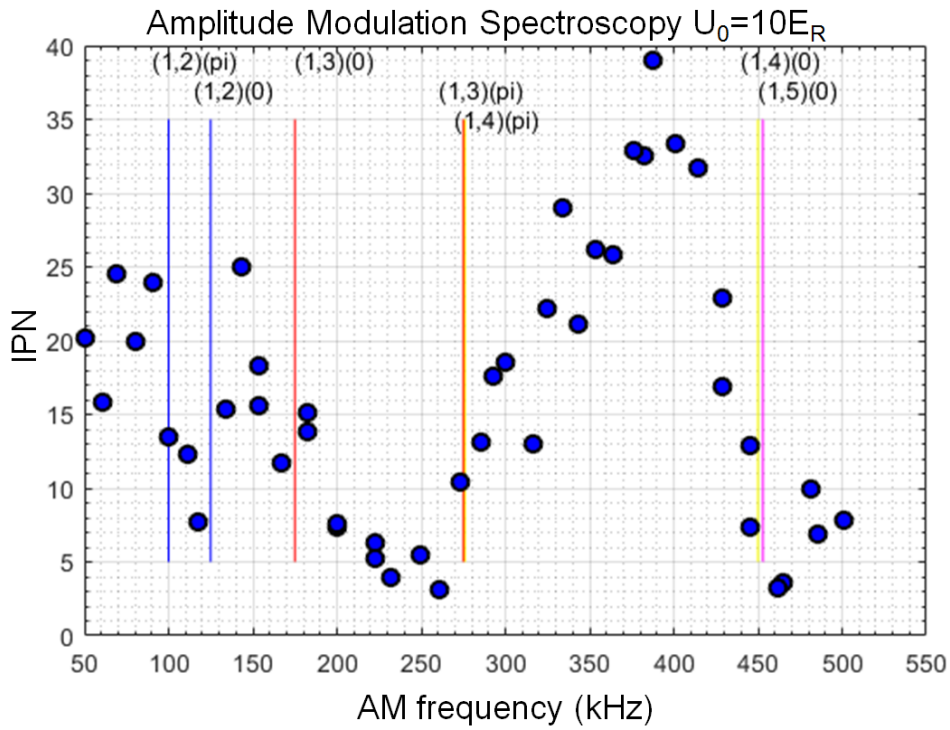

Figure 3.24: Amplitude modulation spectroscopy in a 10 E_R deep lattice. Dips in IPN (blue dots, see 5.24 for description) occur near allowed band transitions (vertical lines) noted as as: (photon number, band number)(quasimomentum). E.g. atoms absorb a single photon resonant with the 1→3 (d-band) transition at $k/k_L = \pi$ when the frequency of amplitude modulation is around 275 kHz.

3.3.3 Optical Confinement and Contact Energy

Atoms in a lattice will interact with each other with a characteristic energy defined as the product of the two-particle s-wave scattering energy g, and the number density of the cloud n such that (following [17]):

$$g = 4\pi\hbar^2 \frac{|a_{\text{scatt}}|}{m}, \tag{3.12}$$

$$E_{\text{contact}} = g \times n = 4\pi\hbar^2 \frac{|a_{\text{scatt}}|}{m} \left(\frac{N}{V}\right). \tag{3.13}$$

We need a good understanding of the number density $n = \rho = N/V$, but we can calculate this from observed atom numbers and parameters of our traps. We make a first estimate

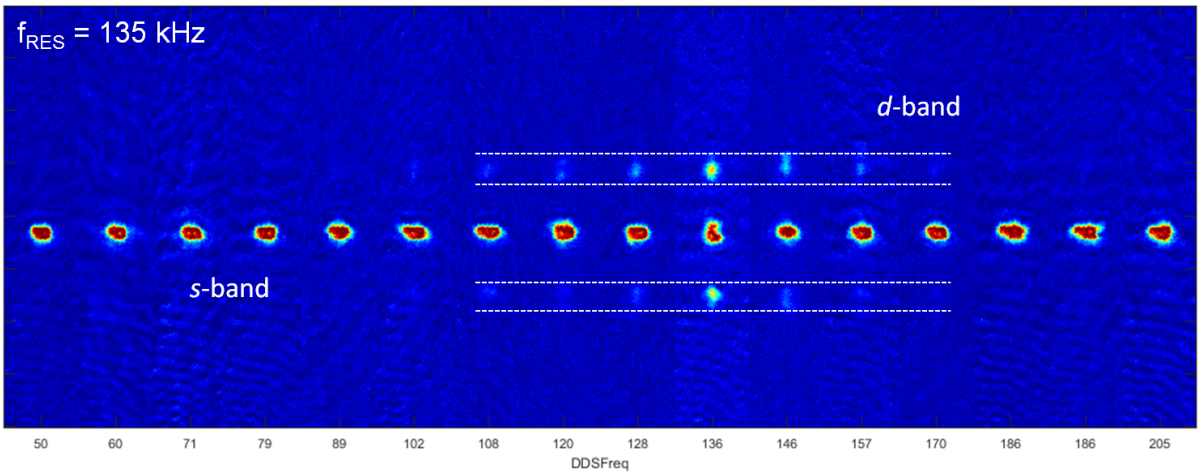

Figure 3.25: Amplitude modulation spectroscopy varying the frequency of modulation (in kHz) in a $5E_R$ deep lattice (20% modulation depth). $1 \rightarrow 3$ (d-band) excitation occurs at ≈ 135 kHz.

of the cloud's spatial extent (for a noninteracting Bose gas) using the observed transverse trap frequencies (in x and y), and the fact that the XODT has twice the confinement in the direction orthogonal to the propagation direction of both beams (z):

$$\omega_x = \omega_y = \frac{1}{2}\omega_z = 1 \text{ kHz}, \tag{3.14}$$

taking the geometric average lets us estimate the spatial extent of the wavefunction a_{SHO}:

$$\omega_{\text{SHO}} = (\omega_x \omega_y \omega_z)^{1/3}, \tag{3.15}$$

$$a_{\text{SHO}} = \left(\frac{\hbar}{m\omega_{\text{SHO}}}\right)^{1/2}. \tag{3.16}$$

The harmonic oscillator length a_{SHO} predicts a cloud size of only 2.7 μm for our system, but this is an underestimate which assumes a noninteracting Bose gas (i.e. $a_{\text{scatt}} = 0$. At finite scattering lengths, the atoms repel each other, causing the spatial extent of the cloud to increase. In this case we can use the Thomas-Fermi approximation of the radius:

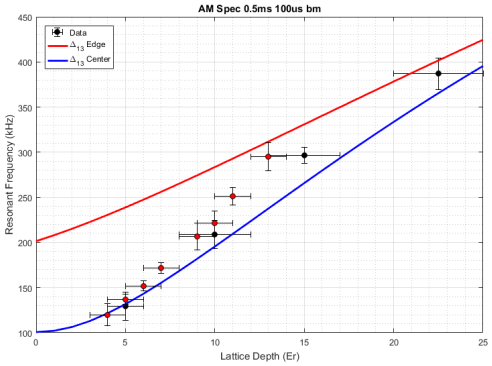

(a) Amplitude modulation data showing measured transition frequency vs. the theoretical prediction. Blue line is predicted energy difference between bands 1 and 3 at the center of the Brillouin zone ($k = 0$). Red line is the 1→3 energy difference at the band edge ($k/k_L = \pi/a$).

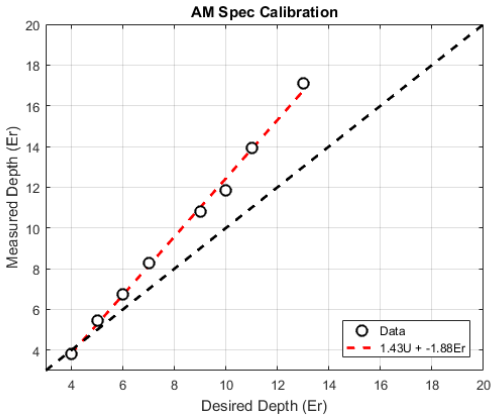

(b) Deviation of the predicted lattice depth vs measured lattice depth, indicating production of a deeper lattice than predicted. Initial prediction comes from high power Kapitza-Dirac diffraction data.

Figure 3.26: Amplitude modulation spectroscopy calibration of optical lattices for shallow lattice depths.

$$R_{\mathrm{TF}} = a_{\mathrm{SHO}} \left(\frac{15 N_{\mathrm{atoms}} a_{\mathrm{scatt}}}{a_{\mathrm{SHO}}} \right)^{1/5}. \tag{3.17}$$

For a comparison, see the much larger apparent size of the BEC at 294 a_0 versus 0 a_0 in Fig. 2.7.3.

For $1{\times}10^5$ atoms at $a_{\mathrm{scatt}} = 1\ a_0$, $R_{\mathrm{TF}} = 5\ \mu$m, which matches our observed BEC sizes rather well, but this is also effectively the smallest sized feature we can resolve in our system (recall the diffraction limited spot size $d = 5\ \mu$m). Along the lattice direction, the confinement can be dramatically tighter, so using the Thomas-Fermi estimate of the size of the harmonic oscillator groundstate wavefunction is incorrect, we must use the tight-binding approximation for the Wannier function. (Recall $E_{\mathrm{R}} = \hbar k^2/2m = 25$ kHz for 1064 nm and ^{7}Li). For an optical lattice of depth U_0 (in units of the recoil energy

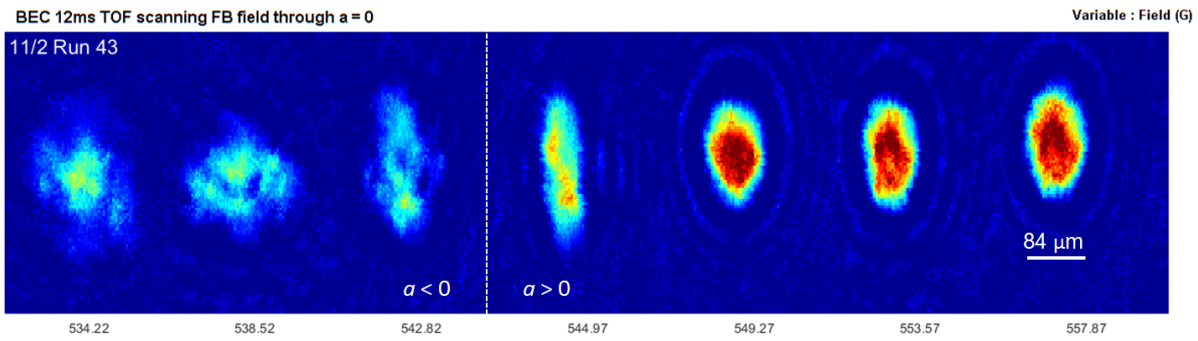

Figure 3.27: BEC TOF after 12 ms of free expansion. Below $a = 0$, the cloud's density drops dramatically as the atoms have attractive interactions and three-body loss depletes the atom number.

E_{R}) we can calculate the spatial extent of the cloud w_0 in a lattice site σ_0:

$$\omega_{\mathrm{lat}} = 2\frac{(U_0 E_{\mathrm{R}})^{1/2}}{\hbar} \tag{3.18}$$

$$\sigma_{\mathrm{lat}} = \left(\frac{\hbar}{m\omega_{\mathrm{lat}}}\right)^{1/2} \tag{3.19}$$

$$w_0 = \frac{1}{\pi^{1/4}\sigma_{\mathrm{lat}}^{1/2}} e^{-x^2/2\sigma_{\mathrm{lat}}^2} \tag{3.20}$$

Numerically solving for the $1/e$ diameter ($2w_0$) yields a much smaller 200 nm for the spatial extent of the ground state in the lattice. For a 1D lattice, we can finally get a good estimate of the volume of each lattice site using $\mathrm{R_{TF}}$ for the transverse directions and w_0 for the lattice direction: $V = 4\pi/3 * R_{\mathrm{TF}}^2 w_0$. This in turn causes the effective energy contribution from the contact interaction to be much higher for atoms in a lattice versus even a crossed optical dipole trap (by roughly a factor of four for $a_{\mathrm{scatt}} = 1\ a_0$, and increasing with decreasing a_{scatt}).

In order to use these approximations of the contact energy, we must know the applied field precisely. To calibrate the absolute field, we can look at the atomic cloud both *in situ* and under time of flight to observe how its spatial distribution and temperature change vs. scattering length (namely, the *in situ* cloud will decrease in size). Pollack and

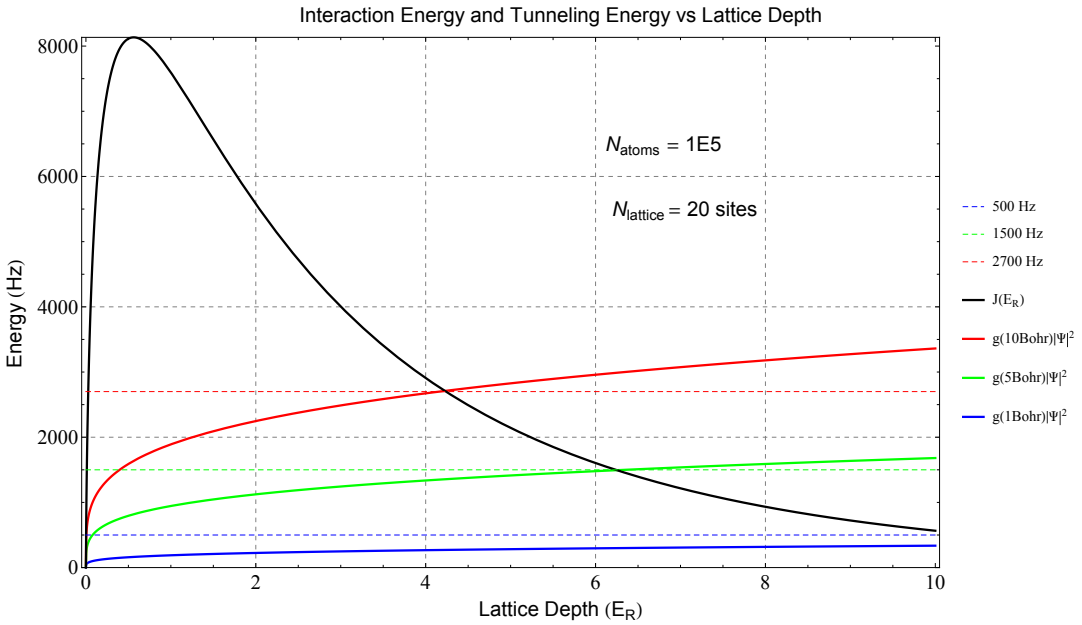

Figure 3.28: Estimated tunneling rates from Eqn. 1.14 compared to mean-field contact energy $g|\Psi|^2$ for assumed values of atom number and density (Eqn. 3.12). Even for modest values of the scattering length (in Bohr) the interaction energy is comparable to the tunneling rate J, even for modest lattice depths.

Dries[10] observe the size of a BEC in an elongated trap to measure the zero crossing. They note that soliton formation (subject to additional optical confinement) occurs just below the $a = 0\ a_0$.

In summary, lattice depths sensitively depend on the alignment of the individual lattice beams relative to the BEC's position. When the size of the lattice beam is comparable to the size of the BEC, different parts of the cloud will experience different effective lattice depths. For deep lattices, the spatial extent of the ground state atomic wavefunction deviates significantly from what is observed with simple imaging systems, and this in turn has substantial effects on the effective interaction energy of the atoms in the optical lattice.

Chapter 4

Mechanical and Electrical Systems

4.1 Vacuum Chamber

The Lithium apparatus is an approximately two-meter-long ultra-high vacuum (UHV) chamber with a source of lithium atoms on one end and a chamber for cooling, trapping, and performing experiments on the other. The middle of the apparatus is taken up by the Zeeman slower, as well as two differential pumping tubes, and two transverse cooling sections (explained in detail below).

Defining features of the apparatus include three re-entrant windows (two for electromagnets, one for a microscope objective), four 6" diameter viewports, and a large pumping manifold which allows the maintenance of extremely low pressures.

All components of our chamber are made of alloy 316L stainless steel where possible, which has a low magnetic permeability. Some viewports and smaller components are made of alloy 304 stainless steel where necessary.

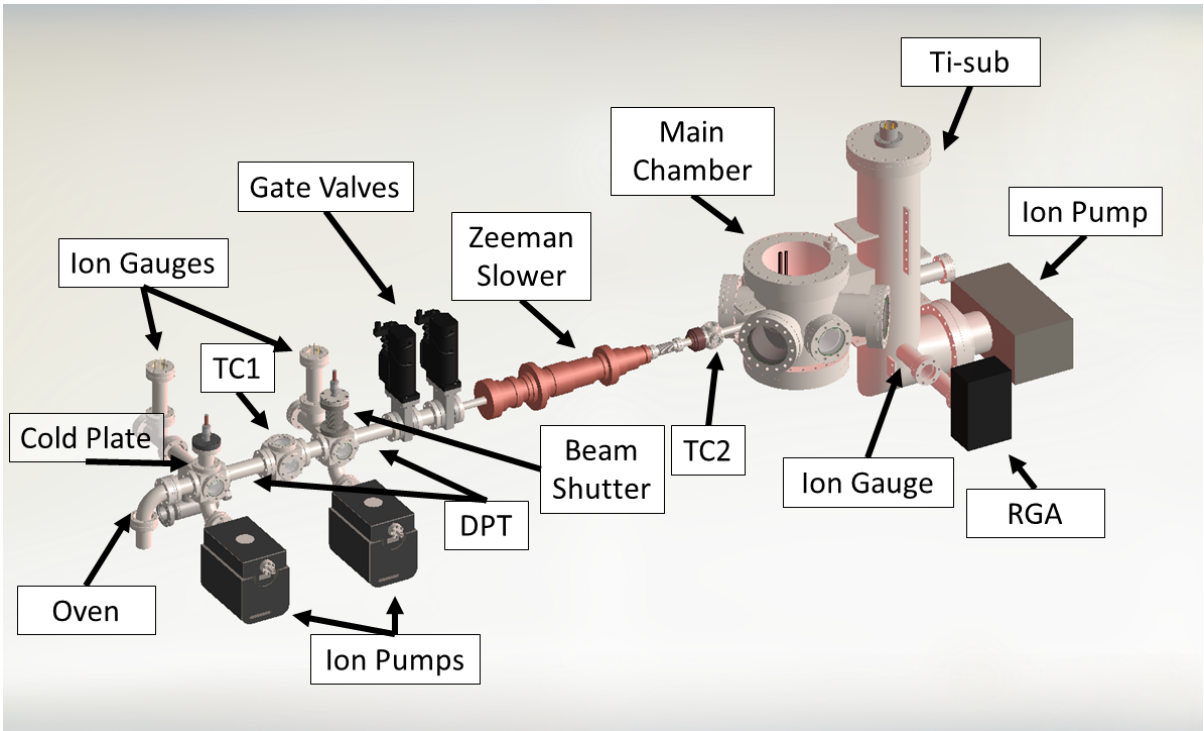

Figure 4.1: SolidWorks rendering of the Lithium vacuum chamber including the Zeeman slower, transverse cooling (TC1 and TC2), differential pumping tubes (DPT) titanium-sublimation pump (Ti-sub), residual gas analyzer (RGA).

4.1.1 Oven and Nozzle

The oven itself is simply a half-nipple with a band heater. We were able to load 25 g of lithium with relative ease into the cup by rolling it into small coils and pushing the lithium into the cup. Loading was done in a glove bag under an inert argon atmosphere to prevent oxidation of the lithium.

The nozzle's novel design was published in the Review of Scientific Instruments[33]. We took the multi-tube approach to its logical extreme by stacking hundreds of microtubes on top of each other to provide excellent collimation and great lifetimes. Despite running our oven above the designed temperature for over three years, we've yet to run out of atoms.

The cold plate is a piece of stainless steel affixed to a copper feedthrough. It has

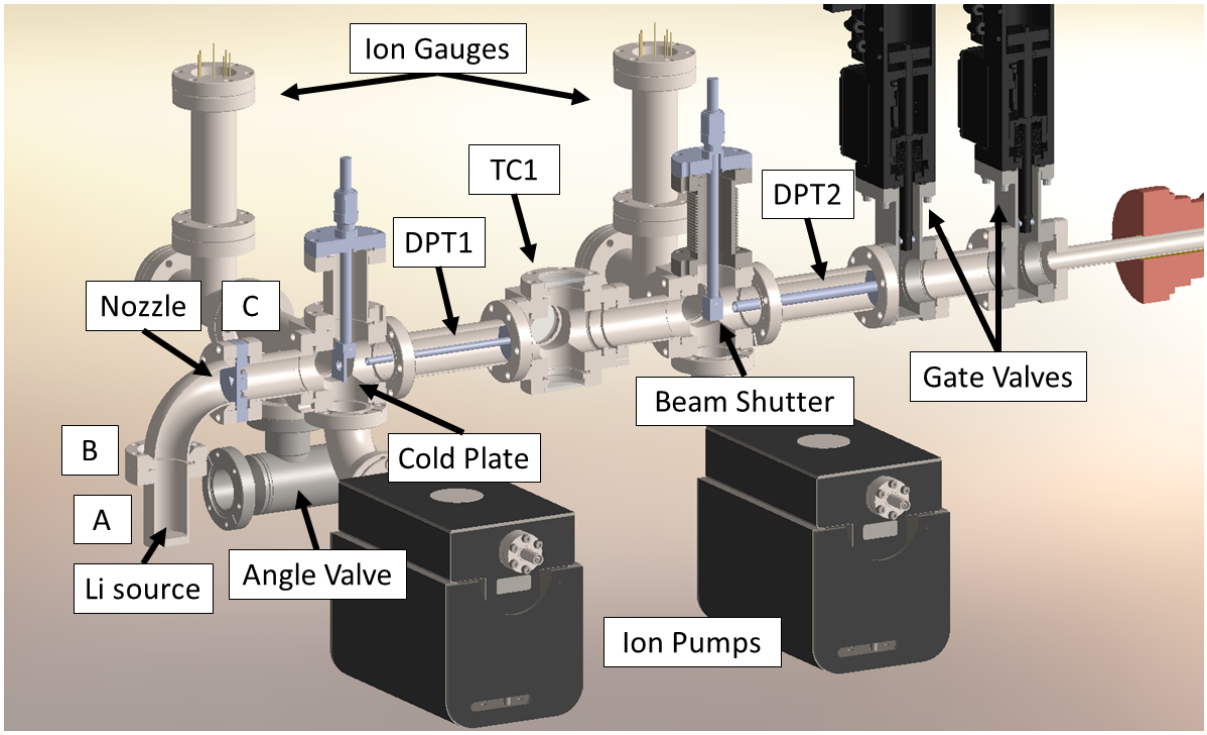

Figure 4.2: SolidWorks rendering of the lithium oven and nozzle. A, B, and C mark the position of band heaters used to heat the oven (and the lithium within it). TC1 is the first transverse cooling cube.

a bore in the center to allow the atomic beam to pass through. Its purpose is to help collect stray lithium atoms coming from the nozzle. In principle, the cold plate can be cooled conductively through its feedthrough, but we currently do not do so.

The differential pumping tubes (DPT) are 6" long tubes, 1/4" OD, 0.18" ID welded onto a disk that keeps them concentric in the CF flanged nipple. Their purpose is to allow atoms into the main chamber, while restricting the flow of other gas molecules from the oven. Each tube supports approximately an order of magnitude pressure difference across it. The two stages of differential pumping allow the main chamber to maintain vacuum below 1×10^{-11} Torr while the oven is usually around 5×10^{-9} Torr (see section 2.2.1 of [34] for a detailed description of atomic ovens).

The beam shutter is another piece of stainless steel (the "beam block") affixed to a

Part	Description	Notes
Oven Ion Pumps (2)	Gamma 45S-DI-2H-SC-N-N	45 l/s
MC Ion Pump	Agilent Vacion Plus Starcell Pump	75 l/s
Ion Gauges	Agilent Varian	UHV-24P B-A
MC Ti-Sub	Agilent Varian Filament TSP	PN 9160050
Residual Gas Analyzer	Extorr	PN XT100M
Oven Band Heater (A)	Tempco MI-PLUS	1.5"×2"
Oven Flange Heater (B)	Tempco MI-PLUS	2.75"×1"
Nozzle Flange Heater (C)	Tempco MI-PLUS	2.75"×1.5"
Feedthroughs (2)	Lesker	PN EFT0313373
Oven Angle Valve	MDC Vacuum, Kalrez, Manual	AV-150M-11
Oven Gate Valves (2)	MDC Vacuum, Kalrez, Pneumatic	GV-1500M-P-1
Main Chamber Gate Valve	MDC Vacuum, All Metal	PN 314003

Table 4.1: Table of parts used to construct the oven.

copper feedthrough. The feedthrough is mounted on a 2.5" long hydroformed bellows. The mechanism of the beam shutter is simple: in its resting position, the atomic beam path is occluded by the beam block. A solenoid, powered by an external power supply and switched with one of our 10 A MOSFETs, pulls the top of the copper feedthrough on the bellows approximately 1.5", clearing the beam path of obstruction and allowing atoms to continue ballistically into the Zeeman slower and toward the main chamber.

4.1.2 Zeeman Slower

The slower section of the main chamber is effectively another long differential pumping tube that connects the oven to the main chamber. The tube itself is a 21" long, 0.75" OD, 0.68" ID piece of stainless steel with two conflat flanges on either end. One end has a split CF flange to enable us to slide the Zeeman slower electromagnets over it. This piece (and the main chamber) were too large to sonicate ourselves, so we had both pieces electropolished by a local supplier (Electromatic, Inc). Strictly speaking, electropolishing does not clean the surface of the metal (rather, it smooths the surface), but our achieved pressures indicate that it is sufficient to achieve UHV.

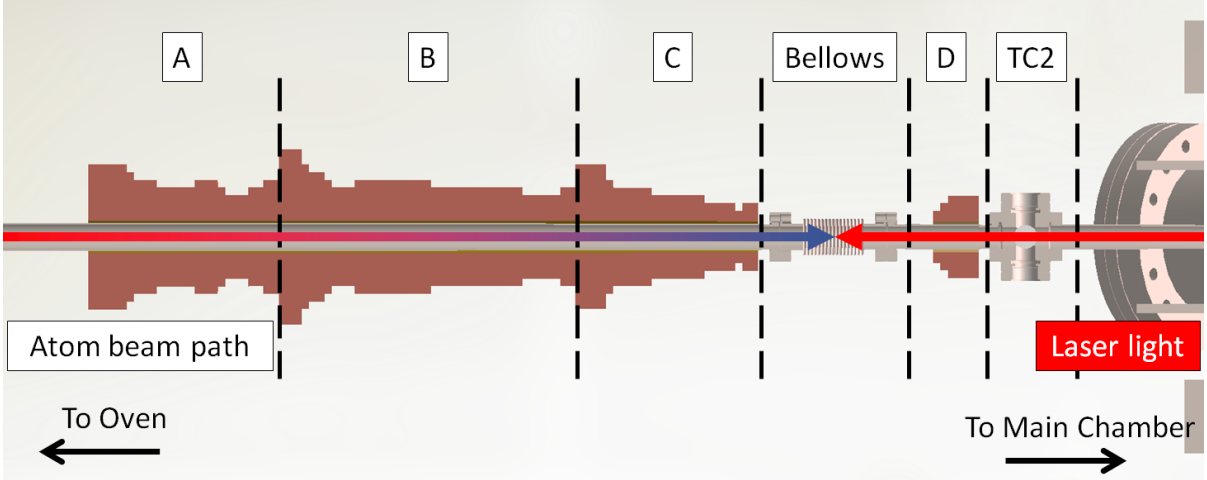

Figure 4.3: SolidWorks cutaway view of the slower tube and designed profile of the electromagnets (A-D, see section 4.3.7 for details). TC2 is the second transverse cooling cube.

The Zeeman slower's electromagnets were wound on a piece of brass tubing with a 1" OD and 0.065" wall thickness. This allowed the electromagnets to be wound and tested separately from the vacuum chamber. Each slower section is supported by a pair of custom plates that support the electromagnet from below and clamp it from the top using a nylon screw.

The spin-flip slower is split into decreasing and increasing field sections by a 3" long hydroformed bellows. This allows the two rigid sections of the machine (oven and slower, and main chamber) to be mechanically decoupled from one another, and provides separation which allows the magnetic fields from the first three sections (A-C) to reach ≈ 0 Gauss which in turn allows the atoms to be pumped into the appropriate spin state for cooling in the increasing field section (D) of the slower. Just beyond the decreasing field section of the slower is a 1.33" CF cube, which allows optical access to the atomic beam for a second stage of transverse cooling (TC2). Construction of the Zeeman slower electromagnets will be discussed in section 4.3.7.

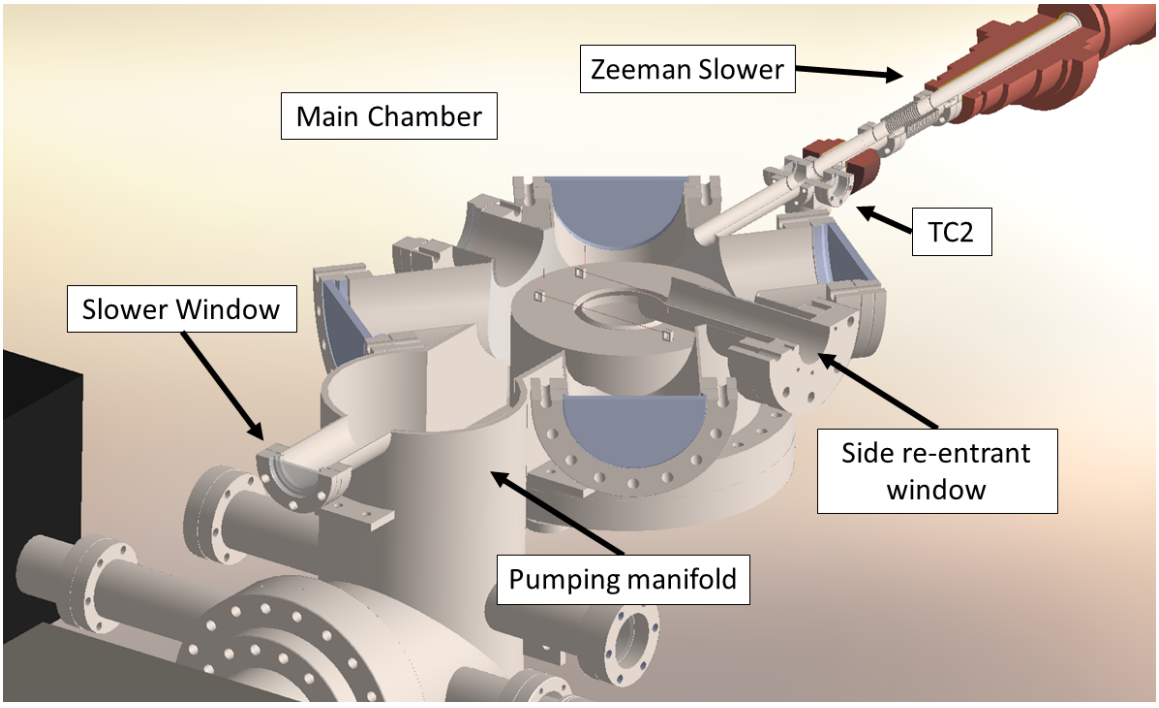

Figure 4.4: SolidWorks top view of the main chamber. The partial cutaway elucidates the connection between the pumping manifold (left), main chamber (center), and Zeeman slower (right). TC2 is the second transverse cooling cube.

4.1.3 Main Chamber

The main chamber has a few defining features. To reduce the number of flanges required, we opted for four large (6" diameter) viewports as the main optical axes on the X-Y plane of the machine. To create the large magnetic field gradients and fields required for magnetic trapping and Feshbach resonances, we used two re-entrant ("bucket") windows on the top and bottom to allow us to place the MOT electromagnets as close to the atoms as possible. To get a relatively high numerical aperture (NA) axis for imaging atoms, we added a side re-entrant window. Finally, to make sure that we could achieve consistently high vacuum, we added a large aperture (high conductance) connection to the pumping manifold (which houses the Varian Ti-sub pump and ion pump). Relevant machine drawings are located in the appendices. The four large viewports define the axes of the MOT beams and were designed with a small angle between them; instead of the

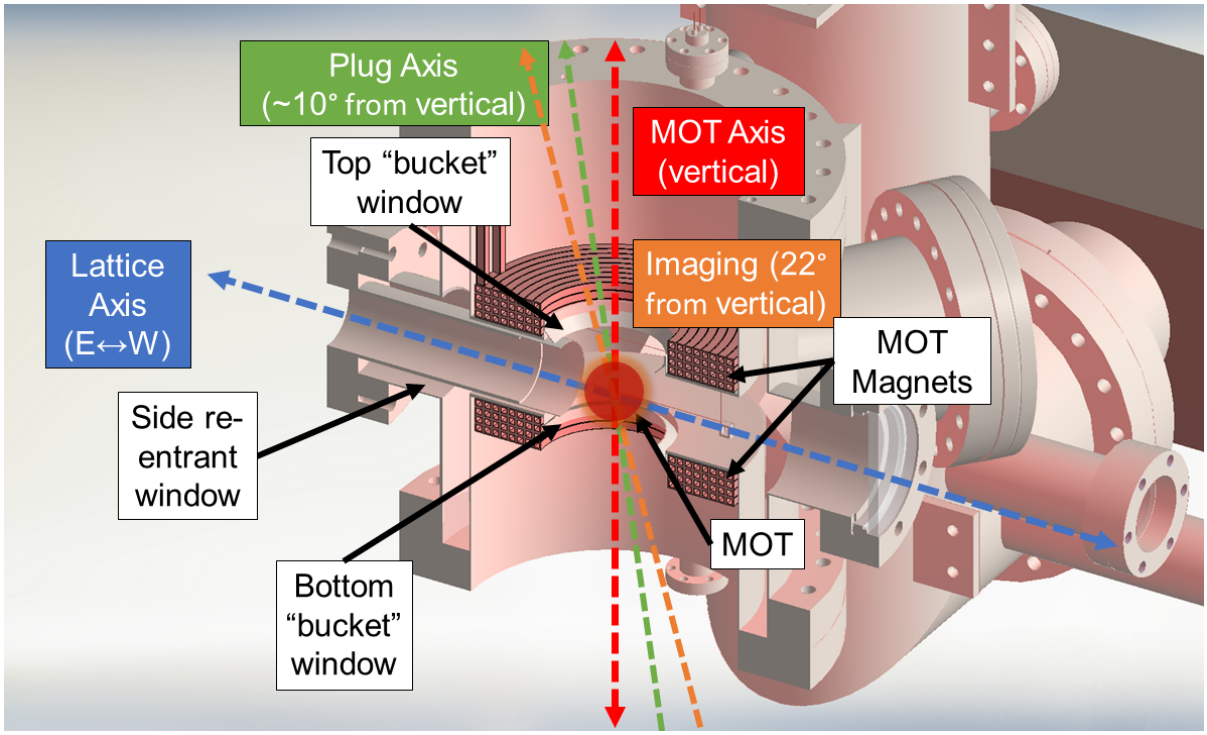

Figure 4.5: SolidWorks cutaway view of the main chamber showing the three side re-entrant windows and MOT coils in cross section.

usual 90° angle, they are at a shallower 75°. We discovered that the size of our MOT beams (approx 1" diameter) and the side re-entrant window's protrusion into the chamber forced us to angle the MOT beams at an even more extreme angle (approximately 65°). Ultimately this meant that our horizontal confinement was insufficient to capture enough atoms in our MOT to make a BEC. We were able to solve this problem by adding MOT beams to the side re-entrant window axis (see section 2.3 for more details on the MOT).

In addition, the main chamber features a viewport along the main axis of the machine (N→S). This slower window has a small oven built around it out of a band heater, spring steel, and a spare viewport and is kept at 140°C to discourage adsorption of lithium onto the window. Further, we have a Thorlabs M405L2 405 nm, 400 mW LED to act as an optical scrubber for deposited lithium, a process called light-induced atomic

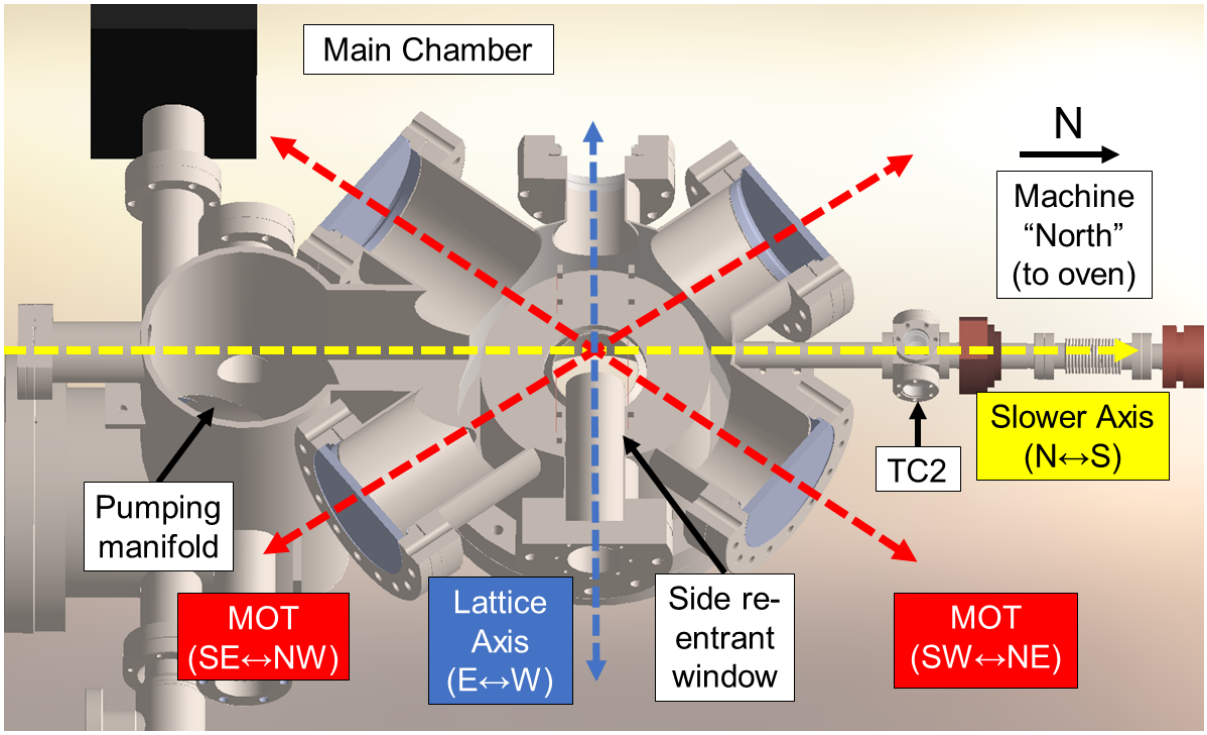

Figure 4.6: SolidWorks top view of the main chamber showing the main horizontal axes of optical access to the atoms.

desorption[35].

Importantly, the chamber's viewports are anti-reflection (AR) for 671 nm and 1064 nm (our main cooling and trapping wavelengths). Coating was done by Kurt J. Lesker Company. Other relevant wavelengths for our experiment are 532 nm and 323 nm (the $2S \rightarrow 3S$ transition), however due to a manufacturing error, only the top and bottom "bucket" windows are coated for those wavelengths.

As a side note, the "bucket" windows each have a small 1.33" CF feedthrough, as well as four stainless steel nuts welded to the interior surface. These mounted copper wire antennas (33 mm $\times$ 111 mm) which were intended to allow us to drive 80 MHz magnetic dipole transitions within the ground state manifold of lithium. After two bakes, both exterior copper connections failed and we were forced to make an external antenna instead (see section 4.3.9).

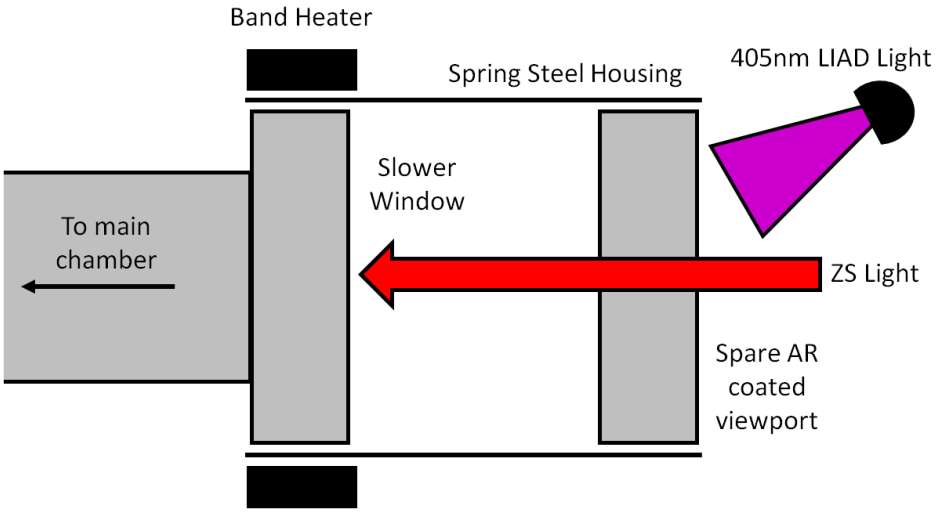

Figure 4.7: Schematic of slower window and mini-oven designed to keep the slower window free of lithium. The band heater is heated to 140°C to keep the slower window hot.

Section	Length	Width
Top	14”	23”
Side (2)	32”	20”
Back	13”	41”

Table 4.2: Sizes of optical breadboards surrounding the main chamber.

4.1.4 Breadboards

To mount optics around the machine, we designed large breadboards that would be attached to the optical table (but independent of the machine). The four breadboads are made from 1” thick Alcoa MIC-6 aluminum. The two side and one back breadboard are 1/4-20 tapped on the top with a 1” grid pattern of holes (identical to our breadboards), while the top breadboard is 1/4-20 tapped through to allow the mounting of optics to both the top and bottom surface of the breadboard. Approximate dimensions of the breadboards are shown below. The breadboards have a additional holes drilled in them to allow laser beams to be pass through them (see Fig. 4.9). See also the machine drawing appendix for specific details.

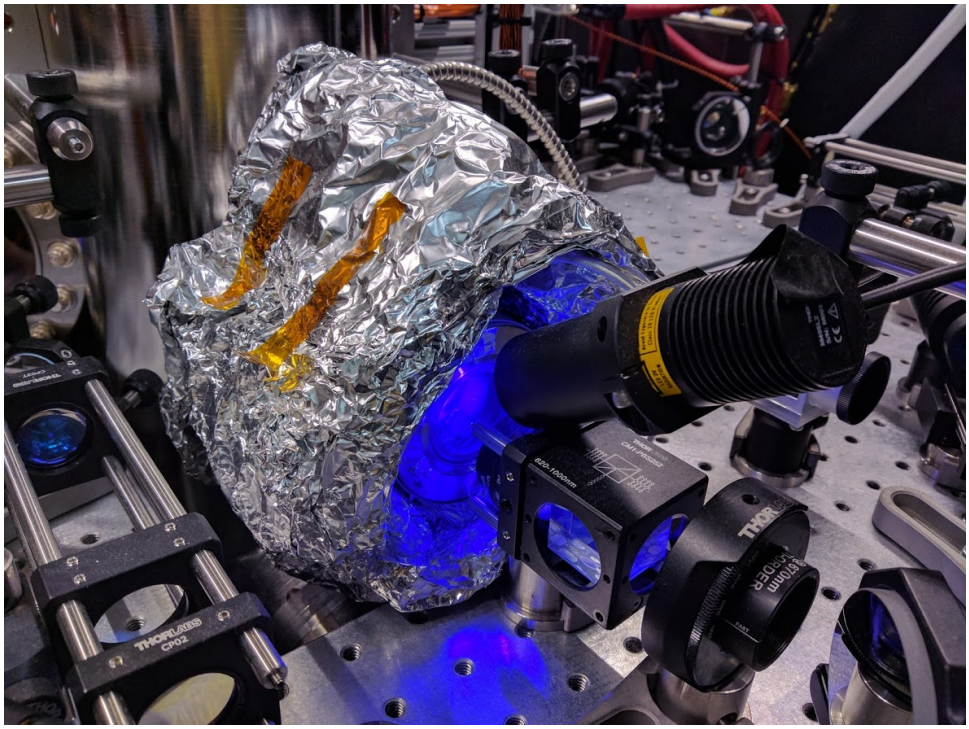

Figure 4.8: Picture of the Zeeman slower window and surrounding mini-oven.

4.2 Baking

Baking out the machine under vacuum is necessary for achieving ultra high vacuum (UHV) below 1×10^{-11} Torr. Better vacuum yields longer BEC lifetimes. The main limiting factor to achieving UHV is water vapor adsorbed onto the surface of the stainless steel, and any surface contaminants. See [36] for a good summary of cleanliness requirements for UHV systems. For the oven and small parts of the machine, we chose to clean the surface of the stainless steel by sonicating the components before assembly. Each part is sonicated for 5 minutes in a detergent bath (Alconox), then rinsed in running deionized water (DI), then sonicated in acetone, and then finally isopropyl alcohol (IPA) or ultra-pure methanol. This cleaning methodology leaves the surface free from contaminants and other substances that might out-gas under extremely low pressures. A secondary issue is hydrogen diffusion from inside the walls of the stainless steel itself,

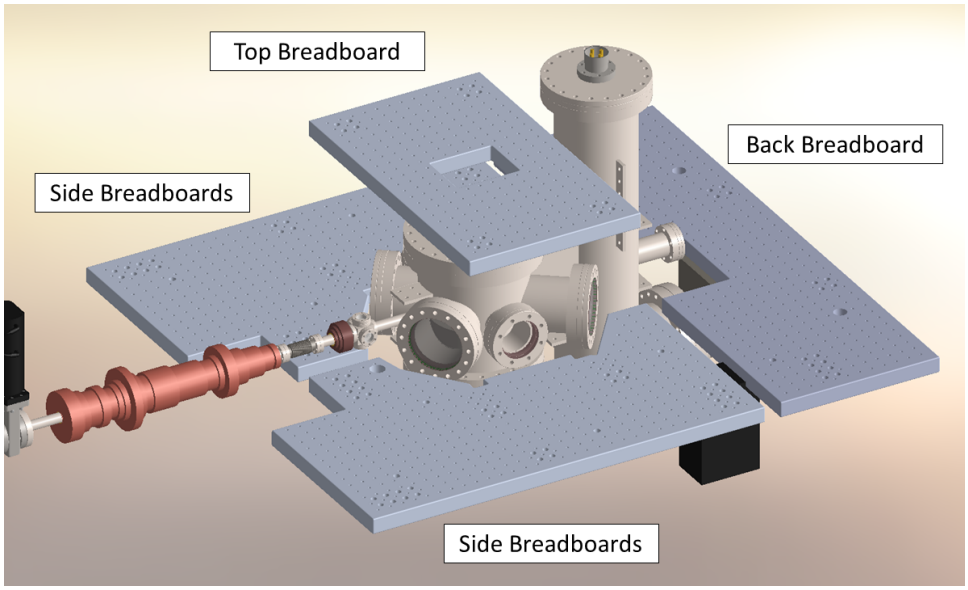

Figure 4.9: SolidWorks view of the main chamber's optical breadboards and their rough position. Supports omitted for clarity.

but the temperatures required to bake out hydrogen from steel are around 400°C, and we found it unnecessary to perform such a step. For larger components (the Zeeman slower, and main chamber), we used a local vendor to electropolish the surface of the steel. Our general assembly and baking methodology is as follows:

- Assemble chamber and check for leaks using a helium leak checker.
- Attach band heaters to large CF flanges.
- Attach thermocouples: use hose clamp where possible, high temperature aluminum foil tape where not. We use J-type thermocouples (McMaster 9251T92) instrumented with digital acquisition boards (Measurement Computing USB TC DAQ).
- Label and test thermocouples, ensure good connection while uncovered.
- Cover large windows with mesh grates to prevent scratching them (sonicate grates prior to baking). Small windows can be left uncovered.
- Wrap machine in multiple layers of aluminum foil using high temperature rated

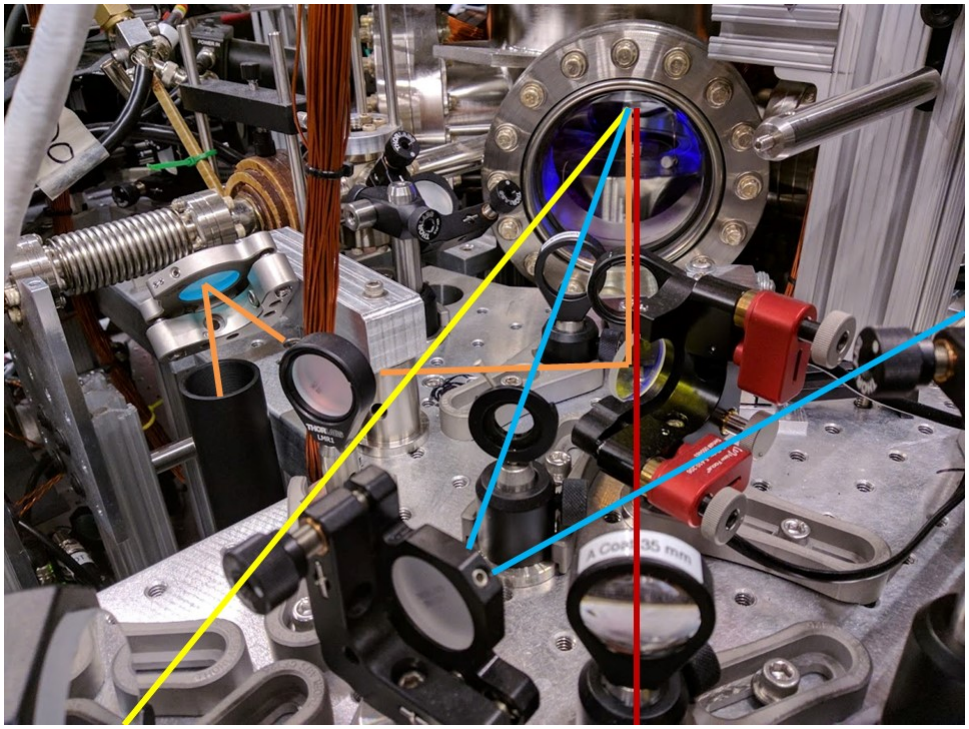

Figure 4.10: Illustration of optics on the side breadboard and multiple beam paths using a single viewport. Blue - gray molasses, Red - Imaging, Yellow - MOT light, Orange - ODT beam. Note the Newport 8821 Picomotor mount which allows for precise control over the ODT beam's position.

Kapton tape to secure.

- Wrap heating tape uniformly around machine. Take care to use larger/longer heating tapes to heat large parts of machine and other thermally "slow" areas.
- Wrap in layers of aluminum foil & fiberglass. Take care to wrap fiberglass in foil to prevent stray fiberglass from coating lab and lungs.
- Once instrumentation has been verified connected and measuring room temperature, begin turning on heating elements, first using heating tape as they are the most gradual (least local) sources of heat.
- Use band heaters to bring up cold spots of the chamber (usually larger steel flanges).
- Ramp to temperature. Try to keep rate of heating around 10°C/hour, if possible

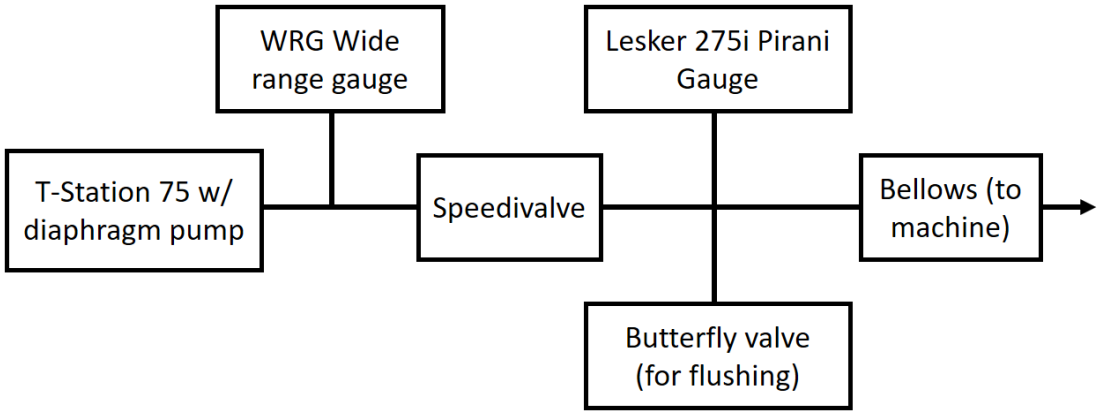

Figure 4.11: Schematic of our pumping manifold showing connections for flushing and various gauges.

keep the hottest and coldest part of chamber within 20°C of each another.

- Hold at desired bake temperature (in our case, 160°C) until turbo pump is no longer able to decrease the pressure (approx 1E-5 Torr for our dry scroll backed turbopump, Edwards T-Station 75).
- Degas all ion gauge filaments.
- Begin to ramp temperatures down, again at a rate of 10°C/hour if possible.
- Close off pumping manifold to prevent machine's vacuum from drawing in material through the pumps.
- Turn on ion pumps as machine cools, should reach 1×10^{-9} Torr.
- Fire titanium sublimation pump. Pressures rise sharply and then settle below 1×10^{-11} Torr.

Our first bake failed when a heating tape that was directly contacting a viewport caused the glass to metal seal to fail. Our updated baking methodology emphasizes gradual and even heating over being able to heat specific areas. Subsequent bakes have achieved desired pressures.

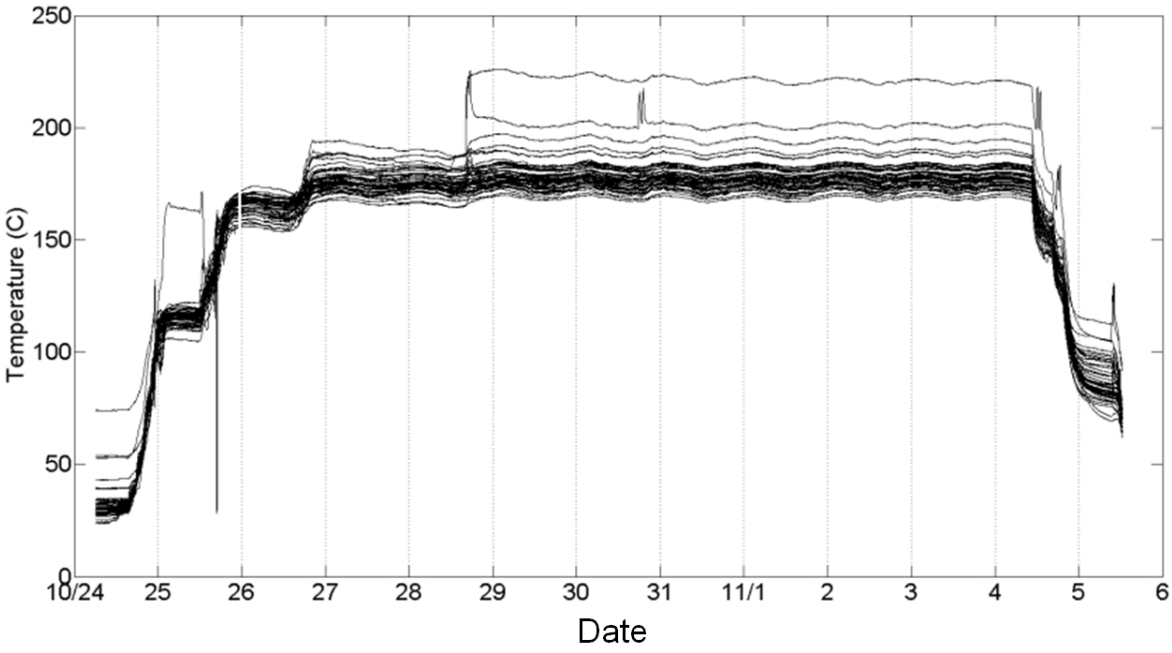

Figure 4.12: Main chamber temperatures during 2nd bake. 10/25 anomaly was a mislabeled thermocouple. Ion gauges are the hot temperatures starting 10/29. Note ion gauge degassing (spikes) on 11/4, as well as a thermocouple detaching from the chamber on 10/28. Anomaly on 10/25 was determined to be a mislabeled band heater.

We use a panel of variable-voltage transformers (variacs) to control the current applied to the band heaters and heating tapes. We manually control the current and aim for a 10°C temperature rise per hour and a maximum temperature difference of less than 20°C across the coldest and hottest parts of the machine. Shankari Rajagopal built a custom MATLAB GUI to allow us to view and record the machine temperature over time. Fig. 4.12 is an example of the recorded temperatures of the approximately fifty thermocouples we used to instrument our main chamber during its second bake. We baked for approximately one week at 160°C, or until our turbopump reached a steady 1×10^{-5} Torr. A summary of the various band heaters, heating tapes, and their associated variacs used for the lithium main chamber bake is below:

Type	Description	Power (W)	Quantity
Heating Tape	STH051-020	156	15
	STH101-020	313	8
	STH051-040	313	3
	STH101-040	627	2
	STH051-080	627	1
	STH101-080	1256	1
Band Heaters	2.75"×1.0"	275	4
Variacs		300	12
		600	12
		800	8
		1440	2

Table 4.3: Table of equipment used to bake the main chamber and oven.

4.3 Electrical System

The apparatus' electrical system largely consists of various solenoids (and their associated power supplies) used to produce precise magnetic fields around the atoms. The main electromagnets are the two MOT coils, which generate Helmholtz (nearly uniform) and anti-Helmholtz (quadrupolar) magnetic fields, and the Zeeman slower's electromagnets, which are effectively a tapered solenoid that generates a decreasing magnetic field in the region of the machine where the atomic beam is slowed before being delivered into the MOT. Other sections discuss shim coils used for canceling out smaller, Gauss-scale magnetic fields, and "push" coils, used for applying weak forces to the atoms during experiments.

4.3.1 MOT Coils

Our MOT coils mounted into re-entrant ("bucket") windows with a separation of 6.7 cm. They are made using the same square, hollow core, copper wire as the Zeeman slower (see section 4.3.7). The coils are wound in a helix four layers deep and eight layers across. They're organized in two groups: the inner four coils (powered by the TDK ESS,

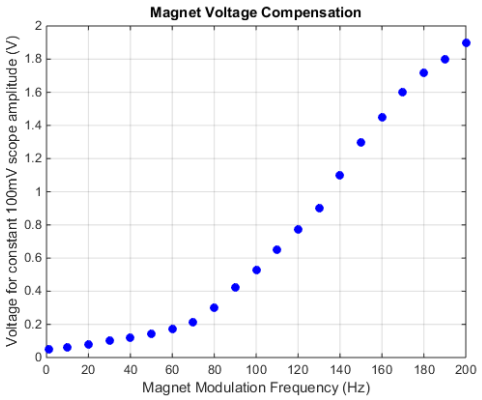

(a) Modulation curve for 543.6±4 G field modulation (± 0.5 a_0). MOT magnets can drive in excess of 200 Hz.

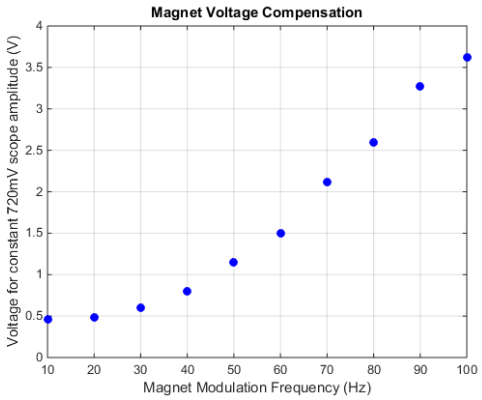

(b) Modulation curve for 543.6±40 G field modulation (± 2.5 a_0). MOT magnets are current limited above 100 Hz (3.5 V = 175 A modulation).

Figure 4.13: Magnetic field modulation for 4 G modulation depth (left) and 40 G modulation (right). Larger amplitude driving compensates the inductive damping observed at high modulation depths.

see section 4.3.2 for details on the high current power supplies) and the outer four coils (powered by the TDK Genesys). The magnets have a low inductance, measured to be approximately 300 μH, which allows for fast switching and ramping. The power supplies (see section 4.3.2) can slew at a peak rate of 8 A/ms, which allows a modulation in excess of of ±40 G at rates of 100 Hz (see Fig. 4.3.1).

Ex-situ measurements were taken with a magnetometer to characterize the magnet's performance and are summarized below:

Coil Layers	**Configuration**	**Strength**	**Unit**
Inner, 1-4	Helmholtz	1.72	G/A
Outer, 5-8	Helmholtz	1.75	G/A
Inner, 1-4	Anti-Helmholtz	0.516	G/cm/A
Outer, 5-8	Anti-Helmholtz	0.33	G/cm/A

Table 4.4: Summary of coil later configurations and strength of field (gradient) in Helmholtz (anti-Helmholtz) configuration.

To water-cool the MOT magnets, we strip approximately 1" of the fiberglass insula-

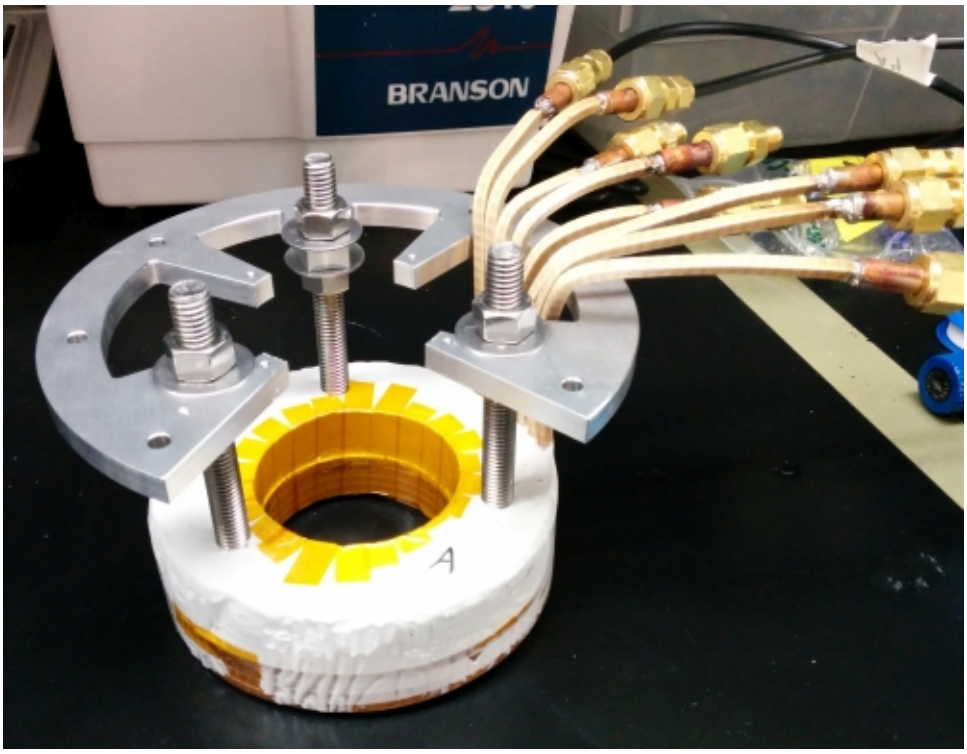

Figure 4.14: MOT magnet, including mounting rig and potting epoxy for fixing it to the chamber, and high pressure water line connections.

tion and cover the end with a length of 1/4" OD copper tubing. We then use a blowtorch and a copious amount of solder to braze the connection between the square wire and the round copper tube. High pressure water fittings (Swagelok type) are attached to this copper tubing. To attach electrical leads, we designed and built clamp-style connectors. Over time, these connections gradually failed as the connection to the high current power supplies (made with 3/0 braided copper wire or "welding cable") oxidized. To fix this problem, we replaced the plastic tubing used for water cooling the magnets with a straight length of 1/4" copper tubing to allow a new electrical connection to be made to the wire. A larger lug was designed to mate a copper compression lug (McMaster-Carr PN 6926K216) to a 2" section of copper tubing (see appendix C). One important lesson learned from this process was to make the leads of the electromagnet long enough to be cut later if needed (but not so long as to voltage-limit the power supplies).

Winding was handled on a modified version of the winding rig that we used to make the Zeeman slower (discussed below). See appendix C for drawings of the winding plate. The winding plate has tapped holes that allow nylon screws to press each layer together as the magnet is wound. We use epoxy (Duralco NM-25) to bind the wire together.

The re-entrant windows were made with 1/4-20 taps to allow a mounting plate to be mated to the top and bottom of the vacuum chamber (see appendix C). Three 1/2" threaded rods are suspended from these mounting plates. The rods are then cast in approximately 1/2" deep Duralco NM25 epoxy (the same kind used to wind the magnets). Nuts sandwiching the rods and mounting plate allow for adjustment of the height and angle of the MOT magnets in the bucket windows. The MOT magnets were mounted externally to the machine in a jig and characterized with a magnetometer.

4.3.2 High Current Power Supplies

We use two 20 V, 500 A power supplies to drive our MOT magnets (used also for magnetic trapping, and generating Feshbach fields). One major limitation we encountered was the lack of 480 V 3-phase electricity in lab; both power supplies instead must operate off of 208 V 3-phase which ultimately limits the available current to around 10 kW. Both supplies are controlled with the -10 to 10 V analog voltage from Cicero (in practice, 0-10 V). The DAC is limited to a 12-bit output, which limits the output resolution of the magnets to 250 mA. In order to prevent high frequency noise generated by clamping these power supplies with our IGBTs, we use isolation amplifiers (Analog Devices AD215) in series with the control voltage to isolate the power supplies from Cicero/NI hardware (see section 4.5 for details), while providing control up to $\approx$ 100 kHz (roughly 10 μs response times, faster than the MOT coils can ramp).

Part Number	Rating
TDK-Lambda ESS 20-500	20 V, 500 A
TDK-Lambda Genesys 20-500	20 V, 500 A

Table 4.5: High current power supplies used for MOT magnets.

Component	Part	Rating
IGBT	Powerex CM600HA-24A	600 A, 1200 V
Varistor	Littelfuse V661BA60	70 kA, 1050 V
Diode	Vishay Spectrol VS-SD1100C12C	1400 A, 1.2 kV

Table 4.6: Main components used in the IGBT current switching box.

4.3.3 Integrated Gate Bipolar Transistors (IGBTs)

Gray molasses and D1 pumping require either no field, or a very small field only to provide a quantization axis. Since GM follows directly after the CMOT, but is not a trap, it is important to be able to turn off the current in the MOT magnets as quickly as possible. The IGBT and ring down diodes can turn off the MOT magnets in 25 μs. Each IGBT and ring down diode must be water cooled to dissipate the heat. An additional varistor provides protection for the power supply against the high voltage induced EMF spike generated when switching the magnets at high currents. In principle, we always ramp down the current in the magnets before switching them to avoid destroying the IGBTs.

4.3.4 High Current Relays

One of the main reasons to build an experiment using lithium is the ability to use a Feshbach resonance to tune the scattering length of the atoms. This allows adjustment of the elastic collision rate for optical evaporation (enabling the formation of large atom number BECs), as well as the possibility of tuning the scattering length through zero, which enables an entire class of experiments not realizable by atoms with a fixed scattering length. In order to use a Feshbach resonance, we must be able to apply a strong DC

magnetic field (in this case, on the order of hundreds of Gauss) to the atoms in a reliable way. While it is possible to wind additional electromagnets near the atoms (say, on top of the MOT magnets), another possibility exists: switch the polarity of the MOT magnets from an anti-Helmholtz configuration to Helmholtz. We use a relay box based around the Kilovac LEV200A4NAA contactor. Four contactors form an "H-bridge" which allows the polarity of the interior conductor (in this case the bottom MOT electromagnet) to be switched. In so doing, the field applied to the atoms switches from a magnetic quadrupole when S1 and S2 are connected (anti-Helmholtz) to forming a magnetic dipole when S3 and S4 are connected (Helmholtz).

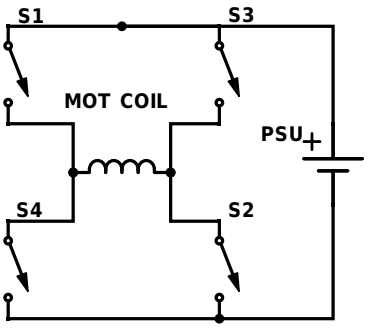

Figure 4.15: Simplified circuit diagram of high current relay box. Either S1 and S2 are connected, or S3 and S4 are.

Initially we were only using the inner set of the MOT coils (layers 1-4 in fig 4.16) to generate the required Feshbach field. We found that this led to thermal instability in our machine which required realignment of the plug beam. Building a second relay box enabled us to use the entire eight layers of the bottom MOT coil to apply the necessary field, which reduced the thermal load on the magnets and more importantly heated the magnets symmetrically, leading to better thermal performance. In mid-2017 we discovered that observed trap oscillation measurements could not be explained solely by a misfocused optical dipole trap and were also caused by the applied magnetic field.

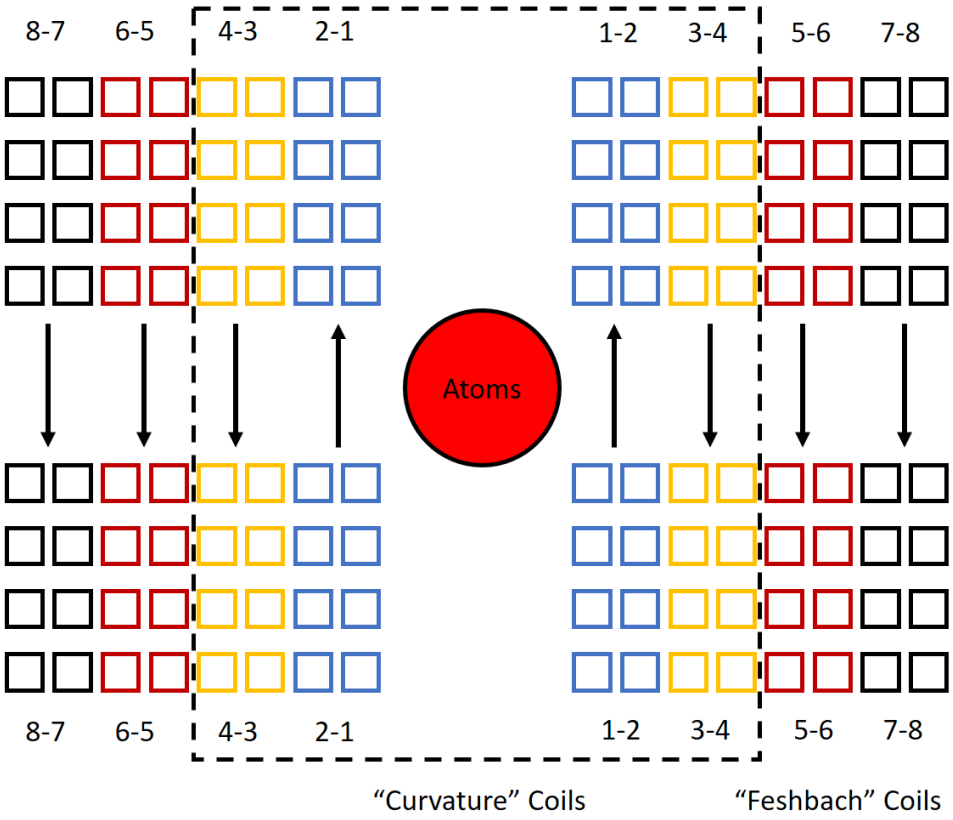

Figure 4.16: Cross-sectional schematic of the MOT coils in Feshbach configuration with "curvature" coils illustrated. Black arrows indicate direction of the magnetic dipole field generated by each set of Helmholtz coils. Compare to Fig. 4.5 to see a schematic of where the magnets are mounted in the main chamber's bucket windows.

Not only do the inner and outer MOT coil layers have slightly different locations of their field zeros (which we knew was the case from magnetic trapping), but they have slightly different field curvatures as well. This meant that there was always a residual force being applied to the atoms, on the scale of 18 m/s^2 in the $x-y$ plane (perpendicular to gravity), an unacceptable condition for Bloch oscillation measurements. We were largely able to mitigate this effect by reconfiguring the magnets so that the outermost (innermost) layers powered by the Genesys (ESS) were common-mode, Helmholtz (differential-mode, still Helmholtz). Essentially, the outer sets of coils generate the Feshbach, DC field, while the inner sets of coils counteract one another, so that their dominant contribution is to

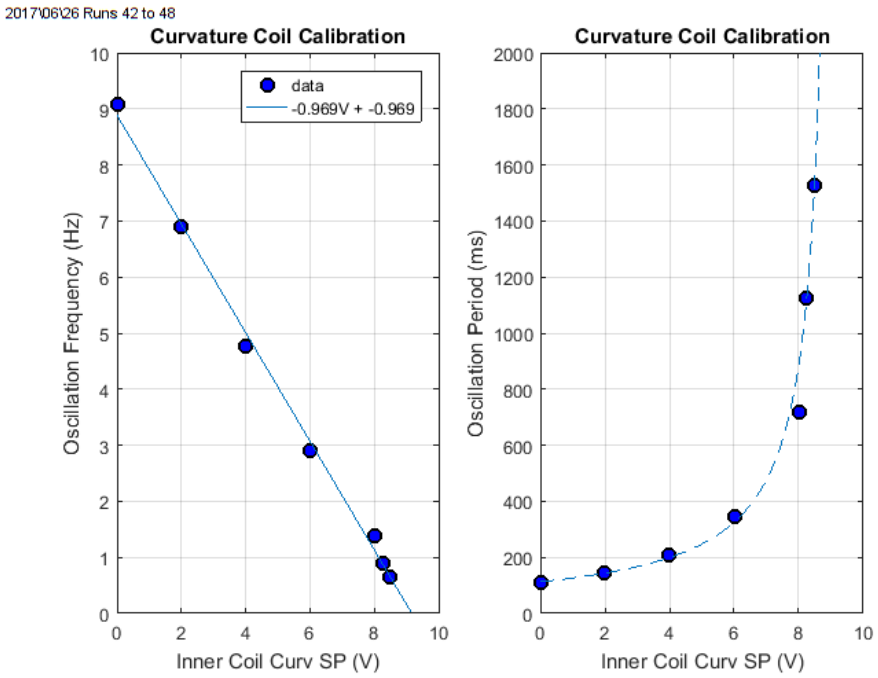

Figure 4.17: Left (right): Observed frequency (period) of BEC undergoing harmonic motion in the ODT2 beam. Calibration indicates that the magnetic field gradient along this direction is centered at the BEC position with the "curvature" coil current set to 9 V (450 A).

provide a "curvature" field in the counter direction of the outer "Feshbach" field.

This curvature is due to the design of the MOT magnets and their final placement around the vacuum chamber. The outer layers were designed to satisfy the anti-Helmholtz condition exactly. However, mounting the magnets left a very slight additional separation that causes the field to decrease in strength along the transverse (horizontal) axis. This causes a residual curvature in the DC field (see figure 4.3.1). Even using the curvature/Feshbach coil combination, we are left with a 13 Hz residual harmonic confinement. Ultimately, this remaining residual force induced by this curvature was compensated by the addition of the "push" coils (see section 4.3.8 for details). This cancellation is only possible once the majority of the field curvature is compensated for in the manner described above, and requires additional coils for each direction to be corrected. Cur-

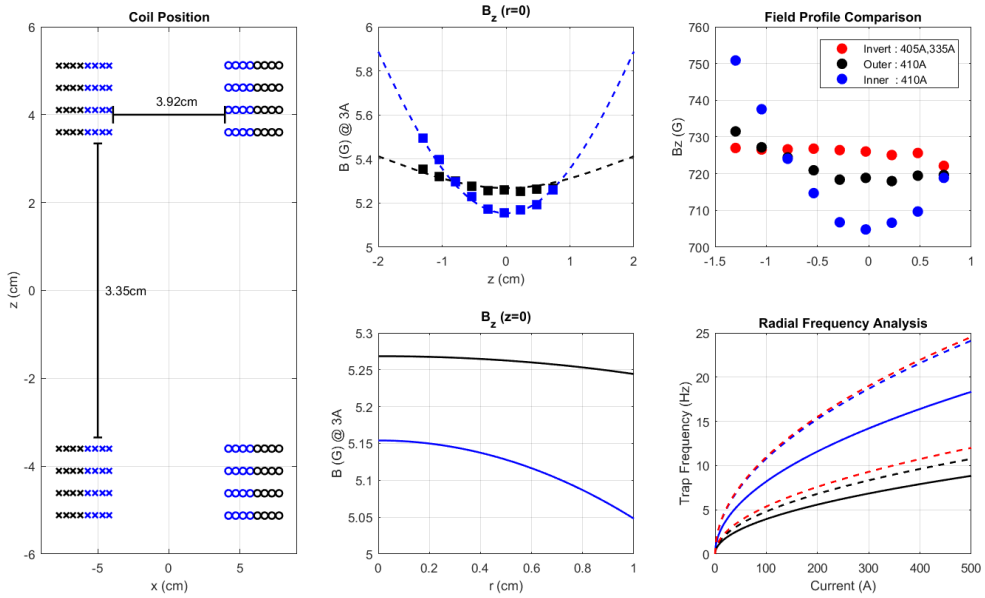

Figure 4.18: Simulation of the curvature of the magnetic field in Feshbach (Helmholtz) configuration. Red dots (top right) indicate re-optimized configuration (Field vs. z(cm).

rently we only correct the direction along the lattice (z), as the transverse confinement provided by the optical lattice is much greater than that of the residual curvature field ($\omega_{\text{latt}} \approx 1$ kHz $\gg \omega_{\text{B}} = 13$ Hz).

4.3.5 High Voltage Power System

For fast switch-on of the magnetic trap, we use a 500 V capacitor bank to quickly turn on the inner set of MOT coils. This design is based off of one from MIT. We charge the capacitor bank for three seconds, which allows us to snap the inner MOT coils on to 80 G/cm (four times the strength of the MOT field gradient) in 100 μs to catch the atoms after gray molasses and load them into the magnetic trap.

Refer to Fig. 4.21 for the basic layout of the 500 V power supply (HVPSU). When IGBT_1 is engaged 1 mA flows from the HVPSU to C_1 and charges with a timescale

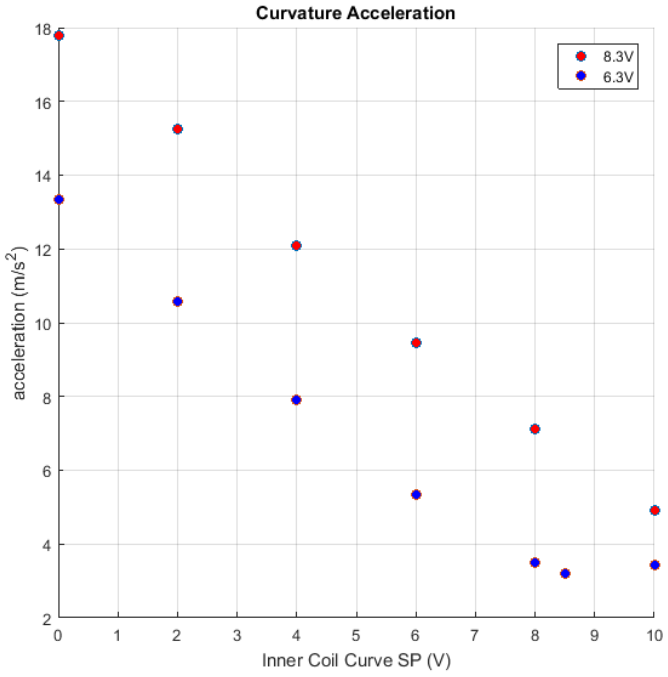

Figure 4.19: Calibration of force applied to the BEC along the lattice (side re-entrant) axis. Curvature coils only null the force to a minimum of ≈ 3 m/s^2 in the lattice direction near the scattering length zero crossing (543 G, blue dots). Red dots indicate applied force on the atoms at the higher magnetic field required for optical evaporation (720 G). In Fig. 4.17, we can use the curvature coil to cancel the acceleration along the direction of ODT2, whereas along the lattice direction the acceleration never reaches zero.

$\tau = 2.5$ s. When IGBT$_2$ is engaged C$_1$ discharges through R$_1$ and the inductive load L$_{coils}$. The damping resistor R$_1$ is critical as an effective RLC circuit is created by adding C$_1$ to the system. If the circuit is underdamped, C$_1$ will be negatively polarized and destroyed. The damping parameter is given by:

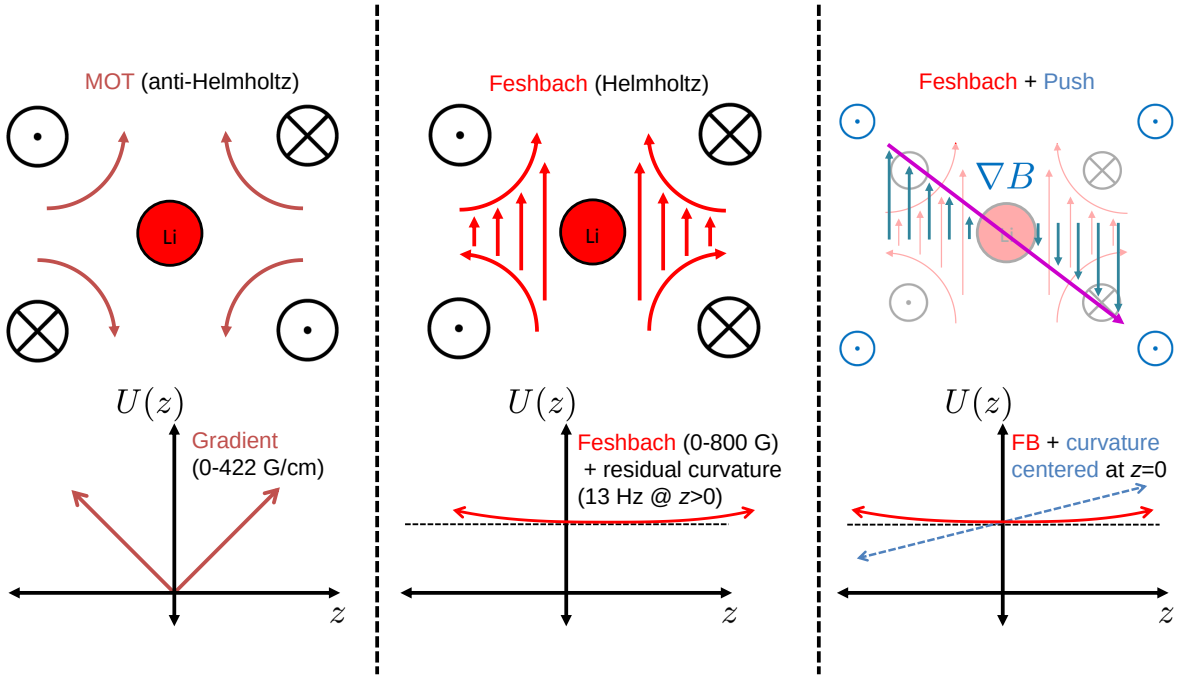

Figure 4.20: Schematic indicating different coil configurations and the fields they produce. The "push" coils apply a weak DC field that offsets the position of the residual curvature left from the Feshbach field. This makes it possible to load atoms on the edge of a harmonic potential (important for experiments, see chapter 5). Here z is the direction of propagation of the lattice, perpendicular to gravity.

$$\zeta = \frac{R}{2}\sqrt{\frac{C}{L}} \tag{4.1}$$

$$= \frac{\mathrm{R}_1 + \mathrm{R}_{coils}}{2}\sqrt{\frac{\mathrm{C}_1}{\mathrm{L}_2 + \mathrm{L}_{coils}}} \tag{4.2}$$

$$\approx \frac{\mathrm{R}_1}{2}\sqrt{\frac{\mathrm{C}_1}{\mathrm{L}_{coils}}} \tag{4.3}$$

$$= \frac{2\Omega}{2}\sqrt{\frac{500\ \mu\mathrm{F}}{300\ \mu\mathrm{H}}} = 1.29 \tag{4.4}$$

Although the actual inductance of the coils is difficult to completely characterize it is critical that the coil inductance and lead inductance not create an underdamped system.

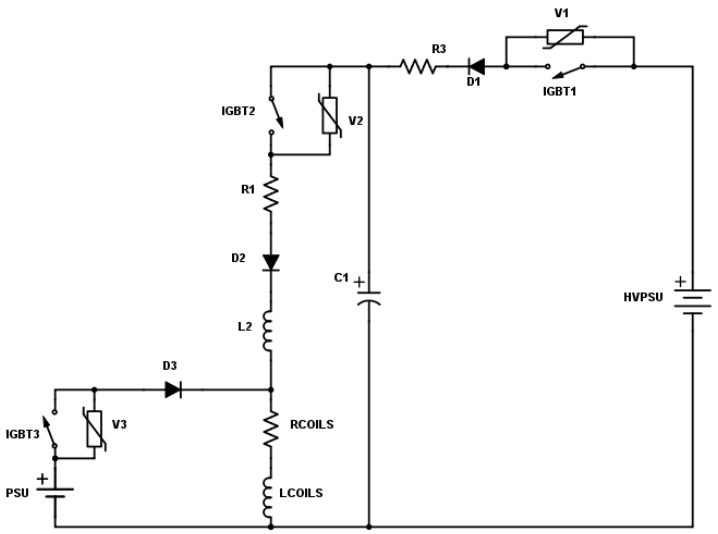

Figure 4.21: Circuit diagram for quick charging circuit.

4.3.6 Shim Coils

The shim coils are large, square electromagnets operated in the square-Helmholtz configuration (where the separation between coils d satisfies $d = 0.5445\ w$, with coil width w) . They are designed to run around 1 A of current to provide DC field offsets of the order of half a Gauss. Their main purpose is to null out the effect of the Earth's magnetic field on the atoms when there are no other applied fields. There are actually two sets of coils for each axis. One set provides Earth field shimming, while the other allows us to apply small DC fields for optical pumping.

Shim	**Turns**	**Width (in)**	**Ideal Separation (in)**	**G/A**
Vertical	18	14.63	7.96	0.79
Slower	18	16.00	8.71	0.72
Transverse	22	24.00	13.07	0.59

Shim currents are crucially important for RF evaporation. If there exists a residual field in the magnetic trap, then the trap center moves in space as a function of the applied field gradient. This means that the zero field "region of death" (the hole in the magnetic trap) moves as well. Our method of plugging this hole relies on a laser beam (discussed

Component	Value
HVPSU	570 V, 2 mA
$IGBT_1$,$IGBT_2$,$IGBT_3$	600 A, 1200 V
V_1,V_2,V_3	Varistors
R_3	5 k, 120 W
D_1,D_2,D_3	500 A, 1.2 kV
C_1	500 μF, 1000 V
R_1	2 Ohm, 200 W
L_2	Lead Inductance
L_{coils}	300 μH
R_{coils}	40 mOhm

Table 4.7: Components used in the high voltage power supply box used for fast turn-on of the magnetic trap.

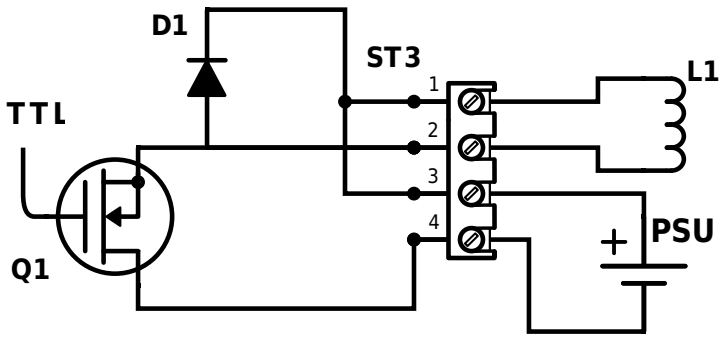

Figure 4.22: Circuit diagram of MOSFET switching and ring down circuit. TTL and PSU must share a ground.

in section 3.2.1) focused to ≈ 30 μm, so motion of the field zero on distance scales greater than this prevents efficient evaporation.

We use a box of high current MOSFETs to quickly turn on and off our shim coils. A ring down diode allows for fast dissipation of the induced magnetic field, which is important for quickly applying small fields.

Power supplies for the shim coils come in two flavors: the Earth shims are powered by Acopian Gold Box power supplies (model YL06MC270C6). These linear power supplies provide a quiet source of current. The other set of shims are powered by benchtop linear

power supplies (Instek GPS-1850D). These are able to be run as slaves with an analog voltage, although in practice we operate them at a fixed current level and simply switch them with the MOSFET box.

Component	Part Number	Rating
MOSFET	IRL3103PBF	30 V, 64 A
Diode	VFT1045BP-M3/4W	45 V, 10 A

4.3.7 Zeeman Slower

The spin-flip slower is built with square, hollow copper wire, alloy 101, OD 0.1875" with a wall thickness of 0.032" (custom from Small Tube Products). It is wrapped in Daglass (polyglass/fiberglass) insulation which is rated up to 180°C by S&W Wireco. We use a thermally conductive, but electrically insulating epoxy (Duralco NM25) to bind the electromagnet together. The square cross section allows us to carefully engineer the profile of the tapered solenoid to match the ideal field configuration, given by:

$$B_{\text{inc}}(z) = B_{\max}\sqrt{1 - \frac{2a\eta z}{v_i^2}} + B_{\text{esc}} - B_0 \tag{4.5}$$

where η is a safety factor (assuming the atoms absorb photons at a rate of 27 ns/η), $a = \hbar k\Gamma/2m$, v_i is the capture velocity (here $v_i = 1$ km/s), B_0 is some offset field chosen to compensate the detuning offset Δ of the slower beam ($B_0 = \hbar\Delta/\mu_b \times 10^4$) and the desired B fields in Gauss (e.g. B_{esc} is the required B field for $v = v_{\text{esc}} = 50$m/s) can be calculated from the velocity as:

$$B(v) = \hbar k v/\mu_b \times 10^4 \tag{4.6}$$

The safety factor consideration led us to design the decreasing field section of the slower to have a total length of approximately 0.6 m. We designed the Zeeman slower to capture atoms with a peak transverse velocity v_i of 1 km/s (compared to the peak at $\approx$

1290 m/s).

Practically speaking, our slower light is detuned from resonance by 400 MHz, which reduces the peak field of our Zeeman slower to around 800 G. The stopping distance d_{stopping} can be related to the capture velocity (v_i), recoil velocity (v_r), and excited state lifetime (τ):

$$d_{\text{stopping}} = 2v_i^2\tau/v_r \tag{4.7}$$

Given that the main transition is 671 nm, we can calculate the Doppler shift and peak field:

$$v_i = 1000 \text{ m/s}, \tag{4.8}$$

$$f_0 = c/\lambda, \tag{4.9}$$

$$f = f_0(1 + v_i)/c, \tag{4.10}$$

$$\delta f_{\text{Doppler}} = f - f_0 = 1.4905 \text{ GHz}, \tag{4.11}$$

$$\delta f_{\text{Doppler}}/\delta f_{\text{Zeeman}} = 1064 \text{ G}. \tag{4.12}$$

Four power supplies divide the slower into a decreasing field section (three power supplies, with decreasing field of 60 A, 45 A, and 30 A), and an increasing field section (one power supply, 50 A). The decreasing and increasing sections create a spin flip slower which allows the light used for slowing to be 400 MHz red detuned of the MOT light. This in turn allows for simultaneous cooling and trapping of the atoms in the MOT without extraneous heating from the Zeeman slower laser beam, while keeping the peak

magnetic field that the slower has to achieve to an experimentally feasible 778 G.

$$B_{\text{peak}} = 1064 \text{ G} \tag{4.13}$$

$$\text{Slower Light Detuning} = \Delta = 400 \text{ MHz} \tag{4.14}$$

$$B_{\text{offset}} = \Delta/1.4 \text{ MHz/G} = 286 \text{ G} \tag{4.15}$$

$$B_{\text{peak}} - B_{\text{offset}} = 778 \text{ G} \tag{4.16}$$

The remaining field (in our case the 286 G from the light detuning) must be made up by the increasing field slower. If however the increasing field were to reach 286 G, the atoms would be slowed to near zero velocity, resulting in the beam turning around and expanding in the transverse direction instead of traveling on toward the MOT. With this consideration in mind (and the design parameters of the MOT), we planned to have a 50 m/s escape velocity, which means the increasing field need only reach a peak field of 142 G.

With these facts in hand, we can calculate the field profile of the increasing and decreasing sections of the slower using Eqn. 4.5. We simulated the Zeeman slower as a sum of single magnetic coils. The ideal profile sets the desired condition for the desired coil configuration of the slower. The overall profile was first found using a computer simulation to get a rough estimate of the coil profile (see Fig. 4.23). Ultimately the final values for the current in each section were determined experimentally by looking at MOT load rates.

We measured the actual field profile (Fig. 4.24) with a peak field of 750 G. The gaps where sections were separated are clearly visible, and cause a dip in the magnetic field of approximately 25 G in magnitude. If left uncorrected, such dips in the field would cause the atoms to no longer be resonant with the slower laser light. In essence the atoms would escape the cooling process at these points and fail to deliver a slowed atomic beam

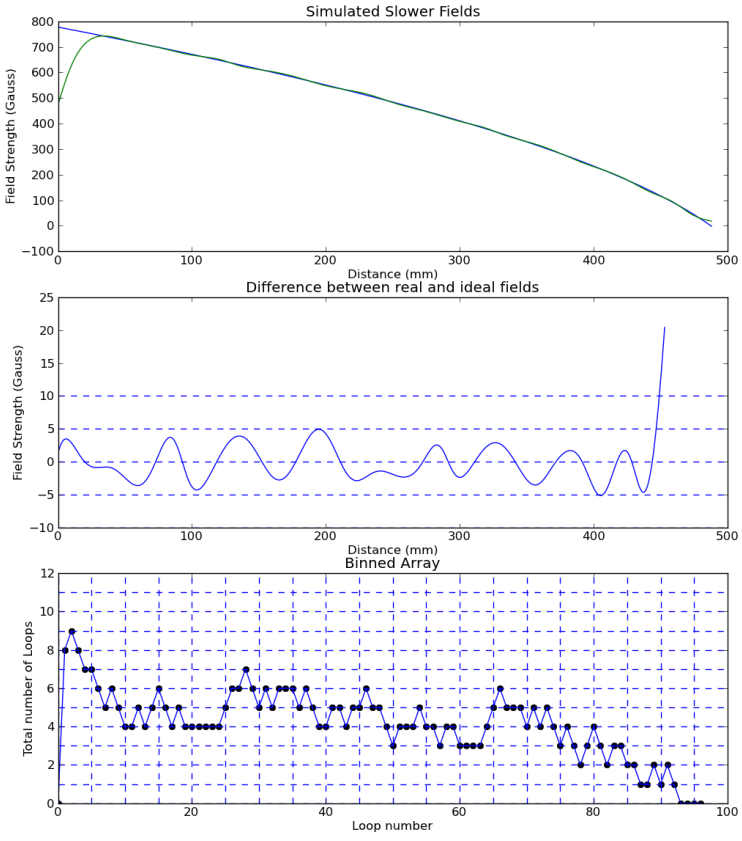

Figure 4.23: MATLAB simulation of the Zeeman slower's tapered profile showing the ideal field, the achieved field, and the difference between the two. Deviations larger than ≈ 5 G cause the atoms to no longer be resonant with the ZS light.

as a result. We concluded that winding extra copper wire in the gaps was sufficient to make up for these deficiencies. The most important of these interstitial coils is the one between section A/B of the slower, which has approximately fifty turns and runs 5 A, producing a field of around 100 G.

Water cooling is primarily important for section B, but the entire slower is water cooled. See [37] for how much water cooling is required to dissipate heat in the turbulent flow regime. For a square-diameter d in cm, D_h the cross-sectional copper area, length

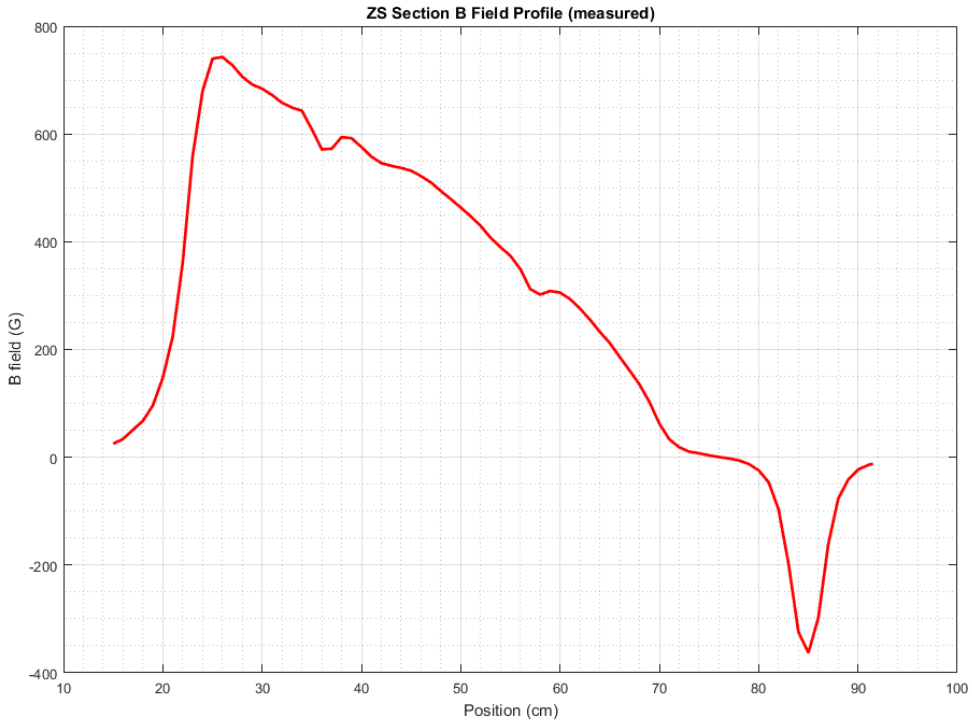

Figure 4.24: Interpolated measurement of the Zeeman slower's magnetic field profile. Note dips in the field profile where the sections A/B and B/C abut (approx. 35 cm and 56 cm).

L in cm, pressure P in atm/cm, and flow rate Q in cm^3/s:

$$Q(P, L) = 6.4 \times 10^3 d^2 \sqrt{\frac{D_h P}{L}}, \tag{4.17}$$

and the corresponding rise in temperature in the wire (in °C):

$$\Delta T = \text{Power}/(4.184Q). \tag{4.18}$$

The Zeeman slower power supplies are switched by a similar circuit to that found in the MOSFET switching box (see section 4.3.6). Instead of a high current MOSFET, we use Crydom solid state relays (SSR) and high power diodes to ring down the current.

Section	Wire Length (m)	Current (A)	Power Dissipated (W)
A	19.6	27	19
B	28.6	56	119
C	12.8	28	13
D	1.90	44	5

Table 4.8: Table of Zeeman slower sections, wire length, operating current, and dissipated power.

Section	Power Supply	Rating	Actual Current (A)
A	Sorensen DLM 8-75	8 V, 75 A	28.7
B	Acopian Y08LXU6400C1M3	8 V, 64 A	55.7
C	Acopian Y08LXU6400C1M3	8 V, 64 A	28.4
D	Sorensen DLM 8-75	8 V, 75 A	45.0

Table 4.9: List of power supplies used for Zeeman slower and operating currents.

4.3.8 Push Coils

In order to cancel the remnant field gradient of the MOT coils when they are in Helmholtz configuration (Feshbach coils), we found it necessary to add four "bar" shaped electromagnets to the main chamber. All four loops are wired in series and powered by two GWInstek GPS-1850D power supplies wired in series to provide up to 5 A of current with analog control via Cicero. Each "bar" is a 4"×8" rectangular loop with 75 turns/coil. The part of the loop that passes close to the chamber dominates the magnetic field applied to the atoms (the other end is sufficiently far away to be neglected). See Fig. 4.20 for a schematic of the push coils and the field they apply. The applied current moves the center of the residual field curvature from the Feshbach/curvature coil combination. This allows us to move the position of this simple harmonic potential relative to the atoms to apply a variable force (with corresponding accelerations of ± 4.9 m/s^2).

Component	Part Number	Rating
SSR	Crydom D1D40	40 A
	Crydom D1D80	80 A
Diode	Powerex CS240650	50 A
	Powerex CS241210	100 A

Table 4.10: MOSFET box components including solid state relays (SSR) and ring–down diodes, capable of switching up to 40 A (D1D40), or 80 A (D1D80).

4.3.9 RF Antenna

We initially planned to use the in-vacuum RF antennae to drive magnetic dipole transitions between the ground states of ^{7}Li atoms. However, when both feedthroughs failed after baking, we had to build an antenna exterior to the vacuum chamber. The antenna was originally just a length of hollow copper tubing but the loop antenna had serious drops in performance over the spectral range of interest (approximately 800-960 MHz). We had difficulty keeping the antenna from shorting to itself and to the chamber, and trouble getting the antenna to be sufficiently close to the atoms to effectively drive transitions.

We designed a simple spiral-type antenna using a flat sheet of copper tape (roughly 10×1 cm) soldered onto an SMA connector. The basic design of the antenna is just a single loop inductor and a parallel plate capacitor. The overlap of the ribbon sets the capacitance of the antenna, while the area of the loop determines the antenna's self-inductance. Both parameters are tuned such that the resonant frequency of the antenna is around 800 MHz, near the ground state splitting of ^{7}Li.

We calculate the inductance L using the magnetic permeability of free space μ_0, the number of wire turns (N, for our ribbon antenna $N = 1$), the area enclosed by the loop A, and the length of the coil l (in this case the width of the copper ribbon)

$$L = \mu_0 N^2 A/l, \tag{4.19}$$

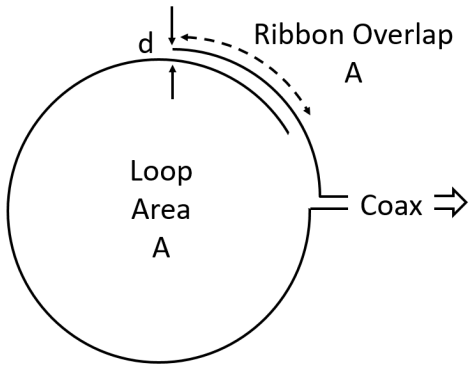

Figure 4.25: Schematic of the loop antenna.

with the capacitance of the antenna calculated as a simple parallel plate capacitor, where ϵ_0 is the permittivity of free space, A is the area of the overlap, and d the spacing between the plates

$$C = \epsilon_0 A/d, \tag{4.20}$$

and finally, resonant frequency is calculated in the usual way

$$f_{\text{res}} = \frac{1}{2\pi\sqrt{LC}}. \tag{4.21}$$

We manually trimmed the length of the copper ribbon to tune the resonant frequency of the antenna. We use a Rigol DSA815-TG spectrum analyzer (with tracking generator) to characterize the performance of the antenna (see Fig. 4.26 for an example spectrum and comparison between the old and new antenna). In order to mount the antenna just above the atoms (for maximum B-field at the atom's location), we designed and 3D printed a holder out of polylactic acid (PLA) plastic to be press-fit into the 3" aperture (see Fig. 4.27). The outer arches act as springs which keep the antenna roughly centered in the chamber. See appendix for drawing of the holder.

The system for generating the RF is simple. An analog voltage from Cicero controls the output of a VCO (Mini-Circuits ZX95-1015+, 750-1010 MHz), which is amplified by

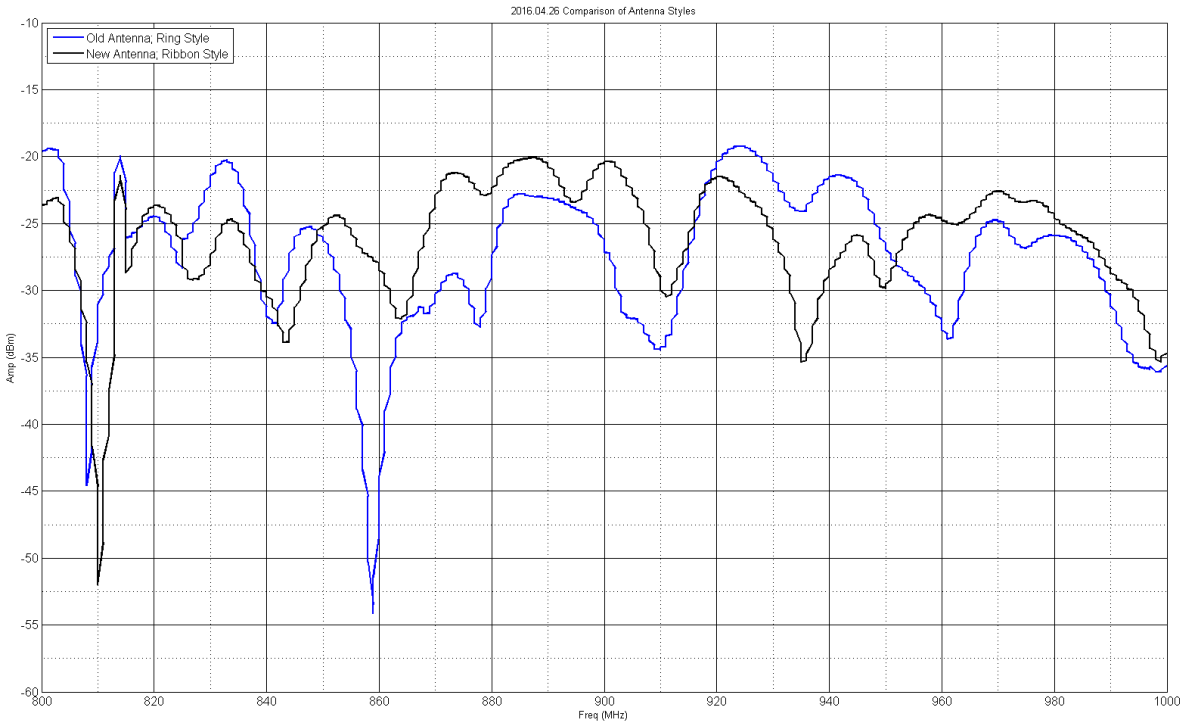

Figure 4.26: Spectral response curve of the "ribbon" style antenna (black) used for optical evaporation compared to an older flat "loop" style antenna (blue). Note the 25 dB improvement around 860 MHz.

an Ophir 5020 (500-1000 MHz, 200 W) and delivered to the antenna placed just above the atoms (approximately 3" above). The high power RF is sent through a circulator (Fairview Microwave SFC6996N) which terminates in a 200 W attenuator (Fairview Microwave SA3N200-40).

4.4 Water Cooling

During the magnetic trap, the apparatus dissipates nearly 20 kW of thermal energy for 2-4 seconds. Removing this heat is critical to the continuous operation of the machine. The water cooling system consists of a Thermo Fisher NESLAB System III closed loop chiller (70 kW cooling capacity) and a high pressure booster pump (2 HP, Flint & Walling PN PB3506A203). These deliver chilled water at 18°C (slightly above the dew point to

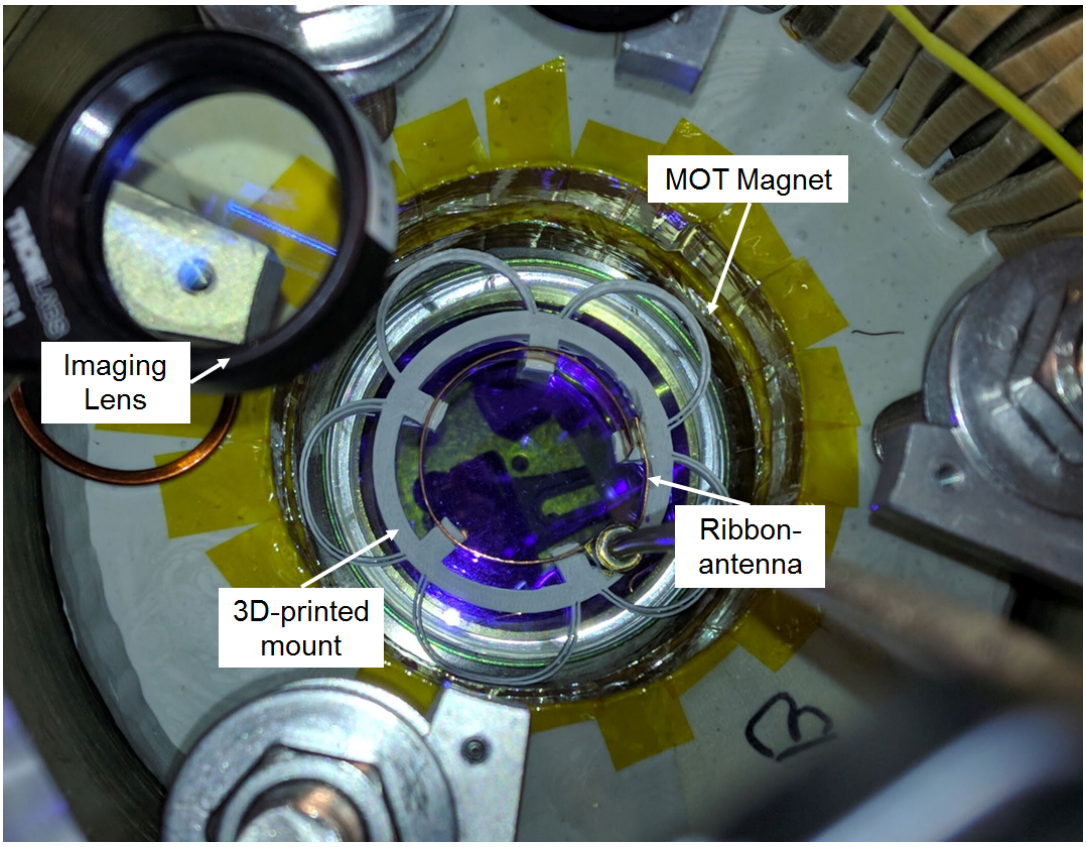

Figure 4.27: View of the top of the machine showing the external mounting of the ribbon antenna and 3D printed mount.

prevent condensation) and 100 PSI to the electromagnets. A variable shunt in parallel with the Lithium experiment and its sister Strontium experiment allows delivery of water at a consistent pressure. A distribution manifold splits the main line into six sections, each of which has a resistance temperature detector (RTD) and a flow meter to measure the temperature of the water returning from the electromagnets. In this way, we're able to monitor the temperature of the magnets in near-real time.

We discovered that the precision alignment of our plug beam (section 3.2.1) is strongly dependent on long time thermal drifts. As such it is important to not only run symmetric electrical currents through the MOT coils, but symmetric amounts of water to ensure even cooling. The magnet wire is usually the maximum impedance element in the cooling

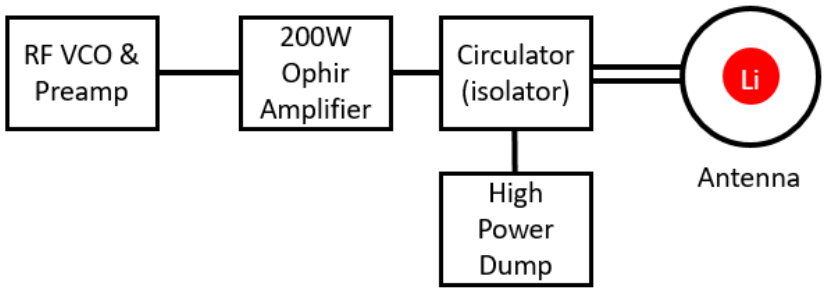

Figure 4.28: Simplified schematic of the RF antenna system.

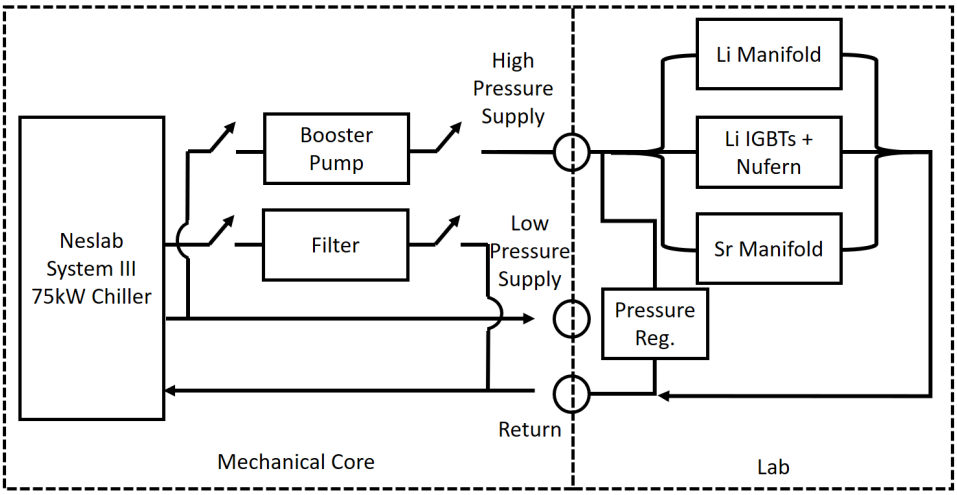

Figure 4.29: Box diagram of the water cooling system. The booster pump is connected in normal operation. The filter is connected nightly to clean the water of particulates.

loop, so splitting lines is sufficient to ensure delivery of even cooling. We designed the water manifold to have flow monitoring, but found it was unreliable and only focus on the main inlet/outlet ratio. Importantly, the high pressure "booster" pump has a minimum flow condition, as it itself is a source of heat. Our first booster pump failed when we ran it with insufficient flow to cool itself. The variable shunt allows us to regulate not only the pressure in the lines, but the minimum flow through the chiller loop. To prevent galvanic corrosion and the accumulation of biological matter in the water cooling lines, we use a mixture of 90% distilled water (NOT DEIONIZED, it will cause galvanic corrosion) to 10% isopropyl alcohol by volume.

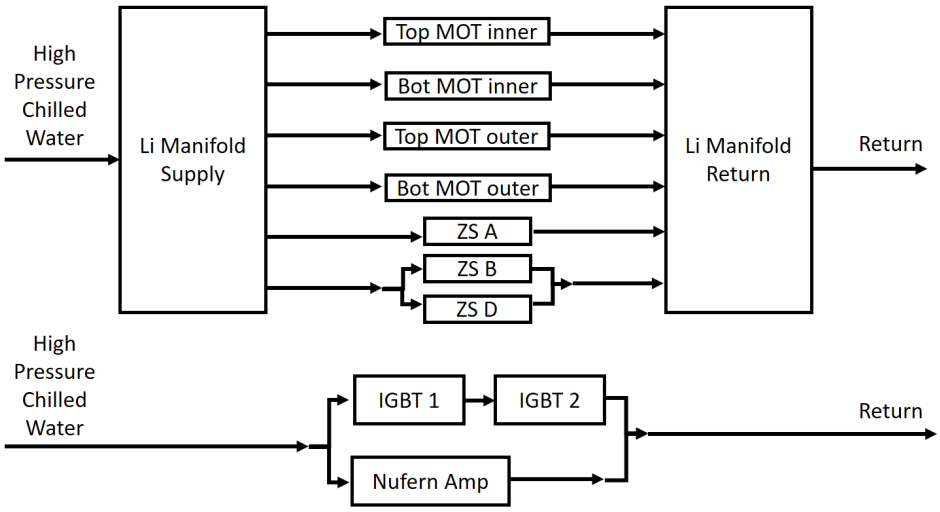

Figure 4.30: Diagram of the water distribution manifold. Zeeman slower section C dissipates sufficiently low power to be air cooled. A platinum resistance thermometer (RTD) in line with each manifold channel monitors the temperature of the water post-apparatus.

Component	Part Number	Notes
Flow Meter (small)	Malema M-10000-S2031-00	0.5-5 L/min, 0-10 V output
Flow Meter (large)	Malema M-10000-S3051-00	2-20 L/min, 0-10 V output
RTD	Omega PR-20-2-100-3/16-2-E-T	100 Ω, $\alpha = 0.00385\ \Omega/\Omega/°C$

Table 4.11: Temperature and flow components of the water distribution manifold. Each line has a small flow meter and RTD. The manifold supply and return lines have a large flow meter to measure the aggregate flow rate.

4.5 Computer Control

We use a program Cicero to handle analog/digital outputs and the creation of sequences for our experiment. It was developed at MIT by Aviv Keshet[31]. Cicero operates a 10 MHz FPGA (Opal Kelly XEM3001) and allows the use of a variable timebase, meaning we can run sequences with output steps of many seconds, or as short as a few μs. Our FPGA's time resolution is effectively limited to 3 μs (any shorter than that results in timing errors on the National Instruments analog/digital cards). We have two home-built digital breakout boxes, each of which houses a National Instruments SCB-68

connector block that interfaces with a National Instruments PCIe-65353 10 MHz digital I/O card, and is capable of 32 digital outputs per box (the box is also capable of manually suppling a 5 V signal on each channel). Analog control is provided through a home-built analog breakout box, which interfaces with two National Instruments PCI-6713 cards, each capable of generating 8, -10 to 10 V, 12-bit output signals.

Chapter 5

Quantum Emulation of Dynamic Systems

The goal of the machine we contstructed is to simulate strongly driven systems. Since the inception of the first superfluid-Mott insulator transition[38], the field of ultracold atoms has increasingly looked to simulate (or emulate) the physics of condensed matter systems using the extreme precision and control afforded by these apparatus. Quantum emulation of extreme non-equilibrium phenomena[39] is a promising new direction for the field of cold atoms. "Floquet engineering"[40][41] with an explicitly time *dependent* Hamiltonian enables the creation of states of matter that can only exist in the presence of strong driving.

For our non-equilibrium dynamics experiments we chose to use lithium as a platform because of its light mass, fast tunneling rates, and broadly tunable Feshbach resonance, which allows the study of a wide variety of systems: noninteracting Bosons, strongly interacting many body systems, and bright solitons, to name a few. We'll first discuss the experimental setup used to engineer bands, and then discuss three key results: a first direct measurement of Bloch oscillations in a cold atom system, the creation of a rela-

tivistic harmonic oscillator via band-engineering, and finally a new method of controlled, long-range, quantum coherent transport. Finally, we'll conclude with current efforts and some experimental extensions the machine can straightforwardly realize in the future.

Background: Early studies[42] of 1D cold atom systems in phase-modulated lattices opened the possibility of observing the effects of dynamical localization[7], weak dynamical localization[43], and quantum random walks[44]. Further studies of the robustness of these effects proved that amplitude noise was not an obstacle to observing the underlying physics, providing an early indication of the stability of strongly driven systems, while indicating phase control of the modulation to be critically important[45].

Further development led to driven optical lattices being used as a platform to modify tunneling rates[46][47][48][49], induce mass transport[50][51][52], and drive phase transitions[53][54].

Floquet Engineering: Time dependent Hamiltonians provide a new tunable parameter for material design. Driven systems exhibit emergent properties (fast tunneling, interband coupling) not found in static systems. The basic idea is to take a Hamiltonian and make it periodic in time such that:

$$\hat{H}(t)U = i\frac{\partial U}{\partial t}, \tag{5.1}$$

$$\hat{H}(t) = \hat{H}(t+T). \tag{5.2}$$

For some unitary operator U such that $|\psi(t)\rangle = U(t,0)\,|\psi(0)\rangle$. The time evolution of wavefunction $|\psi(t)\rangle$ can be calculated as:

$$|\psi(t)\rangle = \sum_n a_n\,|u_n(t)\rangle\,e^{-i\epsilon_n t/\hbar}, \tag{5.3}$$

where $|\psi(t)\rangle$ is a sum of *Floquet eigenstates* $|u_n(t)\rangle$, with associated *quasienergy* ϵ_n (and

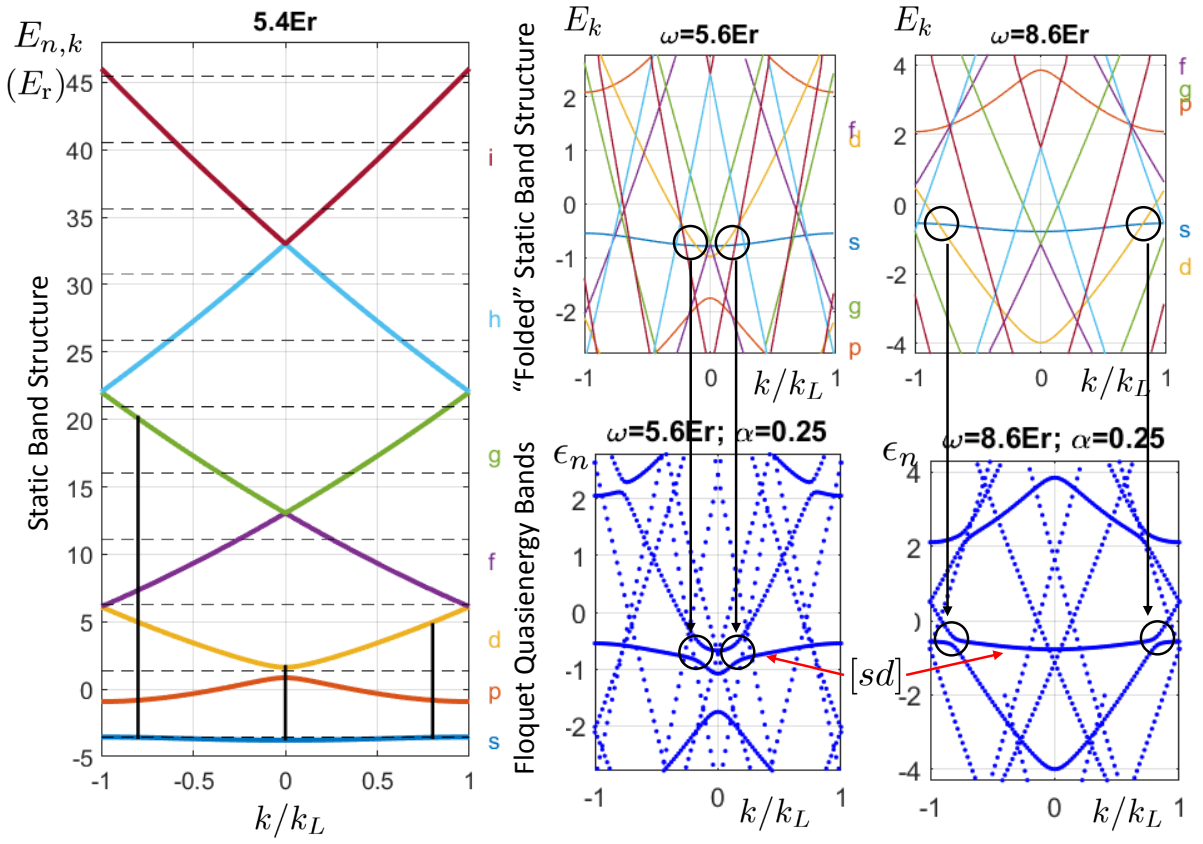

Figure 5.1: Example Floquet engineering of band structure. Left: unperturbed band structure of a $5.4E_R$ lattice. Applying a drive resonant with the s-d transition (5.6, 8.6 E_R) causes the emergence of a new Floquet "folded band" scheme (top right). Static band crossings actually form avoided crossings (gaps) in the Floquet quasienergy band structure (black circles, bottom right), where higher order band crossings are increasingly narrowly avoided crossings. Compare the $[sd]$ Floquet band to Fig. 5.23.

some prefactor a_n). This essentially allows treatment of time as another variable, making the eigenvalue problem a matter of solving:

$$\hat{H}' \left|\psi\right\rangle = \left(H(t) - i\hbar\frac{\partial}{\partial t}\right)\left|\psi\right\rangle = E\left|\psi\right\rangle . \tag{5.4}$$

In the context of amplitude modulation, driving with a given frequency f can be interpreted as moving a copy of the higher bands (p, d, f, etc.) down in energy by

multiples of the drive energy $E = hf$, much in the same way that the bands were created by "folding" the Brillouin zone at $k = \pi/a$, where a is the reciprocal lattice constant ($k/k_L = 1$). While these new Floquet bands (eigenstates of the driven lattice) lose their original energy ordering, we can interpret the resulting motion of an atom as time evolution in the new band (using the new dispersion relation), where avoided crossings are resonances between bands linked by multiples of the drive energy. See Fig. 5.1 for an example numerical calculation of a Floquet engineered band structure.

5.1 Experimental Setup

The basic experimental platform we use is a special kind of amplitude modulated 1D lattice. To enable arbitrary band coupling, we require the ability to modulate the depth of the lattice in excess of 100% (a sign-changing lattice) at frequencies resonant with high-order band transitions (on typically hundreds of kHz to a few MHz). To realize this novel lattice, we spatially overlap two 1D lattices and then retard the phase of one of the lattices to create a $\pi/2$ ($\lambda/4$) phase shift.

RF Generation: We use a custom RF generating box to make the fast-amplitude modulated RF we require for these experiments. It consists of a BeagleBone Black with a programmable real-time unit (like an Arduino on steroids) operating at 200 MHz. The BeagleBone generates an 8-bit digital signal that is sent to a direct digital synthesis (DDS) board (AD9854 signal generator eval board). The DDS outputs two separate RF channels (with a $\pi/2$ relative phase shift), which are separately amplified. The overall RF level is controlled by a voltage-variable attenuator and switched on/off quickly (sub μs) with an RF switch (MiniCircuits ZASWA-2-50DR+). This fast RF box is capable of 100% amplitude modulation at speeds in excess of 2 MHz. In early testing of the RF box we discovered that the built-in clock on the DDS board operated at 300 MHz, which

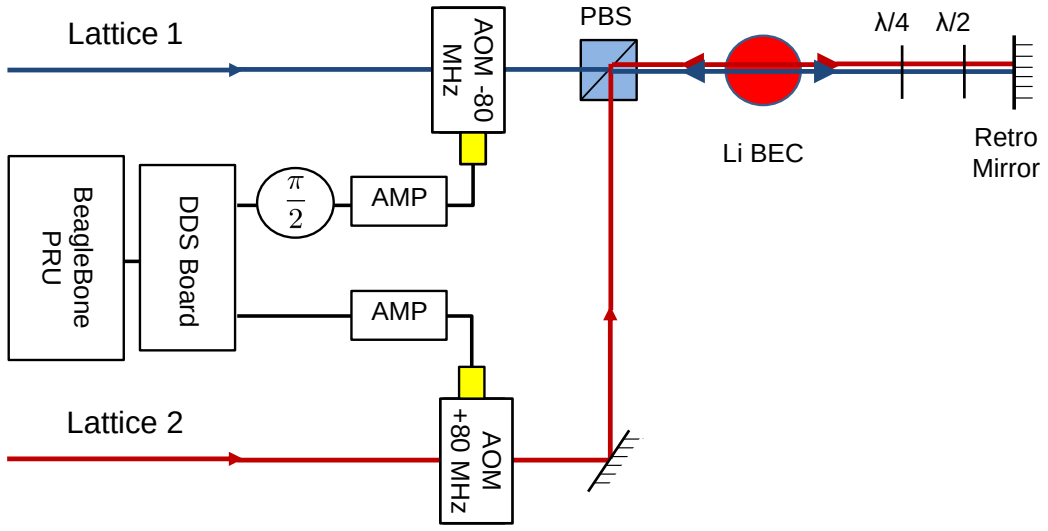

Figure 5.2: Schematic of double lattice setup. BeagleBone directly controls the amplitude of the RF sent to each AOM via a DDS board. The two lattices are overlapped onto a BEC in the chamber. The waveplate stack retards one lattice relative to the other, creating a $\pi/2$ phase shift between the two lattices.

put sidebands on the 80 MHz RF at ± 20 MHz (within the AOM's operating range). To fix this problem, we swapped out the DDS's clock for a 200 MHz clock, which moves the sidebands out to ± 40 MHz (outside the range of the AOM). We also had to take care to align the lattice beams precisely through the AOMs; especially for Kapitza-Dirac measurements, misalignment of the beams on the AOM crystal causes a 200-300 ns delay in the rise time of the lattices.

Modulation Depth: We characterize the modulation depth of this composite lattice with the parameter α, where α is the ratio of the static lattice depth to the maximum modulated lattice depth. For instance, a $U_0 = 5E_R$ static lattice modulated to $\pm 15E_R$ has an $\alpha = 3$. For a single lattice, the maximum possible modulation depth is $\alpha = 1$ (as it is only possible to turn the lattice off, not invert the potential). In this work, we introduce the notion of "ultrastrong" driving, derived from two spatially overlapped but statically phase shifted lattices, as a means of accessing modulation depths in excess

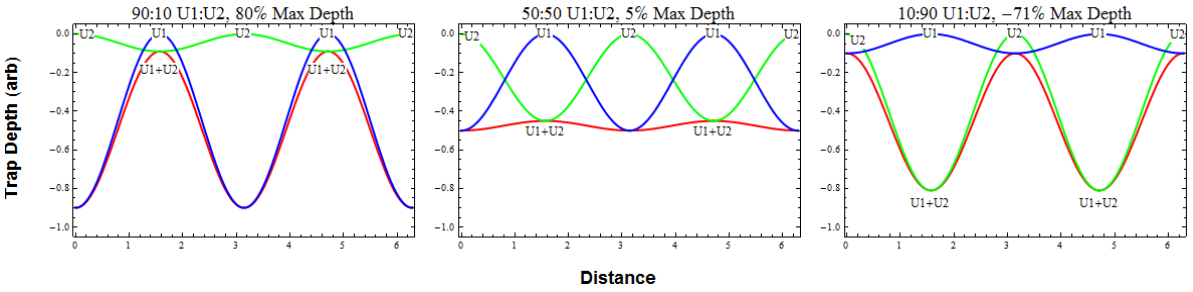

Figure 5.3: Illustration of phase shifted lattices. When U1≫U2, the total lattice (red) has maxima (minima) at $\pi/2$, $3\pi/2$ $(0, \pi, 2\pi)$. When U1≪U2, the total lattice has minima (maxima) at those points instead.

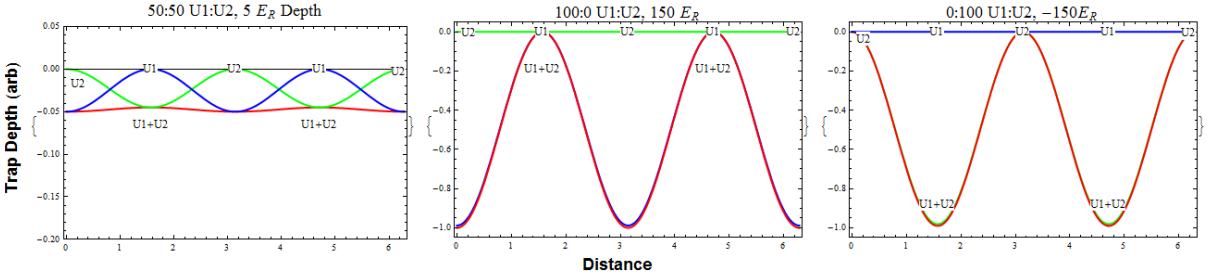

Figure 5.4: Illustration of extreme amplitude modulation. Left: Atoms are loaded into a $U_0 = 5E_R$ lattice (U1+ U2, in red). Middle and right: the Lattices can switch between $\pm 150E_R$ as a function of time, achieving a maximum modulation depth of $150/5 = 30U_0$ ($\alpha = 30$, see Eqn. 5.7).

of 1000% ($\alpha = 10$) and make accessible for the first time new regimes of ultrastrongly driven systems and Floquet physics.

Importantly, this double lattice structure allows us to create an combined optical potential that can change sign, where maxima (minima) become minima (maxima). Mathematically, the sum of the two optical lattices can be expressed as:

$$V_1(x,t) = -A\alpha \cos^2\left(\frac{\omega t}{2} + \frac{\pi}{2}\right)\cos^2(kx), \tag{5.5}$$

$$V_2(x,t) = -A\,(1+\alpha)\cos^2\left(\frac{\omega t}{2}\right)\cos^2\left(kx + \frac{\pi}{2}\right), \tag{5.6}$$

$$V_{\text{tot}}(x,t) = V_1(x,t) + V_2(x,t),$$

$$V_{\text{tot}}(x,t) = -\frac{A}{2}(1+\alpha) - \cos(2kx)\left[\frac{A}{2} + \frac{\alpha A}{2}\cos(\omega t)\right]. \tag{5.7}$$

Here A is the static lattice depth (in E_R) and ω is the modulation frequency (in Hz). Importantly, we can express the frequency of the drive ω in units normalized to the natural frequency of the lattice ω_0, giving us a dimensionless parameter Ω to characterize the speed of the drive:

$$\omega_0 = \sqrt{\frac{2Ak^2}{m}}, \tag{5.8}$$

$$\Omega = \omega/\omega_0, \tag{5.9}$$

which allows for easy comparison between theory and experiment when comparing different static lattice depths A. Fast RF modulation allows for amplitude modulation from DC up to 2 MHz. Our two optical lattices individually have a measured depths of $150E_R$. This allows us to amplitude-modulate the lattices by 1000% ($\alpha = 10$) for a static lattice depth of $15E_R$, or even more for shallower lattices: 3000% ($\alpha = 30$) for $5E_R$.

Lattice Cancellation: A key component of making this double lattice function is the use of two orthogonal polarizations and two different frequencies for the two lattices to avoid interference between them. The two lattice beams are taken off of different AOM orders (separating their frequencies by 160 MHz) on top of being separated by polarization. As illustrated in Fig. 5.2, the two lattices are combined on a polarizing beamsplitter cube, with one lattice beam transmitted through the cube (with horizontal polarization) and the other reflected off the cube (with vertical polarization). We initially tried to use a $\lambda/8$ waveplate to retard one of the lattices by $\lambda/4$ (upon retro-reflection), however such waveplates are hard to source and the one we purchased was too small and clipped the lattice beam after exiting the chamber. Further, we wanted to avoid using lenses to focus the beam down to avoid introducing aberration into the beam path. [55] introduced us to the idea of using a quarter-half-quarter waveplate (QWP-HWP-

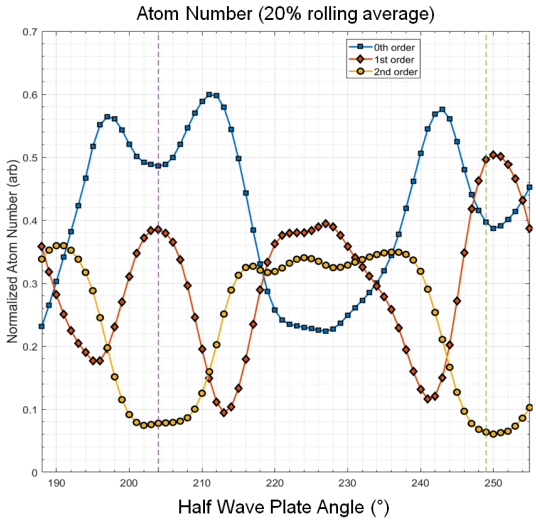

(a) Kapitza-Dirac diffracted order population ($0^{\text{th}}, 1^{\text{st}}, 2^{\text{nd}}$). as a function of half wave plate angle. The 2^{nd} order population linearly increases in this regime, indicating the lattices best offset when we observe a minima of the 2^{nd} order population (dashed vertical lines).

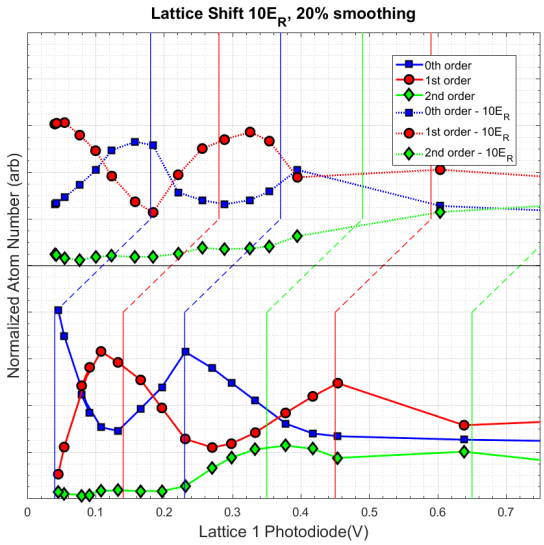

(b) Shift in Kapitza-Dirac population consistent with $10E_R$ lattice subtraction. Lattice 2 fixed at $10E_R$, while the power in lattice 1 is increased. The apparent zero of the distribution is shifted over by $10E_R$, consistent with lattice 2 decreasing the overall lattice strength.

Figure 5.5: Calibration showing subtraction of two phase shifted lattices.

QWP) stack to arbitrarily retard the phase of one lattice relative to another. With a retro-reflected lattice, we found that we could simplify this to a QWP-HWP pair. By changing the angle of the half waveplate we can control the relative phase delay between horizontal and vertical polarizations through the waveplate stack. Specifically, a change in the HWP angle $\Delta\theta$ induces a phase delay of $4\Delta\theta$ in the vertical component. This means that if we control the angle of the HWP to 1°, we can in turn vary the relative phase between the two lattices to $4° = 0.02\pi = 0.01\lambda$. This degree of control is easily achieved with a high-precision waveplate rotator (Thorlabs CRM1P).

Force: The "Push" coils (see section 4.3.8 for design and calibration) allow us to shift the central position of residual magnetic field gradient relative to the position of the atoms in the lattice. Locally, this changes the magnitude of the force the atoms experience (see Fig. 5.6 for illustration). We can use these coils to load the atoms at the

center of this harmonic potential to completely cancel the local force. Additionally, there exists some residual optical harmonic confinement from the lattice beams themselves (the ODT potential of each lattice beams), which will apply a force to the atoms. The "push" coils allow us to cancel this static force.

With this tool in hand, we can explore systems in the presence of extreme driving not only at frequencies hundreds of times faster than the tunneling rate J ($J \approx 1650$ Hz for a $5E_R$ lattice), but also at modulation depths vastly exceeding those previously explored[53] and in the presence of a controllable force field.

5.2 Position Space Bloch Oscillations

A first stop on the road to Floquet engineering is being able to control the initial state of the system. Adiabatic loading of Bose-condensed atoms into the optical lattice will initialize the system into the $k = 0$ quasimomentum state of the lattice. Applying a small force $\vec{F}$ will cause the quasimomentum of atoms in this lattice to time evolve linearly until the atoms reach the edge of the Brillouin zone, where they Bragg scatter off the lattice and their quasimomentum changes sign (from $+\pi/a$ to $-\pi/a$). This phenomenon is known as Bloch oscillation (see Fig. 5.6 for illustration of Bloch oscillations). We can use an applied force (and time) to control the initial quasimomentum state of atoms in the ground band (s-band).

Our system is reasonably well-modeled by a Bose-Hubbard Hamiltonian for atoms in a tilted optical lattice [56],

$$\hat{H} = -J \sum_{\langle i,j \rangle} \hat{a}_i^\dagger \hat{a}_j + \sum_i \frac{U}{2} \hat{n}_i(\hat{n}_i - 1) + F \sum_i i\hat{n}_i \tag{5.10}$$

where J is the tunneling matrix element, U is the on-site interaction energy, and F is

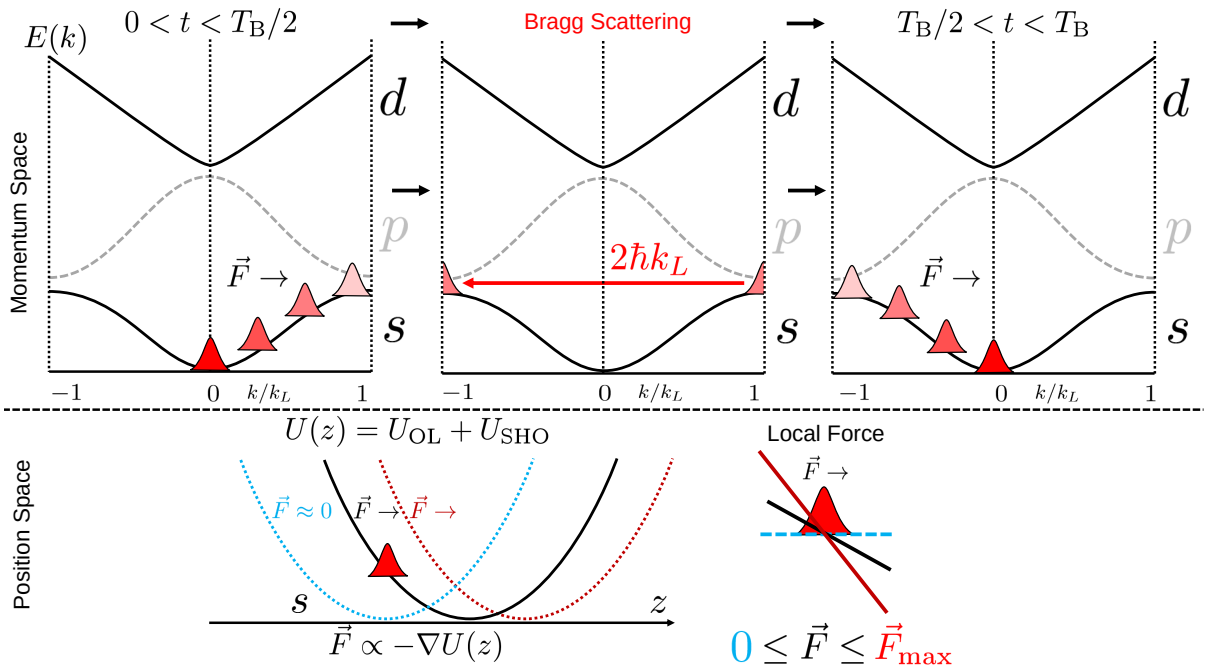

Figure 5.6: Schematic of Bloch oscillation of atoms in an optical lattice U_{OL} subject to simple harmonic confinement U_{SHO}. Top: momentum space evolution under constant force $\vec{F}$. Atoms gain quasimomentum until they reach the edge of the Brillouin zone. At the band edge, they undergo a Bragg scattering process, and emit two lattice photons into the lattice, which changes their momentum by $2\hbar k_L$ (wrapping to the other edge of the Brillouin zone). Bottom: changing the force applied to the lattice by changing the position of a simple harmonic potential.

the applied force ($F \times i$ is the energy difference between adjacent lattice sites i). We work in the limit that $U \ll J$ by tuning the scattering length to be negligibly small using the $|1,1\rangle$ Feshbach resonance to set $a_{scatt} = 0\ a_0$. Unless otherwise noted, measurements are made in a $5.4E_R$ deep lattice. We can directly observe Bloch oscillations (BO) by loading atoms into an optical lattice and allowing them to time evolve in the presence of a DC force $\vec{F}$. We then perform a band mapping operation to map the quasimomentum of the atoms in the band onto momentum, and then allow the cloud to expand freely for some time of flight (illustrated in Fig. 5.7). Fig. 5.8(a) shows this physics, specifically as time increases (from left to right in the figure), the atom's (quasi)momentum increases until it reaches the edge of the Brillouin zone, becomes double valued as it wraps around from

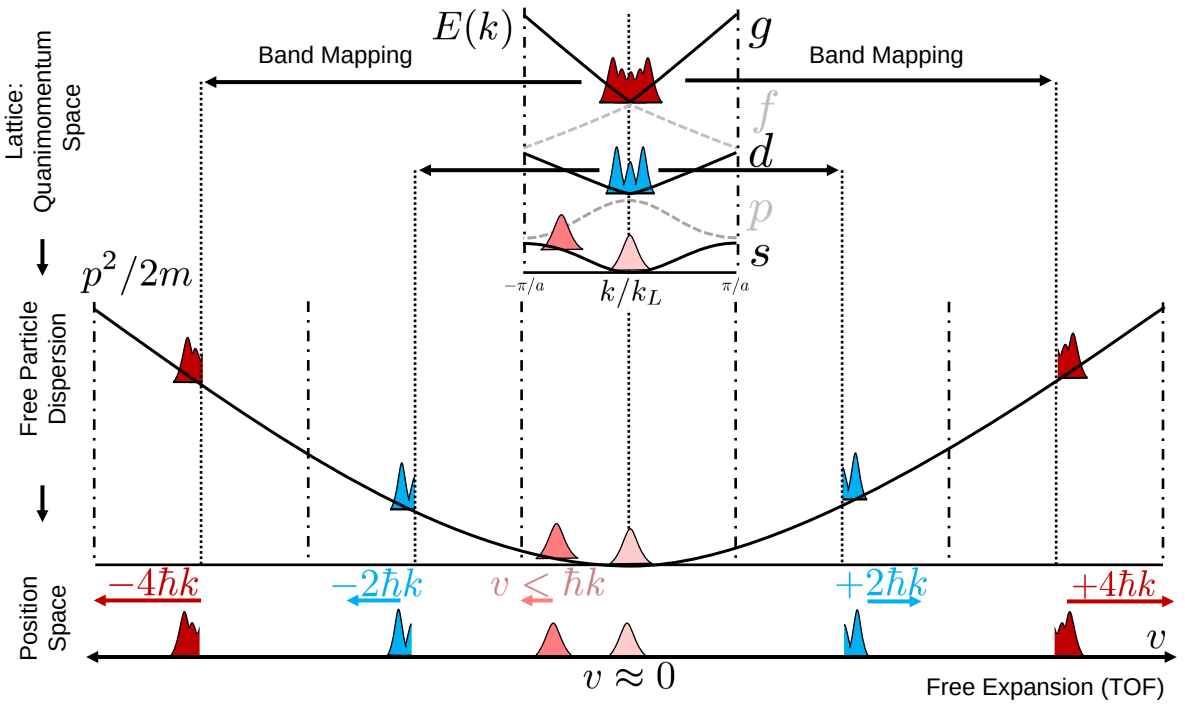

Figure 5.7: Schematic of band mapping. Top: populations of atoms in 1st, 3rd, and 5th bands of an optical lattice (s, d, and g respectively); cartoons are representative of the harmonic oscillator wavefunction squared. Their quasimomentum is restricted to $\pm\pi/a = \pm\hbar k_L$, where $k_L = 2\pi/\lambda$ for the wavelength λ of the lattice photons and $a = 532$ nm ($a = \lambda/2$), the spacing between neighboring lattice sites. Band mapping occurs when the lattice depth is gradually turned off, which projects the lattice quasimomentum onto the dispersion of a free particle $E(k) = p^2/2m$, essentially adding $\hbar k$ for each subsequent higher band the atoms occupied while in the lattice ($+\hbar k$ for p, $+2\hbar k$ for d, etc). These different momentum states are spatially separated by free expansion under time of flight (TOF), after which they are imaged.

π/a to $-\pi/a$, and then continues back around, completing a full cycle in a characteristic time $T_{\text{Bloch}} = h/Fd$, where F is the applied force and d, the spacing between neighboring lattice sites.

Position Space Amplitude: Bloch oscillations can be understood in terms of Wannier-Stark ladders[57][58][59], where atoms bound in adjacent lattice cites are approximated as being localized in harmonic oscillator potentials. The energy offset ($F \cdot d$) between neighboring lattices sites further suppresses tunneling and gives rise to stronger

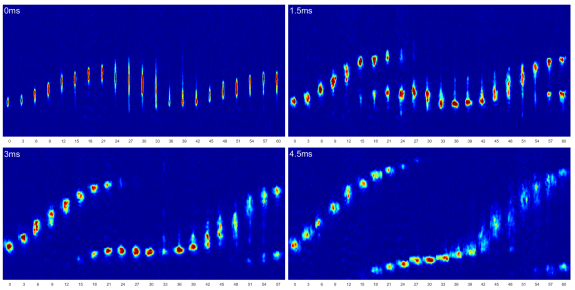

(a) *In situ* Bloch oscillations (top right). Others show quasimomentum populations after various time of flight (1.5, 3, and 4.5 ms).

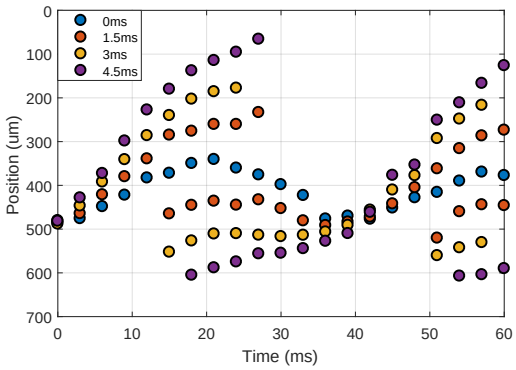

(b) Fitted cloud positions vs. time from (a)

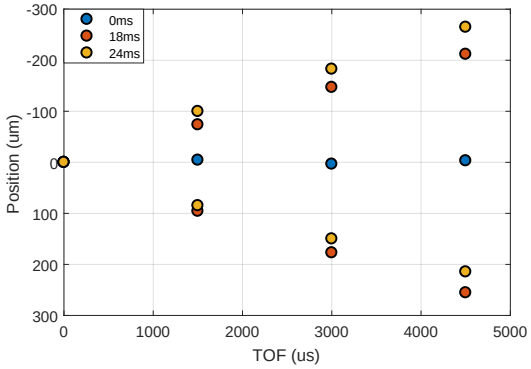

(c) Reconstructed time of flight for various phases of the Bloch oscillation: 0 ms→ $k = 0$, 18 and 24 ms near $k = \pi/a$ (band edge).

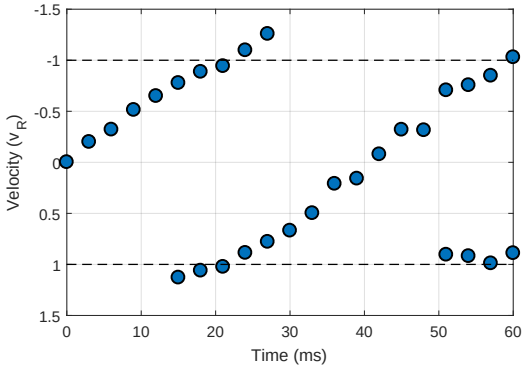

(d) Reconstructed velocity from time of flight data (c). Atom velocity $v \to -v$ near the quasimomentum band edge where $v \approx v_R$.

Figure 5.8: Time evolution of position space Bloch oscillations.

localization. This localization length, known as the Wannier-Stark localization length l_{WS}, is related to the bandwidth of the ground band Δ (proportional to J with $\Delta = 4J$), and the strength of the applied force $\vec{F}$, such that $l_{\mathrm{WS}} = \Delta/F$ [60][61]. It is this localization that gives rise to the characteristic momentum space time evolution commonly known as Bloch oscillations. In contrast to previous work, our experiment uses atoms with a light mass (hence large tunneling rate J, typically a few kHz), and a small applied force $\vec{F}$ (order $1{\times}10^{-25}$ N), meaning that we should expect l_{WS} to be 10-100 times larger than previous experimental studies (inferred amplitude of 3.1 μm[62])[63].

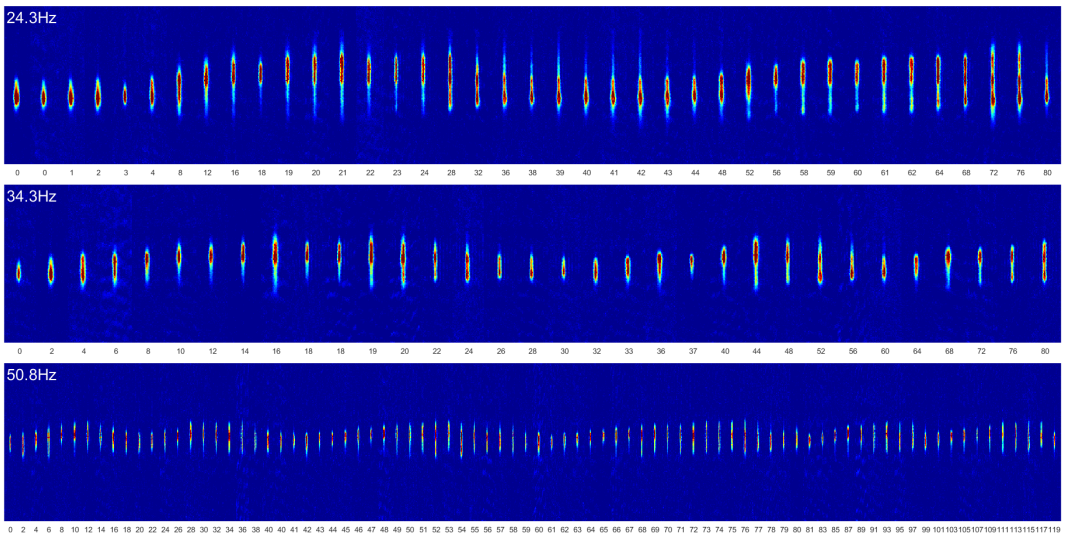

(a) *In situ* Bloch oscillations measured for various applied forces at a constant lattice depth. $f_{\mathrm{B}} = 24.3$, 34.3, and 50.8 Hz.

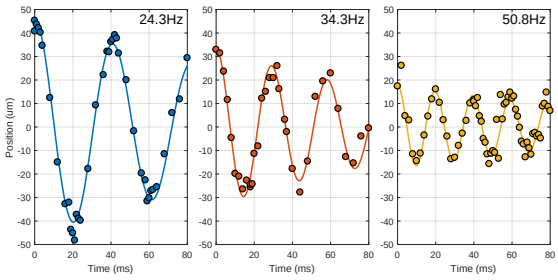

(b) Fitted cloud positions (including a dephasing-induced decay) for experimental runs in (a).

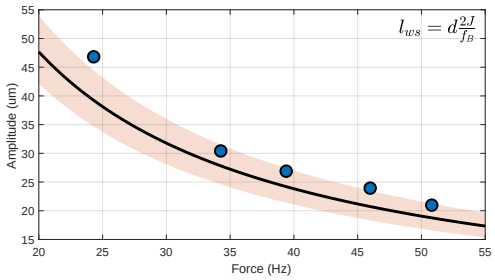

(c) Calculated Wannier-Stark localization length as a function of applied force (in Hz). Bound corresponds to a lattice depth uncertainty of $\pm 0.5 E_R$.

Figure 5.9: Variation of Bloch oscillation amplitude with increasing applied force at a fixed lattice depth of 7.4 E_R.

In order to verify that the observed oscillation is due to the applied force (and not due to a trap oscillation), we allow the atoms to Bloch oscillate in the lattice and then observe them both *in situ* and after some time of flight (Fig. 5.8(a)). The positions of the atoms are tracked and overlaid in Fig. 5.8(b). When the atoms are at the center of the Brillouin zone, their expected momentum is zero and the atoms do not move with time of flight. When the atoms reach the edge of the Brillouin zone they begin to Bragg scatter, and the momentum of the cloud is double valued at $\pm\hbar k_L$ (equivalently, when their velocity

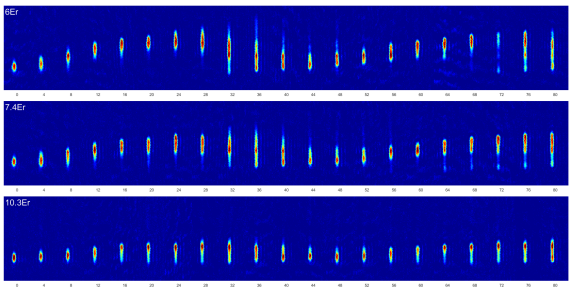

(a) *In situ* Bloch oscillations measured for $U_0 = 6$, 7.4, and 10.3 E_R lattice depths.

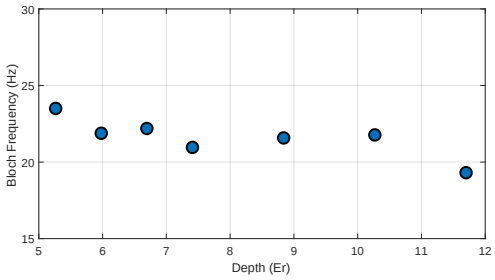

(b) Measured force (expressed in terms of the Bloch frequency).

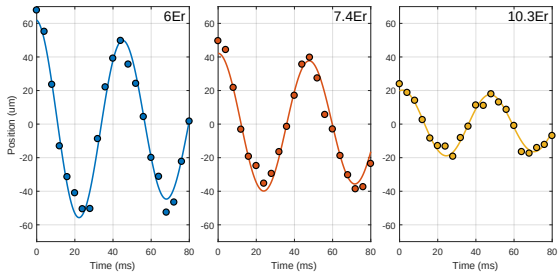

(c) Fitted cloud positions from (a), fit includes dephasing-induced decay.

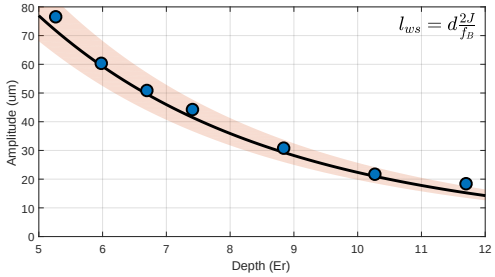

(d) Wannier-Stark localization length as a function of lattice depth E_R. Bounds correspond to a ± 3 Hz uncertainty in the fit.

Figure 5.10: Variation of Bloch oscillation amplitude with increasing lattice depth. Lattice depth calibrated independently using amplitude modulation spectroscopy.

$v = v_R = \hbar k_L/m$ where k_L is the lattice wave vector). These clouds move off with nearly the expected recoil velocity of a lattice photon: $v_{\mathrm{R}} = 53$ μm/ms. Both the spatial and momentum space distributions time evolve in the predicted manner[61]: a sine wave in position, and a sawtooth wave in momentum. The applied force is F=3.1$\times 10^{-26}$ N ($a = 2.65$ m/s^2) , with corresponding frequency $f_{\mathrm{Bloch}} = 25$ Hz and period $T_{\mathrm{Bloch}} = 40$ ms. Importantly, the scale of this oscillation for weak lattice depths and small applied forces is more than 70 μm, which represents a coherent delocalization of the atomic wave function in excess of a hundred lattice sites without any additional modulation[50][64], photon-assisted tunneling[47][65], or "super" Bloch oscillation[52]. Resolving the position-space oscillation of the atoms as they Bloch oscillate gives us the ability to reconstruct the band structure directly by measuring the position and time evolution of atoms in the

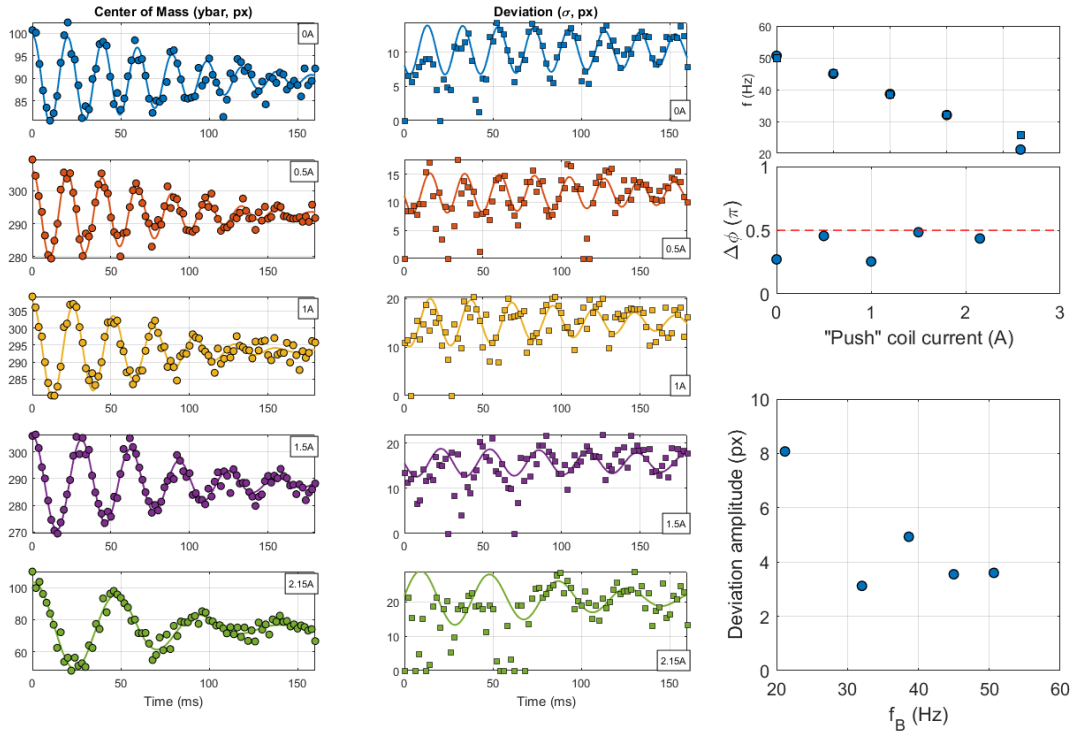

Figure 5.11: Left: center of mass motion ($\bar{y}$) of atoms undergoing position space BO. Middle: amplitude of the cloud's breathing mode about its center of mass motion (σ). Right top: observed Bloch frequency (Hz). Right middle: apparent phase shift between position space Bloch oscillation and breathing mode (theoretically expected to be $\pi/2$. Right bottom: fitted size of breathing mode; expected to be $\propto 1/f_B$.

lattice (see "Band Imaging" below).

We vary both the applied force at a fixed lattice depth (Fig. 5.9) and vary the lattice depth at a constant applied force (Fig. 5.10), and measure resulting localization length (amplitude) of the atom's position-space Bloch oscillation. We can make two independent measurements and cross check them: First measure the *frequency* of Bloch oscillations f_{B} at known lattice depth (using amplitude modulation spectroscopy to calibrate our applied lattice depth and its associated tunneling rate J) and calculate l_{WS} using

$$l_{\mathrm{WS}} = d\frac{2J}{f_{\mathrm{B}}}, \tag{5.11}$$

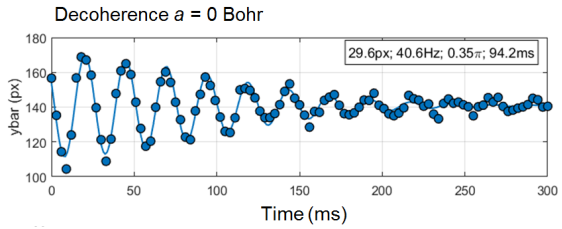

(a) Decay of center of mass motion for a system on Bloch oscillating noninteracting Bosons with 13 Hz external confinement. $\tau = 94.2$ ms.

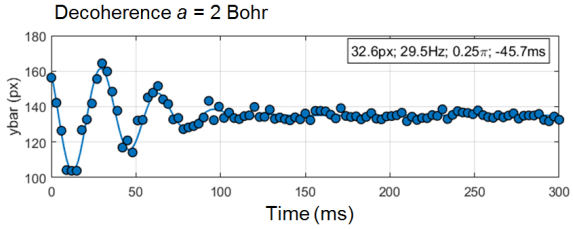

(b) Decay of center of mass motion for a system on weakly interacting Bosons ($a = 2\ a_0$) with 13 Hz external confinement. $\tau = 45.7$ ms.

Figure 5.12: Decoherence of Bloch oscillations for two different interaction strengths after 3 ms of free expansion. Measured $\bar{y}$ (ybar) fit to sine wave with an exponential decay envelope ($e^{-t/\tau}$). See "note on measurement" below for details of how $\bar{y}$ is calculated. Each pixel corresponds to 2.6 μm of distance.

(where $d = 532$ nm is the lattice spacing) and second, measure the *amplitude* of the position space Bloch oscillation directly to measure l_{WS} at a known force (which gives us f_{B}) and calculate the tunneling rate J to compare to a numerical calculation, where

$$J = \frac{1}{2}\frac{l_{\mathrm{WS}}}{d} f_{\mathrm{B}}. \tag{5.12}$$

In both cases we find excellent agreement with the theoretical prediction. Importantly, we believe this constitutes a first direct measurement of the amplitude of Bloch oscillations (equivalently, the Wannier-Stark localization length) in a cold atom context. Previous studies only infer the spatial extent of this oscillation, as the masses of the atomic species used tend to be 10 times higher than lithium's. Further, the applied forces are usually derived from gravitational forces[66][50][67], which again are proportional to the mass of the atom used.

Decoherence: Bloch oscillation is a coherent phenomenon, and resolving the coherent time evolution of the quasimomentum is a measure of how well defined the phase of the BEC is in the lattice. To wit: a BEC initialized in the lattice at quasimomentum $k/k_L = 0$ will undergo cyclic time evolution through $1 \to -1$ and return to 0 only if the

atoms experience a *uniform* force. As the lattice depth and applied force decrease, the atoms explore a larger region of space, and the Bloch oscillations begin to decay due to dephasing effects resulting from the harmonic potential. As discussed in [68], the characteristic dephasing time due to such a potential is $\tau_0 = \hbar/\gamma\nu$, where $\nu = m(2\pi\nu_z)^2 d^2$ and γ is the half-width of the cloud (in number of lattice sites). For our system, the harmonic confinement is $\nu_z = 13$ Hz and the initial spread is $\gamma \approx 50$, indicating a 100 ms characteristic delocalization time (vs. 94 ms measured, see Fig 5.12(a)). Further, Bloch oscillations decay rapidly if the atoms scatter off of one another (this is why they are so hard to observe in solids, as the coherence time is much longer than the time between scattering events). Figure 5.12(b) shows that Bloch oscillations decay nearly twice as fast ($\tau = 45$ ms) even when the scattering length is only 2 a_0. The atoms fail to undergo a single Bloch oscillation when the scattering length is 294 a_0.

Band Imaging: The position space BO is also an image of the band structure. The large spatial extent allows us to track the atomic motion and reconstruct the velocity (and hence the quasimomentum). To see this, consider first the real space evolution:

$$x(t) = \int \frac{\partial E}{\partial k}\frac{1}{m}dt, \tag{5.13}$$

$$= \int dE \frac{\partial t}{\partial k}\frac{1}{m}.^{1} \tag{5.14}$$

During Bloch oscillation, the quasi momentum k evolves linearly with the bloch fre-

[1]This operation probably isn't mathematically rigorous, but the resulting estimate matches the observation well.

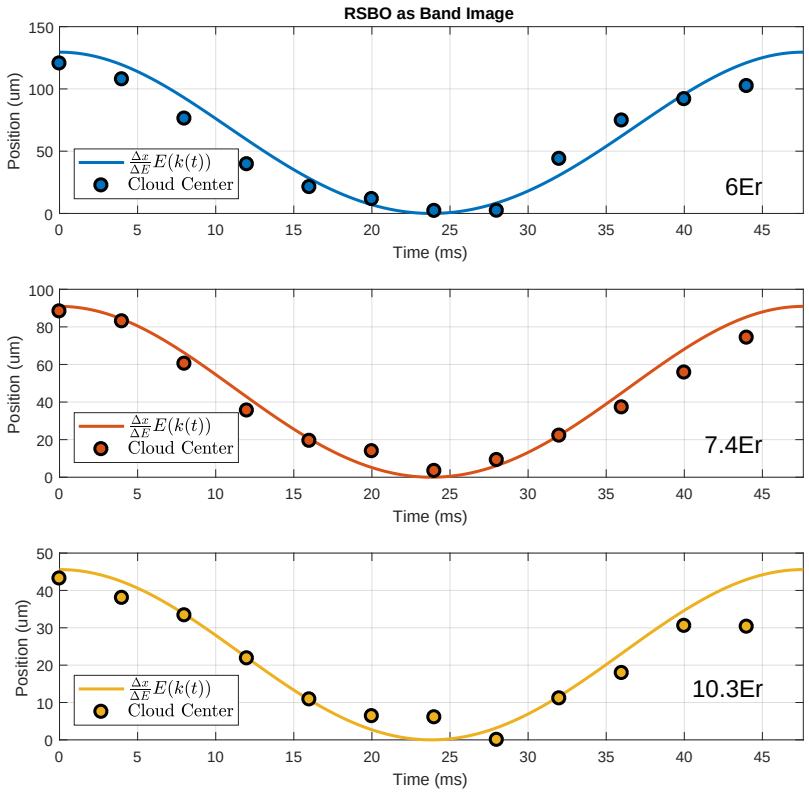

Figure 5.13: Direct imaging of band stricture for the ground (s) band for $6E_R$, $7.4E_R$, and $10.3E_R$ deep lattices. Points are measured cloud positions, lines are the theoretical prediction, not a fit to data.

quency such that:

$$\frac{\partial k}{\partial t} = f_B \hbar \frac{2\pi}{a} m \tag{5.15}$$

where a is the lattice spacing 532nm. Intuitively, this means that in one bloch period, the atomic cloud traverses one Brillouin zone. Using this simplifies the expression:

$$x(t) = \int dE \frac{a}{2\pi f_B \hbar}, \tag{5.16}$$

$$\Delta x = a \frac{\Delta E}{h f_B}. \tag{5.17}$$

Rearranging for the energy:

$$\frac{\Delta E}{E_R} = \frac{\Delta x}{a} \frac{f_B}{f_R} \tag{5.18}$$

where we have renormalized the energy in terms of the recoil energy E_R (25.177kHz). Therefore, there is a one to one mapping from position to energy of:

$$\frac{\Delta E}{\Delta x} = \frac{f_B/f_R}{a}. \tag{5.19}$$

See Fig. 5.13 for a comparison of cloud center position and the energy of the band. Large amplitude Bloch oscillations lets us directly image the band structure. With a more complex calculation it may be possible to resolve the band structure of higher bands. This could potentially be used to image Floquet hybridized bands (such as those created in section 5.4).

Breathing Mode: In the moving atom frame of reference, the cloud will expand and contract with a frequency commensurate with the Bloch oscillation. This phenomenon is known as a breathing mode and is theoretically well explored ([69][70][60]). Observations of breathing mode dynamics have been made in the single atom context (with quantum gas microscopes[71]). Since we have a large position space Bloch oscillation, we explored the possibility of resolving these breathing modes in the many-atom context. Figures 5.11 and 5.11 clearly resolve the breathing mode about the center of mass position, but the large initial spatial extent of the cloud and our diffraction limited spot size of 5 μm limits

the resolution of our measurement. The amplitude of the breathing mode is predicted to be inversely proportional to the initial spatial extent of the cloud, so it is unsurprising to measure a small breathing mode in our system ([72], esp. Eqn. 11-14)).

A note on measurement: the central position of the cloud $\bar{y}$ (ybar) is calculated by taking the weighted average of the optical density and multiplying by pixel number to find the expectation value of the cloud's 'center of mass,' i.e. $\bar{y} = (y \cdot \mathrm{OD}_y)$; this avoids the problem of having to fit a distribution (Gaussian or otherwise) to an extended or possibly double valued cloud. Similarly the cloud's spatial extent σ (the amplitude of the breathing mode, or "deviation") can be calculated as the square root of the variance $\sigma = (\bar{y^2} - \bar{y}^2)^{1/2}$, where $\bar{y^2} = (y^2 \cdot \mathrm{OD}_y)$. These quantities are plotted in Figures 5.11 and 5.12.

We believe the direct measurement of real space Bloch oscillations in the absence of any external modulation constitutes a first observation of this phenomena in a cold atom context. Further, this large spatial extent effectively allows direct addressing of different parts of the band structure in a spatially-resolved way that has not been previously experimentally realized. For only moderate applied forces, the $k/k_L = 0$ and ± 1 points in the Brillouin zone have a corresponding position space (*in situ*) separation of more than 80 μm.

5.3 Relativistic Harmonic Oscillator

The behavior of ground state Bloch oscillations is theoretically and experimentally well studied. An open question is how do atoms in an excited state of the lattice time evolve? The dispersion relation of the 3$^{\mathrm{rd}}$ band (d-band) is interesting because it looks similar to the dispersion relation of a relativistic particle (with $E \propto k$). Applying a short amplitude modulation pulse (0.5 ms duration, 20% V_{OL}) to the lattice allows us to

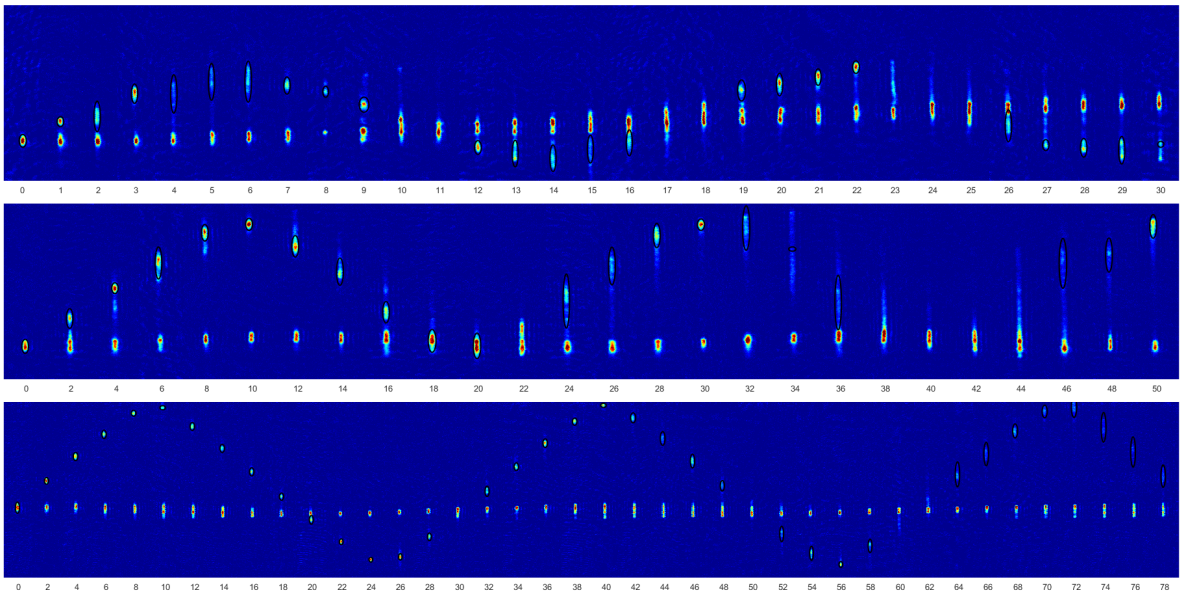

Figure 5.14: Tracking d-band atoms at different excitation amplitudes (s-band Bloch oscillations still visible). Position vs. time (ms).

drive atoms into the d-band in a position-selective way, due to the large spatial extent of the Brillouin zone and the Bloch oscillating atoms. Despite being subject to the same forces as the ground band atoms, we do not observe Bloch oscillation of these d-band atoms. Instead, atoms in the d-band are not well localized in the lattice, and freely explore the simple harmonic (SHO) potential as a function of time. The presence of the optical lattice modifies the atom's dispersion relation in such a way that for large initial excitations (amplitude modulation at a frequency near the band edge) the atoms move as if they were massive relativistic particles (see Fig. 5.15). Namely, for sufficiently large excitation energies, the atoms move with a nearly constant velocity between turning points of the classical SHO potential. These dynamics are well modeled by considering the dispersion relation of the 3$^{\text{rd}}$ band and approximating the atomic motion with the dispersion relation:

$$E(k) = E_R \left(\left(a \frac{k}{k_L} \right)^2 + b^2 \right)^{\frac{1}{2}} - bE_R \tag{5.20}$$

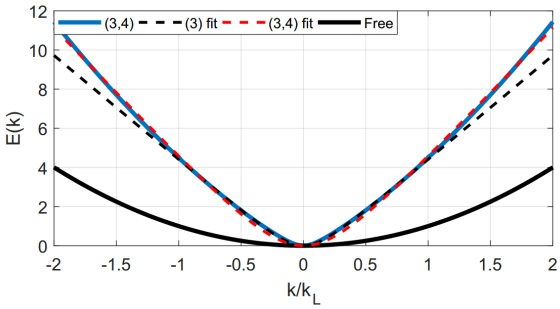

(a) Dispersion relation of 3^{rd} and 4^{th} bands, fit to functional form of eqn. 5.21 for 3^{rd} band only (black dashed) and extended $3^{\text{rd}} + 4^{\text{th}}$ bands (red dashed). cf. free particle dispersion (black).

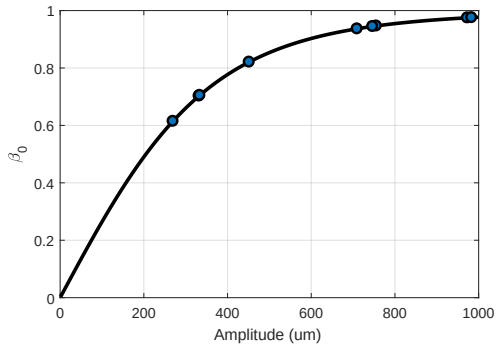

(b) Maximum $\beta(= v/c)$ for a given amplitude. Points indicate expected β for observed oscillation amplitudes in (c).

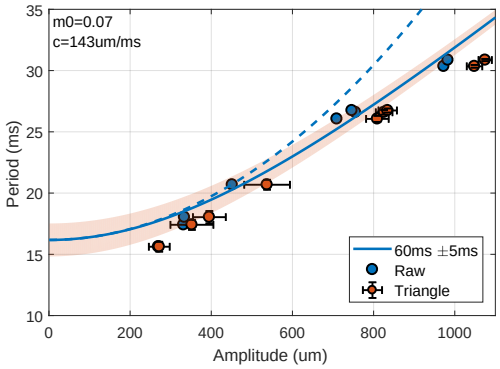

(c) Expected period vs. amplitude response for a relativistic harmonic oscillator with bare period 60 ms. Red circles are fit to triangle wave, blue data derived from raw cloud position, not a fit.

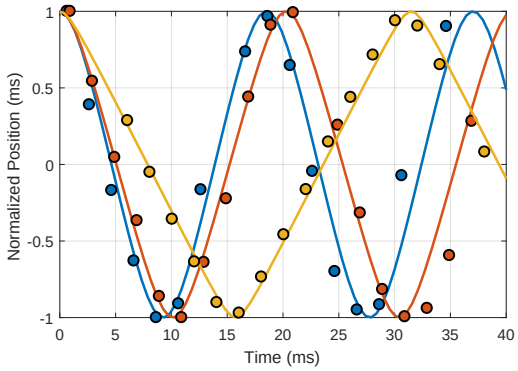

(d) Fitted cloud motion (circles) vs. normalized predicted trajectories for an RHO with the same period (not a fit to data). $\beta = 0.7$ (blue), 0.82 (red), and 0.98 (green).

Figure 5.15: Cold atom relativistic harmonic oscillator.

where $E_R = \hbar^2 k_L^2/2m$, is the lattice recoil energy. If we ignore the constant offset bE_R, we can map this dispersion relation to the relativistic one, using the terms $c = av_R/2$ and $m_0 = E_R b/c^2$ (effective speed of light and mass, recall $v_R = \hbar k_L/m$):

$$= E_R \left(\left(a \frac{k}{k_L} \right)^2 + b^2 \right)^{\frac{1}{2}} = \left(p^2 c^2 + \left(m_0 c^2 \right)^2 \right)^{\frac{1}{2}} \tag{5.21}$$

where a and b are free parameters of the fit, which yield an effective mass $m_0 = 0.07 m_{\mathrm{Li}}$ and a 'speed of light' of $c = 143$ μm/ms. The expected period of the RHO can be calculated simply (following the treatment found in [73]):

$$\tau \approx \tau_0 \left(1 + \frac{3KA^2}{16 m_0 c^2}\right), \tag{5.22}$$

with the measured amplitude of the oscillation A, and the bare spring constant of the SHO potential K:

$$K = m_B \omega_B^2. \tag{5.23}$$

The period of the oscillator depends on the amplitude of the oscillation in a way that deviates from simple harmonic motion (where the period is fixed). For reference τ for a bare oscillator with period 60 ms is plotted in Fig. 5.15(c). In contrast to measurements of Dirac oscillators with microwave resonantors[74], our system realizes a relativistic harmonic oscillator with massive particles.

In summary, we've made a very clean realization of a relativistic harmonic oscillator and studied some of its properties. It would be straightforward to extend these studies to higher bands, where the particles should travel with higher velocities and lower effective masses. We believe this constitutes a first experimental observation of relativistic harmonic motion with massive particles.

5.4 Quantum Coherent Transport

Floquet band engineering opens the possibility of using amplitude modulation to hybridize bands within a lattice. In the static lattice picture, this corresponds to promoting atoms into a higher band of the lattice where they have a different time evolution compared to unperturbed atoms. We leverage this scheme to create a kind of quan-

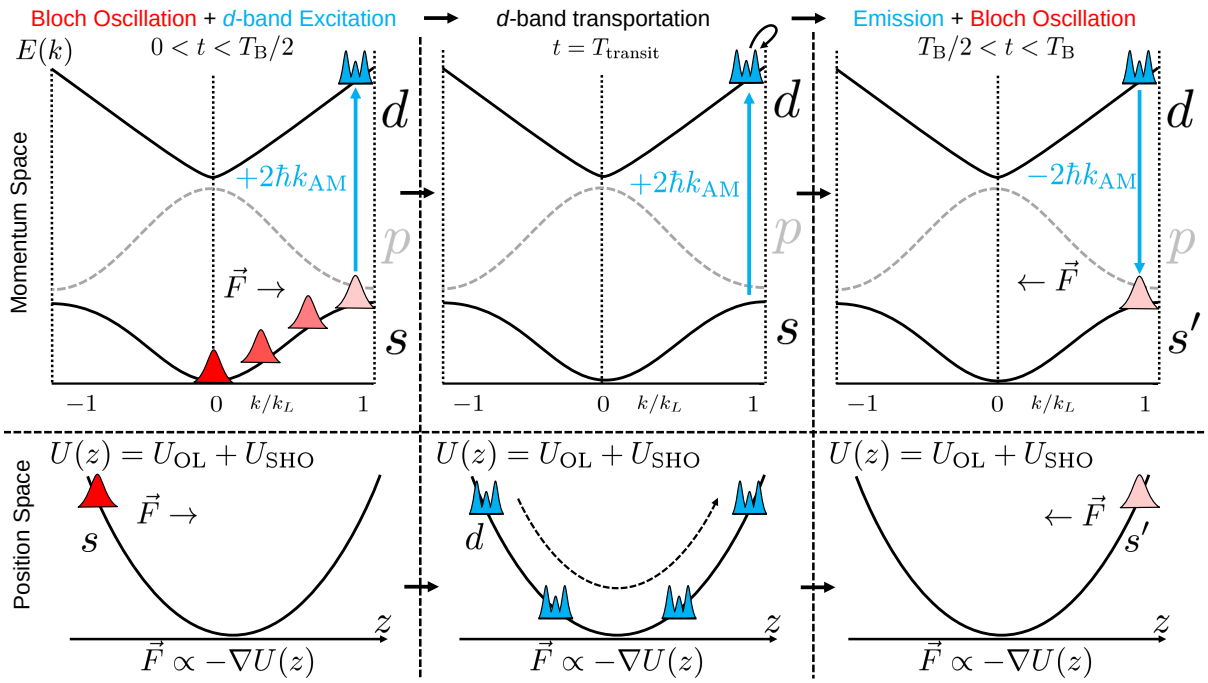

Figure 5.16: Schematic of long range quantum coherent transport scheme via d-band excitation. Atoms absorb two photons ($2\hbar k_{\mathrm{AM}}$, resonant with $s \rightarrow d$ at the band edge), travel though the lattice, and then emit two photons on the exact opposite side of the harmonic potential. Top: momentum-space picture showing time evolution in the s- and d-bands. Bottom: position-space picture. Left: atoms are well localized in the optical lattice (U_{OL}) on one side of the harmonic potential (U_{SHO}) until they Bloch oscillate long enough to become resonant with the amplitude modulation. Middle: once promoted to the d-band, atoms are no longer localized in the lattice and are free to move in the harmonic potential. Right: atoms become resonant with the drive on the opposite side of U_{SHO} and emit two photons into the lattice, entering the s' band.

tum coherent transport: moving atoms macroscopic distances (thousands of lattice sites) while maintaining their coherence in a controlled way.

Experimental Concept: The atoms are confined in a lattice on one edge of a harmonic potential (simple harmonic oscillator potential, or SHO). In their unperturbed state, the atoms remain in the region of the lattice around where they are loaded. The atoms undergo Bloch oscillation in the lowest band of the lattice (the s-band), where we observe their position-space time evolution (see above). If we apply a slight amplitude modulation to the lattice, we can drive resonant excitation to the d-band by means of a

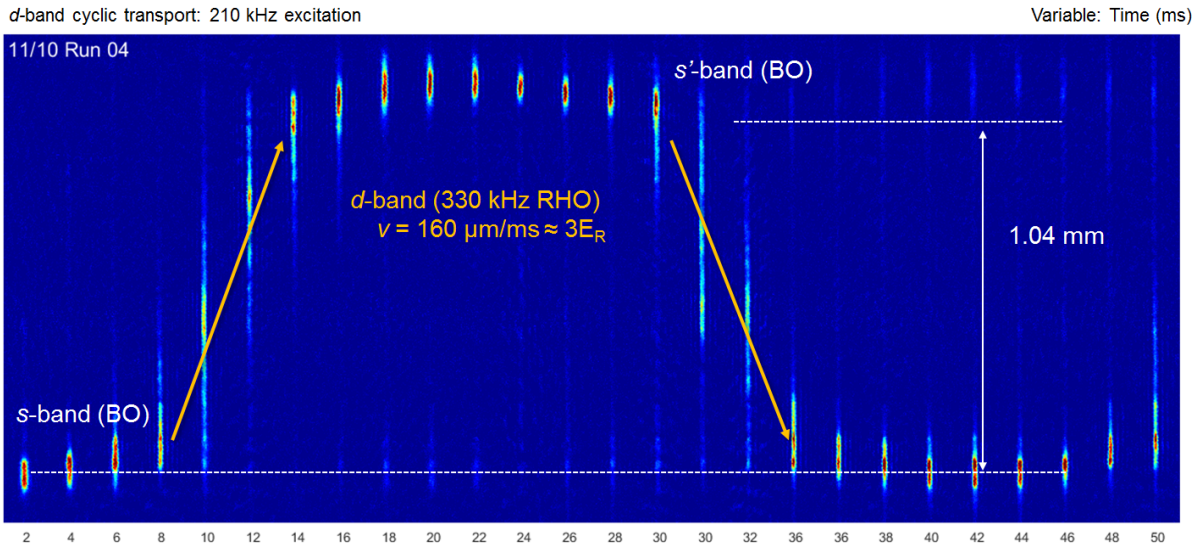

Figure 5.17: 210 kHz d-band transport; oscillation in the $[sd]$hybrid Floquet band (see Fig. 5.23).

two-photon absorption in much the same manner way that amplitude modulation spectroscopy promotes atoms into the d-band. We blue-detune the frequency of amplitude modulation by $f = 110$ kHz, where $E = hf = \hbar k_L$ is the width of the Brillouin zone for a $5E_R$ lattice. This moves the excitation from the $k/k_L = 0$ (center) to the $k/k_L = \pm 1$ (edge) of the band.

The BEC is initialized in the $k/k_L = 0$ state of the lattice via adiabatic loading (increasing the lattice depth from 0 to $5E_R$ in 100 ms). Once the ODTs are turned off (removing the external confinement), their quasimomentum will time evolve in the usual Bloch-prescribed manner: linearly under an applied force $\vec{F}$. When the atoms reach the edge of the Brillouin zone, they absorb energy from the drive and are promoted into a higher band within the lattice. This creates a population of atoms that moves relativistically in the lattice (see section 5.3). They traverse the harmonic potential at relativistic speeds until they reach the mirror opposite position on the other side of the potential, where they are again resonant with the amplitude modulation. At this point, they emit two photons into the lattice field, and enter the s-band again (we indicate

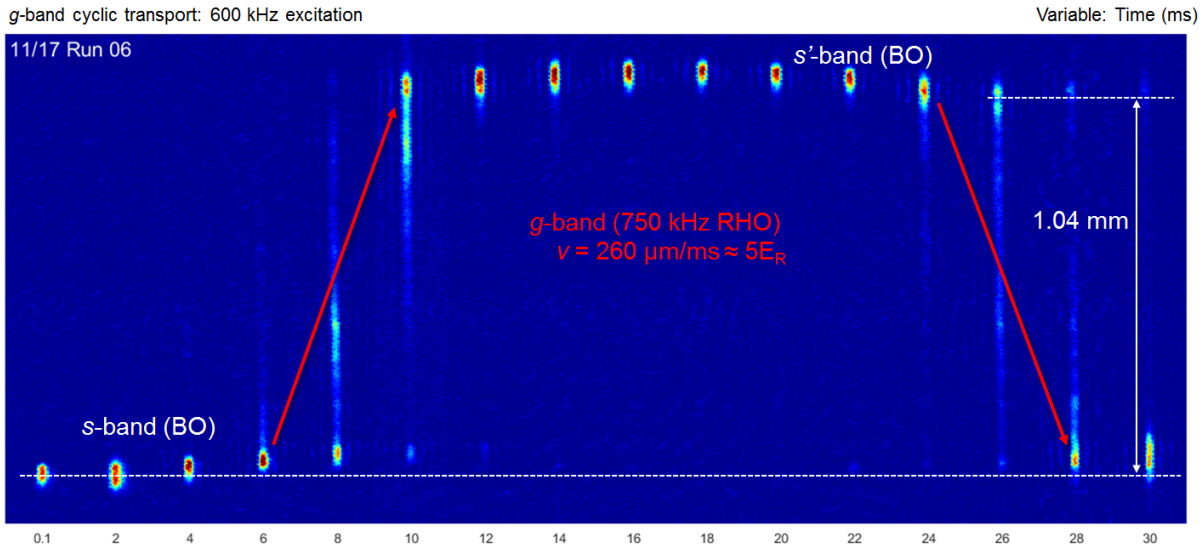

Figure 5.18: 600 kHz g-band transport; oscillation in the [sg]hybrid Floquet band (see Fig. 5.23).

atoms transported in this manner as occupying the s'-band), where they continue to Bloch oscillate. The measured frequency of Bloch oscillation is 24 (25) Hz for the s-band (s'-band) atoms, but in the opposite direction, which indicates that the applied force is the same magnitude, but has changed direction (i.e. $\vec{F} \rightarrow -\vec{F}$). Further, as the atoms continue to Bloch oscillate after transport, we conclude that they have been transported *coherently* (without randomizing their phase). If we continue to apply the drive to the atoms, they will undergo a single period of Bloch oscillation before their quasimomentum evolves to $-\hbar k$, where they absorb two photons and travel back across the harmonic potential. The atoms will acquire a phase-shift in their Bloch oscillation relative to the unperturbed population proportional to the amount of time they spent moving across the harmonic potential (evidenced in figure 5.22). In this manner, we can drive (in some sense "pump") atoms across macroscopic distances coherently. The speed of this transport is what is particularly promising. We have observed near 100% transport for both d-band excitation (2-photon, 210 kHz) and g-band excitation (4-photon, 600 kHz).

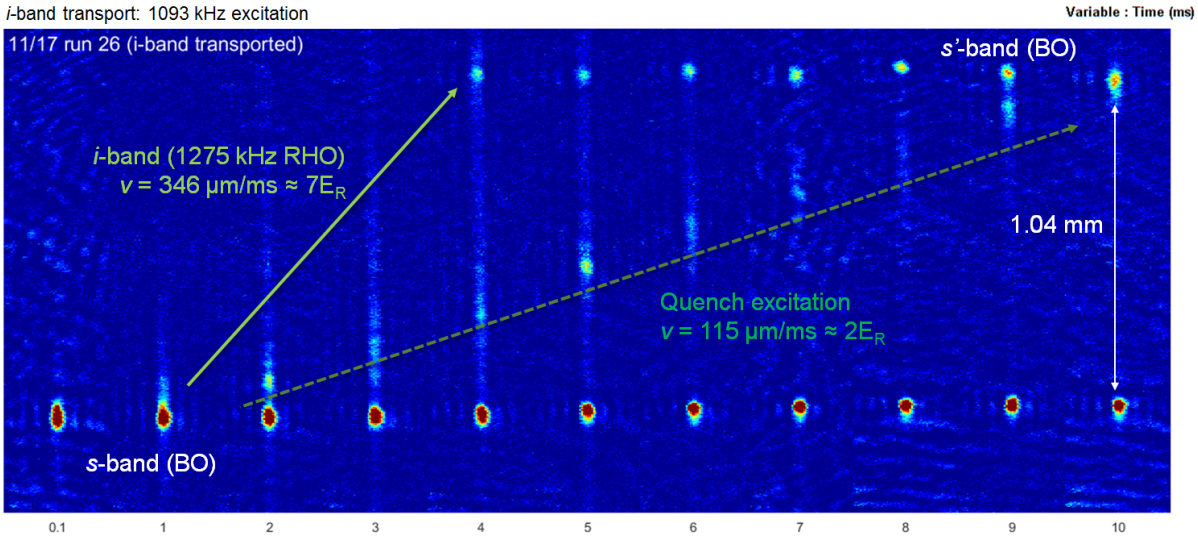

Figure 5.19: i-band transportation. Quench into modulation causes extra excitation, causing a small population of atoms to propagate with $v = 115$ μm/ms $\approx 2E_R$. Only a small fraction of the atoms occupy the hybrid $[si]$-band, likely due to the narrow avoided crossing.

Speed: we can estimate the speed of this transport in one of two ways. (1) we can directly measure the position of the atoms as a function of time by imaging them *in situ* and (2) by calculating the speed of transport from the known frequency of the drive. We know from the RHO observations that for sufficiently large excitation energy the atoms move with near linear velocity across the SHO potential. For atoms undergoing d-band transport, the atoms move across the potential in 6 ms. This means their rate of transport is 1 mm/6 ms $\approx$ 167 μm/ms. This matches (2) the theoretical estimate that the atoms at the edge of the Brillouin zone have quasimomentum $\hbar k$ and acquire an additional $2\hbar k$ when promoted to the d-band, meaning their total momentum is nearly $3\hbar k$ (= 159 μm/ms). We can write their transit speed in units of the recoil velocity: $v_\mathrm{T}/v_R = 3.15$. Further, comparing the speed of this transportation to the s-band tunneling rate J for a $5E_R$ lattice, where $J = 1656$ Hz yield an effective tunneling rate $J_\mathrm{T} = f_\mathrm{T}/J$ (= 190 for d-band transport). Given our lattice spacing $d = 532$ nm, we can compare J_T to the expected s-band transit time: 1 mm / 532 nm $\approx$ 2000 sites; 2000 sites/J = 1.2

s (s-band) vs. $2000/190J = 6.3$ ms (d-band). This matches well the observed speed of atoms moving across the SHO potential in Fig. 5.17(a)). See Table 5.1 below for a comparison of transport rates in the higher bands (g- and i-bands).

Band	f **(kHz)**	$f_{\mathbf{T}}$ **(kHz)**	**t (ms)**	$v_{\mathbf{T}}$ **(μm/ms)**	$v_{\mathbf{T}}/v_{\mathbf{R}}$	$J_{\mathbf{T}}/J$
d (1→3)	210	315	6	167	3.15	190
g (1→5)	600	750	4	250	4.7	452
i (1→7)	1093	1275	3	346	6.53	770

Table 5.1: Transit distance z = 1.04 mm, $J_{\mathrm{T}}/J = f_{\mathrm{T}}/J$ is the effective tunneling rate in this hybrid band, $v_R = 53$ μm/ms, $J = 1656$ Hz (for a $5E_R$ lattice).

We can leverage our ability to modulate the lattice at extremely high frequencies to realize high band excitation (namely the 1→5 (g-band) and 1→7 (i-band) transitions). One interesting observation is that the required modulation depth increases dramatically as a function of band number. For d-band excitation, modulation of $\alpha = 0.05$ is sufficient to transport nearly 100% of the atoms across the potential. For g-band excitation, $\alpha = 1$, and our current scheme for i-band transportation requires $\alpha = 6$[2].

Coherence: this quantum transport is still fundamentally limited by the decoherence induced by the harmonic potential. Atoms in the s- and s'-bands experience the same field curvature and will decohere over the same time scales as if unperturbed. Figure 5.20 demonstrates this effect for atoms transported 600 μm via d-band excitation (210 kHz). The transported atoms (top) undergo real space Bloch oscillation at the same frequency as those that are not transported, because the force the atoms experience has the same magnitude, but a flipped direction. Figure 5.21 shows a single cloud making multiple passages across the harmonic potential until the distribution has largely decohered.

Directional Drive: It is of course possible to disable the modulation that transports the atoms once they've moved across the potential. In this way we can use Floquet

[2]We apply the amplitude modulation diabatically, which causes additional excitation for increasing modulation depth. Ramping on the modulation will likely remove these excitations and improve the efficiency of transport.

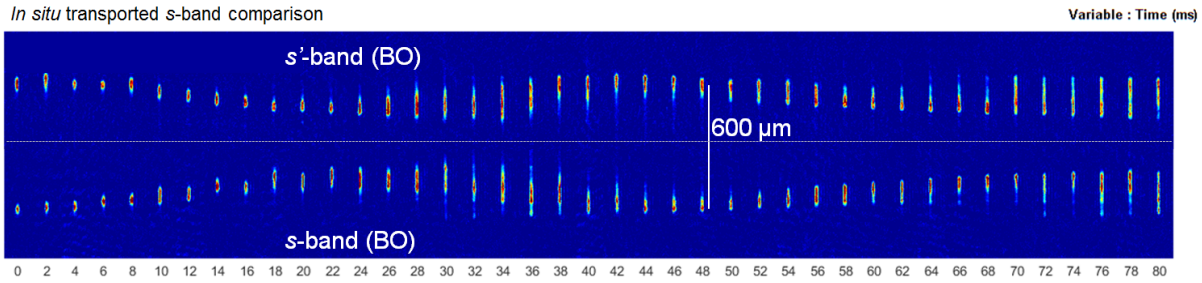

Figure 5.20: Comparison of *in situ* (position space) Bloch oscillation for atoms before (s-band) and after (s'-band) transport. Atoms move 600 μm and continue to undergo coherent time evolution after transportation via d-band, 210 kHz excitation. Transported atoms still exhibit same decoherence induced from the harmonic confinement.

engineering to transport atoms macroscopic distances (in excess two thousand lattice cites). Additionally, the number of atoms that are transferred depends on the amount of time they spend in the momentum-space region in that is resonant with the drive. A stronger applied force therefore causes a fraction of atoms to be transported, while the others remain behind and continue to Bloch oscillate. This is a very direct way of making a copy of a system and transporting it a macroscopic distance in a controlled way. It would then be relatively straightforward to perturb one of these systems and recollide them at some later time to perform atom interferometry, precision force measurement[75] or perhaps measure a kind of out of time order correlation function.

In principle it should be possible to transport atoms even larger distances by relaxing the SHO potential and loading atoms even farther off center. Another possibility is to eliminate the magnetic field curvature entirely and rely on a very long-range optical potential (e.g. loading atoms on one side of the lattice and using the overall optical harmonic potential) to transport atoms on the scale of the Rayleigh length z_R or more.

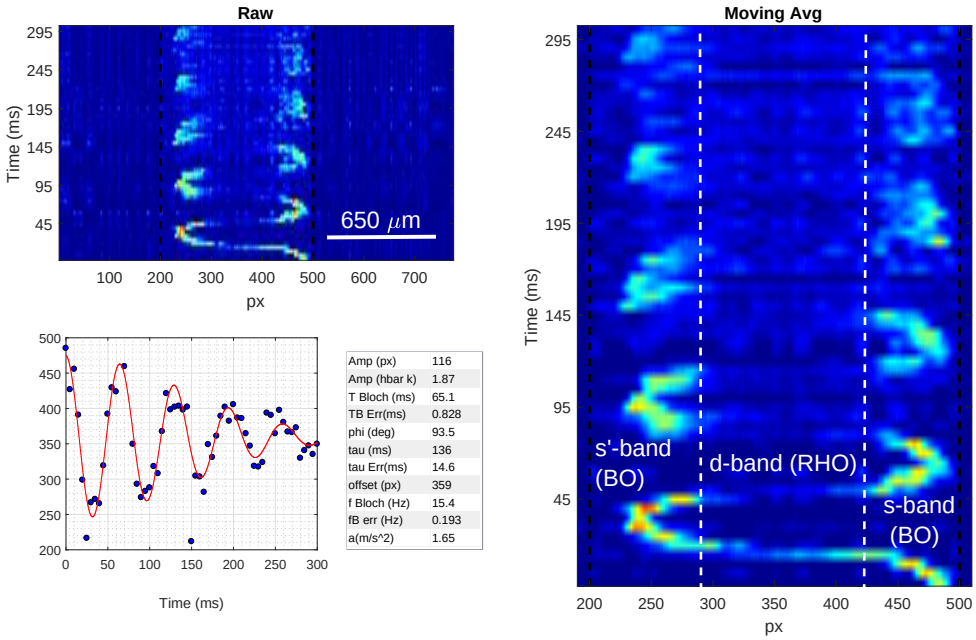

Figure 5.21: Decoherence of atoms undergoing cyclic d-band transport. Atoms move across the harmonic potential and Bloch oscillate on either side. Coherence of the Bloch oscillation, and hence the transportation, both decay with the characteristic timescale associated with the harmonic confinement ($\approx$ 100 ms, here measured to be 136 ms).

5.5 Future Directions

5.5.1 Floquet Band Engineering

One exciting possibility that this work raises is the ability to use bichromatic or even multichromatic amplitude modulation to link excited bands together in this Floquet-Bloch picture. One could in principle simultaneously apply a drive at the s-g and d-g transitions, with the aim of exciting atoms into the g-band on one side of the harmonic potential, transporting them, and then transferring them into the d-band on the other side. This could be one possible avenue to making a fully d-band relativistic harmonic oscillator, instead of using a pulse excitation to create the s+d RHO as we have already

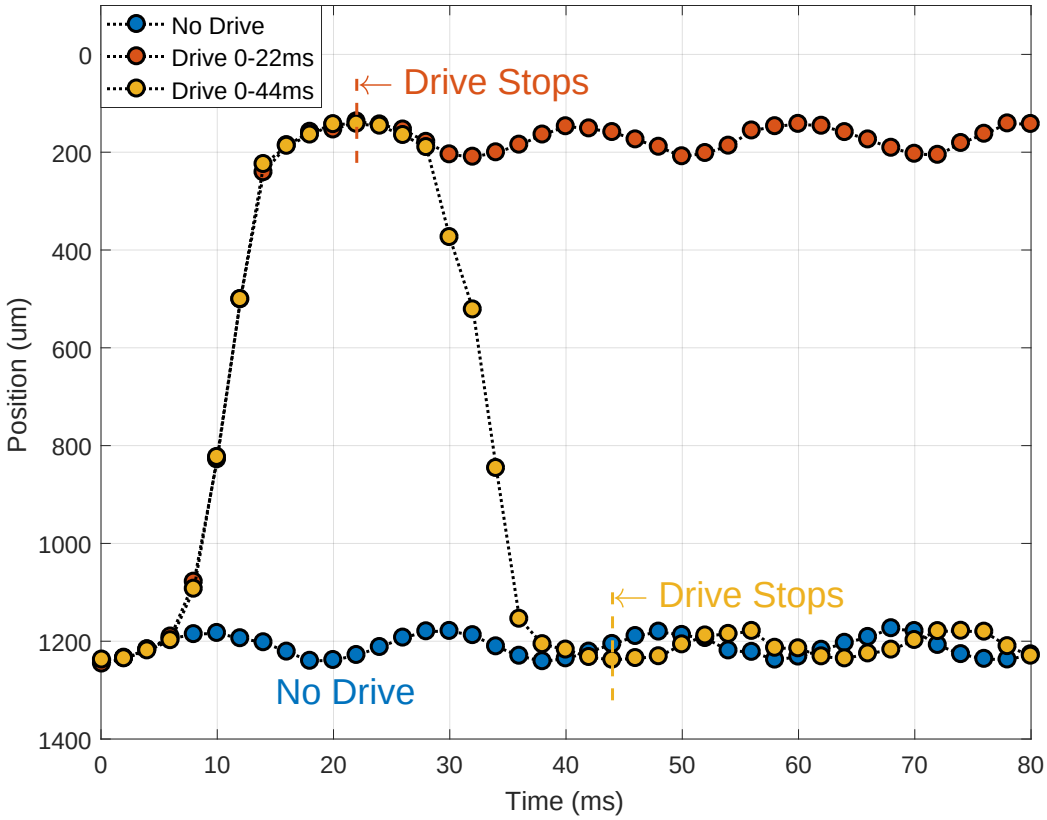

Figure 5.22: Cloud center position during d-band transport across 1 mm distance. Without driving, the atoms Bloch oscillate in the s-band. If the drive is turned off after 22 ms, the atoms move over and then Bloch oscillate in the s'-band. If driving continues for 44 mm, the atoms can be transported back to their original position, where they resume Bloch oscillation in the original s-band. Atoms transported acquire a phase shift in the BO relative to atoms that are not transported.

demonstrated. Time and frequency dependent driving could be used to accelerate atoms into increasingly higher RHO states.

Our system can also study hybridized bands with relative ease. For instance, waiting until the atoms reach the $k/k_L = 1/2$ point in the s-band and then turning on a bichromatic s-d excitation resonant at both $k/k_L = 0$ and 1 would confine the atoms in a hybridized d+s+d band with nontrivial band curvature (see 5.24 for illustration).

Precise control of strongly driven systems afforded by ultracold degenerate gases

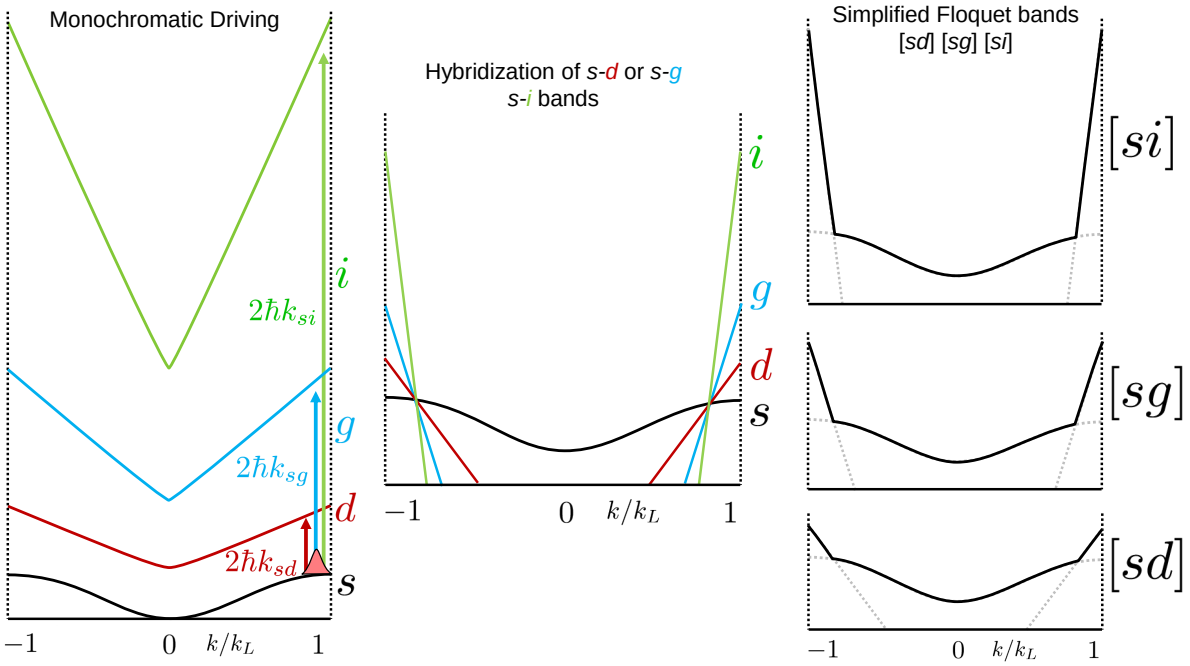

Figure 5.23: Simplified band structure demonstrating Floquet engineering of bands. Amplitude modulation near the band edges mixes the bands near $k/k_L = \pm 1$. The time evolution of our transported system can be understood in terms of atoms moving in these hybridized bands, where the effective mass ($1/m_{\text{eff}} \propto \partial^2 E/\partial k^2$). Even and higher order bands omitted for clarity. Compare $[sd]$ hybrid band to Fig. 5.1.

might also open the pathway to realizing otherwise challenging quantum states, such as the Floquet symmetry-protected topological (SPT) phase[76], frustrated magnets[77], non-abelian gauge fields[78][79], and give rise to metastable states that may exhibit exponentially slow heating rates[80].

5.5.2 Floquet Phase Diagrams

Our current efforts are now studying the broader properties of these Floquet engineered systems using a "Kapitza Pendulum" as a model system. Classically speaking, Kapitza's pendulum is a rigid-rod pendulum where the fixed point of the pendulum is driven with some frequency and amplitude. Under the right driving conditions, the pendulum exhibits stability not only in the downward-pointing (normal) position, but in

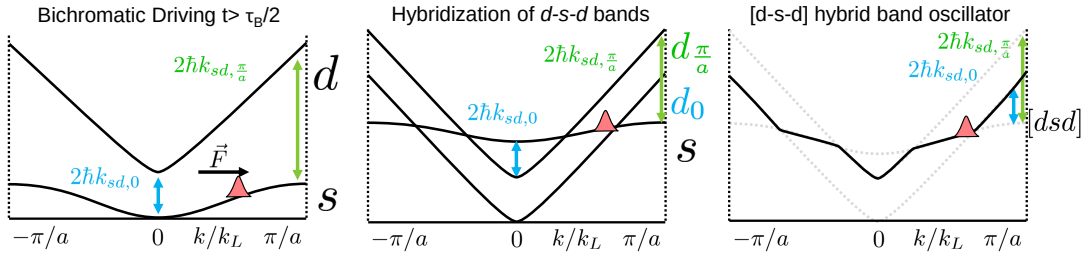

(a) Hybridized *dsd* band system driven by bichromatic amplitude modulation. Initial state preparation possible using Bloch oscillations to control the energy of the atoms in the *s*-band. The effective mass changes as atoms explore the band.

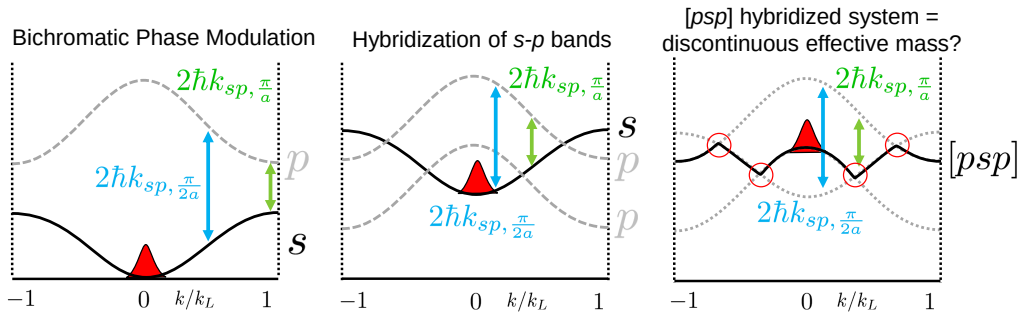

(b) Hybridized *psp* band system driven by bichromatic phase modulation (possible with offset lattices). Effective mass periodically changes sign at band crossings (red circles).

Figure 5.24: Concept of higher-order Floquet hybrid bands including amplitude and phase modulation.

the upward-pointing (inverted) position. While amplitude modulation has been used in the past (often characterized as being "strong"[53]), the potential never entirely inverts. That is, the minima of the optical potential merely becomes a region of very weak trapping when the lattice is turned off, or shifted by $\lambda/4$ (in the case of a phase modulated lattice). In order to reach an inverted state, the optical lattice must be able to invert to apply a sign-changing force to the atoms (equivalent to applying acceleration stronger than g in the classic pendulum picture).

This inverted pendulum is a simple system that exhibits stability in the presence of a very strong applied drive. The basic concept is to use a system of cold atoms loaded into

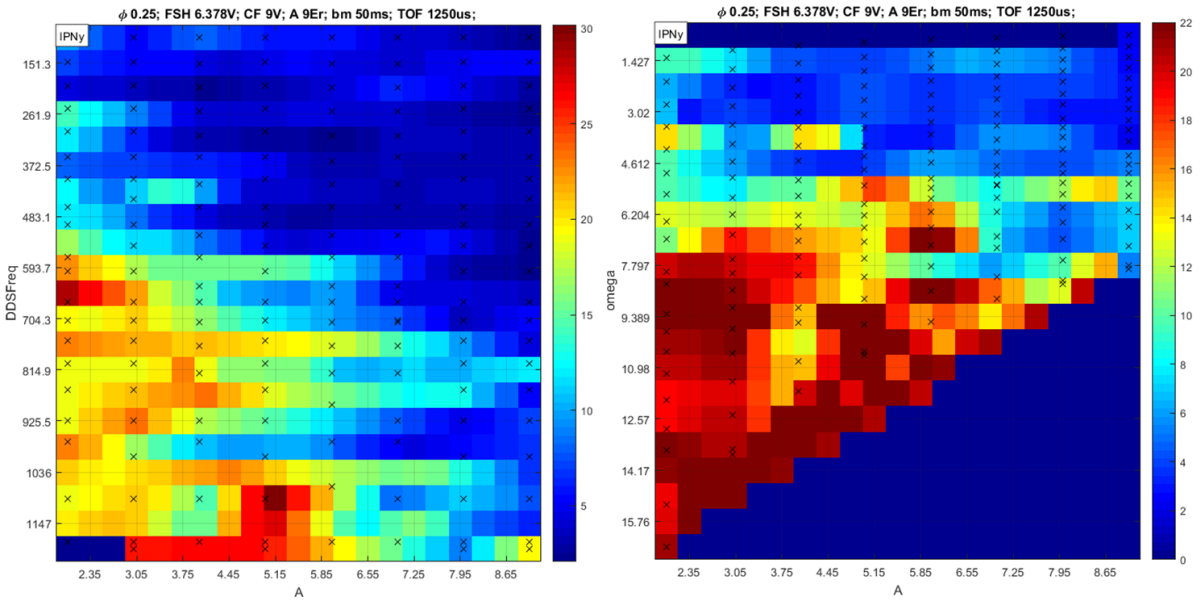

Figure 5.25: Floquet phase diagrams showing inverse participation number (IPN) vs. modulation frequency (in absolute units, left, or dimensionless units Ω, right) and modulation depth A for a $9E_R$ deep lattice. Blue regions indicate regions of phase space where the atoms spread as a function of time. The onset of the $1 \rightarrow 7$ (i-band) transition is visible around 950 kHz.

a lattice to simulate the physics of the classical system (i.e. in a deep lattice where the atoms do not tunnel and quantum mechanics is in some sense 'suppressed'), and then turn on the 'quantum-ness' of the system by either lowering the lattice depth (allowing atoms to tunnel to neighboring lattice sites) or by adding interactions (creating a strongly interacting many body system). In this manner, we propose the ability to study a stability phase diagram by varying the system parameters over a broad range. The "ultrastrong" driven lattice was purpose built for these investigations.

We can use the spatial distribution of the cloud as a measure of its stability over time in the presence of ultrastrong driving. We perform band mapping to project the momentum-space wavefunction onto position space and then calculate the inverse par-

ticipation number (IPN) (a normalized version of the inverse participation ratio "IPR"):

$$\text{IPN} = \frac{\sum_i |\psi_i|^4}{\sum_i |\psi_i|^2} \tag{5.24}$$

which is in some sense a measure of the "peakiness" of the wavefunction. Using this measure, we can analyze how spread the cloud was in momentum-space by imaging them after band mapping. Fig. 5.25 illustrates using IPN as a measure of stability for a system on noninteracting Bosons subject to ultrastrong driving. It not only exhibits an onset of stability at a classically predicted edge, but also shows features indicating the onset of higher band transitions for sufficiently fast and deep modulation. Much of this work is currently ongoing.

Our system gives us the ability to study stability phase diagrams over a very wide range of parameters, including regions where multi-photon transitions to higher bands exist, regions $J \gg U$ (noninteracting systems) or $J \ll U$ (strongly interacting many body systems). We can extend experimental timescales to study the role of prethermalization times[81][82][40], and rates of spreading to study Lyapunov exponents[72][83] and quantum chaos[84] (among others).

5.5.3 Other Ideas

Kapitza crystal: There exists an overlap in the stable regions in the quantum Kapitza pendulum phase diagram for both upward and downward stable points. For a classical system (i.e. a pendulum), the system must decide to point either up or down; while a quantum system such as the one realized here may in fact choose to be both simultaneously. The such a 'Kapitza crystal' might manifest as a spatial halving of the lattice constant (ie. 532 nm $\rightarrow$ 266 nm).

Nonlinear Bloch Oscillations: Our initial attempts to study Bloch oscillations

were motivated by a paper by Driben and Konotop[85], who proposed using an *attractive* nonlinearity (i.e. $a_{\text{scatt}} < 0\ a_0$) to enhance the lifetime of Bloch oscillations. We attempted to observe such an effect in our 1D lattice, but found that our measurement time was limited by the decoherence induced by the overall harmonic potential. Future efforts to remedy or completely cancel this harmonic confinement may lead to a realization of this measurement.

Modulated scattering length: We can modulate the current in the Feshbach coils up to 100 Hz to cause a $\pm 2.5\ a_0$ modulation of the scattering length. It would be relatively easy to study the effects of a scattering length modulation (commensurate or incommensurate) on the Bloch period, or decay time.

Cold atom scanning Fabry-Perot cavity: d- (and higher) band atoms move relativistically in the harmonic potential, with turning points defined by the energy of the excitation and the depth of the harmonic confinement. By changing the field in the curvature coils, we can in principle change the harmonic confinement, and hence the point at which the atoms will "reflect." Modulating or scanning the potential (possible at rates > 100 Hz) in this way would be not unlike changing the length of a cavity with light stored within it. Modulation would pump energy into (or out of) the system.

Edge states: Addition of a blue-detuned beam near the turning points of the lattice potential would give rise to turning points (walls) in space. The Floquet drive would then transport atoms between these two 'edge states' of the system rapidly. Exciting atoms into a relativistic band and then trapping them between blue-detuned walls could also store the excited atoms in the band without having them give up their photon energy on the opposite side of the SHO. Further, changing the position of the walls as a function of time with a spatial light modulator, or bichromatic driving of an AOM (like free space modulated ODTs, but with blue detuned beams, see below), would enable fast modulation of the 'cavity' length.

Quenched lattices: The unique double optical lattice setup we have allows for rapid quenches into and out of very deep lattices in a unique way: we could load atom into one lattice and rapidly invert the optical potential (akin to quickly shifting the lattice over by $\pi/2$) to study quench induced resonant tunneling[86].

Quenched harmonic potential: Initializing the system into a relativistic harmonic oscillator and then diabatically changing the underlying simple harmonic oscillator potential (e.g. by changing the curvature field rapidly) or quenching to a different lattice depth would alter the effective speed of light (possibly the effective mass, not the effective speed of light). This could give rise to the ability to study systems traveling faster than the effective speed of light (Cherenkov radiation?).

Quantum simulation of metamaterials: Floquet band engineering opens the possibility of rapidly changing the band structure to alter the group velocity of the system (as in the case of the RHO). Adding other features to the lattice could locally alter the band structure, allowing alteration of the phase velocity separately from the group velocity. If possible, independently engineering the group and phase velocity would give rise to the quantum simulation of metamaterials.

Modulated optical potential: The double lattice also lets us quench into or out of a lattice while maintaining a constant optical potential, or change the lattice depth without changing the overall optical confinement. Such proposals have been the subject of theoretical study[86].

Solitons seeded from a lattice: Tuning the scattering length to be slightly negative induces the creation of solitons: wave packets that travel without dispersion in a waveguide. Seeding solitons from a lattice (with a well defined phase difference between neighboring solitons) would be an interesting avenue of study, compared to the current method of randomly seeding solitons from a modulational instability[87][88]. The greatest difficulty will be resolving the solitons from one another in our system, as the increased

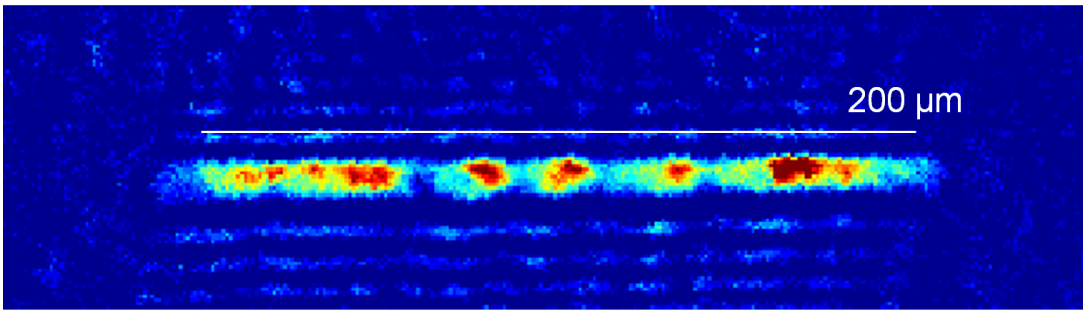

Figure 5.26: Solitons created by quenching the scattering length $a < 0$.

optical confinement will naturally cause them to be close together (perhaps closer than the resolution limit of the current imaging system).

Modulated free space ODTs: Our experiment is atypical in the sense that our ODT beams are free space coupled into the chamber. Specifically, they pass through AOMs without later being fiber coupled. This means that their spatial position is strongly dependent on the frequency of the RF applied to the AOM (as the RF changes the angular deflection of the beam as it passes through). The AOMs that control the power of the ODT beams therefore also control the position of the beams before the enter the chamber. Slight changes to the frequency of the AOM can cause hundreds of microns worth of deflection in the beam in a precisely controllable way. In fact, some experiments[89] use 2D AOMs to create painted potentials using attractive beams. Our AOM driver architecture allows easy control over the frequency applied to the AOMs at tens of kHz time scales (faster than the transverse ODT frequencies). Applying a time-varying voltage to the VCO will create a spread out optical trap (sine, triangle wave), or can in fact split the beam into separate regions of space entirely (bichromatic driving by a square wave voltage modulation). It would be straightforward to use modulated optical lattices to apply time-varying optical potentials to a BEC or atoms loaded into a lattice to realize ring-type traps, or line-type traps at arbitrary angles. Further, applying the modulated ODTs could enable the study of the interaction of 'relativistic' atoms interacting with

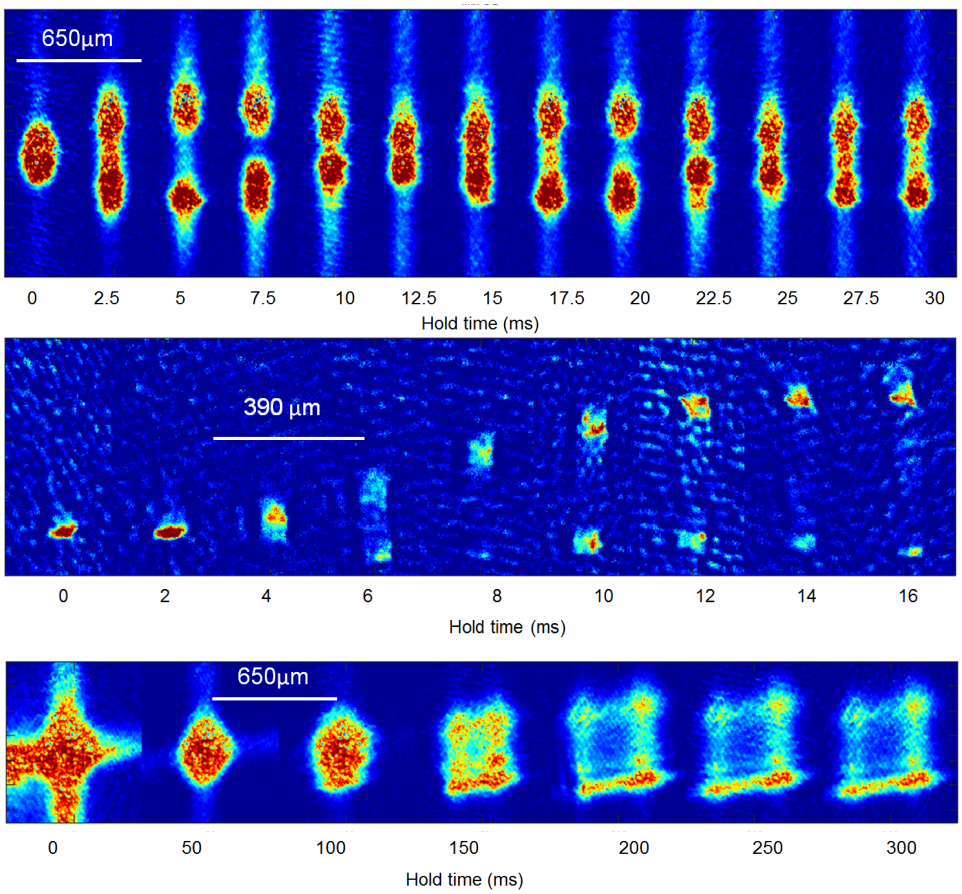

Figure 5.27: Some examples of splitting traps with frequency modulated ODTs. Top: splitting an ODT with square-wave modulation (bichromatic RF). Middle: splitting a BEC, also with a bichromatic drive. Bottom: double modulation creating a nearly-square potential by gradually ramping on a triangle-wave modulation.

point-like defects in the lattice time-disordered potentials (not unlike [90], but with a excited atoms).

5.6 Conclusion

In summary, we've built an incredibly flexible quantum simulator. We've made measurements of long-range pure Bloch oscillations in real space. We've made the first experimental realization of a massive relativistic harmonic oscillator. We've demonstrated

a powerful scheme for engineering band structure and used it to realize a method of controlled, long-range quantum coherent transport. Direct engineering of Floquet-hybridized bands can realize a class of systems that have not existed up to this point. The future possibilities for studying strongly driven systems are vast and exciting.

Appendix A

Properties of 7Li

Here is a brief summary of some properties and constants that are useful to know when making a lithium experiment.

Physical and atomic properties of lithium:

Property	**Value**
Density	0.534 g/cm^3
Melting Point	453.65 K
Heat of Fusion	3.00 kJ/mol
Boiling Point	1603 K
Heat of Vaporization	136 kJ/mol

Table A.1: Selected physical properties of ^{7}Li

Property	**Symbol**	**Value**
Atomic Number	Z	3
Nucleons	Z+N	7
Natural Abundance		92.5%
Nuclear Lifetime	τ_n	Stable
Atomic Mass	m	7.016 u
Total Electronic Spin	S	1/2
Total Nuclear Spin	I	3/2

Table A.2: Selected atomic properties of ^{7}Li

Properties of Optical Transitions in lithium

Name	Transition	Wavelength	Linewidth (MHz)	Lifetime (ns)
D1	$2S_{1/2} \rightarrow 2P_{1/2}$	670.977 nm	5.87139	27.1
D2	$2S_{1/2} \rightarrow 2P_{3/2}$	670.975 nm	5.87123	27.1
UV	$2S_{1/2} \rightarrow 3S_{1/2}$	323 nm	0.15947	998

Table A.3: Selected optical transitions in ^{7}Li

Quantity	Symbol	Value
Saturation Intensity	I_s	2.56 mW/cm^2
Absorption cross-section	σ	2.15E-9 cm^{-2}
Doppler Temperature	T_{Doppler}	140 μK
Doppler Velocity	v_{Doppler}	41 cm/s
Recoil Temperature (671 nm)	T_r	6.06 μK
Recoil Velocity (671 nm)	v_r	83.9 cm/s
Recoil Energy (1064 nm)	E_R	24.869 kHz
Recoil Velocity (1064 nm)	v_R	52.9 cm/s

Table A.4: Useful calculated values

Appendix B

Laser Table Layout

It's on the next page!

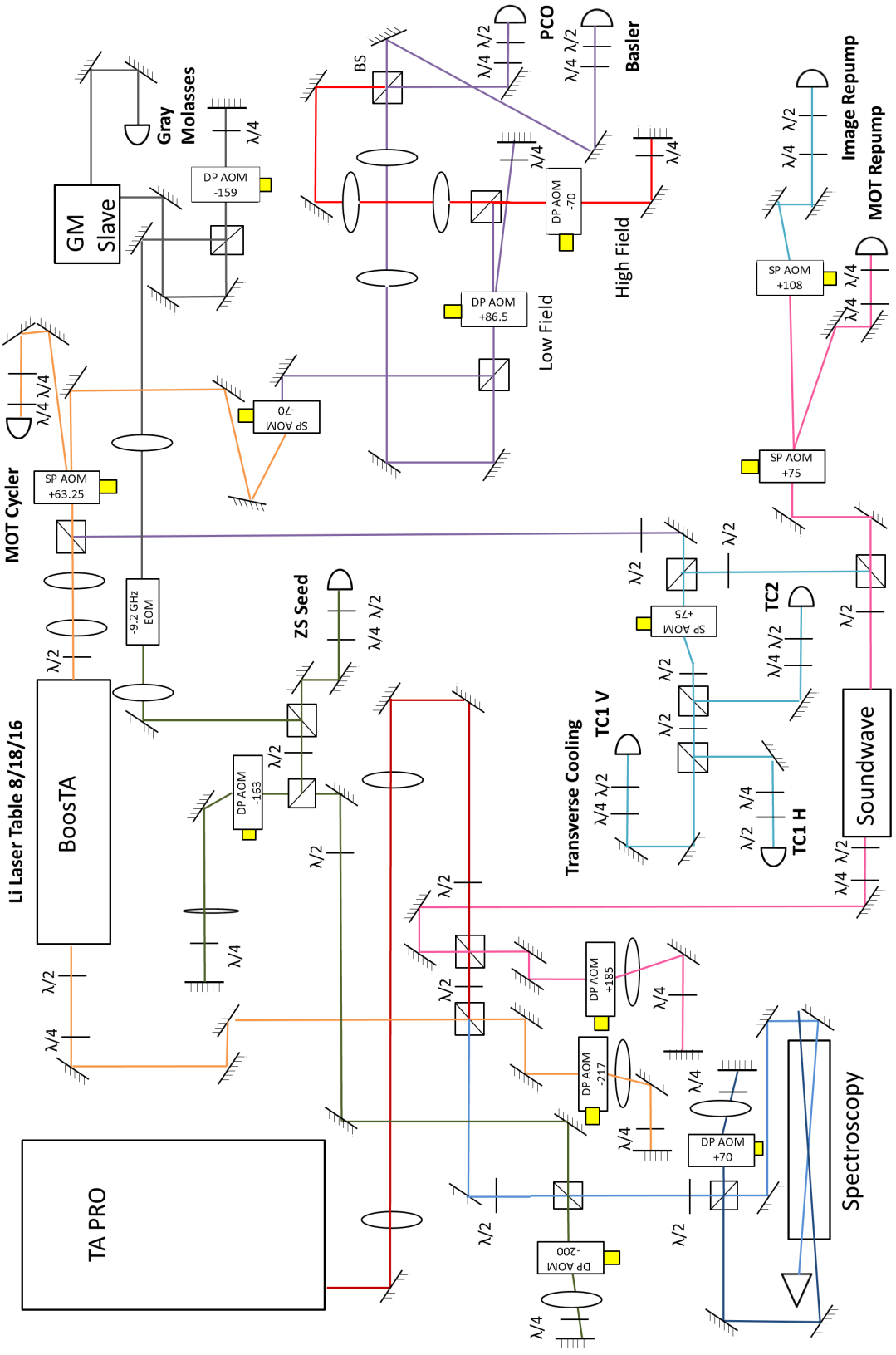

Figure B.1: Schematic layout of the Lithium Laser Table.

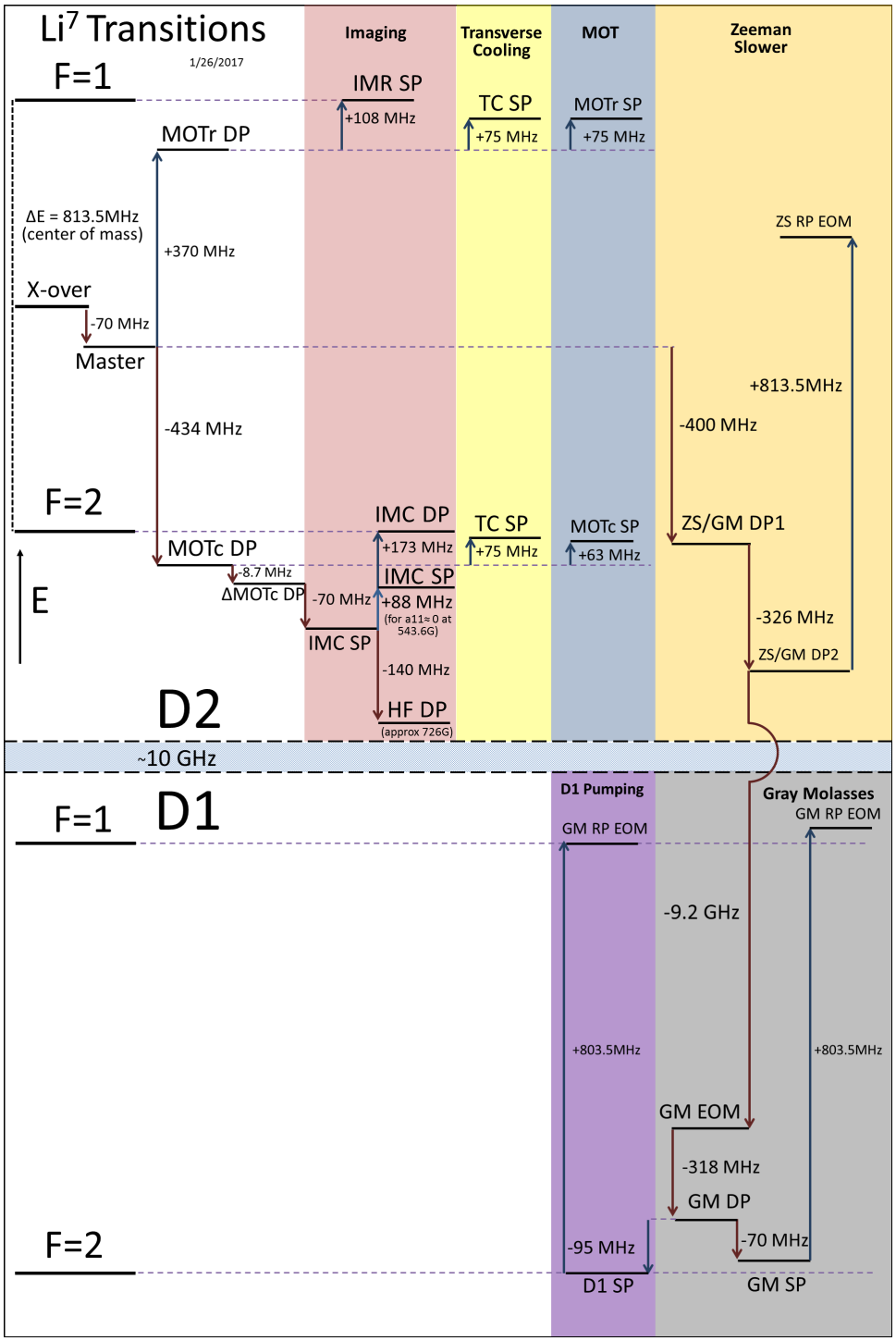

Figure B.2: Energy space diagram of our laser system.

Appendix C

Mechanical Drawings

Drawing
3D Printable Stepper Motor Shutter Mount
3D Printable Ribbon Antenna Mount
Vapor Cell Assembly
Newport 9066 Stage Foot
Baser ace Mounting Plate
AOM to KM100PM Mounting Plate
3/0 (000) Crimp Lug to 1/4" tube adapter
Slower Support (top)
Slower Support (bottom)
Slower Winding Plate
MOT Winding Mandrel
Li Top Breadboard
Li Side Breadboard
Li Back Breadboard
Li Main Chamber
Li Bucket Window

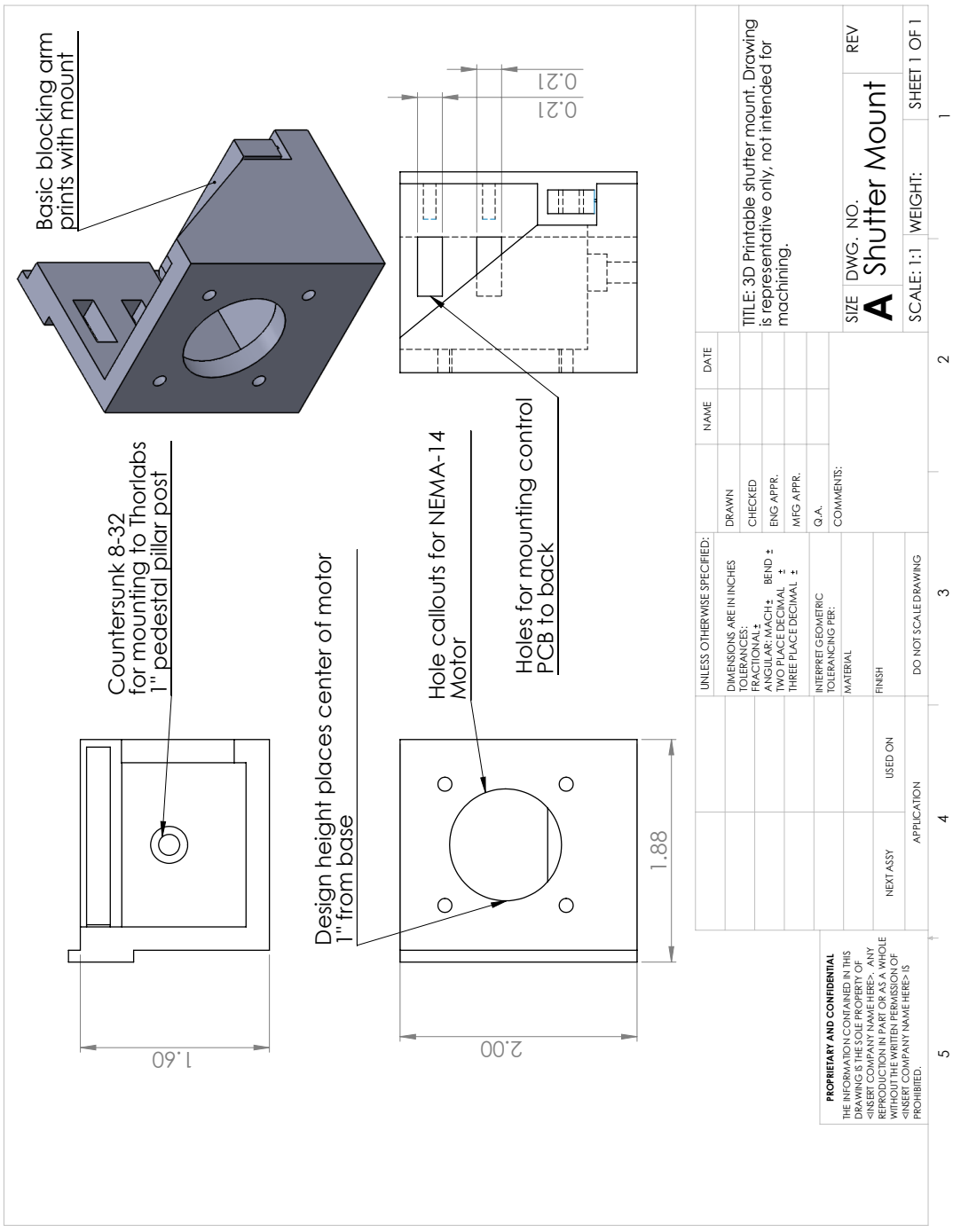

Figure C.1: 3D printable mount for the stepper motor beam shutters.

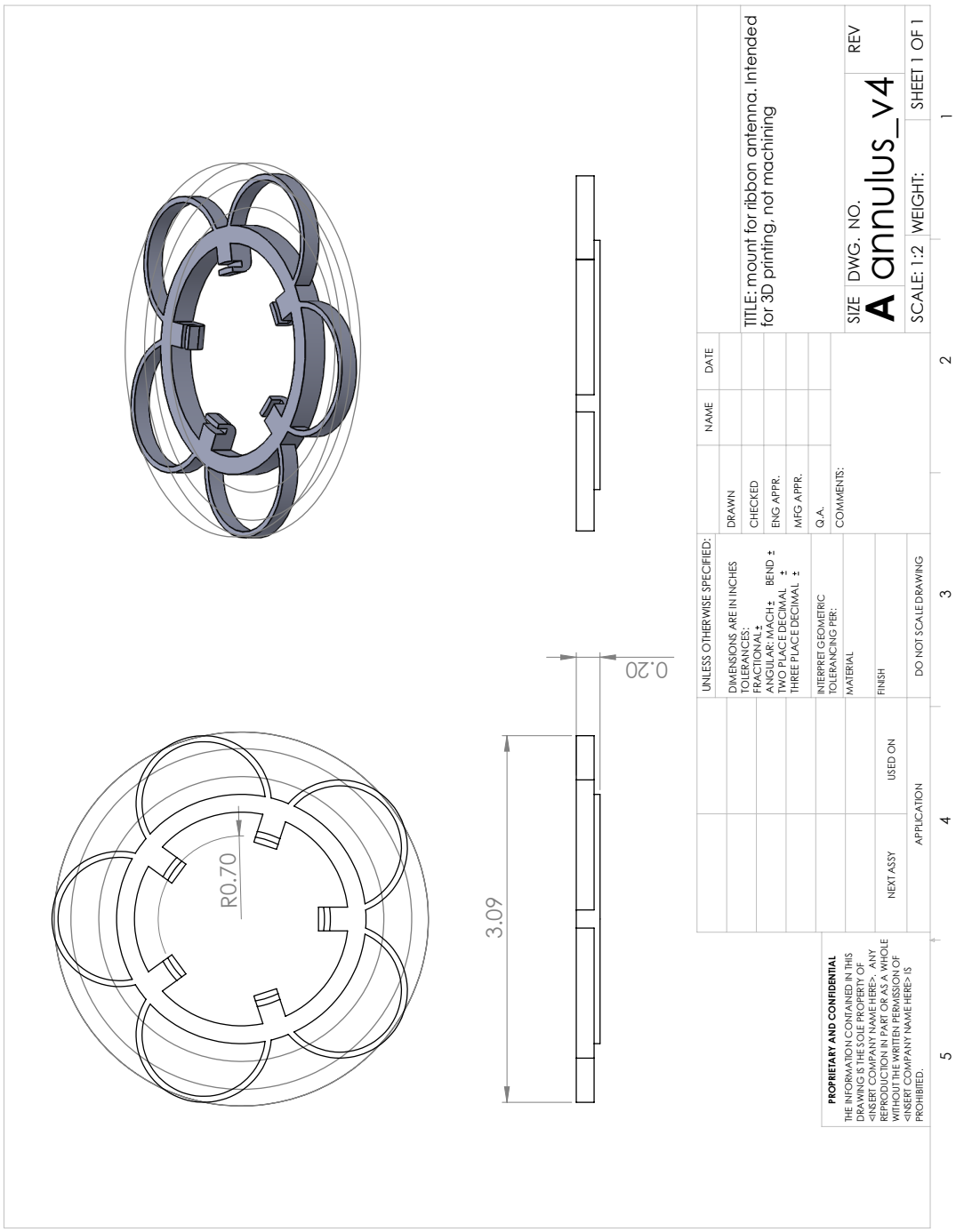

Figure C.2: 3D printable mount for ribbon antenna for RF evaporation.

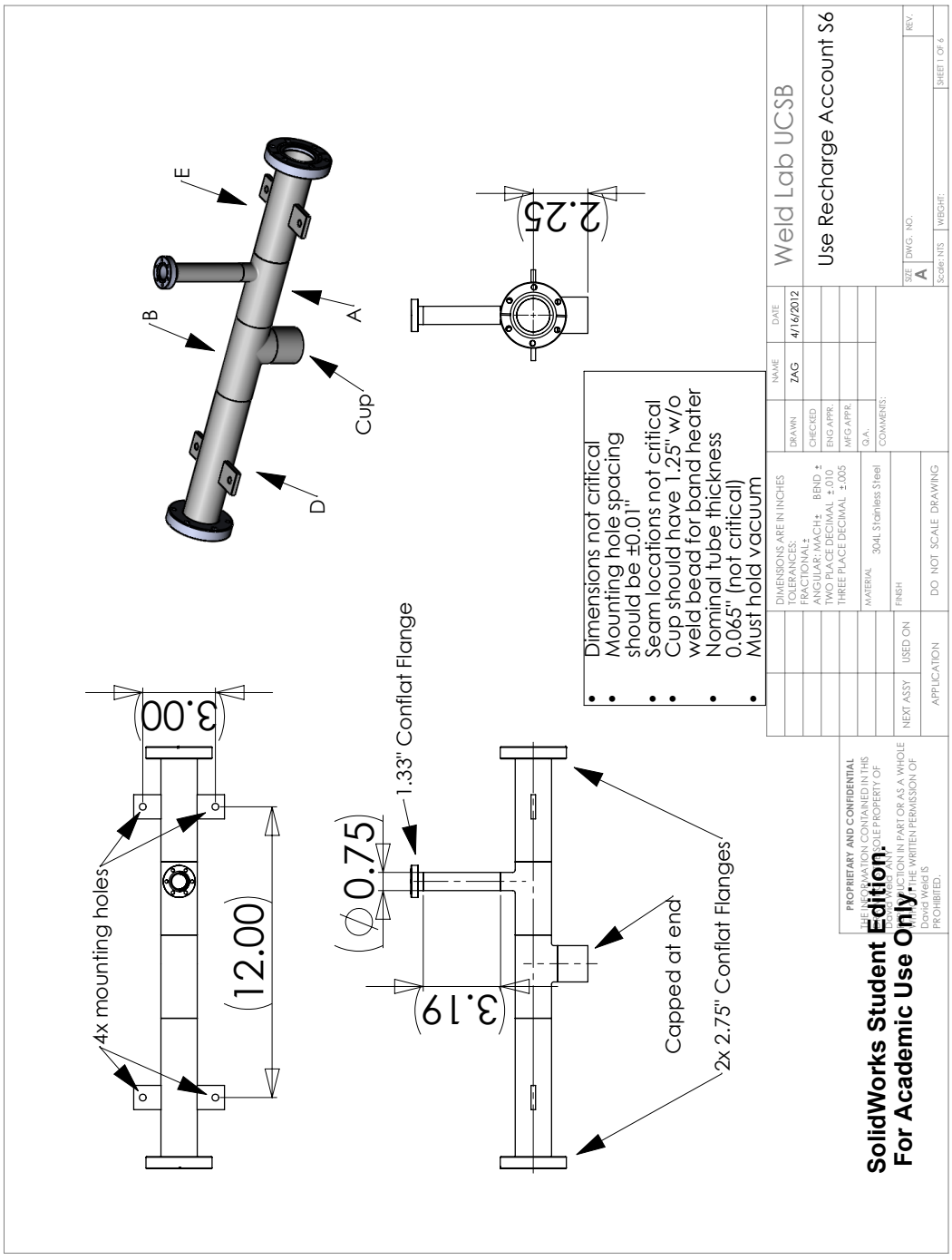

Figure C.3: Mechanical drawing of the lithium vapor cell used for saturation absorption spectroscopy.

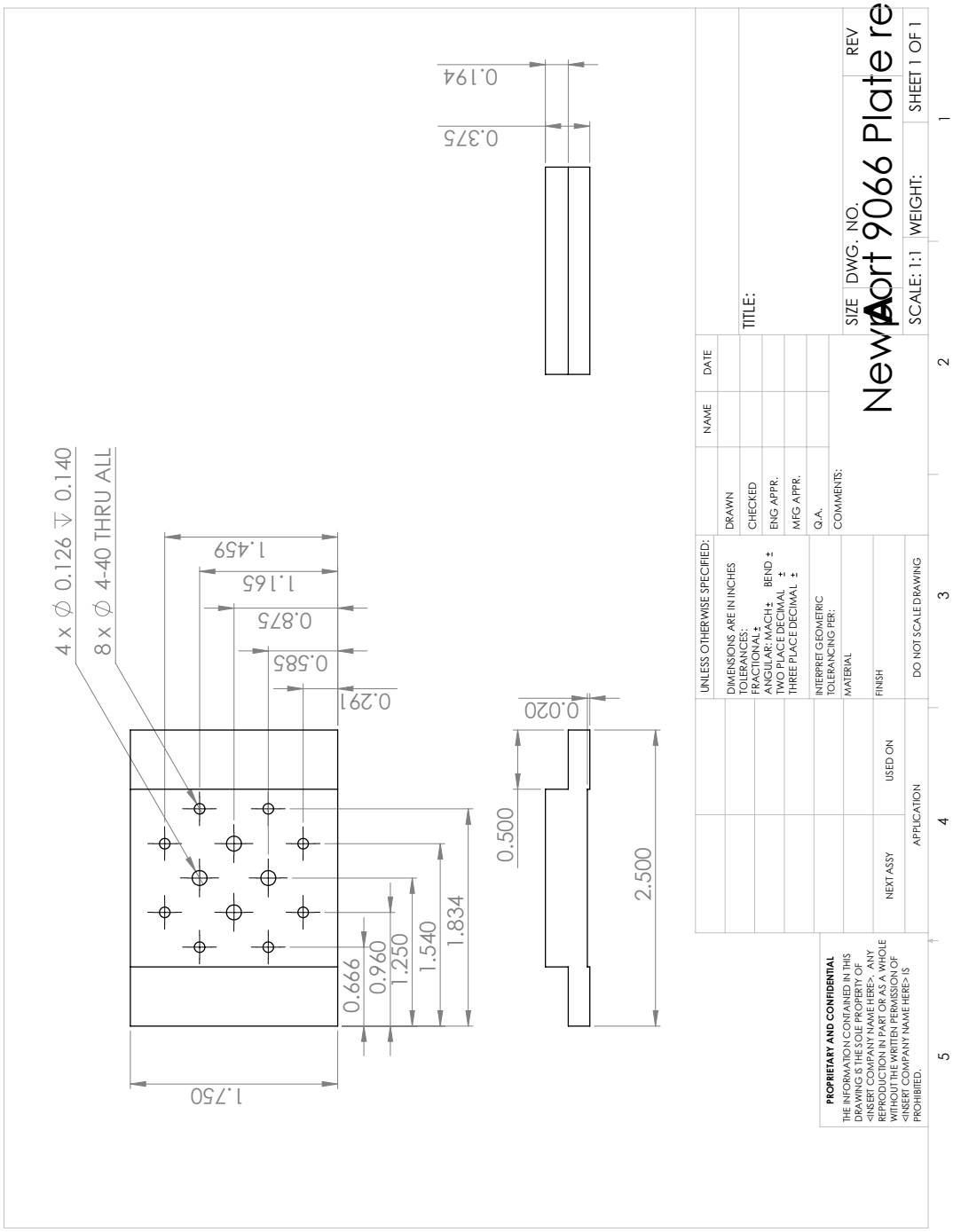

Figure C.4: Base for Newport 9066 stage designed to be clamped to optical table.

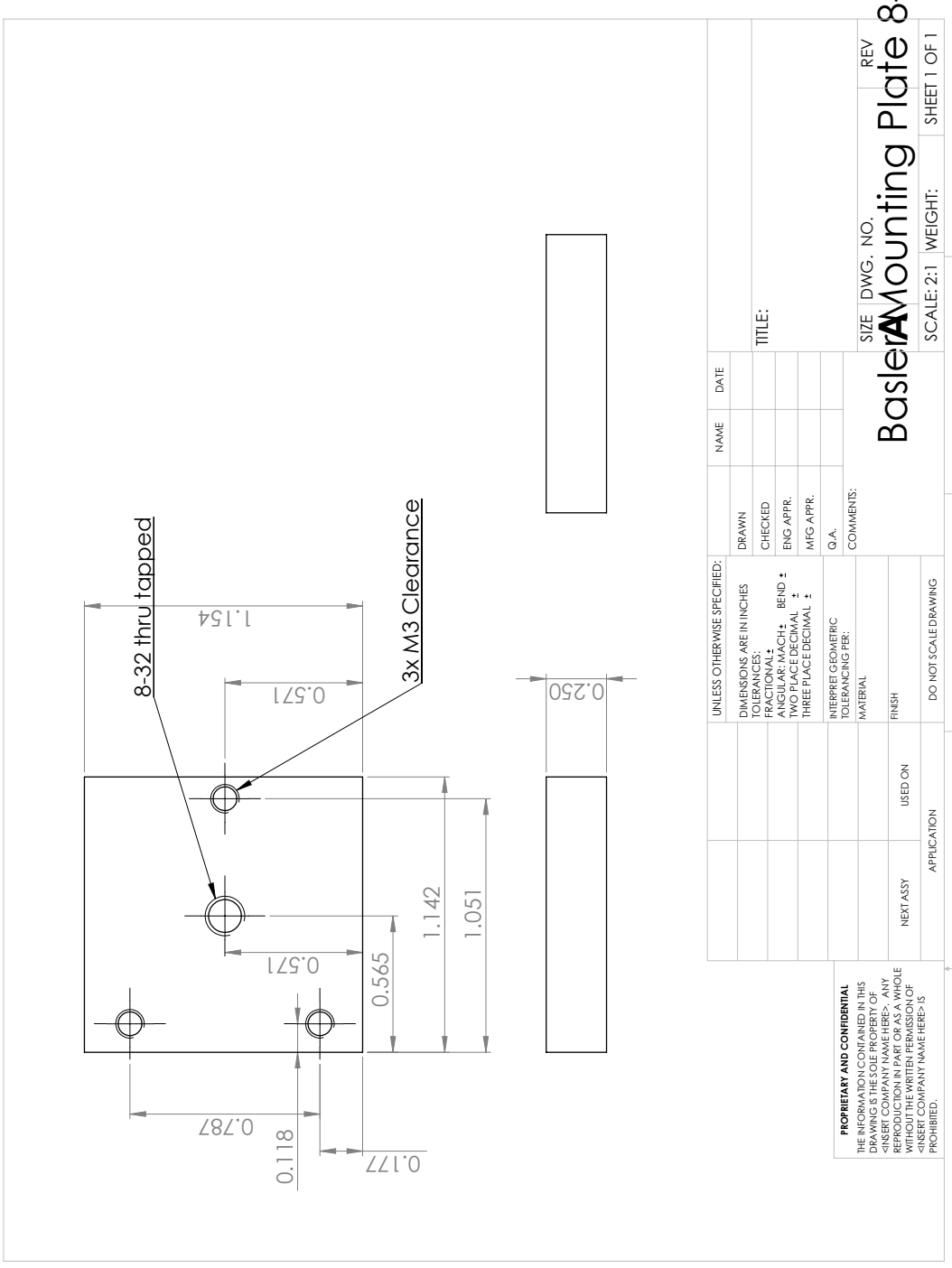

Figure C.5: Base for mounting Basler cameras to 8-32 hardware (e.g. 1/2" optical post).

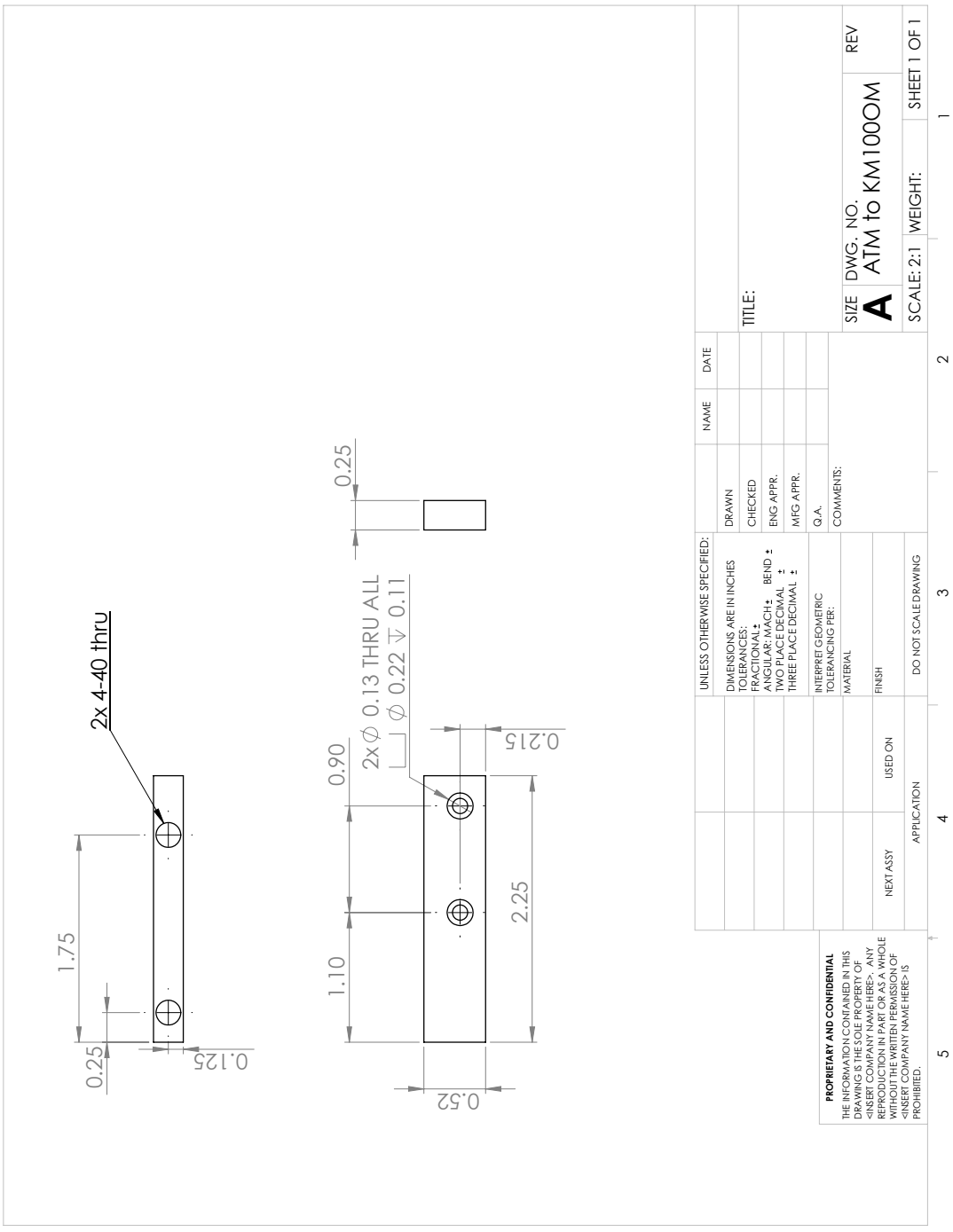

Figure C.6: Base for mounting IntraAction AOMs to Thorlabs KM100PM kinematic mounts).

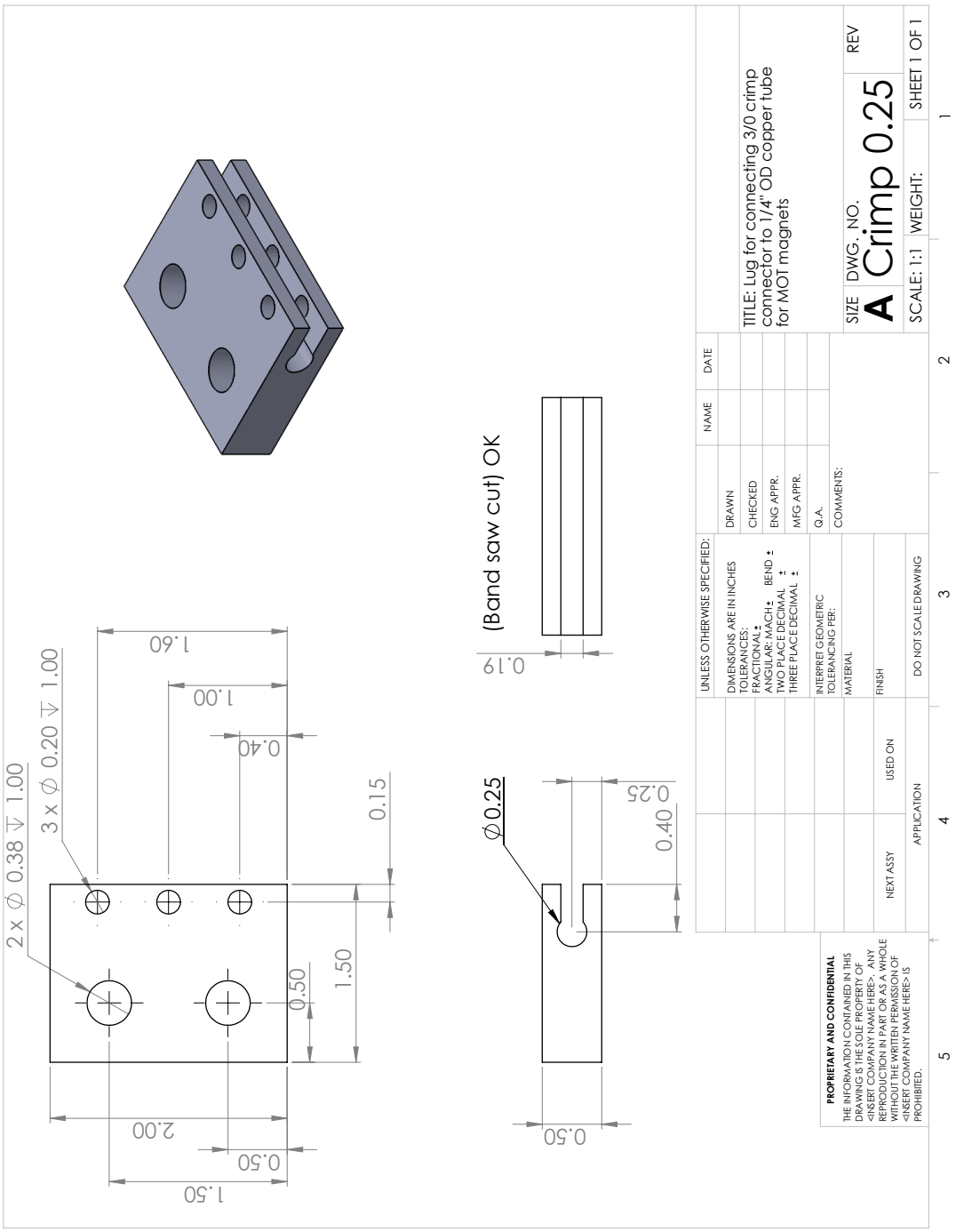

Figure C.7: Lug for connecting 3/0 copper wire to the MOT magnets.

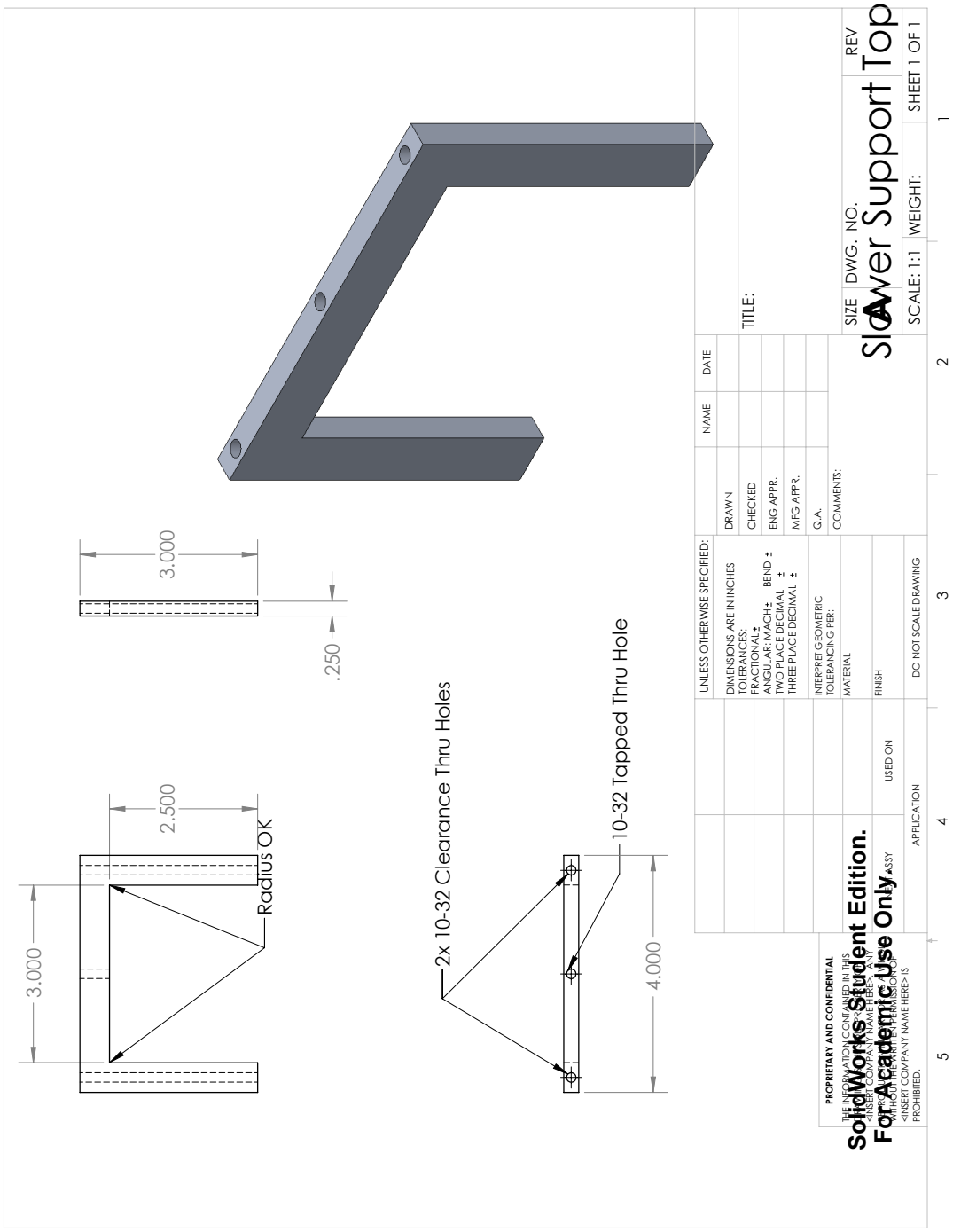

Figure C.8: Top mounting for Zeeman slower.

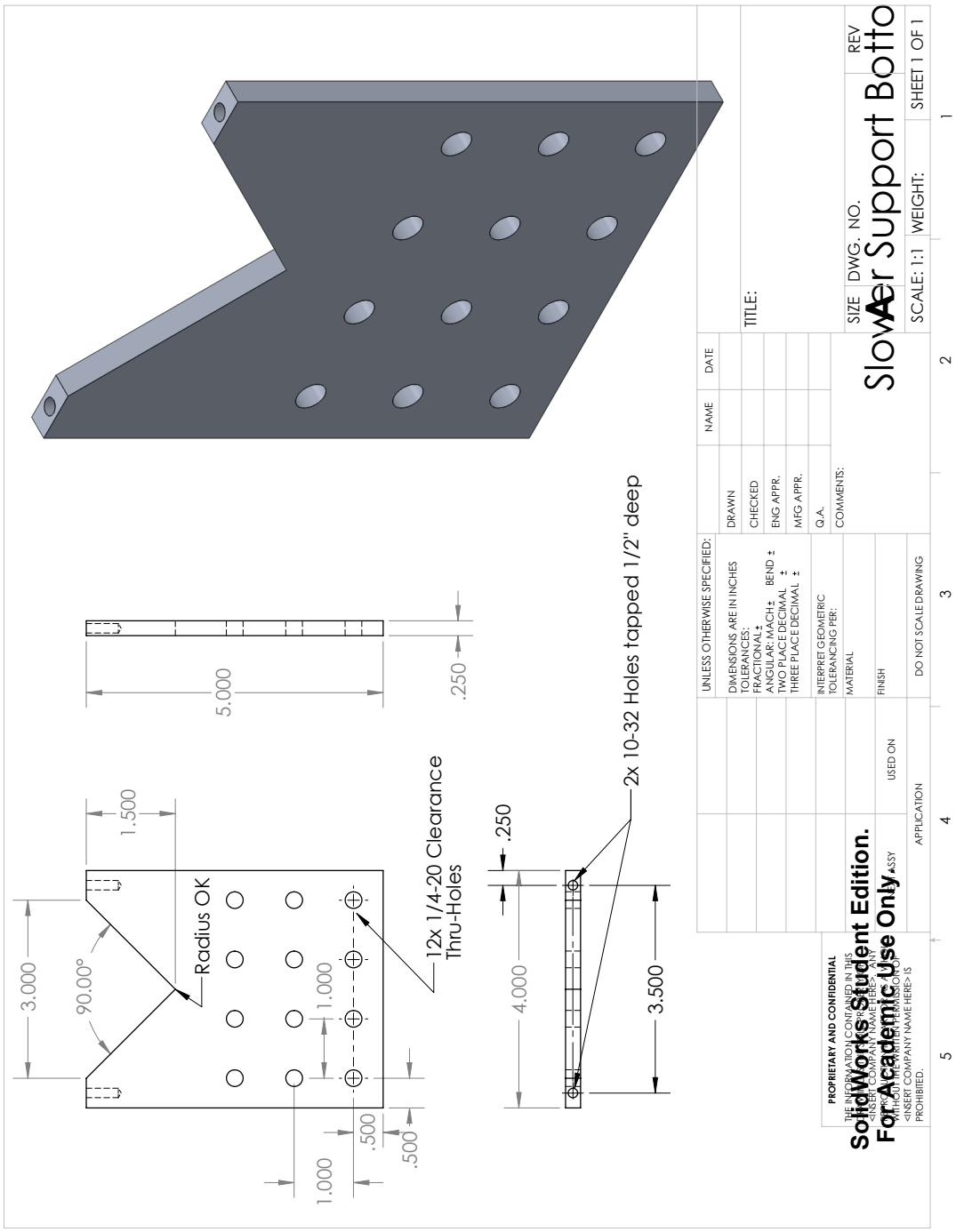

Figure C.9: Bottom mounting for Zeeman slower.

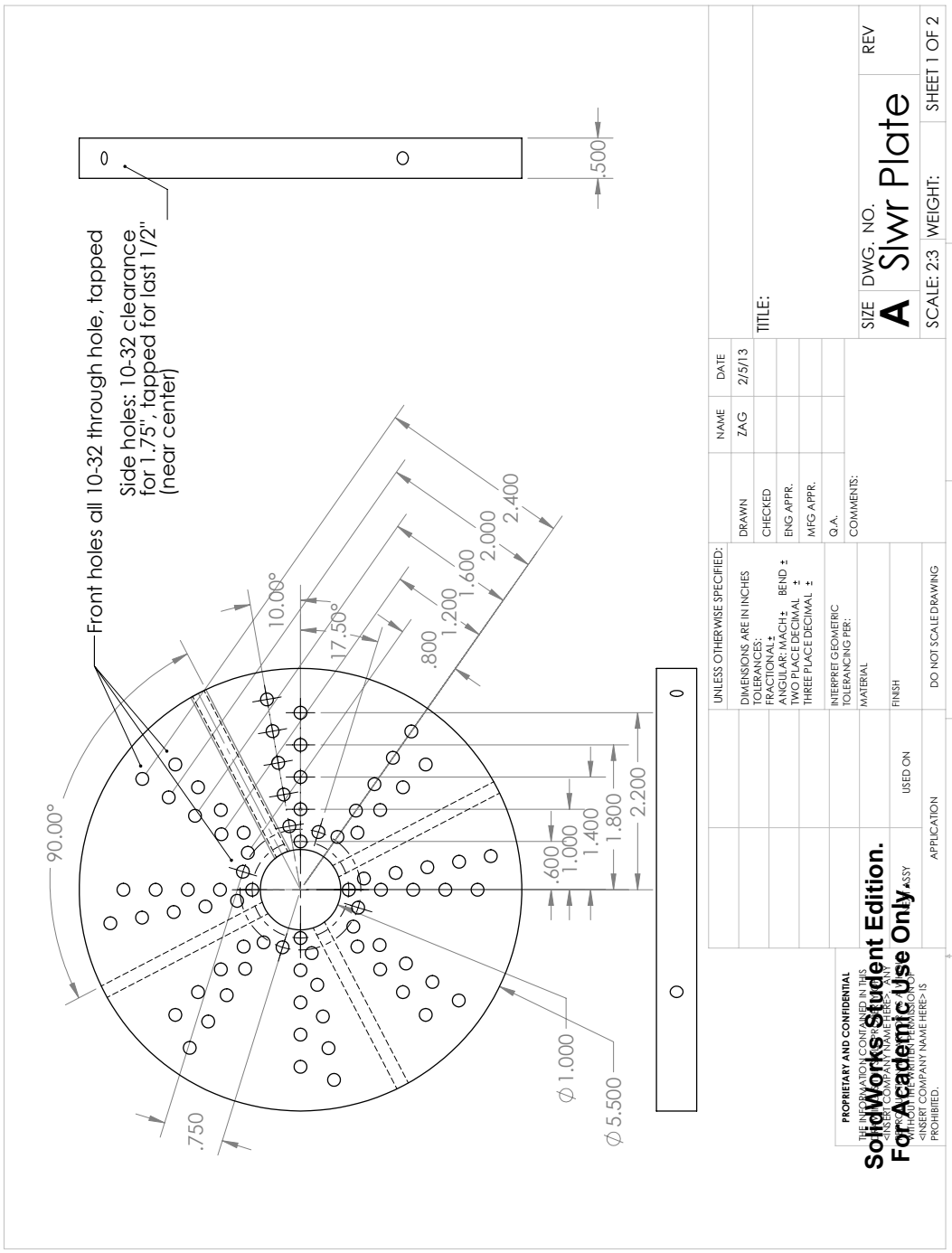

Figure C.10: Anchor plate used for winding the Zeeman slower. Credit: Max Garber

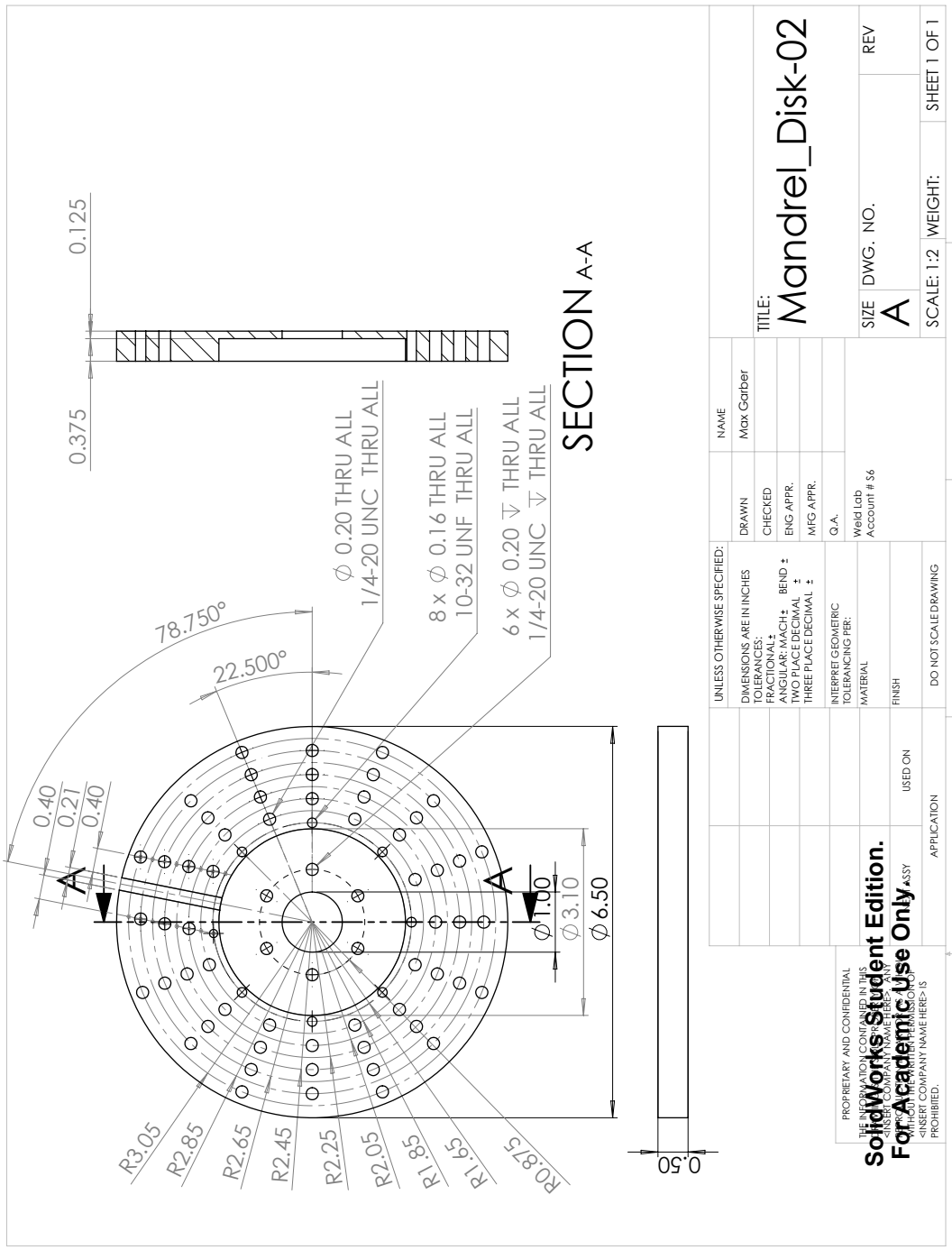

Figure C.11: Plate used for MOT magnet winding. Credit: Max Garber

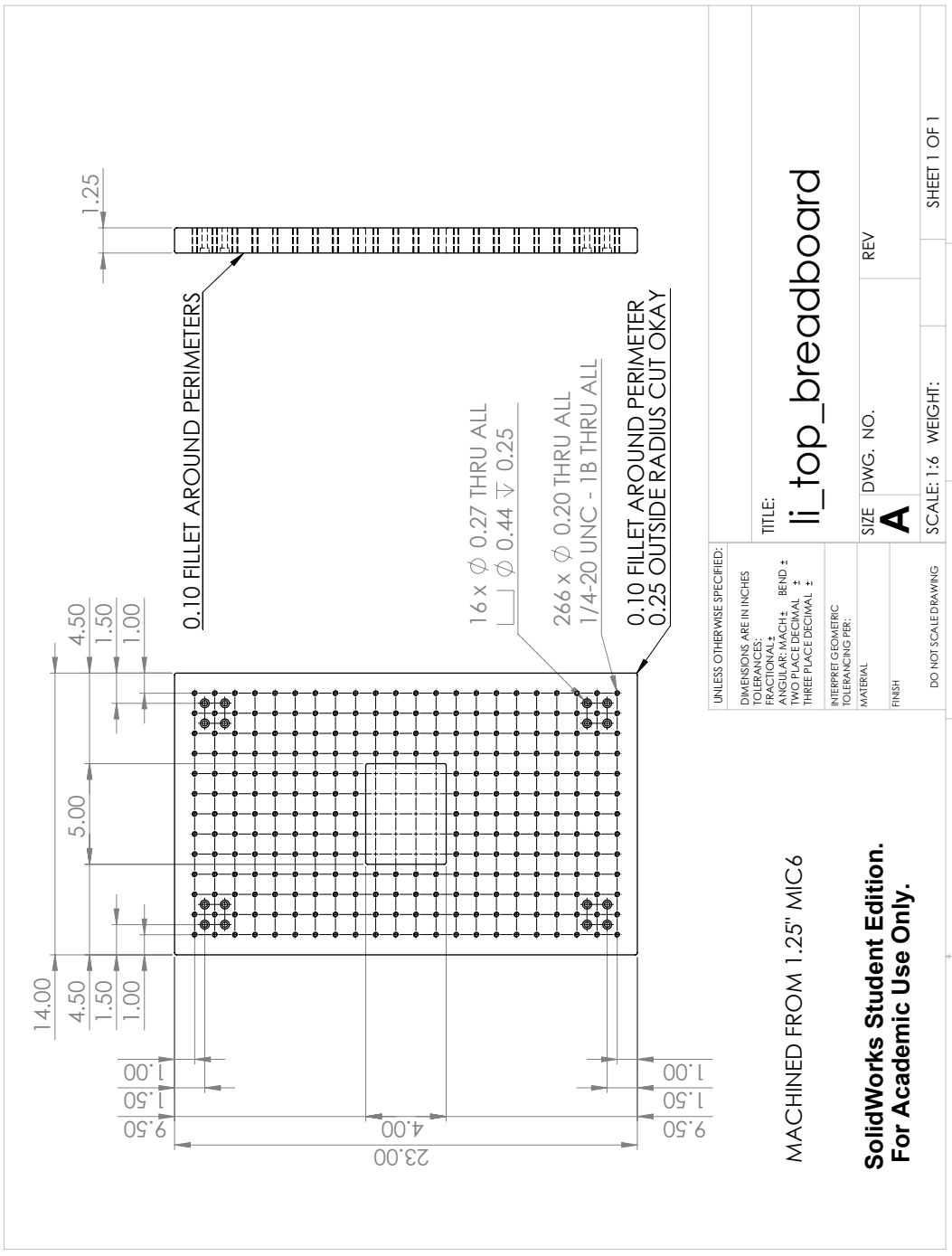

Figure C.12: Main chamber top breadboard. Credit: Shankari Rajagopal

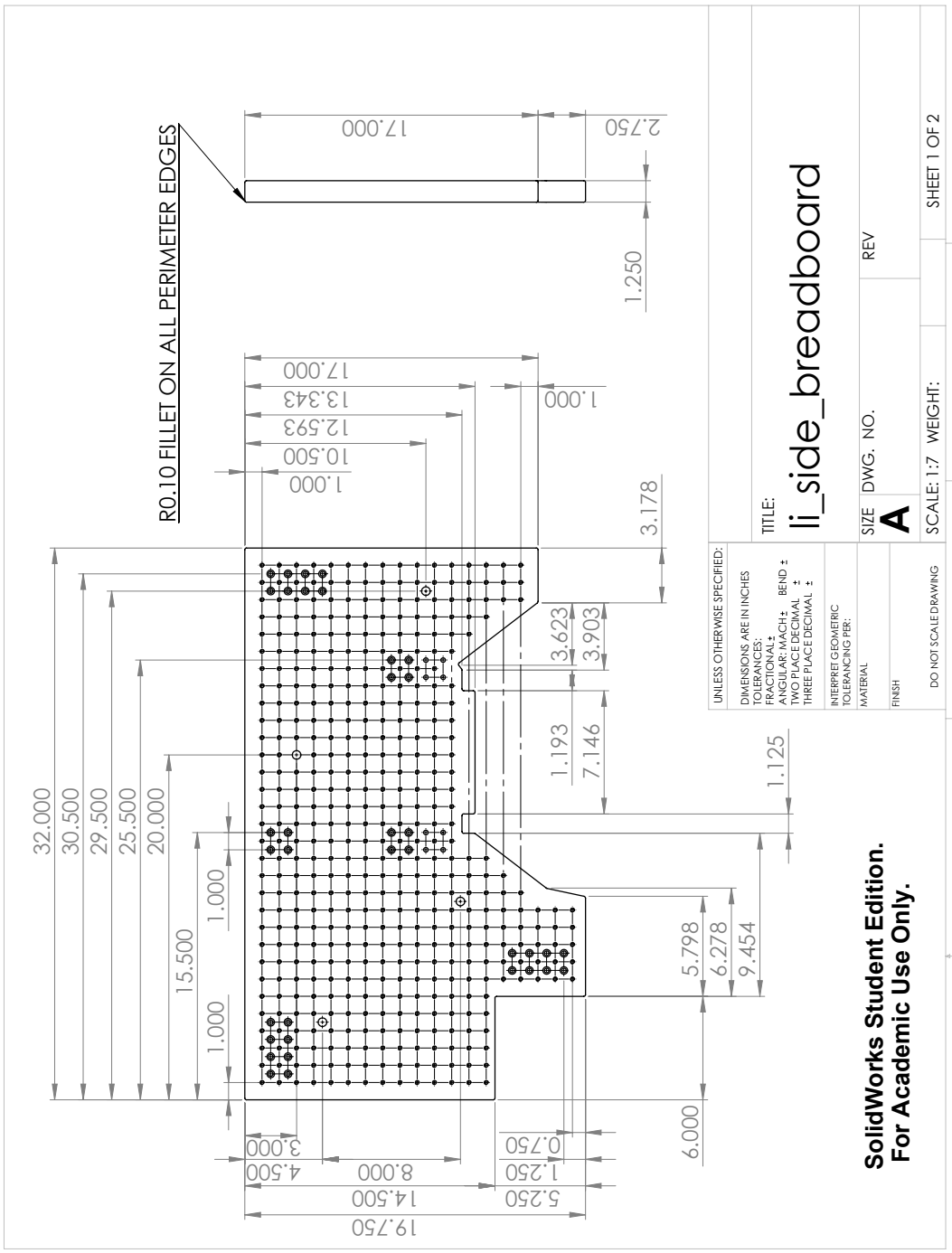

Figure C.13: Main chamber side breadboard. Credit: Shankari Rajagopal

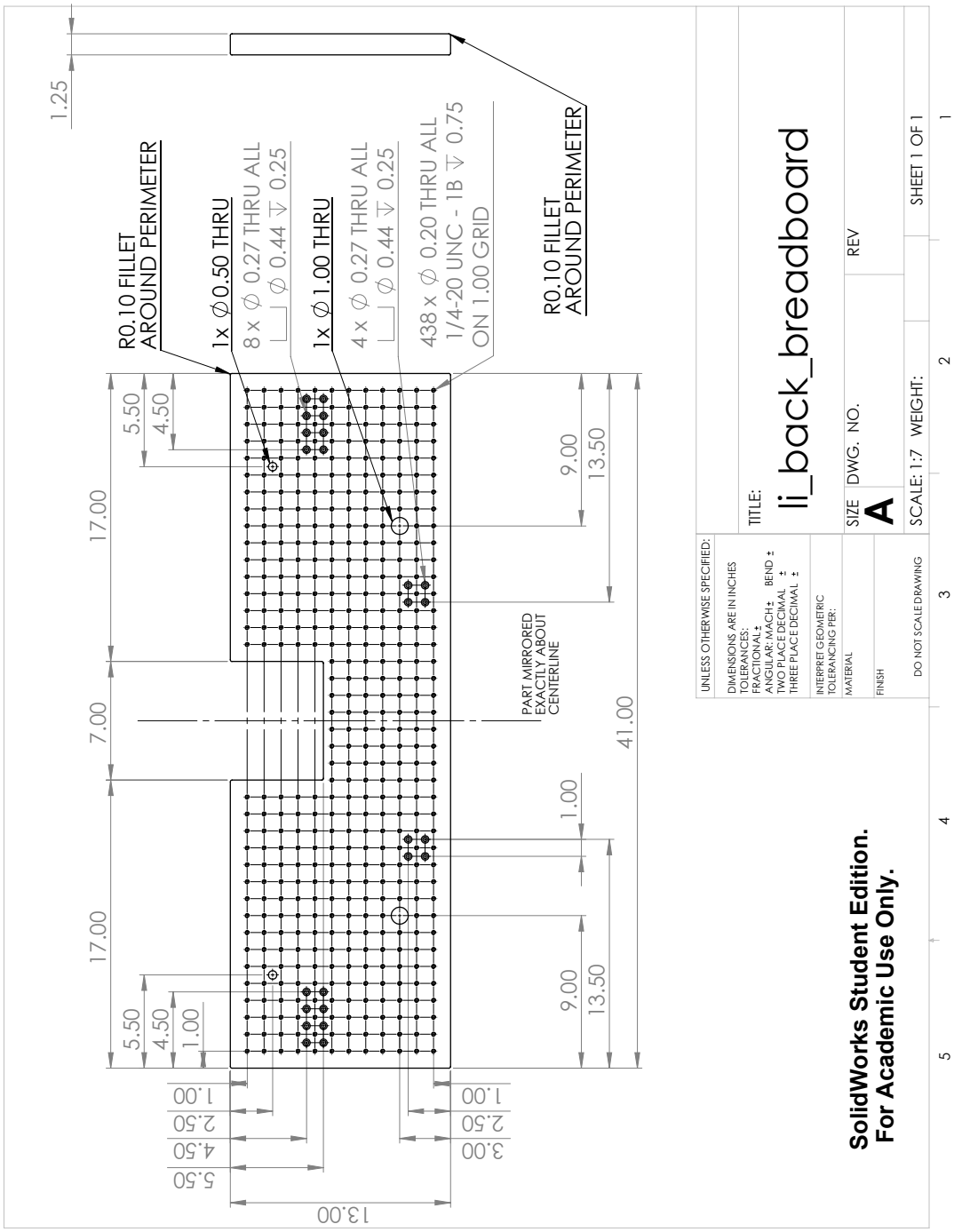

Figure C.14: Main chamber back breadboard. Credit: Shankari Rajagopal

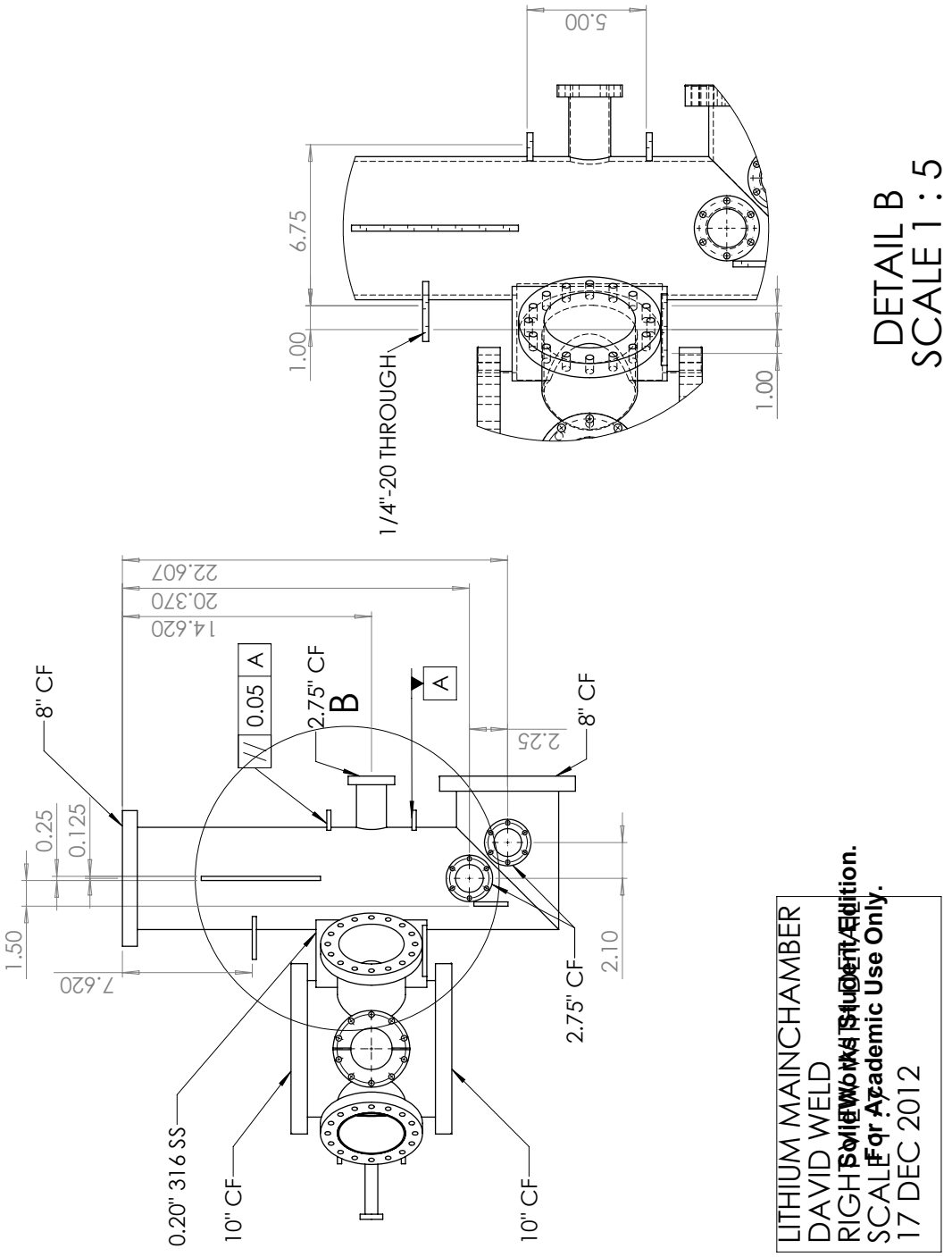

Figure C.15: Lithium main chamber. Credit: Shankari Rajagopal

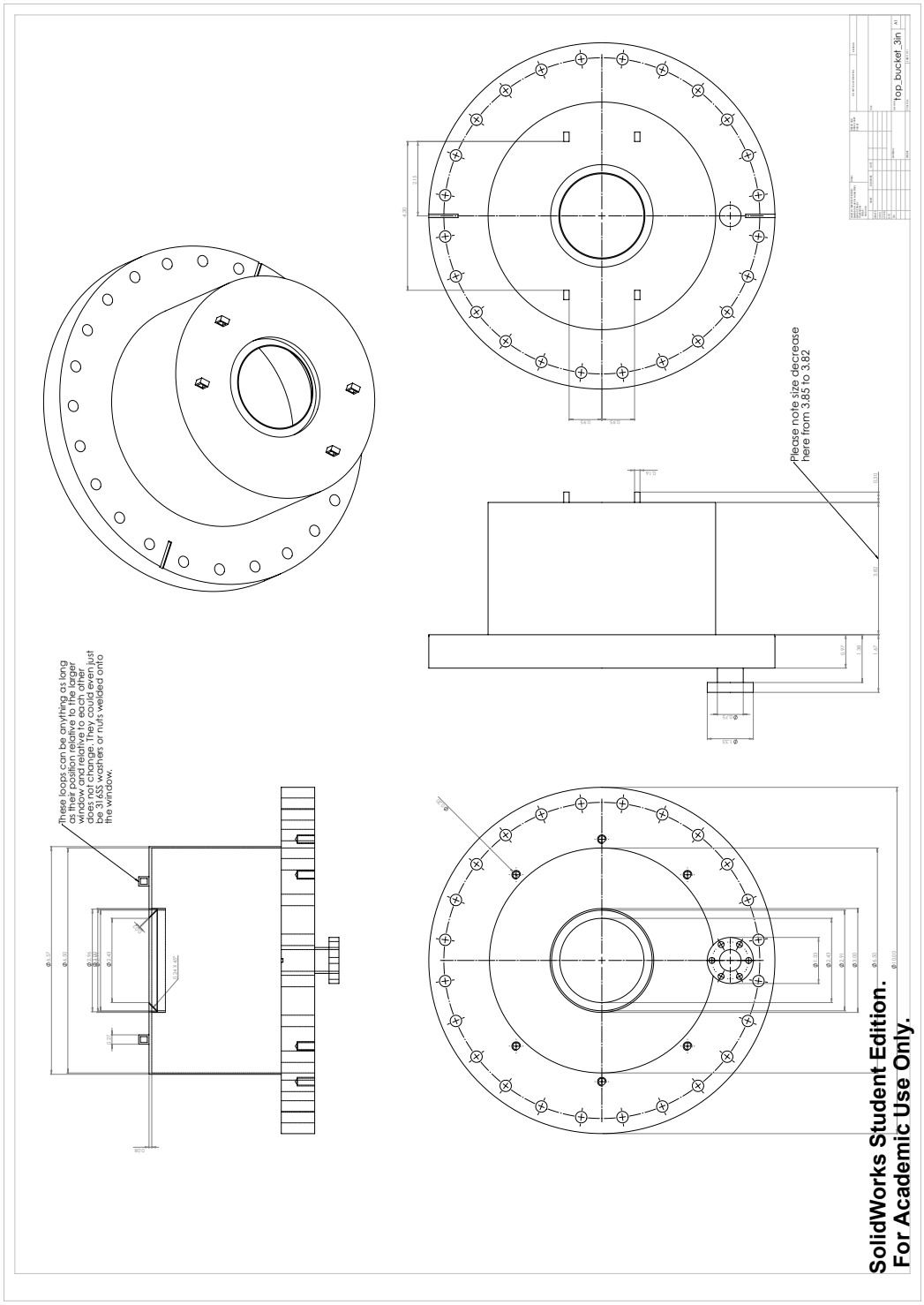

Figure C.16: Lithium bucket window. Credit: Shankari Rajagopal/UKAEA

Appendix D

Optical Shutter Arduino Code

Here is the Arduino code we use to run our optical shutters. The Arduino checks a trigger input pin and generates a pulse train to drive the stepper motor through a fixed number of degrees before putting the motor to sleep to prevent overheating.

```
// motorButtonTriggerFast.ino
#include <avr/power.h>
#define SWITCH 0
#define RESET 1
#define SLEEP 2
#define STEP 3
#define DIR 4
int waitTime = 600; // sets the rate of steps 600 for flag, 2700 for mirror
int timer = 3000000; //length of time to wait before making the motor sleep
int timeNow = 0;
int numSteps = 11; // determines how many steps (what angle), 11 for flag (20
    degrees), 52 for mirror (90 degrees)
```

```
void setup() {
  // set clock to 16MHz
  if (F_CPU == 16000000) clock_prescale_set(clock_div_1);
  // initialize pins
  pinMode(SWITCH, INPUT);
  pinMode(RESET, OUTPUT);
  pinMode(SLEEP, OUTPUT);
  pinMode(STEP, OUTPUT);
  pinMode(DIR, OUTPUT);
  // pullup the SWITCH PIN
  digitalWrite(SWITCH, HIGH);
  // set direction of motor
  digitalWrite(DIR, HIGH);
  // set SLEEP pin to LOW (disable motor)
  digitalWrite(SLEEP, LOW);
  // set RESET pin HIGH (allow rotation)
  digitalWrite(RESET, HIGH);
}
void stepHI(){
   digitalWrite(SLEEP, HIGH); // enable the motor
   digitalWrite(DIR, HIGH); // set the direction to be CW
   delay(2);                // wait 1 ms to allow charge pump to stabilize
   for (int x = 0; x < numSteps; x++) {
      digitalWrite(STEP, HIGH); // ...and step the motor
      //delay(1);
      delayMicroseconds(waitTime);
      digitalWrite(STEP, LOW);
```

```
      delayMicroseconds(waitTime);
   }
}
void stepLO(){
   digitalWrite(SLEEP, HIGH); // enable the motor
   digitalWrite(DIR, LOW); // set the direction to be CCW
   delay(2);               // wait 1ms to allow charge pump to stabilize
   for (int x = 0; x < numSteps; x++) {
      digitalWrite(STEP, HIGH); // ...and step the motor
      delayMicroseconds(waitTime);
      digitalWrite(STEP, LOW);
      delayMicroseconds(waitTime);
   }
}
void loop() {
  if (! digitalRead(SWITCH)) { // if the button is HI
    stepHI();
    while(! digitalRead(SWITCH)){ // while the button is HI
      timeNow = timeNow + 1;
      if(timeNow==timer){ //count down to disable the motor
        digitalWrite(SLEEP, LOW); // disable the motor (prevents overheating)
        }
      }
    timeNow = 0; //reset the timer
    stepLO(); //otherwise switch the motor ASAP
    while(digitalRead(SWITCH)){ // while the button is LOW
      timeNow = timeNow + 1;
```

```
      if(timeNow==timer){ //count down to disable the motor
        digitalWrite(SLEEP, LOW); // disable the motor (prevents overheating)
        }
      }
    timeNow = 0; //reset the timer
    }
}
```

Appendix E

Troubleshooting

Or: what to do when your machine (f)ails you.

Problem	**Possible Cause/Solution**
No MOT	Laser unlocked, HBRIDGE disabled, oven cold
Bad MOT (low final N)	Check power, check polarization
Slow MOT load	MOT Polarization Check ZS power, TC1&2 power
Tiny MOT	Check E-W mirrors, check beam alignment
No BEC	Plug beam out of alignment, check RF evap
Low atom numbers (general)	Ensure MOT is loading at field zero
Hot magnetic trap	GM power, alignment CMOT intensity balance
Low mag trap N	Check earth shims, plug alignment
No imaging light	Check AOMs, make sure no card is blocking
Stray spectroscopy signals	Stray back reflections blocked AOM, multimode master
No high current lock point ($>$ 113mW)	Lock at lower current (105mW)
ODTs/Lattice moving	Stray air currents, voltage noise on VCO
ESS/Genesys currents drooping	Bad lug, check 3/0 lines for heating
Slave laser won't lock	Low seed ($<$200 μW), EOM off (GM), bad diode
Low master power ($<$280 mW)	Master seeding bad
Low MOTc power	BoosTA coupling, 2:6 fiber splitter coupling
Low MOTr power	Soundwave coupling, 2:6 fiber splitter coupling
Vacuum levels rising	Fire the Ti-sub pump
Images out of sync	PCO skipped a day, reset; resync PC clocks
Run finished out of sync	1μs timing bug, avoid timesteps $\pm$1μs (e.g. 9/11)
ODT PD Levels High	Check beam paths, you probably melted a Basler
MATLAB problems	Call Kurt
Morale problems	Call Kevin
Girl problems	I feel bad for you, son.

Bibliography

[1] C. Foot, *Atomic Physics*. Oxford University Press, New York, first ed., 2005.

[2] D. G. Claude Cohen-Tannoudji, *Advances in atomic physics: an overview*. World Scientific Publishing, Singapore, first ed., 2011.

[3] H. Friedrich, *Theoretical Atomic Physics*. Springer, New York, third ed., 2006.

[4] H. S. C. J.Pethick, *Bose-Einstein Condensation in Dilute Gases*. Cambridge University Press, New York, second ed., 2008.

[5] W. Ketterle, D. S. Durfee, and D. M. Stamper-Kurn, *Making, probing and understanding Bose-Einstein condensates*, 9904034.

[6] K. Strecker, *Tunable Interaction in Quantum Degenerate Lithium*. PhD thesis, Rice University, 2004.

[7] D. A. Steck, *Observation of Chaos-Assisted Tunneling Between Islands of Stability*, *Science* **293** (jul, 2001) 274–278.

[8] S. Inouye, M. R. Andrews, J. Stenger, H. J. Mlesner, D. M. Stamper-Kurn, and W. Ketterle, *Observation of Feshbach resonances in a Bose-Einstein condensate*, *Nature* **392** (1998), no. 6672 151–154.

[9] C. Chin, R. Grimm, P. Julienne, and E. Tiesinga, *Feshbach resonances in ultracold gases*, *Reviews of Modern Physics* **82** (2010), no. 2 1225–1286, [arXiv:0812.1496].

[10] S. E. Pollack, D. Dries, M. Junker, Y. P. Chen, T. A. Corcovilos, and R. G. Hulet, *Extreme Tunability of Interactions in a Li7 Bose-Einstein Condensate*, *Physical Review Letters* **102** (mar, 2009) 090402, [arXiv:0811.4456].

[11] Hulet, private communication.

[12] A. J. Moerdijk, W. C. Stwalley, R. G. Hulet, and B. J. Verhaar, *Negative scattering length of ultracold Li7 gas*, *Physical Review Letters* **72** (1994), no. 1 40–43.

[13] C. C. Bradley, C. A. Sackett, and R. G. Hulet, *Bose-Einstein Condensation of Lithium: Observation of Limited Condensate Number*, *Physical Review Letters* **78** (1997), no. 6 985–989, [9604005].

[14] F. Schreck, *Mixtures of Ultracold Gases: Fermi Sea and Bose-Einstein Condensate of Lithium Isotopes*. PhD thesis, University of Paris, 2002.

[15] M. Gustavsson, *A quantum gas with tunable interactions in an optical lattice*. PhD thesis, University of Innsbruck, 2008.

[16] L. Pitaevskii and S. Stringari, *Bose-Einstein Condensation*. Oxford University Press, New York, first ed., 2003.

[17] F. Dalfovo, S. Giorgini, L. P. Pitaevskii, and S. Stringari, *Theory of Bose-Einstein condensation in trapped gases*, *Reviews of Modern Physics* **71** (apr, 1999) 463–512, [9806038].

[18] C. J. Sansonetti, C. E. Simien, J. D. Gillaspy, J. N. Tan, S. M. Brewer, R. C. Brown, S. Wu, and J. V. Porto, *Absolute transition frequencies and quantum interference in a frequency comb based measurement of the* ^{6,7}Li *d lines*, *Phys. Rev. Lett.* **107** (Jul, 2011) 023001.

[19] A. T. Grier, I. Ferrier-Barbut, B. S. Rem, M. Delehaye, L. Khaykovich, F. Chevy, and C. Salomon, Λ*-enhanced sub-Doppler cooling of lithium atoms in D1 gray molasses*, *Physical Review A - Atomic, Molecular, and Optical Physics* **87** (2013), no. 6 1–8, [arXiv:1304.6971].

[20] P. Hamilton, G. Kim, T. Joshi, B. Mukherjee, D. Tiarks, and H. Mueller, *Sisyphus cooling of lithium*, *Physical Review A - Atomic, Molecular, and Optical Physics* **89** (2014), no. 2 [arXiv:1308.1935].

[21] M. Mitsunaga and N. Imoto, *Observation of an electromagnetically induced grating in cold sodium atoms*, *Physical Review A* **59** (1999), no. 6 4773–4776.

[22] D. R. Fernandes, F. Sievers, N. Kretzschmar, S. Wu, C. Salomon, and F. Chevy, *Sub-Doppler laser cooling of fermionic 40K atoms in three-dimensional gray optical molasses*, arXiv:1210.1310.

[23] P. Meystre, *Atom Optics*. Springer-Verlag, 2001.

[24] P. M. Duarte, R. A. Hart, J. M. Hitchcock, T. A. Corcovilos, T. L. Yang, A. Reed, and R. G. Hulet, *All-Optical Production of a Lithium Quantum Gas Using Narrow-Line Laser Cooling*, arXiv:1109.6635.

[25] MIT BEC 5 Group, private communication.

[26] M. H. Anderson, J. R. Ensher, M. R. Matthews, C. E. Wieman, and E. A. Cornell, *Observation of Bose-Einstein Condensation in a Dilute Atomic Vapor*, *Science* **269** (1995), no. 5221 198–201, [1011.1669].

[27] Newport Corporation, *Technical note: Gaussian beam optics*, 2017.

[28] E. A. Donley, T. P. Heavner, F. Levi, M. O. Tataw, and S. R. Jefferts, *Double-pass acousto-optic modulator system*, *Review of Scientific Instruments* **76** (2005), no. 6 3–8.

[29] P. B. Wigley, P. J. Everitt, K. S. Hardman, M. R. Hush, C. Wei, M. A. Sooriyabandara, M. Perumbil, J. D. Close, N. P. Robins, and C. C. N. Kuhn, *Non-destructive shadowgraph imaging of ultracold atoms*, *Optics Letters* **41** (2016), no. 20 4795–4798, [arXiv:1601.0442].

[30] M. Junker, *Single Photon Photoassociation in a ^{7}Li BEC near a Feshbach Resonance*. PhD thesis, Rice University, 2007.

[31] A. Keshet and W. Ketterle, *A Distributed GUI-based Computer Control System for Atomic Physics Experiments*, arXiv:1208.2607.

[32] B. Gadway, D. Pertot, R. Reimann, M. G. Cohen, and D. Schneble, *Analysis of Kapitza-Dirac diffraction patterns beyond the Raman-Nath regime.*, *Optics express* **17** (2009), no. 2002 19173–19180, [arXiv:0907.3507].

[33] R. Senaratne, S. V. Rajagopal, Z. A. Geiger, K. M. Fujiwara, V. Lebedev, and D. M. Weld, *Effusive atomic oven nozzle design using an aligned microcapillary array*, *Review of Scientific Instruments* **86** (feb, 2015) 023105.

[34] C. Stan, *Experiments with Interacting Bose and Fermi Gases*. PhD thesis, Massachusetts Institute of Technology, 2005.

[35] L. Torralbo-Campo, G. D. Bruce, G. Smirne, and D. Cassettari, *Light-induced atomic desorption in a compact system for ultracold atoms*, *Scientific Reports* **5** (2015) 1–10, [arXiv:1312.6442].

[36] M. Taborello, *Cleaning and surface properties*, 2006.

[37] S. B. Montgomery, *Solenoid Magnet Design*. Interscience (Wiley), New York, first ed., 1969.

[38] M. Greiner, O. Mandel, T. Esslinger, T. W. Hänsch, and I. Bloch, *Quantum phase transition from a superfluid to a mott insulator in a gas of ultracold atoms*, *Nature* **415** (2002), no. 6867 39–44.

[39] S. V. Rajagopal, K. M. Fujiwara, R. Senaratne, K. Singh, Z. A. Geiger, and D. M. Weld, *Quantum Emulation of Extreme Non-Equilibrium Phenomena with Trapped Atoms*, *Annalen der Physik* **529** (aug, 2017) 1700008, [arXiv:1705.0430].

[40] A. Eckardt, *Colloquium: Atomic quantum gases in periodically driven optical lattices*, *Reviews of Modern Physics* **89** (mar, 2017) 011004, [arXiv:1606.0804].

[41] M. Holthaus, *Floquet engineering with quasienergy bands of periodically driven optical lattices*, arXiv:1510.0904.

[42] R. Luter and L. E. Reichl, *Floquet analysis of atom-optics tunneling experiments*, *Physical Review A* **66** (nov, 2002) 053615.

[43] C. Tian, A. Kamenev, and A. Larkin, *Weak Dynamical Localization in Periodically Kicked Cold Atomic Gases*, *Physical Review Letters* **93** (sep, 2004) 124101, [0403482].

[44] Z.-Y. Ma, K. Burnett, M. B. D'Arcy, and S. A. Gardiner, *Quantum random walks using quantum accelerator modes*, *Physical Review A* **73** (jan, 2006) 013401, [0508182v1].

[45] M. Sadgrove, A. Milliard, T. Mullins, S. Parkins, and R. Leonhardt, *Observation of robust quantum resonance peaks in an atom optics kicked rotor with amplitude noise*, *Physical Review E - Statistical, Nonlinear, and Soft Matter Physics* **70** (2004), no. 3 2 1–10, [0401161].

[46] H. Lignier, C. Sias, D. Ciampini, Y. Singh, A. Zenesini, O. Morsch, and E. Arimondo, *Dynamical Control of Matter-Wave Tunneling in Periodic Potentials*, *Physical Review Letters* **99** (nov, 2007) 220403, [arXiv:0707.0403].

[47] C. Sias, H. Lignier, Y. P. Singh, A. Zenesini, D. Ciampini, O. Morsch, and E. Arimondo, *Observation of Photon-Assisted Tunneling in Optical Lattices*, *Physical Review Letters* **100** (feb, 2008) 040404, [arXiv:0709.3137].

[48] A. Eckardt, M. Holthaus, H. Lignier, A. Zenesini, D. Ciampini, O. Morsch, and E. Arimondo, *Exploring dynamic localization with a Bose-Einstein condensate*, *Physical Review A* **79** (jan, 2009) 013611, [arXiv:0812.1997].

[49] F. Meinert, M. J. Mark, K. Lauber, A. J. Daley, and H.-C. Nägerl, *Floquet Engineering of Correlated Tunneling in the Bose-Hubbard Model with Ultracold Atoms*, *Physical Review Letters* **116** (may, 2016) 205301, [arXiv:1602.0265].

[50] a. Alberti, V. V. Ivanov, G. M. Tino, and G. Ferrari, *Engineering the quantum transport of atomic wavefunctions over macroscopic distances*, *Nature Physics* **5** (aug, 2009) 547–550, [arXiv:0803.4069].

[51] T. Salger, S. Kling, T. Hecking, C. Geckeler, L. Morales-Molina, and M. Weitz, *Directed Transport of Atoms in a Hamiltonian Quantum Ratchet*, *Science* **326** (nov, 2009) 1241–1243.

[52] E. Haller, R. Hart, M. J. Mark, J. G. Danzl, L. Reichsoellner, and H. C. Naegerl, *Inducing transport in a dissipation-free lattice with super bloch oscillations*, *Physical Review Letters* **104** (2010), no. 20 1–4, [arXiv:1001.1206].

[53] A. Zenesini, H. Lignier, D. Ciampini, O. Morsch, and E. Arimondo, *Coherent control of dressed matter waves*, *Physical Review Letters* **102** (2009), no. 10 1–4, [arXiv:0809.0768].

[54] R. Ma, M. E. Tai, P. M. Preiss, W. S. Bakr, J. Simon, and M. Greiner, *Photon-assisted tunneling in a biased strongly correlated bose gas*, *Physical Review Letters* **107** (2011), no. 9 1–4, [arXiv:1105.4629].

[55] G. Rubino, L. A. Rozema, A. Feix, M. Araújo, J. M. Zeuner, L. M. Procopio, Č. Brukner, and P. Walther, *Experimental Verification of an Indefinite Causal Order*, arXiv:1608.0168.

[56] A. R. Kolovsky, *New bloch period for interacting cold atoms in 1D optical lattices.*, *Physical review letters* **90** (2003), no. 21 213002, [0302092].

[57] S. R. Wilkinson, C. F. Bharucha, K. W. Madison, Q. Niu, and M. G. Raizen, *Observation of Atomic Wannier-Stark Ladders in an Accelerating Optical Potential*, *Physical Review Letters* **76** (jun, 1996) 4512–4515.

[58] U. Peschel, T. Pertsch, and F. Lederer, *Optical Bloch oscillations in waveguide arrays*, *Optics Letters* **23** (1998), no. 21 1701.

[59] M. Glück, A. R. Kolovsky, H. J. Korsch, and F. Zimmer, *Wannier-Stark resonances in semiconductor superlattices*, *Physical Review B - Condensed Matter and Materials Physics* **65** (2002), no. 11 1153021–1153029, [0111132].

[60] T. Hartmann, F. Keck, H. J. Korsch, and S. Mossmann, *Dynamics of Bloch oscillations*, *New Journal of Physics* **6** (jan, 2004) 2–2.

[61] A. R. KOLOVSKY and H. J. KORSCH, *Bloch Ooscillations of Cold Atoms in Optical Lattices*, *International Journal of Modern Physics B* **18** (apr, 2004) 1235–1260, [0403205].

[62] M. Ben Dahan, E. Peik, J. Reichel, Y. Castin, and C. Salomon, *Bloch Oscillations of Atoms in an Optical Potential*, *Physical Review Letters* **76** (jun, 1996) 4508–4511.

[63] R. Zhang, R. E. Sapiro, R. R. Mhaskar, and G. Raithel, *Role of the mean field in Bloch oscillations of a Bose-Einstein condensate in an optical lattice and harmonic trap*, *Physical Review A - Atomic, Molecular, and Optical Physics* **78** (2008), no. 5 1–7, [0806.4893].

[64] A. Alberti, G. Ferrari, V. V. Ivanov, M. L. Chiofalo, and G. M. Tino, *Atomic wave packets in amplitude-modulated vertical optical lattices*, *New Journal of Physics* **12** (jun, 2010) 065037, [arXiv:0903.0724].

[65] V. V. Ivanov, A. Alberti, M. Schioppo, G. Ferrari, M. Artoni, M. L. Chiofalo, and G. M. Tino, *Coherent delocalization of atomic wave packets in driven lattice potentials*, *Physical Review Letters* **100** (2008), no. 4 1–4, [arXiv:0801.1570].

[66] M. Fattori, C. D'Errico, G. Roati, M. Zaccanti, M. Jona-Lasinio, M. Modugno, M. Inguscio, and G. Modugno, *Atom interferometry with a weakly interacting bose-einstein condensate*, *Physical Review Letters* (2008) [0710.5131].

[67] M. Gustavsson, E. Haller, M. J. Mark, J. G. Danzl, R. Hart, A. J. Daley, and H. C. Nägerl, *Interference of interacting matter waves*, *New Journal of Physics* **12** (2010) [arXiv:0812.4836].

[68] F. Meinert, M. J. Mark, E. Kirilov, K. Lauber, P. Weinmann, M. Gröbner, and H.-C. Nägerl, *Interaction-Induced Quantum Phase Revivals and Evidence for the Transition to the Quantum Chaotic Regime in 1D Atomic Bloch Oscillations*, *Physical Review Letters* **112** (may, 2014) 193003, [arXiv:1309.4045].

[69] A. M. Bouchard and M. Luban, *Bloch oscillations and other dynamical phenomena of electrons in semiconductor superlattices*, *Physical Review B* **52** (1995), no. 7 5105–5123.

[70] F. Domínguez-Adame, *Beyond the semiclassical description of Bloch oscillations*, *European Journal of Physics* **31** (2010), no. 3 639–644.

[71] P. M. Preiss, R. Ma, M. E. Tai, A. Lukin, M. Rispoli, P. Zupancic, Y. Lahini, R. Islam, and M. Greiner, *Strongly Correlated Quantum Walks in Optical Lattices*, arXiv:1409.3100.

[72] C. Gaul, E. Díaz, R. P. A. Lima, F. Domínguez-Adame, and C. A. Müller, *Stability and decay of Bloch oscillations in the presence of time-dependent nonlinearity*, *Physical Review A - Atomic, Molecular, and Optical Physics* **84** (2011), no. 5 1–13, [arXiv:1109.2798].

[73] K. McDonald, *Relativistic harmonic oscillator*, 2013.

[74] J. A. Franco-Villafañe, E. Sadurní, S. Barkhofen, U. Kuhl, F. Mortessagne, and T. H. Seligman, *First experimental realization of the dirac oscillator*, *Physical Review Letters* **111** (2013), no. 17 1–5, [arXiv:1306.2204].

[75] M. G. Tarallo, A. Alberti, N. Poli, M. L. Chiofalo, F. Y. Wang, and G. M. Tino, *Delocalization-enhanced Bloch oscillations and driven resonant tunneling in optical lattices for precision force measurements*, *Physical Review A - Atomic, Molecular, and Optical Physics* **86** (2012), no. 3 1–16, [arXiv:1207.2123].

[76] I.-D. Potirniche, A. C. Potter, M. Schleier-Smith, A. Vishwanath, and N. Y. Yao, *Floquet Symmetry-Protected Topological Phases in Cold-Atom Systems*, *Physical Review Letters* **119** (sep, 2017) 123601.

[77] J. Struck, C. Ölschläger, R. Le Targat, P. Soltan-Panahi, A. Eckardt, M. Lewenstein, P. Windpassinger, and K. Sengstock, *Quantum Simulation of Frustrated Classical Magnetism in Triangular Optical Lattices*, *Science* **333** (aug, 2011) 996 LP – 999.

[78] P. Hauke, O. Tieleman, A. Celi, C. Ölschläger, J. Simonet, J. Struck, M. Weinberg, P. Windpassinger, K. Sengstock, M. Lewenstein, and A. Eckardt, *Non-Abelian Gauge Fields and Topological Insulators in Shaken Optical Lattices*, *Physical Review Letters* **109** (2012), no. 14 145301, [arXiv:1205.1398].

[79] M. Aidelsburger, S. Nascimbene, and N. Goldman, *Artificial gauge fields in materials and engineered systems*, arXiv:1710.0085.

[80] F. Machado, G. D. Meyer, D. V. Else, C. Nayak, and N. Y. Yao, *Exponentially Slow Heating in Short and Long-range Interacting Floquet Systems*, arXiv:1708.0162.

[81] R. Moessner and S. L. Sondhi, *Equilibration and Order in Quantum Floquet Matter*, 1701.0805.

[82] P. Liang, M. Marthaler, and L. Guo, *Floquet Many-body Engineering: Topological and Many-body Physics in Phase Space Lattices*, arXiv:1710.0971.

[83] E. Michon, C. Cabrera-Gutiérrez, A. Fortun, M. Berger, M. Arnal, V. Brunaud, J. Billy, C. Petitjean, P. Schlagheck, and D. Guéry-Odelin, *Out-of-equilibrium dynamics of a Bose Einstein condensate in a periodically driven band system*, 1707.0609.

[84] E. J. Meier, J. Ang'ong'a, F. A. An, and B. Gadway, *Exploring quantum signatures of chaos on a Floquet synthetic lattice*, arXiv:1705.0671.

[85] R. Driben, V. V. Konotop, T. Meier, and A. V. Yulin, *Bloch oscillations sustained by nonlinearity*, *Scientific Reports* **7** (2017), no. 1 3194.

[86] G. M. Koutentakis, S. I. Mistakidis, and P. Schmelcher, *Quench-induced resonant tunneling mechanisms of bosons in an optical lattice with harmonic confinement*, *Physical Review A* **95** (jan, 2017) 013617.

[87] P. J. Everitt, M. A. Sooriyabandara, M. Guasoni, P. B. Wigley, C. H. Wei, G. D. McDonald, K. S. Hardman, P. Manju, J. D. Close, C. C. N. Kuhn, Y. S. Kivshar, and N. P. Robins, *Observation of Modulational Instability in Bose-Einstein condensates*, arXiv:1703.0750.

[88] J. H. V. Nguyen, D. Luo, and R. G. Hulet, *Formation of matter-wave soliton trains by modulational instability*, *Submitted for Publication* (2016) [arXiv:1703.0466].

[89] R. Roy and F. Harper, *Floquet topological phases with symmetry in all dimensions*, arXiv:1610.0689.

[90] D. Dries, S. E. Pollack, J. M. Hitchcock, and R. G. Hulet, *Dissipative transport of a Bose-Einstein condensate*, *Physical Review A - Atomic, Molecular, and Optical Physics* **82** (2010), no. 3 1–13, [arXiv:1004.1891].